Impact of atmospheric variability on a solar based power system in West Africa

Inaugural-Dissertation
zur
Erlangung des Doktorgrades
der Mathematisch-Naturwissenschaftlichen Fakultät
der Universität zu Köln

vorgelegt von
Ina Neher
aus Friedberg (Hessen)

Köln, 2020

Berichterstatter:
Prof. Dr. Susanne Crewell
Prof. Dr. Stefanie Meilinger
Prof. Dr. Stephanie Fiedler

Tag der mündlichen Prüfung:
26.06.2020

Abstract

For a sustainable development the electricity sector needs to be decarbonized. In 2017 only 54% of the West African households had access to the electrical grid. Thus, renewable sources should play a major role for the development of the power sector in West Africa. Above all, solar power shows highest potential of renewable energy sources. However, it is highly variable, depending on the atmospheric conditions.

This study addresses the challenges for a solar based power system in West Africa by analyzing the atmospheric variability of solar power. For this purpose, two aspects are investigated. In the first part, the daily power reduction due to atmospheric aerosols is quantified for different solar power technologies. Meteorological data at six ground-based stations is used to model photovoltaic and parabolic trough power during all mostly clear-sky days in 2006. A radiative transfer model is combined with solar power model. The results show, that the reduction due to aerosols can be up to 79% for photovoltaic and up to 100% for parabolic trough power plants during a major dust outbreak. Frequent dust outbreaks occurring in West Africa would cause frequent blackouts if sufficient storage capacities are not available. On average, aerosols reduce the daily power yields by 13% to 22% for photovoltaic and by 22% to 37% for parabolic troughs.

For the second part, long-term atmospheric variability and trends of solar irradiance are analyzed and their impact on photovoltaic yields is examined for West Africa. Based on a 35-year satellite data record (1983 - 2017) the temporal and spatial variability and general trend are depicted for global and direct horizontal irradiances. Furthermore, photovoltaic yields are calculated on a daily basis. They show a strong meridional gradient with highest values of 5 kWh/kWp in the Sahara and Sahel zone and lowest values in southern West Africa (around 4 kWh/kWp). Thereby, the temporal variability is highest in southern West Africa (up to around 18%) and lowest in the Sahara (around 4.5%). This implies the need of a North-South grid development, to feed the increasing demand on the highly populated coast by solar power from the northern parts of West Africa. Additionally, global irradiances show a long-term positive trend (up to +5 W/m^2/decade) in the Sahara and a negative trend (up to -5 W/m^2/decade) in southern West Africa. If this trend is continuing, the spatial differences in solar power potential will increase in the future.

This thesis provides a better understanding of the impact of atmospheric variability on solar power in a challenging environment like West Africa, characterized by the strong influence of the African monsoon. Thereby, the importance of aerosols is pointed out. Furthermore, long-term changes of irradiance are characterized concerning their implications for photovoltaic power.

Zusammenfassung

Um eine nachhaltige Entwicklung umzusetzen muss der Stromsektor dekarbonisiert werden. Im Jahr 2017 waren 54% der westafrikanischen Haushalte nicht an das Stromnetz angeschlossen. Deshalb sollte dort für die Entwicklung des Stromnetzes auf erneuerbare Ressourcen gesetzt werden. Wegen des hohen Potentials wird insbesondere Solarenergie eine entscheidende Rolle spielen. Jedoch ist diese stark von den atmosphärischen Bedingungen abhängig.

In dieser Arbeit werden die Herausforderungen für ein solar betriebenes Energiesystem in Westafrika untersucht. Dabei wird im ersten Teil der Einfluss von atmosphärischen Aerosolen quantifiziert. Meteorologische Daten aus dem Jahr 2006 von überwiegend klaren Tagen an sechs Messstationen werden genutzt, um den Ertrag eines potentiellen Photovoltaik- und eines Parabolrinnenkraftwerkes zu modellieren. Während eines Sandsturms können Aerosole für eine Ertragsreduktion von bis zu 79% bei Photovoltaik- und von bis zu 100% bei Parabolrinnenkraftwerken verantwortlich sein. Im Durchschnitt reduzieren Aerosole den Ertrag von Photovoltaikanlagen um 13% bis 22% und von Parabolrinnenkraftwerken um 22% bis 37%.

Im zweiten Teil werden die langfristige atmosphärische Variabilität und generelle Trend analysiert und deren Einfluss auf Photovoltaikerträge in Westafrika beleuchtet. Basierend auf Satellitendaten (1983 - 2017) werden sowohl zeitliche und räumliche Variabilität als auch Trends der Global- und Direktstrahlung bestimmt. Außerdem wird der Photovoltaikertrag anhand von Tageswerten berechnet. Der Ertrag zeigt eine starke meridionale Abhängigkeit mit höheren Erträgen und niedrigerer Variabilität in der Sahara und Sahel Zone (mehr als 5 kWh/kWp und etwa $\pm$ 4.5%) und niedrigeren Erträgen und höherer Variabilität im südlichen Westafrika (etwa 4 kWh/kWp $\pm$ 18%). Hier wird sichtbar, dass ein Netzausbau in Nord-Süd Richtung notwendig ist, um die bevölkerungsreiche Küste mit Solarstrom aus der nördlichen Region zu versorgen. Zusätzlich ist ein positiver Trend (bis zu +5 W/m^2/Dekade) der Globalstrahlung in der Sahara und ein negativer Trend (bis zu -5 W/m^2/Dekade) im südlichen Westafrika zu erkennen. Setzt sich dieser Trend weiter fort, werden sich die regionalen Unterschiede im Solarenergiepotential in Zukunft noch verstärken.

Diese Arbeit verbessert das Verständnis der atmosphärischen Einflüsse auf Solarenergie in einer vielfältigen Region wie Westafrika. Die Bedeutung des Aerosoleinflusses wird deutlicher, insbesondere in Wüstenregionen. Außerdem werden langzeitliche Veränderungen der Strahlung charakterisiert und deren Einfluss auf Photovoltaik aufgezeigt.

Contents

Chapter 1

Introduction

1.1 Motivation and state of the art

One of the biggest challenges for humanity is to sustainably live on the Earth to keep it livable for future generations. To achieve sustainable development the United Nations defined 17 goals as a call for action. These Sustainable Development Goals (SDG) aim to "end poverty, protect the planet and ensure that all people enjoy peace and prosperity" (United Nations 2015). All these aims can be highly connected to climate conditions. The Intergovernmental Panel on Climate Change (IPCC) predicts an increasing risk for extreme weather events like droughts, floods and heat waves due to climatic changes (IPCC 2014a). These events might cause a lack in agricultural production, military conflicts or land degradation and flooding, to name only the obvious consequences. Especially greenhouse gas (GHG) emissions impact the Earth climate and force climatic changes. These GHG emissions are mainly driven by population growth and lifestyle, i.e. higher use of resources.

Globally the electricity sector is responsible for around one quarter of GHG emissions (IPCC 2014b). The seventh goal of the SDGs proposes to "ensure access to affordable, reliable, sustainable and modern energy for all". With the Paris Agreement (UNFCCC 2015) and according to international law the total decarbonization of the electricity sector is requested. The electricity sector depends on future demand and available technologies as well as on political decisions. Currently, the most promising solution to decarbonize the electricity sector are renewable energies (Delucchi and Jacobson 2011).

Especially in poor regions of the world, renewable energies can contribute to a sustainable and more reliable electricity system. In this study we focus on West Africa, where grid connected electricity is currently mainly based on gas, oil and hydro power (Sterl et al. 2020a, IRENA 2018a). The electrification rate lies below 50% (in 2010-2011) in many West African countries (ECOWAS 2014) and only 54% of the households have access to the electric grid (in 2017) (Abdulrahman and

Paco 2019).[1] Therewith, the West African energy sector is confronted with two major challenges. First, the rising demand and current lack in electricity supply needs to be served. Second, climatic changes and international agreements (e.g. Paris Agreement (UNFCCC 2015)) require carbon neutral solutions (e.g. renewable energies). Many West African countries are moving toward this decarbonization of the power sector by setting high targets for renewable energy use (ECOWAS 2014).

Globally the highest technical potential of renewable energy sources is given by direct solar energy[2] (SREEN 2012). By being prone to high solar insolation year around West Africa is suitable for solar based power systems (Solargis 2019). However, the yield of solar power systems is highly variable and depends on the frequently changing atmospheric composition (Sengupta et al. 2017). The dependency of power supply on atmospheric conditions increases with a rising share of solar power in the electricity system. Therefore, the integration of solar power into the electricity system raises challenges for the dimensioning of power plants and storage as well as for network stability and grid development (Lorenz et al. 2011). Only with the knowledge of temporally and spatially high-resolved solar power resources, profits can be estimated and thus stimulate large scale private investments in the solar power sector. Furthermore, they are necessary for the integration of solar power plants into the electricity system and to secure network stability.

Shortwave global irradiance at ground is the major modulator of solar power (e.g. Sengupta et al. 2017). Its variability highly depends on atmospheric properties, such as clouds, aerosols and water vapor as well as on the daily and seasonal cycle, due to the Earth's orbit around the sun (Perez et al. 2016). The latter one is well known and can be calculated from astronomical formulas. The atmospheric variability depends on local conditions, which are variable in space and time. A high temporal resolution (less than one hour) of atmospheric data is required to estimate the power variability over the course of the day (Gueymard and Wilcox 2011). Therefore, the impact of clouds, aerosols and water vapor on solar irradiance needs to be investigated to enable the calculation of potential solar power. However, these quantities (clouds, aerosols and water vapor) show the largest uncertainties in weather and climate models (e.g. Rieger et al. 2017, Sengupta et al. 2017, Boucher et al. 2013).

Only a few studies investigated solar power in West Africa, focusing on different aspects, e.g. site assessment (Yushchenko et al. 2018, Ramdé et al. 2013), grid development (Adeoye and Spataru 2018) and future potential (Bazyomo et al. 2016, Köberle et al. 2015). For such studies information on solar irradiance is needed which is taken from either global climate models or long-term yearly averages. However,

[1] Numbers are given for the Economic Community of West African States (ECOWAS), including Benin, Burkina Faso, Cabo Verde, Cote d'Ivory, The Gambia, Ghana, Guinea, Guinea Bissau, Liberia, Mali, Niger, Nigeria, Senegal, Sierra Leone and Togo.

[2] Direct solar energy is defined here as the direct use of solar irradiance to produce electricity, including photovoltaic and concentrating solar power. Note that the term 'direct' connects to the direct use of solar irradiance for power generation, by using diffuse and direct irradiance.

no temporally highly resolved solar irradiance data is used to determine the power yield of solar based systems.

There are three major types of surface solar irradiance data: measurements (including ground-based or satellite data), models (including numerical models for weather and climate prediction) and reanalyses (combining observations and models). While ground-based measurements provide the most accurate information on irradiance at a certain location, such measurements are not available over larger domains. Satellite data aim to fill this gap. However, satellite retrievals are based on reflectance measurements in the visible and near-infrared spectral range. The derivation of surface radiation, requires assumptions on aerosol distribution, which is typically taken from climatologies (Mueller et al. 2015, Boucher et al. 2013). Radiative transfer models are well suited to investigate the impact of single atmospheric parameters (e.g. gases, clouds, aerosols). However, they depend on the accuracy and availability of the atmospheric input data and need high computational times. Reanalyses provide high temporal and spatial resolved best estimates from historical atmospheric information combined with advanced modeling and data assimilation systems. However, the accuracy of the data highly depends on the correct description of atmospheric phenomena and needs to be validated for each new product.

West Africa is a region with very few routine meteorological measurements. Prominent international projects concerning the characterization of the climate were recently undertaken in West Africa, the African Monsoon Multidisciplinary Analysis (AMMA) since 2002 (Redelsperger et al. 2006) and the Dynamics-aerosol-chemistry-cloud interactions in West Africa (DACCIWA) project since 2013 (Knippertz et al. 2015). The main goal of AMMA was to investigate the West African climate and to achieve a better understanding of the West African Monsoon (WAM). The DACCIWA project aims to quantify the natural and anthropogenic emissions over southern West Africa and their impact on the atmospheric composition. During both projects many additional meteorological instruments have been deployed for continuous and temporal measurements. The DACCIWA campaign included aircraft and ground-based measurements in June-July 2016 covering the pre and post-onset phase of the WAM. Furthermore, three supersites were established for longer term measurements. The data of these campaigns were analyzed concerning changes of atmospheric parameters (e.g. aerosols (e.g. Deetz et al. 2018, Cavalieri et al. 2011, Matsuki et al. 2010), clouds (e.g. Babić et al. 2019, Kniffka et al. 2019, Penide et al. 2010) and their interaction (e.g. Taylor et al. 2019, Crumeyrolle et al. 2008)). Furthermore, the measurements were used for the evaluation of numerical weather prediction and climate models (e.g. Hannak et al. 2017, Hourdin et al. 2010). However, up to now the campaign data have not been used to assess the potential of solar power in the region of West Africa which is the topic of the thesis at hand.

1.2 Thesis overview

Solar energy will play a key role in the future global sustainable electricity-mix. Here this technology is analyzed concerning the impact of atmospheric variability on power yields. West Africa is used as study region for several reasons. First, it is a region with high solar insolation year around with an average annual sum of global irradiance up to 2400 kWh/m^2 (Solargis 2017). Second, the region is suffering from a lack of electricity as well as energy infrastructure and the energy system needs to be expanded to serve current and future demand.

West Africa is a particular challenging region due to the WAM, which leads to a typical annual cycle of clouds and precipitation in south and central West Africa. This implicates regular dry and wet seasons and related variable solar irradiance. During the dry season, with only few clouds, frequent dust outbreaks and therewith extreme aerosol loads occur. A detailed analysis of extreme aerosol loads, resulting in high reductions of solar power, can be undertaken for this region.

The central research question of this thesis "What is the impact of atmospheric variability on solar based power systems in West Africa?" is divided into two sub-questions, each representing the focus of one result chapter.

1. What is the impact of atmospheric aerosols on concentrating and photovoltaic solar power plants (Chapter 4)?

2. How do long-term atmospheric variability and trends affect photovoltaic yields in West Africa (Chapter 5)?

In this thesis different types of solar irradiance data are used. Ground-based measurements are utilized to validate newly developed models (the "Solar Power modeling including atmospheric Radiative Transfer" (SolPaRT) model and a linear photovoltaic yield model) and satellite retrievals. A radiative transfer model, calculating surface irradiances for a given atmospheric state, is applied to analyze the aerosol impact at several locations where ground-based measurements of aerosol optical properties are available. Novel satellite retrievals covering the full region of West Africa are exploited to investigate the long-term trends and variability of solar irradiance and its implications on photovoltaic power. How these different data sets and tools are used to answer the two main questions is detailed in the following.

1. Impact of atmospheric aerosols on solar power

Solar based power system are impacted by the atmospheric variability of the incoming solar irradiance. This variability is mainly driven by the absorption and scattering of solar radiation by aerosol and cloud particles as well as trace gases (e.g. Wendisch and Yang 2012, Wallace and Hobbs 2006). Even if clouds are a more efficient modulator of solar radiation, this part of the thesis focuses on the impact of

aerosols on solar power for three reasons. First, especially in a desert environment like in the Sahel and the Sahara aerosols can become the decisive factor, limiting the availability of solar irradiance, during the dry season (Kothe et al. 2017). Second, frequent dust outbreaks might cause severe power reductions, which need to be regarded by planing a storage and grid system for the power sector (Rieger et al. 2017). Third, aerosols are often only included as climatology in global climate models and satellite retrievals (e.g. Pu and Ginoux 2018, Mueller et al. 2015, Boucher et al. 2013) and therefore their temporal variability is neglected.

Depending on their physical and chemical composition aerosols reduce global horizontal irradiance (GHI) (e.g. Boucher 2015, Kaufman et al. 2002, Hess et al. 1998). Direct normal irradiance (DNI) is strongly lowered while diffuse horizontal irradiance (DHI) is changed concerning its direction and increased to some maximum. Different solar irradiance components are used by different solar power technologies. While concentrating solar power (CSP) plants only exploit DNI, non-concentrating technologies, such as photovoltaic, use GHI.

The central question of this part of the thesis can be refined into:

1. What is the magnitude of the impact of aerosols on solar power?

2. How sensitive are photovoltaic and concentrating solar technologies to aerosol conditions?

3. Which challenges need to be considered during a desert dust outbreak?

To answer these questions first a model framework ("Solar Power modeling including atmospheric Radiative Transfer" - SolPaRT) to separate the aerosol effect from other atmospheric quantities is developed. This model combines a radiative transfer model with solar power calculations and explicitly considers the impact of aerosols on solar irradiance. The impact of clouds is ruled out by considering clear sky situations only. For the quantification of the aerosol impact on solar power the aerosol-free and aerosol-loaded atmosphere are compared. The model is validated by using measurements in Sankt Augustin, Germany. Furthermore, a location (Niamey, Niger) with detailed observational data and high solar insolation is used to give answer to the first sub-question (see Section 4.1). The second and third sub-questions then are addressed by analyzing historical data at six well distributed locations in West Africa (see Section 4.2).

2. Variability of solar irradiance and its implications for photovoltaic power

A detailed analysis of the variability as well as long-term trends of solar irradiance is necessary to identify suitable sites for photovoltaic power plants. To determine

economically promising sites for photovoltaic power plants a regional analysis of the resource over total West Africa is needed.

Ground-based measurements have a limited availability. Satellite based data instead are available over larger regions and long time periods (Gueymard and Wilcox 2011). In particular, geostationary satellites can provide data having a temporal resolution of one hour or less to analyze the intraday variability. The Meteosat satellites are geostationary and operated by the European Organisation for the Exploitation of Meteorological Satellites (EUMETSAT). The Satellite Application Facility on Climate Monitoring (CM SAF) provides the Surface Solar Radiation Data Set-Heliosat, Edition 2 (SARAH-2.1) by using Meteosat satellite data. SARAH-2.1 is a 35-year long climate record for solar irradiance at ground with an half hourly resolution, covering the whole of Europe and Africa (Pfeifroth et al. 2019).

In this part, the central question is split into two sub-questions:

1. How variable is solar irradiance and therewith photovoltaic power potential between 1983 and 2017 in West Africa?

2. What are the trends of solar irradiance during these 35 years and how do they impact photovoltaic potential?

To answer these questions the global and direct horizontal irradiance of the SARAH-2.1 data record is analyzed for West Africa (3°N to 20°N; 20°W to 16°E, see Chapter 5). The objectives of the analysis are fourfold. First, the satellite data record is validated with ground-based measurements at three sites to determine their suitability. Second, the variability and trends of solar irradiances are estimated annually as well as for the dry and wet season separately with a spatial resolution of 0.05°x0.05°. Third, the temporal variability is analyzed by monthly anomalies along a meridional gradient which exhibits the strongest variations. Finally, a simple approach is derived which allows to derive photovoltaic yields for the full region of West Africa and subsequently addresses their variations.

Structure of the thesis

In the following, this thesis first provides background information on the West African climate, solar power, solar irradiance and atmospheric aerosols (Chapter 2). Chapter 3 summarizes the used data sources and models as well as the newly developed model chain SolPaRT. The impact of aerosols on solar power is presented in Chapter 4. Chapter 5 points out the potential of photovoltaic power in West Africa. Finally, Chapter 6 gives an overall conclusion and outlook.

Chapter 2

Background

This chapter gives an overview on the background of this thesis. First, West Africa with its current climatological conditions is described, including solar power, the climate and aerosols. Second, different solar energy technologies are characterized. Third, solar irradiance and its interaction within the atmosphere is presented by giving a short introduction to the radiative transfer theory. Finally, aerosol properties and their interconnection to land use conditions are summarized, as the atmospheric composition of aerosols depend among other factors on local land use properties.

2.1 West Africa

West Africa is located at the westernmost edge of Africa, including Benin, Burkina Faso, Cape Verde, The Gambia, Ghana, Guinea, Guinea-Bissau, Ivory Coast, Liberia, Mali, Niger, Nigeria, Senegal, Sierra Leone and Togo, also known as the Economic Community of West African States (ECOWAS). In the west and south the region is limited by the Atlantic Ocean. The northern boundary is the central Sahara and in the east an imaginary north-south boundary at 10°E delimits the region. West Africa is the habitat of around 350 million people and covers more than 5 million square kilometers of land. Vegetation in West Africa is diverse and can be classified into five east-west vegetation belts, the Saharan, Sahel, Sudanian, Guinean and Guinean-Congolian regions (from north to south, see Figure 2.1). The

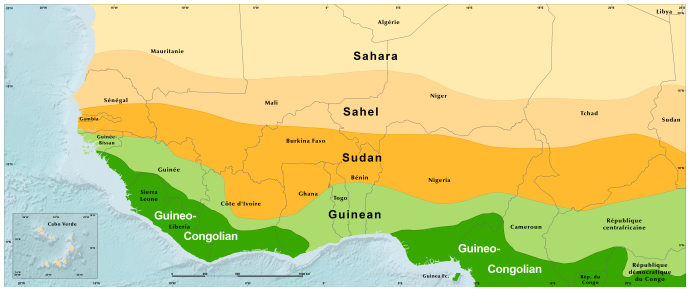

Figure 2.1: Landscapes of West Africa (CLISS 2016).

Saharan region is dominated by arid and sandy landscapes. The Sahel is a home for grass and bush lands as well as for the Sahel-acacia-Savanna. In the Sudanian region vegetation ranges from open tree savannas to wooded savannas and open woodlands. The landscape in the Guinean region manly consists of forests, with a tree height of around 18 to 20 m. The wettest region is the Guinean-Congolian, with dense forests and trees reaching up to 60 m height and the highest population density. (CLISS 2016)

2.1.1 Solar energy

Currently solar power plays hardly any role in West Africa with far less than 1% of final energy consumption and 454.5 MW installed capacity (in 2018) (IRENA 2018b). Thereby up to today only photovoltaic (PV) power is used, there are no CSP plants running or planed for West Africa. The usage of PV power in West Africa is twofold. On the one hand, small solar home systems and mini-grids connect rural areas to electricity (especially in Sierra Leone, Senegal, Mali, Niger, Nigeria, Benin and Togo). On the other hand, a few larger PV power stations exist in Burkina Faso, Ghana, Niger, Senegal and Cabo Verde (ECOWAS 2019). The largest grid connected PV power plant is Zagouli in Burkina Faso with 33.7 MW (Sterl et al. 2020b).

The future energy plan for the West African region is projected from different organizations, including all renewable sources, with hydro power having the largest share. The ECOWAS projects around 7.6 GW installed capacity of renewable energies (48% of total installed capacity) by 2030 (ECREE 2017). The West African Power Pool (WAPP) Master Plan, and the ECOWAS Renewable Energy Policy (EREP) propose to increase the share of renewable energy production to 23% by 2020 and 31% by 2030. The International Renewable Energy Agency (IRENA) estimates that more than 25% of West Africa's power will come from renewable sources in 2030 (with an installed capacity of 65% of renewable energies) (IRENA 2018b). Furthermore, IRENA estimates an overall PV power potential of more than 100.000 TWh/year and an overall CSP potential of around 22.000 TWh/year (Hermann et al. 2014). With around 7 GW of currently planned PV power plants over the region, solar energy use is already accelerating (Sterl et al. 2020b).

Many West African countries have their own policy targets for renewable energies. Cabo Verde has the highest target, with 50% grid connected renewable energies in 2020. In other West African countries the targets of renewable energies range from 10% (in Ghana and Niger) to 35% (in The Gambia) for 2020. (ECOWAS 2014)

2.1.2 Regional climate and aerosols

The West African climate is highly variable due to its location between the humid equatorial region and the dry subtropical desert regions. The northern region in the

Sahara is mainly influenced by the high pressure belt due to the so-called Hadley circulation causing the dry trade winds (also called Harmattan). Thus, in the northern regions arid, desert conditions prevail. The southern coast is humid all-year round and there is a transition zone to the north which has distinct dry and wet seasons, influenced by the WAM. These sharp contrasts between the two regions are caused by the global circulation system. The Hadley circulation characterizes an upward motion of the air in the equatorial region and identifies the Intertropical convergence zone (ITCZ) (Kraus 2004). In contrast, the northern desert region is influenced by the subsiding air branch of the Hadley cell.

According to the Köppen-Geiger climate classification (Peel et al. 2007), climatic conditions range from tropical climates (equatorial, monsoon and tropical savanna climate) near the coast in the south over a narrow belt of warm semi-arid climate in the central latitude of West Africa to a warm desert climate in the Sahara (see Figure 2.2). Tropical climates show average temperatures of 18°C or higher for the coldest month and typical precipitation pattern. A warm semi-arid climate represents a savanna climate and a warm desert climate an arid desert climate, both are defined due to their low precipitation, whereby the desert climate shows lower precipitation than the semi-arid climate. (Peel et al. 2007)

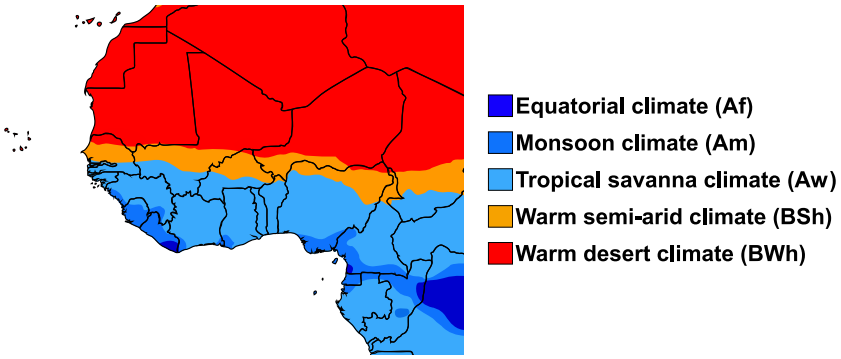

Figure 2.2: Map of West Africa with Köppen-Geiger climate classification (derived from Peel et al. (2007)).

The averaged annual sum of GHI between 1994 and 2016 varied in West Africa between about 1600 kWh/m^2 and 2400 kWh/m^2 (see Figure 2.3, (Solargis 2019)). Compared to other regions in the world incoming solar irradiance is high in West Africa, especially in the Saharan region. Between 1983 and 2015 the Sahara was one of the most sunny regions on Earth (see Figure 2.4 from the CM SAF). Sunshine hours go up to 4000 hours/year. For the whole West African region, sunshine hours vary between around 2400 hours/year (6.6 hours/day) near the Guinean coast to up to 4000 hours/year (more than 10 hours/day) in the desert region (Kothe et al. 2017).

In West Africa, radiative transfer is mainly conditioned by the WAM circulation in the southern parts, causing the formation of clouds and their variability. The relevance of dust from the Sahara and biomass burning on solar irradiance increases

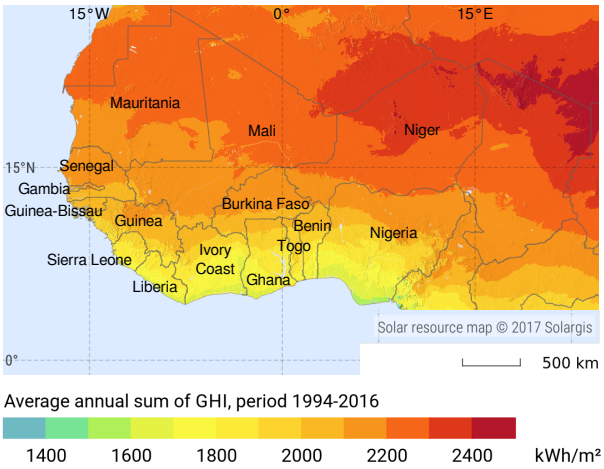

Figure 2.3: Averaged sum of global horizontal irradiance (modeled by Solargis) in West Africa (adapted from Solargis (2019)).

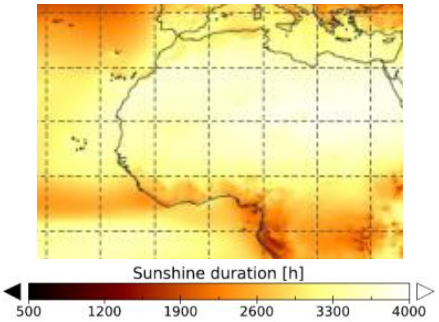

Figure 2.4: Mean annual sum of average sunshine hours in West Africa between 1983 and 2015 (derived from Kothe et al. (2017), who used the SARAH-2.1 data record).

towards the north (Miller et al. 2012). In the Sahel zone precipitation is connected to the dry and wet season (Lélé and Lamb 2010, Yoshioka et al. 2007). During the dry season (October-April) hardly any rainfall is observed in this region, while during the wet season precipitation fluxes reach up to 5 mm/day (Miller et al. 2012). Over the total region the mean annual rainfall ranges from less than 100 mm to over 1.800 mm (see Figure 2.5) (Niang et al. 2014). Months with more than 50 mm rainfall range from 0 in the Sahara to 10 at the Guinean coast. The effective cloud albedo between 1983 and 2017 (see Figure 1 c in Chapter 5) is low in the north of West Africa and increases towards the south. Near to the coast it reaches up to 0.3.

The aerosol composition in West Africa consists of a complex mixture of combustion aerosols and dust particles from the Sahara (Marticorena et al. 2011, Liousse et al. 2010, Haywood et al. 2008). Major emitters for combustion aerosols are biomass burning (mainly in the savanna during the dry season), fossil fuels (from traffic and industry, mainly in urban areas, year around) and fires for domestic use (cooking with fuelwood and charcoal, distributed over rural areas, year around). Mineral dust is ubiquitous in West Africa, it is present all year around especially in

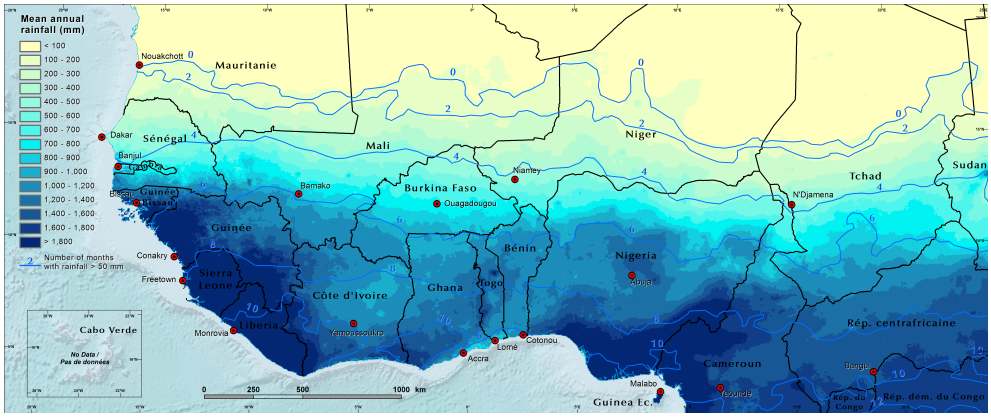

Figure 2.5: Mean annual rainfall in West Africa (Derived from data from the IPCC 5th Assessment Report (Niang et al. 2014) for West Africa).

the northern part. However, there exist a typical dust cycle over the course of the year. Dust concentrations peak during the dry season, with frequent dust emissions (Cowie et al. 2014). Also in the beginning of the wet season high dust concentrations of more than 4000 µg/m^3 are present (Marticorena et al. 2011). Especially in the dry season, the Harmattan winds transport the dusty air from the Sahara towards the south, while the air loaded by biomass burning aerosols mainly remains south. Especially near the ITCZ the dusty air is mixed with air loaded by biomass burning aerosols. Some secondary organic aerosols formed from vegetation (Capes et al. 2009), nitrates from soil (Delon et al. 2010) and maritime aerosols (Marticorena et al. 2011) (especially near the coast) can be found as well. Satellite retrievals, remote sensing and ground measurements show annual mean aerosol optical depth (AOD) of up to 0.6 in the Sahara (see Figure 2.6, (Kinne et al. 2013)). In the global view, West Africa is one of the regions with highest annual AOD. In many regions of the world, the AOD lies under 0.2 (see Figure 2.6). When looking at ground measurements, AOD can go beyond 4 in the West African region and is highly variable in time (Slingo et al. 2006).

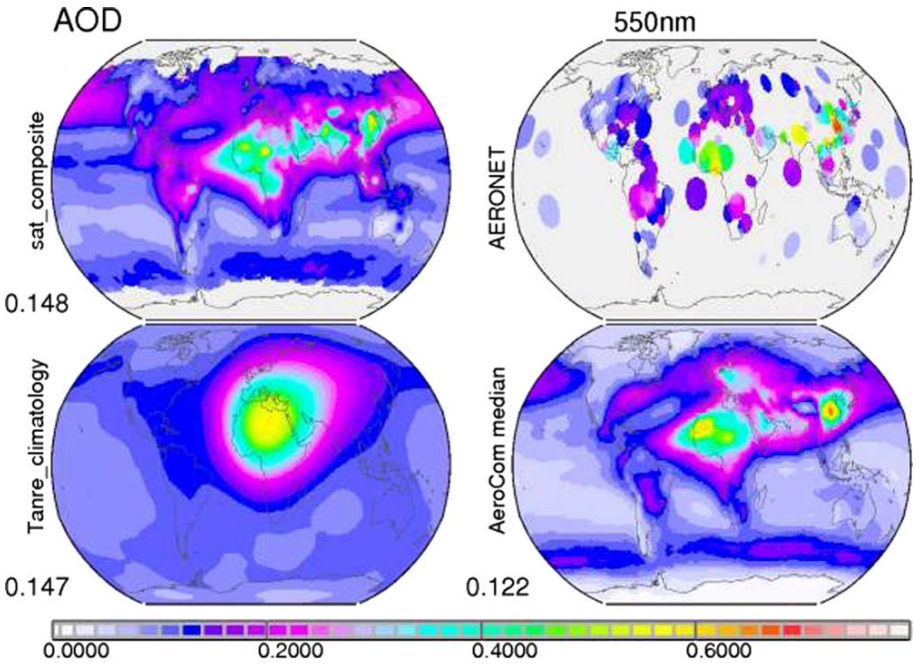

Figure 2.6: Global distribution of AOD at 550nm from four different data sources. A a combination of different satellite retrievals, including MODIS, MISR, and AVHRR (top left), the Tanre climatology (Tanre et al. 1984) (bottom left), AErosol RObotic NETwork ground data (top right), and a global model median (bottom right, the used 14 models are given at AeroCom (2020) for phase I). Values below the labels indicate global averages. (Kinne et al. 2013)

2.2 Solar power

There exist several technologies to generate solar power. Due to the physical power generating process two main groups can be distinguished from each other - PV and thermal. PV power systems directly transform solar irradiance to electrical power using the photoelectric effect. Solar thermal power systems instead utilize the heat from the sun to run an electric generator with a steam or gas turbine. Solar thermal power plants include CSP like parabolic trough (PT) power plants and solar tower power plants. This sections describes PV and PT power, the latter representing a concentrating technology, with their advantages and disadvantages, as these technologies are used for the analysis in this thesis.

2.2.1 Photovoltaic systems

Photovoltaic cells (from Greek "photos" - light and "volt" - the unit of electric voltage) can directly convert solar irradiance into electrical power. The first PV cell was built in 1954 in the American Bell-Laboratories with an efficiency of 5% (Quaschning 2011). Nowadays, crystalline PV cells reach efficiencies far over 20% in the laboratories (RECP 2019). Costs are still falling from year to year and annual new installations increase. In 2018, the worldwide PV power generation was 585 TWh,

which covers over 2% of global electricity need (IEA 2019), with an installed total capacity of over 500 GW (RECP 2019) (with only 0.1% being installed in West Africa). PV systems have one important advantage. They are based on a modular technology which allows to build up large power plants as well as small systems for single households or even off-grid applications. A grid-connected PV installation consists of PV modules (arranged in parallel or in row and build up from several PV cells) and an inverter to convert the direct current (DC) to alternating current (AC).

The photovoltaic effect is the physical basis of PV systems and creates voltage and electric current while the cell is exposed to light. Photovoltaic cells are made of semiconductors. The mainly used semiconductor for PV cells is silicon (the global market share was 90% in 2014 (Armaroli and Balzani 2016)). Silicon has four valence electrons. These electrons can be elevated to the conduction band under the exposure to light. The remaining empty space in the valence band is called hole. To generate electricity several layers of doped semiconductor material need to be arranged. For the doping of silicon, one atom is replaced by an atom from the III (p-doping, often with Bor) or the V main group of the periodic table (n-doping, often with Phosphor). Due to the additional (n-doping) or missing electron (p-doping) in the material local positive or negative charge preponderance occurs. By connecting the two differently doped layers to a p-n-junction a depletion region is built up in the middle. In this region charge carriers are separated due to the different local charge preponderance. Electrons drift towards the n-layer and holes towards the p-layer. This evokes a current subtended to the forward direction of the p-n junction which can be diverted by the connection of a consumer (see Figure 2.7). (Quaschning 2011)

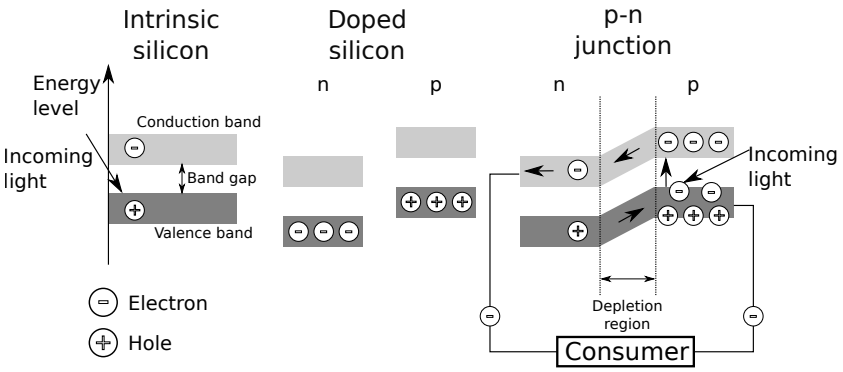

Figure 2.7: Electric bands for intrinsic and doped silicon as well as for the p-n-junction.

Beside the p-n-junction, the PV cell has additional layers. To divert the current a front and a back layer, including the electrical contact need to be installed. Furthermore, an antireflection layer is applied on the front of the PV cell to reduce optical losses of incoming solar irradiance.

Modeling PV power implies to accurately simulate the current (I) - voltage (U) curve during each modeling step. Therefore at least three points are necessary to accurately represent the I-U curve, the maximum power point (MPP), the open-circuit voltage (U_{OC}) and the short-circuit current (I_{SC}) (see Figure 2.8).

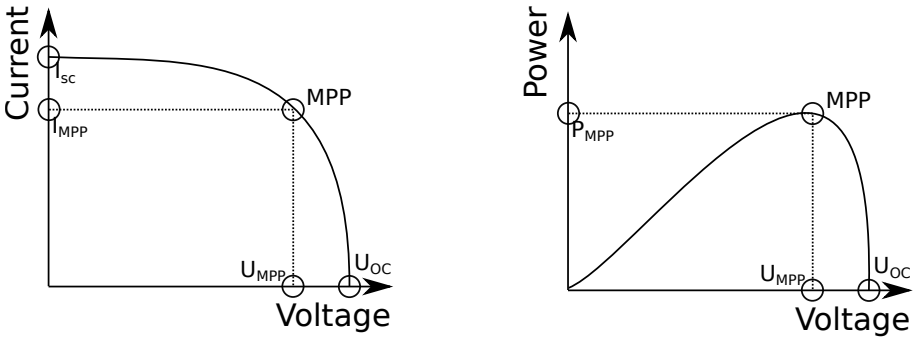

Figure 2.8: Typical curse of the I-U and Power-U curve of a PV cell, with MPP, U_{OC} and I_{SC}.

The optically generated charge carriers are exposed to the recombination and diffusion processes. For the ideal PV cell these processes can each be represented by a diode. However, losses must be taken into account for real PV cells. The two diode model represents the optimal characterization of a crystalline PV cell (for detailed description see Section 3.3.2). Thereby losses can be summed up in one series- and one parallel resistance term. The series resistance represents the losses of the semiconductor material and contacts and the parallel resistance the defects in the p-n-junction and the leakage currents over the surface (Fischbach 1982).

2.2.2 Parabolic trough power plant

The utilization of CSP dates back to the seventh century B.C.. In these times, it was used to light fire using glass or mirrors to concentrate the direct radiation. Nowadays, CSP is developed as a modern technology to produce power, e.g. as PT power plants. The technology is attractive due to its combination with traditional thermal gas or steam turbines coupled to a generator and used in the fossil fuel based energy system. Therefore, a combination with fossil fuels is possible. Parabolic trough power plants (PTPP) are one of the most established CSP technologies. For PTPP heat levels of around 250°C to 400°C are needed. To achieve such temperatures the concentration of the solar irradiance is necessary. The concentration of solar irradiacne is only possible for the direct component of irradiance, which makes CSP attractive for regions with a low share of clouds and aerosols. To analyze the impact of aerosols on solar power a PTPP is used as an exemplary CSP plant in this thesis. (Quaschning 2011)

The PT technology consists of single line concentrators in the shape of a parable. Parallel rays are collected by reflection on the reflector and focused to one receiver

tube (see Figure 2.9). The reflectors are usually built of glass mirrors because of their long life time. The receiver tube is filled with a working fluid (e.g. thermal oil), able to capture high temperatures. The parabolic trough tracks the sun with a single-axis in East-West direction to capture the solar irradiance perpendicular to the aperture. The heated working fluid evaporates and overheats water, which

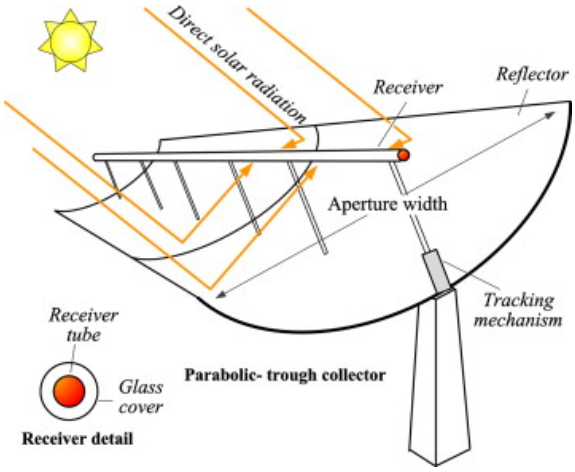

Figure 2.9: Parabolic trough collector (Cabrera et al. 2013: Fig. 2).

then drives a steam turbine with a generator producing electrical power. A PTPP is generally constructed by several parabolic collectors in series, named assembly, and multiple assemblies are connected in parallel. The Andasol I (see Figure 2.10) power plant in Spain is used for theoretical calculations in this thesis. For this power plant 12 typical collectors (the line-focusing Eurotrough, (Luepfert et al. 2003)) are used in one assembly and 624 assemblies are connected in parallel. The heat collector elements are PTR70 by Schott (SCHOTT Solar 2013) and for the power block, a Steam Rankine process is used. The SST-700 turbine was developed by Siemens. The solar field efficiency of Andasol I lies around 50% and the efficiency of the entire plant, including the steam turbine process, at around 15% (Solar Millenium 2008).

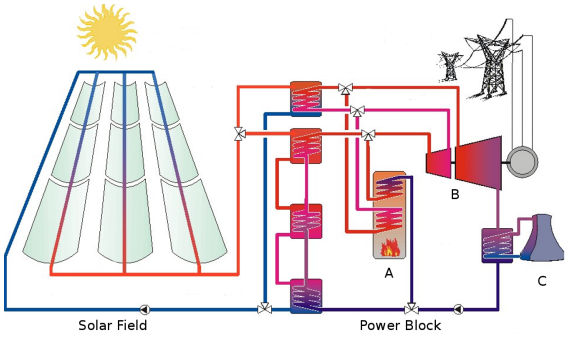

Figure 2.10: Diagram of the Andasol I power plant without storage (A: possible secondary combustion, B: Steam turbine with generator, C: Cooling tower).

2.3 Solar irradiance

Solar (or shortwave) radiation is emitted by the sun's photosphere and incident on the top of the Earth's atmosphere. The sun emits mainly in the wavelength λ range between 100 and 4000 nm (Petty 2006: p.68). Thereby the shape of the extraterrestrial spectrum follows a Planck curve of the sun's surface temperature of approximately 5777 K (Petty 2006), with a maximum at about 500 nm (see Figure 2.11). The mean irradiance arriving at the top of the atmosphere is specified

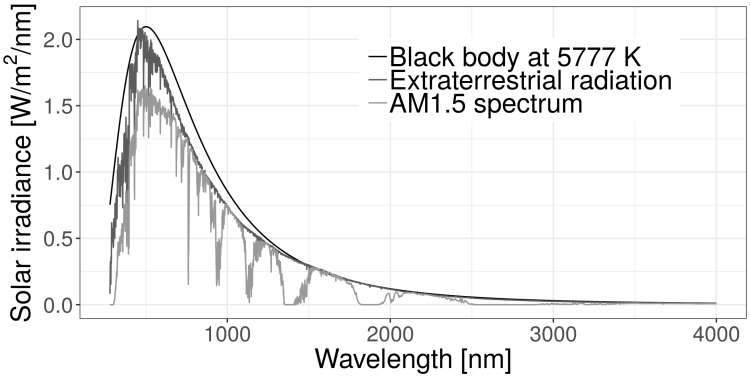

Figure 2.11: The extraterrestrial solar spectrum with a corresponding Planck curve at 5777 K (temperature of the sun) and the AM1.5 spectrum (American Society for Testing and Materials 2003).

as the total solar irradiance, having a value of 1361.1 W/m^2 (Gueymard 2018). The solar constant is influenced by the Earth elliptical orbit around the sun and the sun's 11-year solar cycle. Due to the elliptical orbit of the Earth around the sun, the top of the atmosphere solar radiation varies from 1330 W/m^2 in summer to 1420 W/m^2 in winter (Petty 2006: p. 50). The 11-year solar cycle has an amplitude of about 0.12%, so it plays only a secondary role (Kopp and Lean 2011). On its way to the Earth's surface, solar irradiance interacts with the Earth's atmosphere.

Solar irradiance at the Earth surface (global horizontal irradiance - GHI) consists of two components: direct horizontal (DIR) and diffuse horizontal irradiance (DHI). GHI can be calculated as: GHI = DIR + DHI. The direct component is the part of the extraterrestrial light which passes the atmosphere without interaction with particles and molecules, it comes from the direction of the sun. The diffuse component arrives at the ground from several directions after being scattered by trace gases, aerosols or clouds (see Figure 2.12). They absorb, reflect and scatter the incoming light and therewith affect the intensity as well as the spectral composition of the irradiance. About 30% of the incoming solar irradiance is reflected by the Earth's atmosphere while about 20% is absorbed there (Stocker et al. 2014).

A very simple consideration of the atmosphere can be undertaken by using the air mass (AM) factor. This factor defines the direct optical path length through the atmosphere compared to the vertical path length. In the solar energy community the

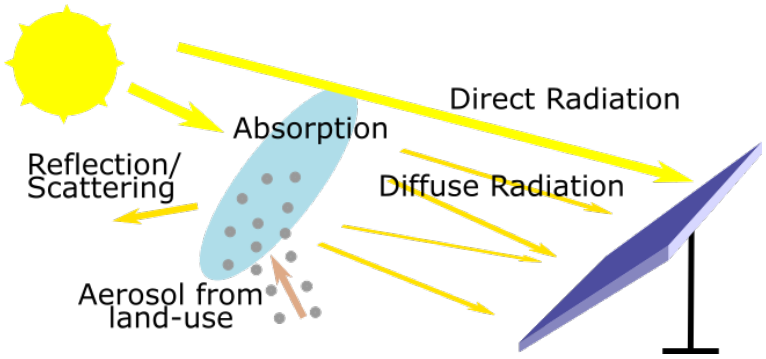

Figure 2.12: Way of the irradiance through the atmosphere to the plane of a PV module.

AM1.5 spectrum, which is defined at 25°C (see Figure 2.11), is used as a standard spectrum for terrestrial power generation (cloud free atmosphere with a rural aerosol loading). In this thesis, however, detailed radiative transfer calculations will be used to determine irradiance on the Earth surface. Therefore the propagation of solar radiation, through the atmosphere will be discussed in more detail in the following.

2.3.1 Absorption and scattering

In the atmosphere solar radiation is scattered and absorbed by gases, aerosol and cloud particles. The reduction of solar radiation by scattering and absorption in the atmosphere is called extinction. The fraction of radiation passing the atmosphere to the Earth surface is called transmittance.

Depending on the size extent and composition, molecules and particles absorb the solar radiation at typical wavelengths and transform the radiance into thermal or electronic energy. Thereby they induce rotational, vibrational and electronic transitions. Transmittance lines and bands for the major atmospheric gases are shown in Figure 2.13 in a wavelength range between 200 nm and 70 µm. By comparing the absorption bands of the single trace gases with the spectral range of the incoming solar radiation, one can clearly see that absorption and scattering by water vapor has the major influence on the solar spectrum (under 4000 µm). The effect of absorption and scattering by nitrous oxide (N_2O), oxygen (O_2), ozone (O_3), carbon dioxide (CO_2) and methane (CH_4) has only a slight influence on the incoming solar spectrum.

Scattering processes change the direction of the incoming radiation. Depending on the size of the particles and the wavelength, various scattering behaviors are differentiated (see Figure 2.14). The size parameter x is defined as

$$x = \frac{2\pi r}{\lambda}, \tag{2.3.1}$$

with r being the radius for a spherical particle. For larger particles and smaller

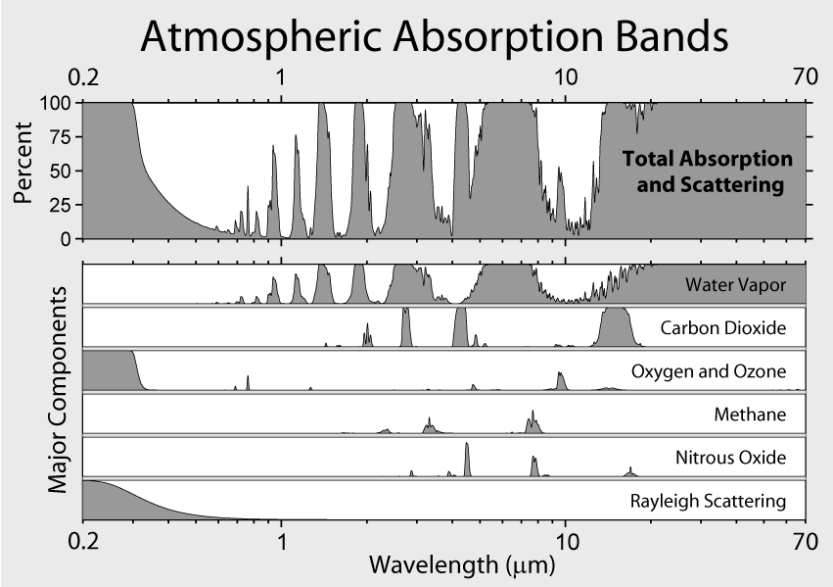

Figure 2.13: Spectral absorption bands of major atmospheric trace gases (Worldpress 2012).

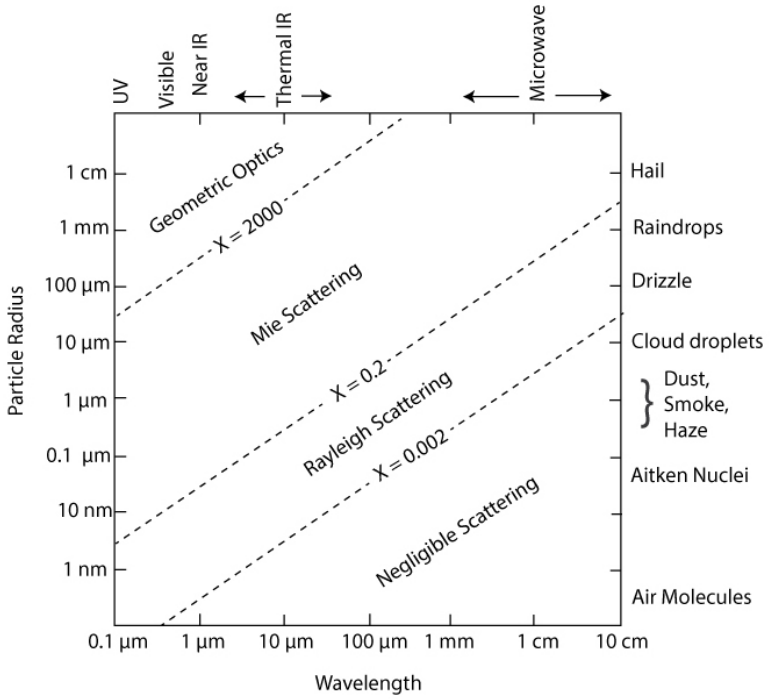

Figure 2.14: Relationship between particle size, wavelength and scattering behavior for atmospheric particles. The dashed lines represent rough boundaries between the different scattering regimes (Petty 2006: p. 346).

wavelengths ($x \geq 2000$) the scattering process follows geometric optics. For the incoming solar radiation (in a wavelength range between 100 to 4000 nm) particles with radii larger than about 100 nm follow Mie scattering ($0.2 \leq x \leq 2000$). Smaller particles are either Mie or Rayleigh scattered depending on the certain wavelength.

For the mathematical description of the extinction of radiation on particles some basic parameters and equations are introduced here. The effective surface which interacts with the radiation perpendicular to its direction of propagation is called the absorption σ_{abs} and accordingly the scattering cross section σ_{sca} is defined, both in [m^2]. Therewith the absorption Q_{abs} and scattering efficiency Q_{sca} can be defined as

$$Q_{abs} = \frac{\sigma_{abs}}{\pi\, r^2} \qquad \text{and} \qquad Q_{sca} = \frac{\sigma_{sca}}{\pi\, r^2} \tag{2.3.2}$$

Generally it is assumed that clouds and aerosols are spherical particles. The extinction efficiency Q_{ext} is then defined as the sum of the absorption and scattering efficiency to $Q_{ext} = Q_{abs} + Q_{sca}$.

The absorption β_{abs} and scattering coefficient β_{sca}, both in [m^{-1}], characterize the absorption and scattering process depending on the wavelength and the particle nature. They are defined as the cross section times the particle number concentration N_C [m^{-3}]

$$\beta_{abs} = \sigma_{abs} \cdot N_C \qquad \text{and} \qquad \beta_{sca} = \sigma_{sca} \cdot N_C. \tag{2.3.3}$$

The extinction coefficient β_{ext} is again defined as the sum of the absorption and scattering coefficient to $\beta_{ext} = \beta_{abs} + \beta_{sca}$. The single scattering albedo (SSA) specifies the share of scattering of the whole extinction

$$SSA = \frac{Q_{sca}}{Q_{ext}} = \frac{\beta_{sca}}{\beta_{ext}} = \frac{\sigma_{sca}}{\sigma_{ext}}. \tag{2.3.4}$$

If SSA = 0 the particle is solely absorbing and if SSA = 1 the particle is solely scattering.

Besides the scattering efficiency it is important to analyze the direction of the scattered light after interacting with a particle. The dimensionless phase function $p(\Omega, \Omega')$ describes the scattering of light from the spatial direction Ω' into the spatial direction Ω. A widely used approximation of the phase function for scattering processes on aerosols (where the size parameter lies in the Mie regime) is the Henyey-Greenstein phase function depending on the cosine of the scattering angle ν

$$p(cos\,\nu) = \frac{1 - g^2}{(1 + g^2 - 2\,g\,cos\,\nu)^{2/3}}. \tag{2.3.5}$$

This equation includes the dimensionless asymmetry parameter g being defined as the cosine-weighted average of the probability of irradiance being scattered in a given direction

$$g = \frac{1}{2} \int_{-1}^{1} cos\,\nu \cdot p(cos\,\nu)\, d\, cos\,\nu. \tag{2.3.6}$$

Thereby it can reach values between $-1 \leq g \leq 1$. A value of -1 defines only backward, a value of 1 only forward and a value of 0 isotropic scattering. (Petty 2006, Wendisch and Yang 2012)

2.3.2 Radiative transfer theory and numerical solution methods

The theory of radiative transfer describes the propagation of irradiance in a medium based on the particle description of light. The radiative transfer equation (RTE) is the mathematical description of the interaction between electromagnetic radiation and particulates (including molecules, aerosol and cloud particles). It includes all absorption, emission and scattering processes in a spectral dependency. The monospectral radiance[1] $I_\lambda(\Omega)$ in the spatial direction Ω derived along its path $\vec{s}$ depends on all sinks (first term, including absorption and scattering) and all sources (second and third term, including thermal emission and scattering)

$$\frac{dI_\lambda(\Omega)}{d\vec{s}} = \underbrace{-(\beta_{\lambda,abs} + \beta_{\lambda,sca}) \cdot I_\lambda(\Omega)}_{Sinks} + \underbrace{\beta_{\lambda,abs} \cdot B_\lambda(T) + \frac{\beta_{\lambda,sca}}{4\pi} \int_{4\pi} p_\lambda(\Omega, \Omega') \cdot I_\lambda(\Omega')\, d\Omega'}_{Sources}. \tag{2.3.7}$$

Thereby $B_\lambda(T)$ is the temperature dependent Planck function.

Analytical mathematical solutions can only be found for a few very simplified cases in a plane-parallel atmosphere (Petty 2006). In general, numerical solutions are necessary. Radiative transfer (RT) models, using information on the atmospheric state as input, can be used to calculate the radiative flux profiles in the atmosphere. For a detailed description of the radiative transfer theory see for example Wendisch and Yang (2012) or Petty (2006).

The majority of algorithms to solve the RTE can be classified into two categories, Discrete-Ordinate and Monte-Carlo methods. Here, the DIScrete Ordinate Radiative Transfer (DISORT) algorithm by Stamnes et al. (1988) is described because it is applied in this thesis. DISORT mathematically describes the transfer of monochromatic unpolarized radiances in a plane parallel atmosphere where scattering, absorption and emission takes place. Furthermore bidirectional reflection and emission at the lower boundary is considered. DISORT can calculate radiances, irradiances and actinic fluxes for the direct beam and the diffuse incidence with a pre-described atmospheric state from the ultra violet to the microwave region of the electromagnetic spectrum. The DISORT solver approximates the irradiance into a Fourier cosine series to separate the azimuth dependence. To find an analytical solution the atmosphere is split into a finite number of plane parallel layers. For

[1] The radiance is defined as the irradiance per unit of solid angle.

each layer the phase function and the SSA are assumed to be constant, but can vary from layer to layer. Then, the optimal solution can be approximated by Gaussian quadrature, with at least n notes for polynomial functions of the order $2n - 1$. (Stamnes et al. 2000, 1988)

2.4 Atmospheric aerosols

Atmospheric aerosols (from latin "aer" - air and "solutio" - solution) are solid or liquid suspended particles (excluding hydrometers) in the air. Aerosols are always present in the atmosphere and interact with clouds and radiation. Aerosol-radiation interaction occurs due to scattering and absorption of the incoming solar radiation. This is called the direct aerosol effect. Furthermore, aerosols have an impact on cloud formation, the size of cloud droplets and the lifetime of clouds. This is called the indirect aerosol effect. Due to these interactions aerosols have impacts on the energy budget and the climate of the Earth (Boucher et al. 2013). The human eye is not able to identify single aerosols, but if the concentration gets high enough people can realize the effect of aerosols by a reduced visibility (for example during desert dust storms, smog in large cities or the smoke from fossil fuel combustion). Aerosols vary in size and chemical composition. In Figure 2.15 radiative forcing (being the change of the difference between energy radiating down to earth and being radiated back to space caused by a certain driver) by different greenhouse gas emissions and aerosols is shown. The impact of aerosols on radiative forcing has still high uncertainties and ranges from negligible to significant (up to -0.77 W/m^2). Depending on the type of the aerosol this impact can result in a radiative warming or cooling (Srivastava et al. 2014, IPCC 2013). Under clear sky conditions aerosols show the highest influence on the irradiance budget at the surface (Hoyer-Klick et al. 2015).

Aerosol concentrations are extremely variable in space and time, because of their various sources and relatively short residence time of hours to weeks in the atmosphere. The size of single aerosols can vary between some nanometers to some micrometers (Wallace and Hobbs 2006: p. 169 - 173).

2.4.1 Aerosol formation and classification

Aerosols are either directly emitted into the atmosphere or formed by condensation or nucleation (secondary aerosols). There are two major classifications by source. Anthropogenic aerosols include remaining particles from the combustion of fossil and biofuels, fires by humans, industrial and agricultural activities against what natural aerosols are mainly emissions from soil, vegetation, ocean, wild fires and volcanoes (Boucher 2015, Boucher et al. 2013).

By physical properties aerosols can be classified into three major groups,

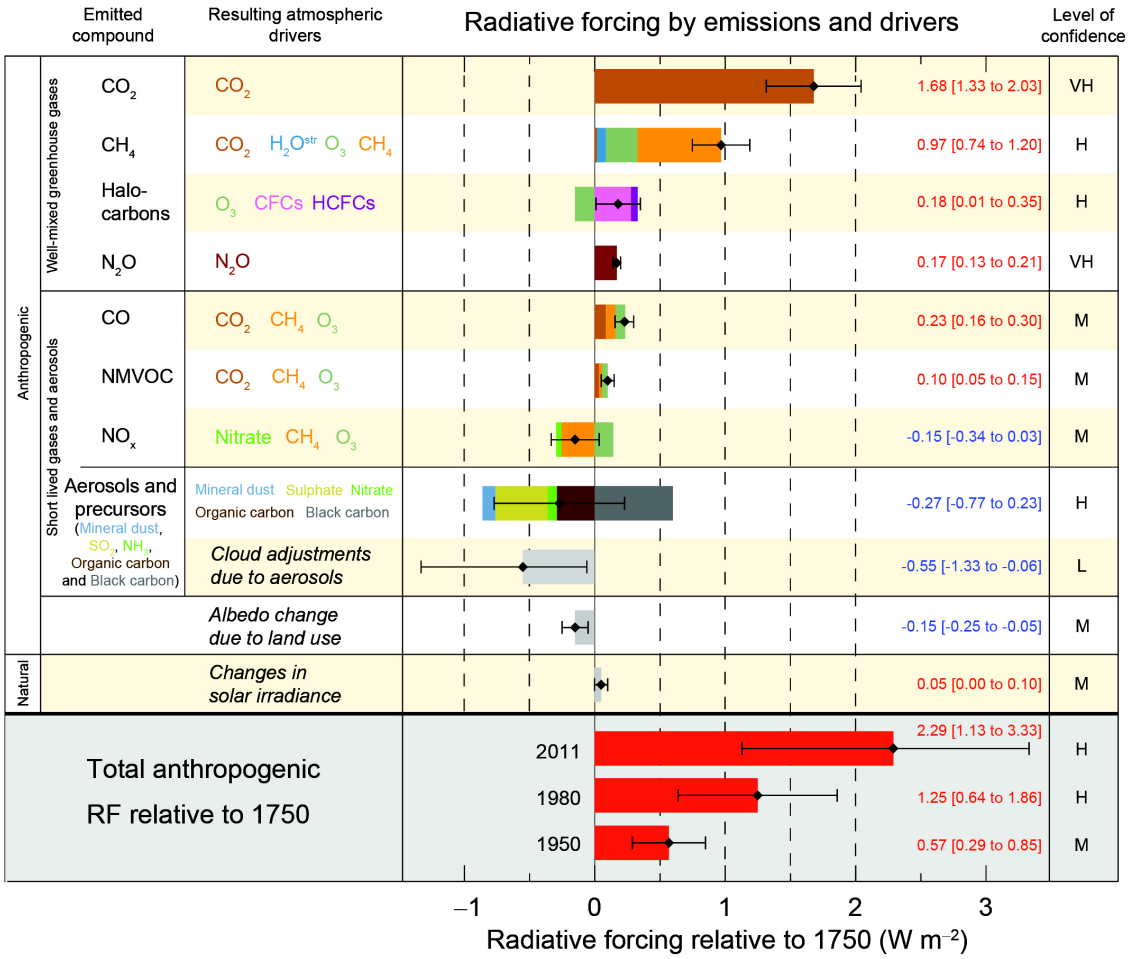

Figure 2.15: Radiative forcing by greenhouse gases and aerosols relative to 1750 (IPCC 2013: p.12).

nucleation-, accumulation- and coarse mode. Each of these groups represents a maximum in the size, surface and accordingly volume distribution. Furthermore a classification depending on chemical properties (chemical species and mixture) can be undertaken. The composition of aerosols can be in an internal or external mixture. External mixtures are composed of aerosols with different chemical composition, while realistic internal mixtures consists of different chemical species within single particles. Different chemical species of aerosols are organic, inorganic and black carbon aerosols. Their physical and chemical properties are needed for radiative transfer calculations (Boucher 2015).

2.4.2 Aerosol optical properties

The most important aerosol optical properties is the AOD. Furthermore the above described SSA and the asymmetry factor g give information on the scattering-absorption rate and the direction of scattering, respectively. These parameters are

needed to analyze the direct radiative forcing of aerosols (Boucher 2015, Fiebig and Ogren 2006, Wallace and Hobbs 2006).

For most applications aerosol optical properties can be described by the Mie theory with the assumption of spherical particles (Horvath et al. 2016). To define the AOD the extinction efficiency Q_{ext} has to be integrated over the whole size distribution $n(r)$, so that one can specify the extinction coefficient β_{ext} to

$$\beta_{ext} = \int_0^\infty \pi\, r^2\, Q_{ext}(r)\, n(r)\, dr, \tag{2.4.1}$$

where r is the radius of the aerosol particle. The AOD integrated over the vertical dimension of the atmosphere is defined as

$$\mathrm{AOD} = \int_0^{z(\mathrm{TOA})} \beta_{ext}(z)\, dz. \tag{2.4.2}$$

Whereby z is the vertical height and z(TOA) is the height of the top of the atmosphere.

This AOD still depends on wavelength. Generally the AOD decreases with increasing wavelength λ (Sakerin and Kabanov 2006). In the shortwave range the wavelength dependency of AOD can be described with the Ångström exponent α

$$\alpha = -\frac{ln(\mathrm{AOD}_1) - ln(\mathrm{AOD}_2)}{ln(\lambda_1) - ln(\lambda_2)} \tag{2.4.3}$$

and the following relation

$$\mathrm{AOD} = \mathrm{AOD}_0 \cdot \left(\frac{\lambda}{\lambda_0}\right)^{-\alpha}, \tag{2.4.4}$$

with AOD_0 being a reference AOD at wavelength λ_0.

Boucher (2015) indicates some typical values for the Ångström exponents α. Molecular scattering gives Ångström exponents of $\alpha \approx 4$, scattering on aerosol particles in accumulation mode $\alpha \approx 2$ and on particles in coarse mode $\alpha \leq 0$.

2.4.3 Standard aerosol profiles

Hess et al. (1998) defined ten standard surface aerosol types (depending on the surrounding land-use conditions), which are continental (clean, average and polluted), urban, desert, maritime (clean, polluted and tropical), arctic and antarctic, summarized in the Optical Properties of Aerosols and Clouds (OPAC) library. Furthermore, they provide typical values for aerosol optical properties of theses aerosol types. The types are composed out of ten different aerosol components, namely insoluble, water-soluble, soot, sea salt in two modes (accumulation and coarse), mineral in three modes (nucleation, accumulation and coarse), mineral-transported

and sulfate droplets. The following list gives more information about the aerosol particles in these components (Hess et al. 1998, Koepke et al. 1997):

- **Insoluble** aerosol particles (INSO) are mainly soil particles including organic matter.
- **Water-soluble** aerosols (WASO) are made up of sulfates, nitrates and other water-soluble substances which where build by gas to particle conversion.
- **Soot** (SOOT) represents black carbon particles, can not take up humidity.
- **Sea salt** aerosol particles are as the name implies composed of salt from sea-water. There are two modes defined because of larger particles being deposited faster due to gravity, sea salt in accumulation mode (SSAM) and sea salt in coarse mode (SSCM).
- **Mineral** aerosols consist mostly of clay and quartz. They occur mainly in desert regions or areas with intensive agriculture. This aerosol component is defined in three modes (nucleation - MINM, accumulation - MIAM and coarse - MICM) and an additional transported component (MITR). The mineral-transported aerosol describes especially desert dust which is transported over long distances.
- **Sulfate droplets** (SUSO) are found in the antarctic aerosol and the stratospheric background aerosol. They contain about 75% of H_2SO_4.

Chapter 3

Data and models

In this thesis different data sources (ground-based measurements, satellite products and models of different kind) are used. The sources provide information about a variety of atmospheric parameters. To simulate solar power, the GHI and DNI is needed. However, all atmospheric parameters modulating solar irradiances like clouds, aerosols and trace gases have an additional impact on solar power. Furthermore, for realistic solar power modeling, ambient temperature, wind speed and direction, humidity as well as pressure need to be included. This chapter aims to give an overview over the different data sources and models used for calculations. Furthermore, the development of the combined radiative transfer - solar power model SolPaRT is described.

3.1 Ground-based measurements

Ground-based measurements are used as input for model calculation or to validate modeled parameters in this thesis. Ground-based measurements well represent the situation encountered by a solar power system, which is also located at ground. Meteorological ground-based measurements are distributed all over the world and several networks with different foci and standards exist. Compared to Germany, the ground-based measuring network in West Africa shows larger gaps in spatial distribution (e.g. there are 17 AErosol RObotic NETwork (AERONET) stations in Germany (357 386 km^2) and 18 AERONET stations in West Africa (5 112 903 km^2), distributed over seven countries).

3.1.1 Aerosol Robotic Network

Aerosol optical properties and information about trace gas concentration is needed for several locations to solve the radiative transfer equation. The AERONET (NASA 2018) combines worldwide aerosol standardized data including several locations in West Africa. Furthermore, measurements of precipitable water vapor (PWV) are

available at most stations. The quality assured (Level 2.0, V3) data is used as an input for the radiative transfer model in this thesis.

AOD, Ångström exponent and PWV are retrieved (based on Giles et al. (2019)) from solar radiances measured by an automatic Cimel 318A spectral radiometer. The sun photometer has a viewing angle of about 1.2° and two detectors, one for the direct sun and one for the global radiance. The direct sun is measured in eight spectral bands between 340 nm and 1020 nm and the global radiance at four spectral bands between 440 nm and 1020 nm. The maximum temporal resolution is approximately 3 min. Data accuracy of the retrieved AOD is better than 0.01 for wavelengths longer than 440 nm and better than 0.02 for smaller wavelengths. For PWV the accuracy is better than 12% (Holben et al. 1998).

3.1.2 Energy meteorological laboratory at University of Applied Science Bonn-Rhein-Sieg

The measured power of a single PV module at University of Applied Science Bonn-Rhein-Sieg (HBRS) is used to validate the PV power model. The energy meteorological laboratory is located at the rooftop of HBRS (50.8°N 7.2°E), where continuous measurements of solar irradiance, PV power of a typical polycrystalline module and weather specific parameters are undertaken.

The SOLYS 2 sun tracker from Kipp & Zonen measures the GHI and DHI as well as the DNI. The SOLYS2 is equipped with two CMP11 pyranometers (Kipp & Zonen 2016) (one of them is shaded) and one CHP1 pyrheliometer (Kipp & Zonen 2008). The shaded pyranometer measures the DHI, the free pyranometer measures the GHI and the pyrheliometer measures the DNI in a 1-min temporal resolution. Thereby, the measuring uncertainties are 2% for hourly totals of DNI and 3% of hourly totals for DHI and GHI.

The full I-U curve of the SW235poly, a polycrystalline PV module from Solar World (SolarWorld 2012), is measured in a 1-min resolution. The measuring stand is equipped with a variable load (B&K Precision 8502). A labVIEW (LABoratory Virtual Instrumentation Engineering Workbench) program regulates the current, starting from the short circuit current to zero in about 140 equidistant steps. For each current the voltage is measured. The total I-U curve is looped up every minute and the MPP is calculated as the maximum of the product of I and U. The measurement accuracy is about 3% at the MPP under standard test conditions (STC).

A weather station at HBRS measures wind speed and ambient temperature among other parameters in a 10-min temporal resolution. The weather station is operated in cooperation with Meteomedia (MeteoGroup 2019). The ambient temperature is recorded with a Pt100 1/3 class B, which has a measuring uncertainty of ± 0.1°C (Thies Clima 2005). The wind speed is measured with an anemometer of an accuracy of less than 2% of the measurement or 0.5 m/s (Thies Clima 2019).

3.1.3 Further observational data

Meteorological observational data is rare in West Africa. However, some local campaigns were undertaken since the early 2000s and some synoptic observations (SYNOP) exist and could be used as input within this thesis.

The AMMA program started with long-term measurements in 2002, to investigate the West African climate, involving comprehensive field observations. The AMMA data base (AMMA 2018) provides atmospheric data (including ambient temperature, wind speed and direction, humidity, pressure and GHI) between 2002 and 2012 at three mesosites, Agoufou (Mali), Banizoumbou (Niger) and Djougou (Benin).

For the total year 2006 the ARM Mobile Facility (AMF) was deployed in Niamey, Niger (13.5°N, 2.2°E, (Slingo et al. 2008, 2009)). During this campaign a comprehensive set of meteorological parameters was measured, which enables to investigate atmospheric effects on solar power. The AOD, SSA, Ångström exponent, ambient temperature, wind speed and direction, GHI, DNI, DHI, upwelling irradiances, precipitable water, humidity and pressure were used for the analysis in Chapter 4.

Meteorological data (ambient temperature, wind speed and direction, humidity and pressure) were use from SYNOP stations in Dakar (Senegal) and Maine (Niger). Further information on the used data sources is given in the single publications of Chapter 4, Chapter 5 and their Supplementary Material.

3.2 Satellite products

Since the 1970s meteorological satellites are orbiting the Earth. Their measurements can be used to retrieve surface irradiances globally, assuming several meteorological parameters, such as aerosol optical properties, gas concentrations, ground albedo, etc. For West Africa the satellites of the Meteosat series are the most relevant satellites. They provide images of solar reflectance and thermal infrared emission every half-hour or better, which are used to retrieve several meteorological parameters like GHI, DNI and cloud properties.

The SARAH-2.1 data set (Pfeifroth et al. 2019) is based on the images measured by the Meteosat series. It is the second release of the SARAH data record, provided by the EUMETSAT CM SAF. The data set includes the surface incoming shortwave radiation (GHI), the surface incoming direct radiation (DIR), the direct normal radiation (DNI) and the effective cloud albedo (CAL). Furthermore, a climate data record of monthly and daily sunshine duration (SDU) and monthly spectral resolved irradiance (SRI) is given. The parameters of SARAH-2.1 are retrieved from the geostationary Meteosat satellite series of the first and second generation, covering total West Africa with a half-hour temporal and a 0.05° spatial resolution. For

the retrieval the Heliosat algorithm to estimate the effective cloud albedo (Hammer et al. 2003) is combined with a cloud free radiative transfer model (Mueller et al. 2009). Furthermore, several climatological parameters are included: the precipitable water vapor (ERA-interim, where ERA stands for ECMWF Re-Analysis), monthly aerosol climatology (taken from the European Center for Medium Range Weather Forecast (ECMWF), Monitoring Atmospheric Composition and Climate (MACC)), monthly ozone climatology (standard United States atmosphere) and the ground albedo (Surface and Atmospheric Radiation Budget (SARB) data from Clouds and the Earth's Radiant Energy System (CERES)). A detailed description of the retrieval is given in Mueller et al. (2015).

The first generation Meteosat satellite is equipped with a Visible-InfraRed Imager (MVIRI), a passive imaging radiometer with three spectral channels (visible channel - 0.5 to 0.9 µm; two infra-red channels - 5.7 to 7.1 µm and 10.5 to 12.5 µm). On board of the second generation Meteosat satellite are the Spinning Enhanced Visible and InfraRed Imager (SEVIRI) and the Geostationary Earth Radiation Budget (GERB) instrument. With the GERB instrument (visible-infrared radiometer) shortwave and longwave solar irradiances are measured at the top of the atmosphere. The SEVIRI contains 12 spectral channels, which provide more information then the former MVIRI. A consistent product over both satellite generations is available.

3.3 Model development

In this thesis, different models are developed to answer different questions. To quantify the impact of atmospheric aerosols on solar power the model chain "Solar Power modeling including atmospheric Radiative Transfer" (SolPaRT) is developed. SolPaRT aims to accurately model PV and PT power by including a radiative transfer model, which uses explicit aerosol optical properties as an input. To analyze the impact of long-term atmospheric variability and trends on PV power a simplified linear model is fitted with reference data (see Chapter 5 for a detailed description). This simplified model allows to estimate daily PV yields over total West Africa and for 35 years.

SolPaRT includes three sub models, the atmospheric radiative transfer model libRadtran (Section 3.3.1), a specifically developed PV power model (Section 3.3.2) and the PT power model (*greenius*) (Section 3.3.3) (see schematic overview in Figure 3.1). The single modeling steps are described in detail in the following sections. At some instances model components from the literature are compared to choose the most accurate for the model chain.

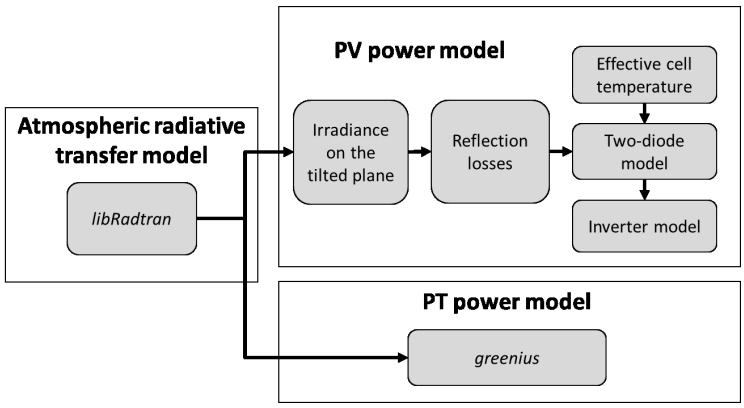

Figure 3.1: Schematic overview on the single modeling steps in SolPaRT.

3.3.1 Atmospheric radiative transfer model

The library of radiative transfer (libRadtran) is a freely available software package to calculate radiative transfer (Emde et al. 2016, Mayer et al. 2015, Mayer and Kylling 2005). LibRadtran was developed at the German Aerospace Center in Oberpfaffenhofen. The library includes various functions and data sets to calculate irradiances, radiances (also polarized) and actinic fluxes for the single irradiance components (direct, diffuse up- and downwards directed) over the solar and thermal spectrum. The main tool is the *uvspec* program, which works with individually arranged input files (see Figure 3.2 for the structure of *uvspec*). The *uvspec* program is built up of three parts. First, atmospheric profiles are converted to optical properties, which are needed as an input to solve the RTE. Therefore, standard atmospheres by Anderson et al. (1986), extraterrestrial irradiance by Kurucz (1994) and typical aerosol profiles by Hess et al. (1998) (OPAC library) are provided by the libRadtran library and can be modified individually. Aerosols optical properties are calculated using the Mie theory by Wiscombe (1980) or Bohren and Huffman (1998) which assumes spherical particles. Typical aspherical mineral aerosol optical properties can be estimated by using the T-matrix method (Mishchenko and Travis 1998). Second, the RTE solver calculates radiances, irradiances and actinic fluxes. There are different algorithms included in *uvspec* to solve the radiative transfer equation (e.g. `DISORT`, `twostream`, `polradtran`, `MYSTIC` and `sdisort`). However the relative difference between for example `DISORT` and `MYSTIC` is only less than 0.05% (Emde et al. 2016). `DISORT` is used for the calculations in this thesis. For radiative transfer calculation, especially broadband calculations, line-by-line algorithms for absorption are time consuming. With band transmissions like the correlated-k method by Kato et al. (1999) computing times can be reduced. With libRadtran both, line-by-line and band transmission calculations can be undertaken. However, to reduce computing times, the correlated-k method for molecular absorption is applied in the most of

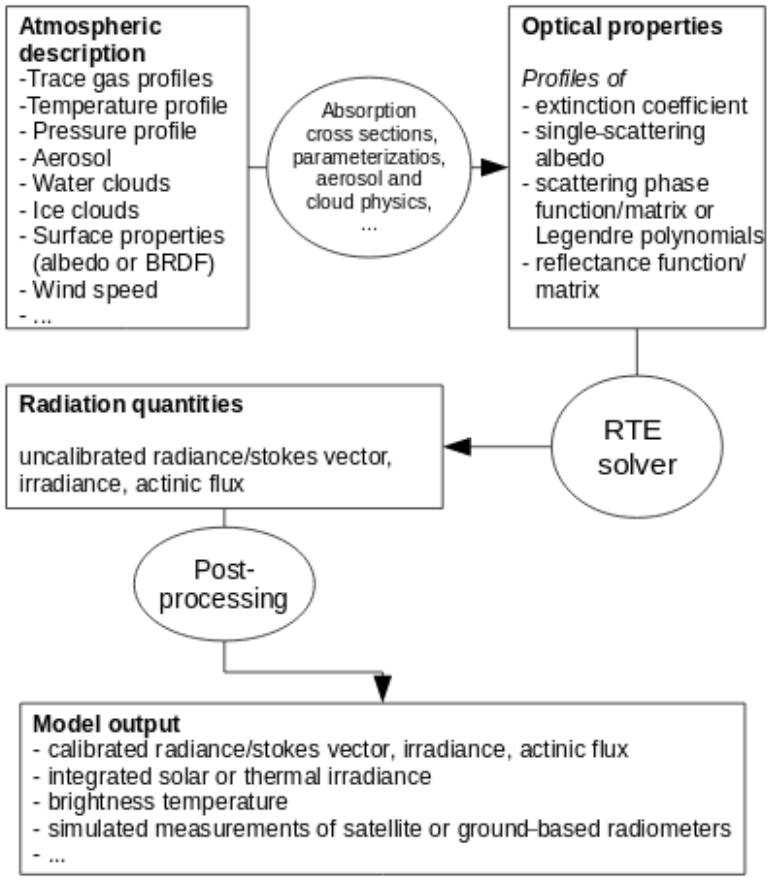

Figure 3.2: Structure of the *uvspec* program (Mayer et al. 2015: p. 18).

the calculations within this thesis. The third part of *uvspec* combines all post processing, e.g. correction of Earth-Sun distance, integration or sum over wavelength, depending on the users choice. Further explanations on the libRadtran library can be found in the user manual (Mayer et al. 2015).

Box 3.1. Model sensitivity for trace gases

To quantify the influence of different trace gases, relatively low and high values for their concentration are selected from literature (see Table 3.1) and used as input for libRadtran. Three days at diverging times of the year (2016-06-21, 2016-09-23 and 2016-12-21) are analyzed at a location at 50.8°N and 7.2°E (Sankt Augustin, Germany), where the influence of seasons is well perceptible.

The simulations for low and high concentrations are compared by using two statistical parameters (Bias and root mean square error (RMSE), see Table 3.1). The Bias gives a dimension of the systematical error while the RMSE shows the absolute variance of the data points. In the table, one can clearly see that even extreme values of oxygen (in %), carbon dioxide (in parts per million - ppm) and methane (in ppm) have rarely any influence on the incoming solar

irradiance. Ozone (in Dobson units - DU, defining the thickness in units of 10 µm) a secondary influence on solar irradiance, which will be neglected in some of the calculations of this thesis, as no measurements are available. However, the variability of water vapor (in mm, which specifies the precipitable water in kg/m^2) in particular shows impacts of over 80%. Therefore, water vapor variability will be included explicitly into radiative transfer calculations in this thesis.

Table 3.1: Sensitivity of libRadtran calculations on trace gas concentrations. High (low) values of O_2 are estimated to be 1% above (underneath) the current level. For O_3 the minimum of 2016 is used as low value, while the high value is the maximum in NASA (2016b). For CO_2 and CH_4 the low value represents preindustrial levels and the high value the double of the current numbers from the IPCC (Myhre et al. 2013). The low and high value for water vapor are taken from the scale extremes in (NASA 2016a).

	O_2	O_3	CO_2	CH_4	Water vapor
high value	22%	500 DU	820 ppm	2.668 ppm	60 mm
low value	20%	130 DU	278 ppm	0.722 ppm	0 mm
Bias [%]	0	-2.4	0	0	-21.2
RMSE $[W/m^2]$	0.04	7.3	0.01	0	80.5

3.3.2 Photovoltaic power model

To accurately model the power of a PV module several calculation steps are needed (see Figure 3.1).

Irradiance on the tilted plane: Global irradiance on a tilted plane (GTI) is divided into three parts, direct tilted (DRT) and diffuse tilted irradiance (DTI) as well as reflections from the ground (REF). DRT can be derived analytically from the horizontal parameters. The angle of incidence (AOI), which describes the angle between the incoming direct irradiance and the normal on the module plane can be derived from of the suns zenith γ and azimuth angles α_{sun}, the tilt angle of the module Φ and the modules azimuth angle α_{PV} (King et al. 1997)

$$\mathrm{AOI} = arcos\left[cos(\Phi)cos(\gamma) + sin(\Phi)sin(\gamma)cos(\alpha_{sun} - \alpha_{PV})\right]. \tag{3.3.1}$$

Therewith DRT can be calculated as

$$\mathrm{DRT} = \mathrm{DIR}\,\frac{cos(\mathrm{AOI})}{cos(\gamma)}. \tag{3.3.2}$$

In comparison to the DRT, the DTI can not be derived analytically. There

are various model approaches for describing the spatial distribution of the diffuse irradiance. These can be divided into two groups, isotropic models (for example (Badescu 2002, Liu and Jordan 1963)) and anisotropic models considering two (for example (Hay 1979) or three components (for example (Perez et al. 1990, Reindl et al. 1990) as shown by Gracia and Huld (2013). Two component anisotropic models include a circumsolar and an isotropic component of the irradiance while three component models also account for horizon brightening (Loutzenhiser et al. 2007). This third component is most pronounced in clear-sky conditions (Duffie and Beckman 1976).

The accuracy of different model approaches (a simple isotropic model by Liu and Jordan (1963), the model by Reindl et al. (1990), which uses the transmittance to determine the share of each component and a widely used three component anisotopic model by Perez et al. (1990)) are compared to analytical calculations with libRadtran (see Section 4.1 and Neher et al. (2017), the models are described in Box 3.2). The Perez model performs best and is therefore used to calculate the diffuse irradiance on the tilted plane in this thesis.

Box 3.2. Diffuse radiation models

Liu-Jordan model: The isotropic model assumes that the total diffuse irradiance is evenly spread over the whole sky. For a tilting angle Φ the diffuse tilted irradiance DTI can be calculated as

$$\mathrm{DTI} = \mathrm{DHI}\left(\frac{1 + cos\,\Phi}{2}\right). \tag{3.3.3}$$

Reindl model: In comparison to the simple correlation by Liu and Jordan (1963) the Reindl model adds a circumsolar and a horizon brightening component. The transmittance through the atmosphere for DNI is described by the anisotropy index A

$$A = \frac{\mathrm{DNI}}{\mathrm{EXI}}, \tag{3.3.4}$$

where EXI is the extraterrestrial irradiance. The anisotropy index is used to quantify the part of diffuse irradiance being treated as circumsolar irradiance. Furthermore a function f_R, quantifying the intensity of diffuse irradiance coming from the horizon, is introduced

$$f_R = \sqrt{\frac{\mathrm{DIR}}{\mathrm{GHI}}}. \tag{3.3.5}$$

With these two coefficients the diffuse irradiance on the tilted plane can be calculated as

$$\mathrm{DTI} = \mathrm{DHI}(1-A)\left(\frac{1+cos\,\Phi}{2}\right)\cdot\left[1 + f_R sin^3(\frac{\Phi}{2})\right]. \tag{3.3.6}$$

Perez model: The Perez model uses empirical parameters for the circumsolar F_1 and the horizontal brightening F_2 parts. Furthermore, two components to calculate the incident angle of the sun on the tilted plane a and b are used to determine DTI

$$\mathrm{DTI} = \mathrm{DHI}\left[(1-F_1)\frac{1+cos\,\Phi}{2} + F_1\frac{a}{b} + F_2\,sin\,\Phi\right]. \tag{3.3.7}$$

The four components can be computed by Equations 3.3.8 to 3.3.11

$$a = max(0°, cos\,\mathrm{AOI}), \tag{3.3.8}$$
$$b = max(cos\,85°, cos\,\gamma), \tag{3.3.9}$$
$$F_1 = max\left[0, (f_{11} + f_{12}\Delta + \frac{\pi\gamma}{180}f_{13}\right], \tag{3.3.10}$$
$$F_2 = f_{21} + f_{22}\Delta + \frac{\pi\gamma}{180}f_{23}. \tag{3.3.11}$$

Thereby the parameter Δ defines the brightness and can be computed as

$$\Delta = m_r\,\frac{\mathrm{DHI}}{\mathrm{EXI}}, \tag{3.3.12}$$

where m_r is the relative optical air mass and f_{11}, f_{12}, f_{13}, f_{21}, f_{22} and f_{23} are coefficients derived due to empirical data at certain locations.

The reflected part of the irradiance on the ground for the tilted plane can be calculated if the near by albedo factor *alb* is known, with

$$\mathrm{REF} = \mathrm{GHI}\,alb\,\frac{1-cos\,\Phi}{2}. \tag{3.3.13}$$

Reflection losses: After knowing the tilted irradiance arriving on the surface of the PV module an additional reduction occurs due to reflectance on the top layer of the module (Martin and Ruiz 2001). Increasing AOI results in rising reflection losses (De Soto et al. 2006). The reflection losses for direct irradiance can be described by the incident angle modifier (IAM). De Soto et al. (2006) showed that the simple air-glass model based on Snell's law of refraction and the Beer–Lambert–Bouguer law is in accordance with experimental models (Sjerps-Koomen et al. 1996). Therefore it can be used as a good approximation (De Soto et al. 2006). To calculate the angle of refraction ϕ_r the effective index of refraction n of the top module layer (mainly

glass, $n = 1.526$) and the angle of incidence AOI is needed

$$\phi_r \; = \; arc\, sin(1/n\, sin\, \mathrm{AOI}). \tag{3.3.14}$$

The transmittance τ then can be calculated by considering reflection losses by the top layer and absorption within this layer of

$$\tau(\mathrm{AOI}) \; = \; exp(-\frac{KL}{cos\phi_r}) \left[1 - \frac{1}{2}\left(\frac{sin^2(\phi_r - \mathrm{AOI})}{sin^2(\phi_r + \mathrm{AOI})} + \frac{tan^2(\phi_r - \mathrm{AOI})}{tan^2(\phi_r + \mathrm{AOI})}\right)\right]. \tag{3.3.15}$$

K denotes the glazing extinction coefficient ($K = 4$ m^{-1} for "water white" glass) and L the glazing thickness (with $L = 2$ mm being a reasonable value for most PV modules). The IAM is finally the ratio of Equation 3.3.15 for 0° and the AOI

$$\mathrm{IAM} \; = \; \frac{\tau(\mathrm{AOI})}{\tau(0°)} \tag{3.3.16}$$

and must be multiplied with the tilted direct irradiance to include reflection losses on the top layer of the module. For the diffuse irradiance this procedure can be similarly undertaken by using each single radiance with its direction (see Neher et al. (2017) in Chapter 4 for further description).

Effective cell temperature: The operating cell temperature T_c has an important role for projecting PV power due to altering the effective electrical efficiency of the cell (Barry et al. 2020, Skoplaki and Palyvos 2009). Thereby several expressions for T_c can be found including atmospheric parameters like the ambient temperature T, wind speed v_w and GHI. Skoplaki and Palyvos (2009) reviewed dozens of implicit correlations for the cell temperature. For calculating the cell temperature it is important how the module is mounted, for example open rack, roof integrated or transparent PV and of which material the cell is based. Most models are assumed for open rack constructions and silicon-type cells since PV installations basically are mounted in open rack constructions and still the majority is based on silicon.

A model comparison of three models (see Box 3.3 for model description) was undertaken in Sankt Augustin for ten clear sky days during 2015/2016 (see Section 4.1, Neher et al. (2017)). It was found, that the King model (King et al. 2004) performs best with "close to roof" parameters for the installation in Sankt Augustin and is therefore used for the calculations. A reason for this might be the unusual mounting option on the roof. Thereby a black plastic tub is used to mount the PV module (see Figure 3 b in Chapter 4 for a visualization). The temperature of the cell might be much higher for the construction in Sankt Augustin than for an open rack mounting, because the wind is not able to cool down the back of the module. Because with the King model "close to roof" parameters could be used this model may came out best. The other models give only parameters for open rack constructions. A further

fact which could be identified is that a poor cell temperature estimation leads to high uncertainties of PV power calculations. However, with the model by King et al. (2004) the cell temperature can be predicted with an uncertainty of ± 5°C, by using empirical data.

Box 3.3. Temperature models

Simple model (Ross and Gonzalez 1980):

$$T_c = T + \frac{T_{c,NOCT} - T_{a,NOCT}}{I_{NOCT}} \,\mathrm{GHI}, \tag{3.3.17}$$

with NOCT defining the certain parameter at nominal operating cell temperature (NOCT) conditions (I_{NOCT} = 800 W/m^2 and $T_{a,NOCT}$ = 20°C).

Model for different technologies: Compared to the simple model the model developed by Tamizhmani et al. (2003) also includes the wind speed beside the ambient temperature and global irradiance

$$T_c = w_1\, T + w_2\, \mathrm{GHI} + w_3\, v_w + const. \tag{3.3.18}$$

Furthermore, the model differentiates between six technologies based on several materials, namely amorphous, mono-crystalline, poly-crystalline and EFG^a-poly-crystalline silicon as well as copper indium diselenide (CIS) and cadmium telluride (CdTe). The four experimentally derived constant parameters w_1, w_2, w_3 and *const* are given for all six technologies in the named reference. This model assumes an open rack construction.

Kind model: The model designed by King et al. (2004) has the advantage to distinguish between different mounting options, namely open rack, close to roof, insulated back and tracker. The operating cell temperature can be calculated as

$$T_c = T + \frac{\mathrm{GHI}}{1000\, W/m^2}\, \Delta T + \mathrm{GHI} \cdot exp(a + b\, v_w). \tag{3.3.19}$$

a and b denote empirically determined coefficients defining an upper limit of the cell temperature at weak wind speeds and high incoming irradiance and a rate for the correlation between rising wind speed and dropping cell temperature, respectively. ΔT gives a value for the difference between the operating cell temperature and the temperature at the modules back at 1000 W/m^2. These

parameters are given for the different mounting options for flat-plane modules of different manufactures.

[a]"Edge-defined film-fed growth" is a cutting technique with minimal amount of cutting scrap. This procedure was developed by the californian company *ASE Solar*.

Two-diode-model: The two-diode-model represents the optimal characterization of a crystalline PV cell, in particular during low light situations (see Figure 3.3 for the equivalent circuit diagram, (Quaschning 2011: chapter 5)). Thereby, two

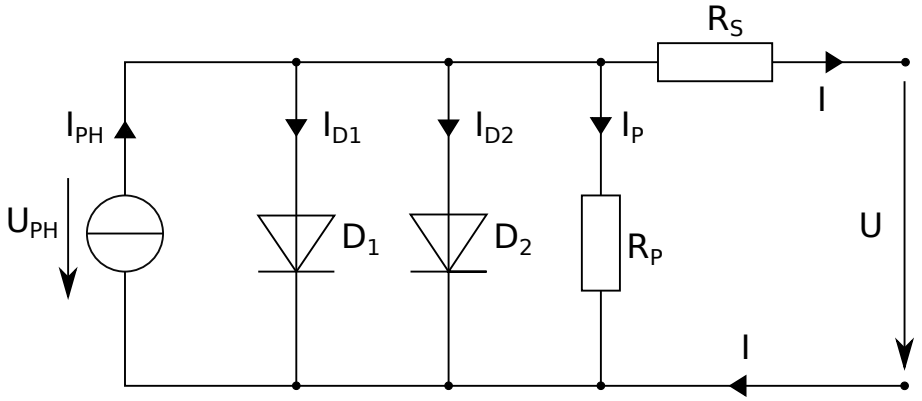

Figure 3.3: Equivalent circuit diagram for the two-diode-model.

diodes (D_1 and D_2) are connected in parallel, with differing saturation currents (I_{D1} and I_{D2}) and constant diode ideality factors (n_1 and n_2, (Salam et al. 2010)). Furthermore, two resistors are connected, for the description of leakage currents (in parallel R_P) and for the description of voltage drops (in series R_S). For the irradiated solar cell a parallel current source can be assumed. The current source produces the photocurrent I_{PH} depending on the global tilted irradiance. With the Kirchhoff' law the two-diode-equation can be written as

$$I(U) = I_{PH} - I_{D1}\left(e^{\frac{U+I\cdot R_S}{n_1\cdot U_T}} - 1\right) - I_{D2}\left(e^{\frac{U+I\cdot R_S}{n_2\cdot U_T}} - 1\right) - \frac{U + I\cdot R_S}{R_P}, \quad (3.3.20)$$

with U_{PH} being the cell voltage and U_T defining the thermal voltage as

$$U_T = \frac{N_s\, k_{boltz}\, T_c}{q}, \quad (3.3.21)$$

with the number of cells in series N_s, the elementary charge $q = 1.6{\cdot}10^{-19}$ C, the Boltzmann constant $k_{boltz} = 1.38{\cdot}10^{-23}$ J/K and the cell temperature T_c.

The PV power at the MPP can be derived as the maximum of the product of I and U after finding a solution of Equation 3.3.20 with an iterative procedure.

Inverter model: In SolPaRT the PV power plant is connected to the grid with a single inverter. To simulate the inverter the model by King et al. (2007) is applied.

This model uses empirical parameters to simulate the system performance of a grid connected inverter. The empirical parameters are provided for several inverters, ranging from residential to commercial size in King et al. (2007). The basic equation of the model relates the DC power (PVDC) to the AC power (PVAC)

$$\mathrm{PVAC} = \left((\frac{\mathrm{PVAC_0}}{A-B}) - C(A-B) \right) \cdot (\mathrm{PVDC} - B) + C(\mathrm{PVDC} - B)^2, \quad (3.3.22)$$

with

$$A = \mathrm{PVDC_0} \cdot (1 + C_1(V_{MPP} - V_0^{DC})) \quad (3.3.23)$$

$$B = \mathrm{PVDC_S} \cdot (1 + C_2(V_{MPP} - V_0^{DC})) \quad (3.3.24)$$

$$C = C_0 \cdot (1 + C_3(V_{MPP} - V_0^{DC})). \quad (3.3.25)$$

Thereby C_i identify the empirical parameters, V_{MPP} is the voltage at the MPP, the underscored 0 gives each parameter at reference operating conditions and $\mathrm{PVDC_S}$ shows the DC power which is needed to start the inversion process.

This model includes different characteristics of an inverter, self-consumption of the inverter, limit of the inverter and efficiency performance characteristics. The accuracy between modeled and measured inverter efficiency is around 0.1% (King et al. 2007).

3.3.3 Parabolic trough power model

To simulate PT power an existing tool, the "green energy system analysis tool" *greenius*, is applied. Greenius allocates detailed technical as well as economic calculations of multiple technologies (such as solar trough power plants, photovoltaic systems, wind parks or Dish/Stirling systems) (Quaschning et al. 2001a,b). It was developed at the German Aerospace Centre (DLR) and provides an interface for specific meteorological input for a certain location. For PV power calculations a new tool calculating the specific I-U curve is developed (see Section 3.3.2) in this thesis, as greenius works only with efficiency correlations, which have higher uncertainties. However, PT power plants are the technology with most detailed models in greenius. Therefore, it is used to calculate PT power performance. A detailed description on the model and all underlying equations can be found in Dersch (2014).

Chapter 4

Impact of atmospheric aerosols on solar power

Within the scope of analyzing the impact of atmospheric aerosols on solar power, this chapter shows the quantitative impact of aerosols at distributed locations in West Africa. Furthermore, the impact of aerosols during a desert dust outbreak is highlighted. The chapter is based on two publications (Neher et al. 2017, 2019). In the first one, a model chain is developed, calibrated and tested for a single location and a single solar power technology, photovoltaic (Section 4.1 - Model development and relevance). In the second one, the study is extended to another solar power technology, parabolic trough power, and a wider region for the reference year 2006 (Section 4.2 - Analysis at six measuring locations).

4.1 Model development and relevance

This section is published as a conference proceeding: Neher, I., Buchmann, T., Crewell, S., Evers-Dietze, B., Pfeilsticker, K., Pospichal, B., Schirrmeister, C., and Meilinger, S. (2017). Impact of atmospheric aerosols on photovoltaic energy production - Scenario for the Sahel zone. *Energy Procedia*, 125:170–179,

Author contributions: IN is the first author of the publication. She designed the model and performed all the data analysis. For the model development a special focus was on the photovoltaic power model part, for which single components were tested and validated with observational data. BED and CS maintained the measuring station at University of Applied Science Bonn-Rhein-Sieg and allocated the measurement data which was used for the validation of the model. BP helped with the preparation of the data from the ARM measuring station in Niamey. TB and KP were involved in scientific discussions at Heidelberg university. SC and SM provided the overall scientific guidance and discussed results. IN prepared the

manuscript, which was commented and discussed with all co-authors. IN created all figures (except for Figure 3, in this thesis Figure 4.3). The pictures for Figure 3 were taken by BED.

Available online at www.sciencedirect.com

ScienceDirect

Energy Procedia 125 (2017) 170–179

Energy Procedia

www.elsevier.com/locate/procedia

European Geosciences Union General Assembly 2017, EGU
Division Energy, Resources & Environment, ERE

Impact of atmospheric aerosols on photovoltaic energy production Scenario for the Sahel zone

Ina Neher[a,b,*], Tina Buchmann[c], Susanne Crewell[b], Bernd Evers-Dietze[a], Klaus Pfeilsticker[c], Bernhard Pospichal[b], Christopher Schirrmeister[a], Stefanie Meilinger[a]

[a] *International Center for sustainable development, University of Applied Science Bonn-Rhein-Sieg, Grantham-Allee 20, 53757 Sankt Augustin, Germany*

[b] *Institute of Geophysics and Meteorology, University of Cologne, Albertus-Magnus-Platz, 50923 Kln, Germany*

[c] *Insitute of Environmental Physics, Heidelberg University, Grabengasse 1, 69117 Heidelberg, Germany*

Abstract

Photovoltaic (PV) energy is one option to serve the rising global energy need with low environmental impact. PV is of particular interest for local energy solutions in developing countries prone to high solar insolation. In order to assess the PV potential of prospective sites, combining knowledge of the atmospheric state modulating solar radiation and the PV performance is necessary. The present study discusses the PV power as function of atmospheric aerosols in the Sahel zone for clear-sky-days. Daily yields for a polycrystalline silicon PV module are reduced by up to 48 % depending on the climatologically-relevant aerosol abundances.

Peer-review under responsibility of the scientific committee of the European Geosciences Union (EGU) General Assembly 2017 – Division Energy, Resources and the Environment (ERE).

Keywords: energy meteorology; photovoltaic; aerosol; irradiance; Sahel zone

1. Introduction

The 7th goal of the United Nation's Sustainable development goals "Ensure access to affordable, reliable, sustainable and modern energy for all" [1], mandates a shift away from the traditional fossil-fuel powered energy system towards renewable energy. PV energy is one option to serve the rising global energy demand at low environmental impacts [2,3]. Building an energy system, with a considerable share of PV power, requires long-term investment and a careful investigation of potential sites. Therefore, understanding the influence of varying regional and local atmospheric conditions on PV energy production is crucial for energy yield projections. Specifically, the incoming solar radiation is modified in the atmosphere due to absorption and scattering on trace gases, aerosol and cloud particles

* Corresponding author. Tel.: +49 2241 865 780; fax: +49 2241 865 8780.
E-mail address: Ina.Neher@h-brs.de

1876-6102
Peer-review under responsibility of the scientific committee of the European Geosciences Union (EGU) General Assembly 2017 – Division Energy, Resources and the Environment (ERE).
10.1016/j.egypro.2017.08.168

[4,5]. However, information about these parameters is not easily available in a reasonable spatiotemporal resolution. In attempts to counter this absence of local measurements, different approaches have been estimating solar radiation at the ground by using simple models that are based on scaling long term averages [6], numerical radiative transfer (RT) models [7,8], or simulations relying on satellite data and weather models [9,10].

Modeling PV power requires considering the direct and diffuse solar radiation in the module plane, reflection losses and cell temperature [11]. Furthermore, determining the cell temperature requires the knowledge of ambient temperature and wind speed. PV cell performance models usually use either inputs from ground-based measurements, satellite data and/or numerical weather simulations for the solar radiation at the ground [12–15]. In atmospheric science, detailed RT models, using information of the atmospheric state as input, are used to calculate the radiative flux profiles in the atmosphere [16]. However, these models do not support PV power calculations. In this study, we combine various tools known in the atmospheric- and PV-community by coupling a multi-layer RT model with a two-diode based PV power model. Thereby we take into account the variation of radiation due to aerosols, the transformation of horizontal radiation to the tilted plane of the module, reflection losses on the module front and cell temperature behavior. The PV power model is designed to simulate a representative PV module, i.e., a polycrystalline Solar World silicon module, with a maximum power at standard test conditions (STC) of 235 Wp (in brief a SW 235 poly) [17].

In the present study, we use the combined model chain to assess the PV potential in the Sahel region for several reasons. First, it is a region suffering from the lack of energy infrastructure. Second, local solutions for power production based on PV are attractive due to the high solar insolation year around. Third, the region is characterized by its diversity in land use and its large seasonal changes due to the influence of the West African monsoon. In the dry season conditions are arid and dusty while the wet season is moister and cloudier. Finally, the deployment of the Atmospheric Radiation Program (ARM) Mobile Facility (AMF) in Niamey, Niger (13.5 N, 2.2 E) throughout 2006 [18,19] offers detailed data sets to investigate atmospheric effects on solar radiation. With less than 10 % cloud fraction observed during the AMF observational period [20,21] the major variability of solar radiation is caused by the presence of atmospheric aerosols [19].

The effect of aerosols on solar radiation strongly depends on their physical, i.e., aerosol size distribution and particle shape, their chemical composition, and land surface conditions [22–24]. Depending on their optical properties, aerosols reduce the direct solar radiation component and modify the direction of the diffuse component, compared to aerosol-free atmospheric conditions. To investigate the aerosol effect on PV power in detail, we select 69 clear-sky-days observed by AMF for our model calculations.

After this brief introduction, the model chain is described in section 2. Its calibration is performed in Sankt Augustin using collocated meteorological data and PV power measurements (in section 3). The fourth section shows the prediction of the impact of aerosols on daily PV yields in Niamey, using the model chain with a theoretically mounted module. Our results are then discussed in section 5, and the study is concluded with our main findings in section 6.

2. Model description

For estimating aerosol impact in Niamey, PV yields are simulated for an aerosol-free and an aerosol-loaded atmosphere using the model chain depicted in Fig. 1. Based on the atmospheric state as an input (see section 4 for detailed parameters) we use the library of RT programs and routines (libRadtran) [8,25] to calculate the direct and diffuse solar radiation for a horizontal surface. The modelled libRadtran irradiances and radiances are used to calculate the effective radiation on the tilted PV module. This is determined in two steps. First the radiation is transformed to the tilted plane and second reflection losses on the module front are taken into account. Furthermore, the cell temperature is simulated from ambient temperature and wind speed. Based on this input, depending on atmospheric parameters, and subsequently using PV module characteristics (provided by manufacturer) as additional input for the two-diode model, PV power calculations are undertaken. For all simulations we use hourly data.

The main libRadtran function uvspec can compute radiances, irradiances and actinic fluxes for pre-described atmospheric states. In our model chain the RT equation is numerically solved by using the DISORT (DIScrete Ordinates Radiative Transfer solver) algorithm [26]. The irradiance is calculated using 6 streams while radiances are calculated using 16 streams. The radiation is integrated over the wavelength interval from 290 nm to 2600 nm, covering the total spectral range relevant for PV cells. For the molecular absorption a correlated k method developed by Kato et al. [27]

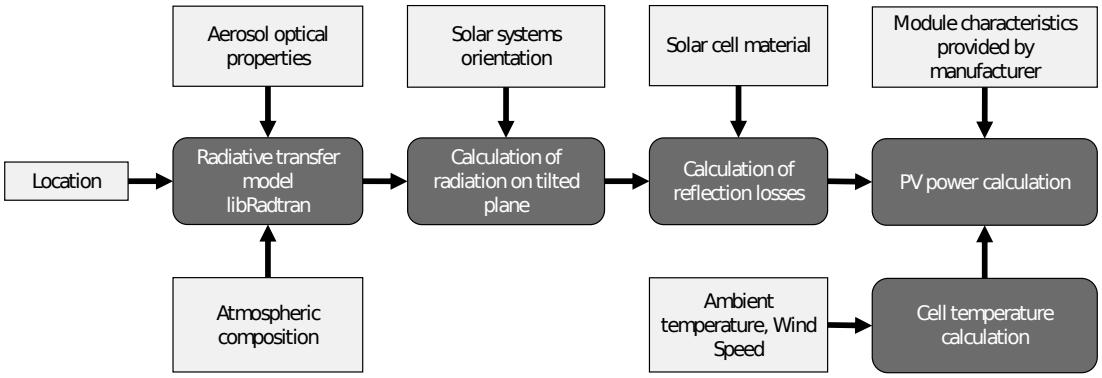

Fig. 1. Schematic overview on the model structure (input data light grey, single model steps dark grey).

is applied to reduce the computing time. Local measurements of trace gases and aerosol optical properties are used to define the atmospheric state. Missing parameters are included by using a standard tropical atmosphere and a typical desert aerosol composition defined by the Optical Properties of Aerosols and Clouds (OPAC) library by Hess et al. [24].

The effective radiation used from the PV cell is calculated by transforming the single components of the radiation to the tilted plane and considering reflection losses on the modules surface. Direct radiation I_{dir} can be analytically transformed to the tilted plane I_{dir}^{tilt} using an Eulerian transformation with the solar zenith being γ and α the solar azimuth angle as well as the PV modules orientation (azimuth α_{PV} and tilting angle Φ)

$$I_{dir}^{tilt} = I_{dir} \frac{cos(\Phi)\,cos(\gamma) + sin(\Phi)\,sin(\gamma)\,cos(\alpha - \alpha_{PV})}{cos(\gamma)}. \quad (1)$$

The diffuse radiation on the tilted plane I_{diff}^{tilt} is determined from the calculated spatial distribution of the incoming diffuse radiation $I_{diff}(\gamma, \alpha)$. LibRadtran allows explicit modelling of the diffuse radiance distribution over the whole sky dome. However, this is computationally costly. The computing time is reduced by using the horizontal component of diffuse radiation calculated by libRadtran and by deriving its spatial distribution using a parametrized model. In general, several models for the spatial distribution of diffuse radiation are documented in literature [28,29]. The different models for the effective diffuse radiation received on the tilted plane are tested by using the diffuse radiation calculated by libRadtran. The different streams are analytically transformed to the tilted plane (using Equation 1) before integrating them over all azimuth and zenith angles. The model which shows the least difference to the libRadtran results is then taken in our model chain. For this study, one isotropic model developed by Liu and Jordan [30] and two three-component models [31,32] are compared assuming an aerosol load typical for deserts. The three-component models take one isotropic, one circumsolar and one horizontal brightening component into account. The model of Reindl et al. [31] uses the transmittance to determine the fraction of each diffuse component, while the model by Perez et al. [32] uses empirical parameters. Diffuse radiation is calculated for solar zenith angles from 0° to 75° in 15° steps, a solar azimuth angle of 180° and tilt angles of the PV module between 0° and 90° in 5° steps for a south orientated module. For each tilt angle of the PV module the percentage bias and root mean square error (RMSE) are calculated for each single model using the analytically transformed radiation as a reference (Fig. 2). Among all tested models, the Perez model performs similarly well as the libRadtran calculation for tilt angles of the PV module around 15°, with a bias of 2 % and a RMSE of 13 W/m^2. Therefore, we use the Perez model to calculate the effective diffuse radiation on the tilted plane.

Reflection losses in the surface layer of the PV cell are calculated by using the incidence angle modifier (IAM) described in De Soto et al. [33]. For the calculation a glazing extinction coefficient of 4 m^{-1} (water white glass), a glazing thickness of 2 mm and a refractive index of 1.526 (glass) is used, which are typical parameters for PV modules [33]. Reflection losses of the direct radiation can be calculated by using the incidence angle on the module and Snells law. For the diffuse radiation an isotropic, horizon and reflective IAM are calculated. The isotropic IAM is the mean over IAMs from all directions of the sky dome in azimuthal steps of 2° and elevation steps of 0.5°. The horizon IAM is assumed to be the mean over all IAMs of radiation coming from the horizon (with azimuthal steps of 2°). The reflective IAM is calculated similar to the isotropic IAM, but for radiation received from the ground.

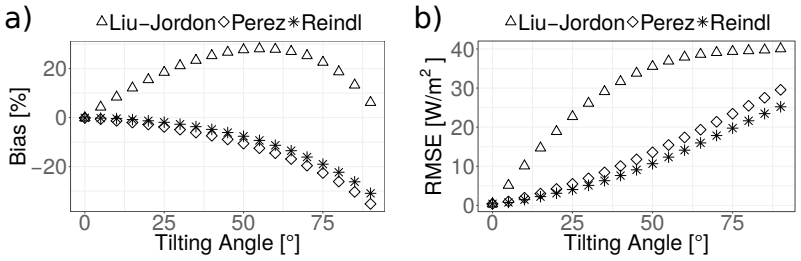

Fig. 2. Bias (a) and RMSE (b) of various diffuse radiation models, namely Lui-Jordon (triangle), Perez (diamond) and Reindl (star) using the libRadtran calculations of radiances for varying tilting angles in a desert aerosol regime as a reference.

Considering the PV cell temperature is important because rising cell temperatures reduce the efficiency of PV modules [34]. The cell temperature can be derived using different model approaches [35]. Each model approach has been developed for a certain mounting option, building geometry and module material. For the model calibration calculations (see section 3) a model accounting for the closed mounting system on the measuring site in Sankt Augustin is used. The model has been developed by King et al. [12] from the Sandia National Laboratory, allowing to account for different mounting options. It is able to predict the cell temperature within 5 °C with a minimum amount of input, if the correct mounting option is assumed [35,36]. Parameters for the closed roof mount option and the required input for ambient temperature and wind speed are employed.

Modeling PV power requires the estimation of a non-linear I-U curve. One simple approach is to assume the electrical behavior of a PV module as a single diode. This model approach is in good agreement to outdoor measurements for polycrystalline silicon modules [14]. However, for low irradiance calculations it comes with high uncertainties [37,38]. The two diode model allows improved I-U calculations especially suited for low irradiances [39]. In this study the simple model approach designed by Ishaque et al. [37] is applied. It requires four parameters to describe the current equation, which makes it fast compared to other models using seven parameters [40] and still brings reliable results. For different temperatures, relative errors for the maximum power point are smaller than 1 % as compared to measured data for all tested modules [37].

3. Model calibration at the measurement site in Sankt Augustin

Since the beginning of 2015 we have been continuously measuring global, diffuse and direct normal radiation as well as PV power of a polycrystalline silicon module at the University of Applied Science Bonn-Rhein-Sieg in Sankt Augustin, Germany (50.7 N, 7.2 E) (Fig. 3). These measurements are used to calibrate our PV power model. The skylight radiation has been measured using a SOLYS 2 sun tracker with two CMP 11 pyranometers and a CHP 1 pyrheliometer from Kipp & Zonen, and the PV power is from the SW 235 poly [17]. The module is orientated at 191° azimuth and 14° tilt angle. Furthermore, detailed local meteorological parameters have been measured, e.g. ambient temperatures and wind speed. The PV power model, designed for a SW 235 poly, is validated with running the model using hourly measured data of the global and diffuse radiation, ambient temperature and wind speed. The model output is compared to the SW 235 PV power measured in Sankt Augustin on an hourly resolution for ten clear-sky-days during 2015/2016. The ten days are distributed over all seasons to cover a wide range of celestial and atmospheric conditions. An albedo of 0.18 is assumed because of gravel in the near environment of the measurement site [41]. Hourly measured and simulated PV power is shown in Fig. 4. For zenith angles < 75°, percentage bias and RMSE between simulated and observed PV power is deter-

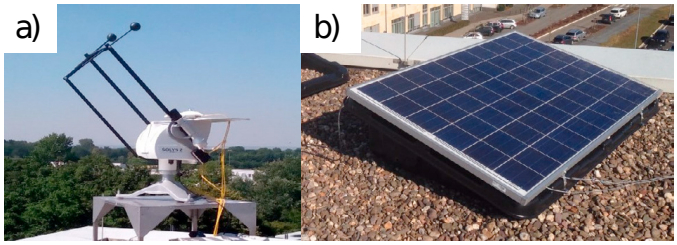

Fig. 3. Equipment for measuring global, diffuse and direct normal radiation (a) and PV yields of a SW 235 poly module (b) at University of Applied Science Bonn-Rhein-Sieg in Sankt Augustin, Germany (50.7 N, 7.2 E).

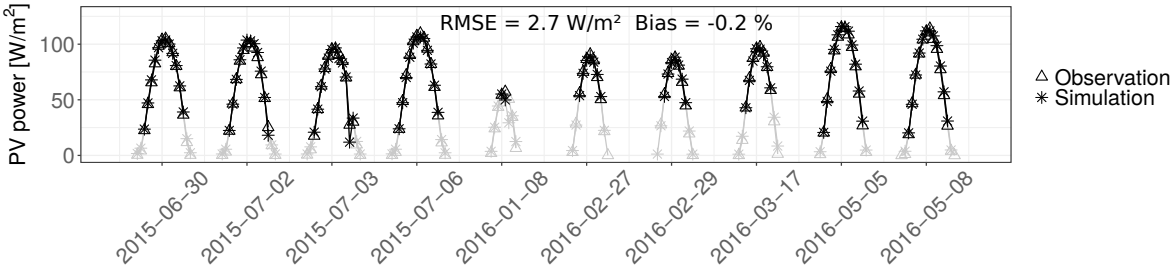

Fig. 4. Comparison of measured PV yields in Sankt Augustin, Germany (triangles) and those modelled using the novel developed PV power model (stars) on an hourly basis for ten clear sky days in 2015/2016. Biases and RMSEs are calculated for zenith angles below 75°, the used points are marked in black.

mined. We discarded measurements at high solar zenith angles because of disturbing reflections from the roof fringe in early morning and late evening hours. The PV power model performs well with a relative bias of -0.2 % and a RMSE of 2.7 W/m^2 compared to the PV power measurements on clear-sky-days.

4. Impact of desert aerosols on PV energy in Niamey, Niger

After having calibrated our PV power model with measurements performed in Sankt Augustin, Germany, we apply the model to a prospective plant located at Niamey airport (13.5 N, 2.2 E). From there excellent solar irradiance data are available from the "Radiative Divergence using AMF, GERB and AMMA (African Monsoon Multidisciplinary Analysis) Stations" (RADAGAST) campaign in 2006 [18,19,42]. Within the framework of the campaign, the U.S. AMF as a mobile base deployed a set of instruments to collect atmospheric and climate data [43]. The instrumentation provides measurements of optical properties of aerosols, trace gas concentration, broadband radiation, etc. The locally measured data are used to first simulate direct and diffuse radiation using libRadtran and second to project PV power of a theoretically mounted SW 235 poly module, orientated at 191° azimuth and 14° tilt angle, similar to the measurement set-up in Sankt Augustin.

The whole model chain (see section 2) is applied to simulate 69 clear-sky-days in Niamey that occurred in 2006. Eight of the analyzed days lie in the wet season between May and September while the remaining days were in the dry season. Atmospheric data from the RADAGAST campaign and the Monitoring Atmospheric Composition and Climate (MACC) reanalysis data base by European Centre for Medium-range Weather Forecasts [44] are used as input for the libRadtran simulations (Table 1).

Table 1. Data implemented in libRadtran with indicating the data base, the data format and the way of implementation.

Parameter	Data base	Description	Implementation
Water vapor	ARM	Column value	Scaled for atmospheric layers
Ozone	MACC	Column value	Scaled for atmospheric layers
AOD	ARM	At 500 nm	Scaled for all wavelength and atmospheric layers
Angstrom exponent	ARM	Using AOD at 500 nm and 870 nm	Used for scaling of AOD
Angstrom coefficient	Calculated	From angstrom exponent and AOD at 500 nm	Used for scaling of AOD
SSA	ARM	At 550 nm	Scaled for all wavelength and atmospheric layers
Surface albedo	Calculated	From up- and down-welling global radiation	Averaged value is implemented

For the calculation, measured total atmospheric water vapor, ozone, aerosol optical depth (AOD) at 500 nm and single scattering albedo (SSA) at 550 nm are used. Angstrom exponent inferred from the measured AOD at 500 nm and 870 nm, Angstrom coefficient are subsequently calculated from the Angstrom exponent and AOD at 500 nm. Down- and up-welling total radiation is applied for calculating the ground albedo. Furthermore, we assume a desert aerosol composition profile from the OPAC data base [24]. The data base contains typical mass concentration and aerosol optical properties like AOD, SSA and asymmetry parameter, which are used for missing values or parameters which were not measured [24].

The atmospheric RT simulations are compared with the broadband down-welling solar radiation observed during the RADAGAST campaign (Fig. 5). The simulations agree well with the measurements with a slight underestimation during high aerosol loads and an overall relative bias of -0.3 % and RMSE of 29 W/m^2. Especially without knowing the aerosol characteristics, e.g. size distribution, shape, chemical composition, over the full vertical profile it is impossible to improve the simulations. The simulation including aerosols is called ”aerosol-loaded” scenario in the following. A second set of calculations address the aerosols-free case, which will be called the ”aerosol-free” scenario. For this purpose, the simulations are repeated as described above with the only difference that no aerosols are included in the atmospheric RT calculations. The down-welling radiation from both scenarios is then used for all further steps of the modeling chain (see section 2) to calculate PV power.

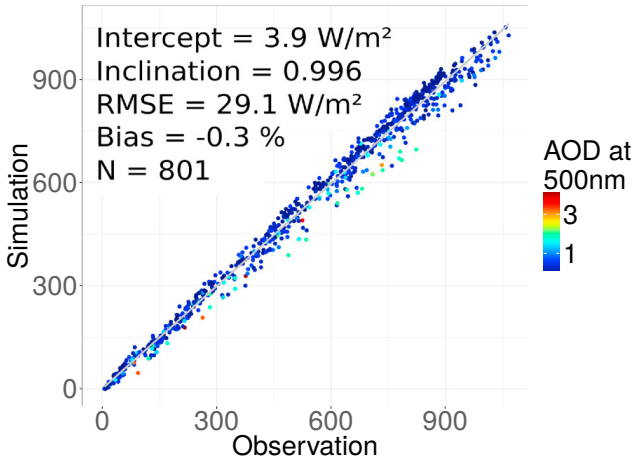

Fig. 5. Comparing hourly simulated values of global radiation with hourly observed global radiation during 69 clear-sky-days in 2006 in Niamey using the whole daily data set. The color scale shows the observed value of aerosol optical depth at 500 nm.

Fig. 6 shows modeled PV power for all 69 days at 1200 UTC noon and diurnal variations for three exemplary days with different aerosol loads. March 8, 2006 comprises a day with a sand storm when the AODs went up to 4. In contrast, on December 27, 2006 the aerosol load was low, with an AOD of about 0.1. On March 17, 2006 the AOD was about 0.5, typical for an average aerosol load on clear-sky-days in 2006. It can be clearly seen, that on an hourly basis for the ”aerosol-free” scenario higher PV power is obtained compared to the ”aerosol-loaded” scenario for all

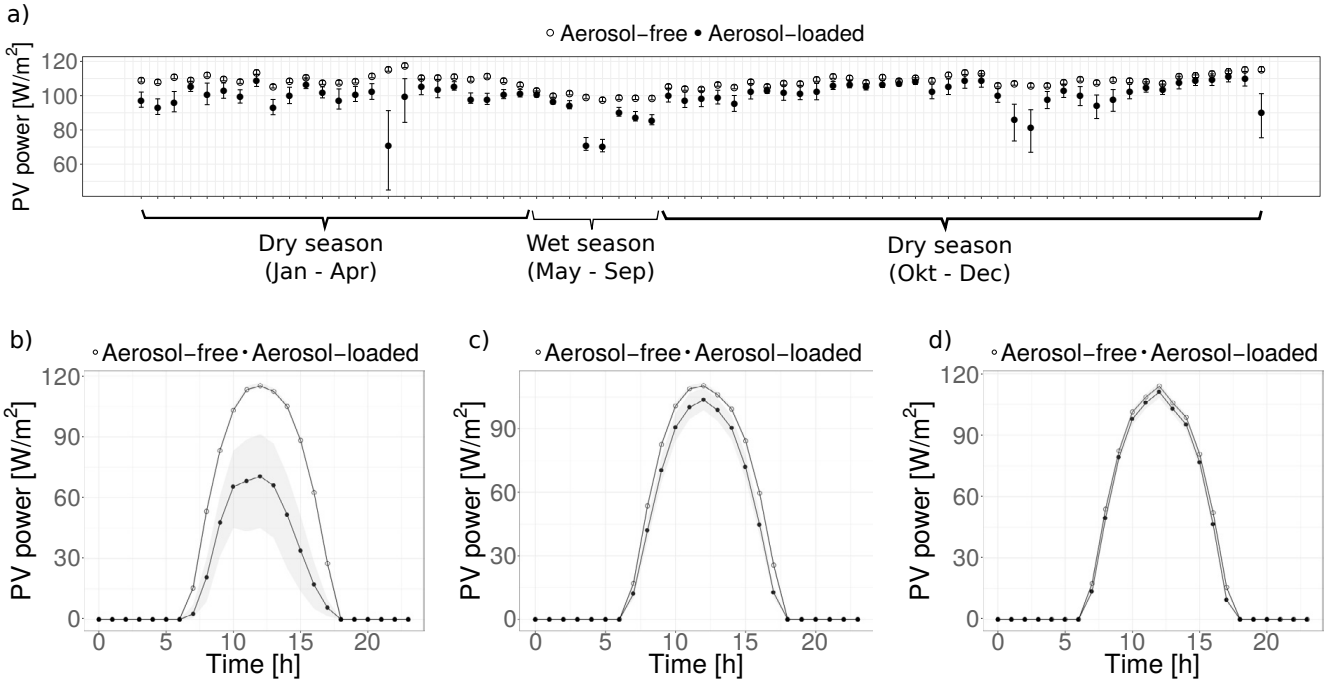

Fig. 6. Modeling PV power in an aerosol-free (blanc circle) and an aerosol-loaded (filled circle) scenario at 1200 UTC noon on 69 clear-sky-days (a) and for three special days, with an extreme (b), an averaged (c) and a low aerosol impact (d) on March 8, March 17 and December 27 respectively in 2006 in Niamey.

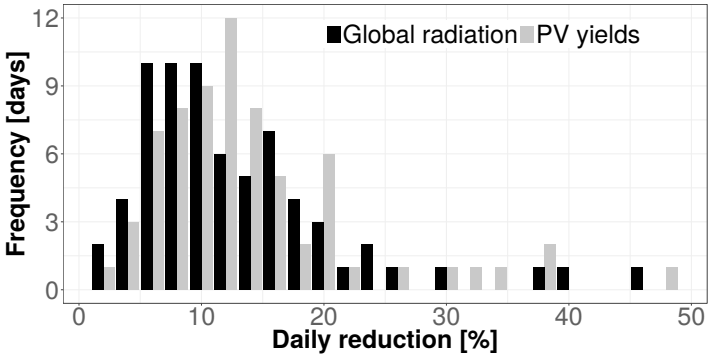

Fig. 7. Frequency of occurrence of daily reduction due to the presence of aerosols for daily global radiation (black) and PV yields (grey) on clear-sky-days in 2006 in Niamey.

aerosol loads. In a next step, the daily reduction of PV yields and global radiation due to the presence of aerosols is computed as the percentage difference between the two scenarios as a day integral for each day (Fig. 7). The mean daily reduction of PV yields and global radiation for all 69 days is 14 % and 13 %, respectively. However, during extreme events, i.e., dust storms, daily reduction in PV yields are as large as 48 %.

5. Discussion

We show that due to the presence of aerosols on average daily global radiation and daily PV yields for a poly-crystalline module are reduced by 14 % and 13 % respectively in Niamey on otherwise mostly clear sky days (see Fig. 7). These reductions in global radiation and PV yield are calculated using a coupled RT model for global radiation (libRadtran) and a subsequent PV power model (two-diode model) (see section 2), comparing ”aerosol-free” and ”aerosol-loaded” scenarios. In our model chain, we consider cell temperature, effective radiation on the tilted plane and reflection losses. The modeled global radiation on the horizontal plane is validated with measured data collected during the RADAGAST campaign in 2006. In contrast, simulated PV power are purely theoretical estimates since no data is available for this location and time period. However, the applied model chain combines knowledge from the atmospheric- and PV-community, assesses different characteristics of PV modules and considers all relevant factors, namely projecting the effective radiation on the tilted plane, reflection losses and cell temperature. Considering the difference of daily reduction in global radiation and PV yields (Fig. 7), the importance of details in such model chains is evident.

Apparently, the results of RT calculations largely depend on the atmospheric composition (e.g. trace gases and aerosols) in each atmospheric layer [25]. However, the knowledge of all relevant input parameters for each specific location is limited. In Niamey simulations, detailed measurements of the relevant input parameters are used which are not available for most locations. The used data sets for Niamey are total column amounts measured on the ground. While information on atmospheric gases are obtained from reanalysis or measurements with reasonable accuracy the situation is more difficult for aerosol. Here we consider measured aerosol optical properties combined with the assumption of a standard desert aerosol distribution profile [24]. Thus, uncertainties due to the spreading of column values over all atmospheric layers, the scaling to all wavelengths (Table 1), and the accuracy of measurements themselves are evident. All of these effects may cause sizable differences between measured and simulated radiation. Maximal errors due to measurement uncertainties are calculated by considering a scenario with lowest and highest global radiation. In order to span the maximal range of uncertainties, minima and maxima for AOD, water vapor, ozone, SSA and surface albedo are used in these simulations, depending on their effect on global radiation. Consequently, our simulations indicate mean daily reduction of PV yields ranging from 8 % to 20 % providing an uncertainty estimate of the mean of 14 %. Our calculations thus demonstrate that due to the presence of aerosols PV yields are reduced on average of at least 8 % in Niamey on clear-sky-days.

The PV power model includes a two-diode model for the I-U relation proposed by Ishaque et al. [37]. This approach is validated for three different module types, namely multi crystalline, mono crystalline and thin film. The simulation of all modules show relative errors of the power yields below 1 % for the relevant temperature range from -25 °C

to 75 °C compared to measurements [37]. Our model chain also includes an effective cell temperature model and a model to derive effective radiation on the tilted plane depending on the direction of diffuse radiation. Cell temperature consideration highly depends on the mounting option of the module [35] as investigated by Kurnik et al. [45]. As open rack mounting is frequently used for PV installations [12], they compared open rack and roof integrated mounting options. In particular, Kurnik et al. [45] found that due to the reduced cooling, roof integrated modules suffer more from temperature related reduction in the PV power than open frame systems. Therefore, when considering the cell temperature, the knowledge of the mounting option of a module is necessary. For our PV power calculations in Niamey, we assume a close roof mounting, because of the comparability to our measuring site in Sankt Augustin (see section 3). However, to generalize the model approach different mounting options should always be considered systematically when analyzing and predicting PV yields. The effective diffuse radiation is calculated using the Perez model [32]. In literature studies comparing diffuse radiation models do not recommend the same models [29,46,47]. Here the different diffuse radiation models are compared to simulations of the RT model libRadtran. For low tilt angles (e.g. of 14°) the different models predict similar diffuse radiation (Fig. 2).

One further factor important for PV power calculations but not yet considered in the present model chain is the variation of the atmospheric spectrum due to e.g. the varying near infrared absorption of water. Here we consider a polycrystalline silicon module, for which the uncertainties due to spectral effects only lie between 1 % and 4 % [48,49].

6. Conclusion

Accurate modelling of PV power is one key element for the development of a renewable energy based power system, especially in developing countries with high solar insulation. In this study, a model chain is set-up which couples an atmospheric RT model with a PV power model. This newly developed model chain is used to investigate the impact of aerosols on PV power for a polycrystalline silicon module over the course of the year in a sub-Saharan region i.e., Niamey, Niger. PV power is predicted based on detailed meteorological information for 69 clear-sky-days there during 2006. Daily reductions in PV yields due to the presence of aerosols are found to range from 2 %, 48 % with a mean of 14 %. A maximum reduction of 48 % is predicted during a sand storm event. Decreasing daily PV yields with increasing atmospheric aerosol load is of particular concern in the light of anthropogenic impacts on atmospheric aerosol concentration [50]. In semi-arid regions like the Sahel zone ongoing desertification might be caused by land use changes [51]. For system operators and project planners the related changes are important to know especially in light of strong seasonal and regional variability of dust storm frequency [52].

It is worth noting that daily global radiation does not directly relate to PV yields (Fig. 7) implying the necessity of the full modelling chain. By using both, meteorological and PV engineering knowledge, we are able to model PV yields involving cell temperature consideration, radiation on the tilted plane and reflection losses on the modules front. However, to generalize the model further research is needed to include different mounting options and spectral effects. Furthermore, a detailed analysis of diffuse radiation models using different solar zenith angles and module tilting angles in comparison to measured data has to be undertaken.

Acknowledgements

The first author, Ina Neher, is thankful for a PhD fellowship from the Heinrich Böll Foundation, and Tina Buchmann is grateful for a PhD fellowship from the Deutsche Bundesstiftung Umwelt (German Federal Environmental Foundation). Furthermore, we thank Bernhard Meyer and Claudia Emde for their helpful tips concerning the simulations with libRadtran. The authors would like to thank numerous data providers: Data in Niamey were obtained from the Atmospheric Radiation Measurement (ARM) Climate Research Facility, a U.S. Department of Energy Office of Science user facility sponsored by the Office of Biological and Environmental Research and from ECMWF/MACC project. Data in Sankt Augustin have been obtained in close collaboration with MeteoGroup. The installation of the equipment was partly financed by the ministry for Innovation, Science and Research of the federal state Nordrhein-Westfalen, Germany.

References

[1] United Nations (2015) "Transforming our world: the 2030 agenda for sustainable development." available from undocs.org/A/RES/70/1

[2] Solangi, K.H., M.R. Islam, R. Saidur, N.A. Rahim, and H. Fayaz. (2011) "A review on global solar energy policy." *Renewable and Sustainable Energy Reviews* 15.4 (2011): 2149–63.

[3] Haegel, Nancy M., Robert Margolis, Tonio Buonassisi, David Feldman, Armin Froitzheim, Raffi Garabedian, Martin Green, Stefan Glunz, Hans-Martin Henning, Burkhard Holder, Izumi Kaizuka, Benjamin Kroposki, Koji Matubara, Shigeru Niki, Keiichiro Sakurai, Roland A.Schindler, Williams Tumas, Eicke R. Weber, Gregory Wilson, Michael Woodhouse, and Sarah Kurtz. (2017) "Terawatt-scale photovoltaics: Trajectories and challenges." *Science* 356.6334 (2017): 141–3.

[4] Wallace, John M., and Peter V. Hobbs. (2006) "Atmospheric Science: An Introductory Survey." Second Edition. Elsevier

[5] Boucher, Olivier (2015) "Atmospheric Aerosols: Properties and Climate Impacts." Springer

[6] Gueymard, Christian A. (2003) "Direct solar transmittance and irradiance predictions with broadband models. Part I: detailed theoretical performance assessment." *Solar Energy* 74 (2003): 355–79.

[7] Gueymard, Christian A. (1995) " SMARTS2: a Simple Model of the Atmospheric Radiative Transfer of Sunshine: Algorithms and performance assessment." *Florida Solar Energy Center* (1995).

[8] Mayer, Bernhard, and Arve Kylling. (2005) "Technical note: The libRadtran software package for radiative transfer calculations - description and examples of use." *Atmospheric Chemistry and Physics Discussions* 5 (2005): 1855–77.

[9] Hammer, Annette, Detlev Heinemann, Elke Lorenz, and B. Lückehe. (1999) "Short-term forecasting of solar radiation: a statistical approach using satellite data." *Solar Energy* 67.1 (1999): 139–50.

[10] Hammer, Annette, Detlev Heinemann, Carsten Hoyer, Rolf Kuhlemann, Elke Lorenz, Richard Müller, and Hans Georg Beyer. (2003) "Solar energy assessment using remote sensing technologies." *Remote Sensing of Environment* 86.3 (2003): 423–32.

[11] Inman, Rich H., Hugo T.C. Pedro, and Carlos F.M. Coimbra. (2013) "Solar forecasting methods for renewable energy integration." *Progress in Energy and Combustion Science* 39.6 (2013): 535–76.

[12] King, D.L., W.E. Boyson, and J.A. Kratochvil. (2004) "Photovoltaic array performance model." SAND2004-3535, Sandia National Labratories.

[13] Lo Brano, Valerio, Aldo Orioli, Giuseppina Ciulla, and Alessandra Di Gangi. (2010) "An improved five-parameter model for photovoltaic modules." *Solar Energy Materials and Solar Cells* 94.8 (2010): 1358–70.

[14] Makrides, George, Bastian Zinsser, Markus Schubert, and George E. Georghiou. (2013) "Energy yield prediction errors and uncertainties of different photovoltaic models." *Progress in Photovoltaics: Research and Applications* 21.1 (2013): 500–16.

[15] Sengupta, M., S. Kurtz, A. Dobos, S. Wilbert, E. Lorenz, D. Renné, D. Myers, S. Wilcox, P. Blanc, and R. Perez. (2015) "Best Practices Handbook for the Collection and Use of Solar Resource Data for Solar Energy Applications.", National Renewable Energy Laboratory, available at www.nrel.gov/publications

[16] Petty, Grant W. A. (2006) "First Course in Atmospheric Radiation." Sundog Publishing

[17] Solar World. (2012) "Data sheet of solar world 235 poly module." available at http://www.shop-muenchner-solarmarkt.de

[18] Slingo, A, N.A. Bharmal, G.J. Robinson, J.J. Settle, R.P. Allan, H.E. White, P.J. Lamb, M. Issa Lélé, D.D. Turner, S. McFarlane, E. Kassianov, J. Barnard, C. Flynn, and M. Miller. (2008) "Overview of observations from the RADAGAST experiment in Niamey, Niger: Meteorology and thermodynamic variables." *Journal of Geophysical Research Atmospheres* 113.D13 (2008): 1–18.

[19] Slingo, A, H.E. White, N.A. Bharmal, and G.J. Robinson. (2009) "Overview of observations from the RADAGAST experiment in Niamey, Niger: 2. Radiative fluxes and divergences." *Journal of Geophysical Research* 114.D13 (2009): 1–19.

[20] Kollias, Pavios, Mark A. Miller, Karen L. Johnson, Michael P. Jensen, and David T. Troyan. (2009) "Cloud, thermodynamic, and precipitation observations in West Africa during 2006." *Journal of Geophysical Research Atmospheres* 114.D13 (2009): 1–16.

[21] Pospichal, Bernhard. (2009) "Diurnal to annual variability of the Atmospheric Boundary Layer over West Africa: A comprehensive view by remote sensing observations." PhD Thesis, University of Cologne, available at https://kups.ub.uni-koeln.de/id/eprint/2985

[22] Gunderson, I., S. Goyette, A. Gago-Silva, L. Quiquerez, and A. Lehmann. (2014) "Climate and land-use change impacts on potential solar photovoltaic power generation in the Black Sea region." *Environmental Science & Policy* 46.0 (2014): 70-81.

[23] Kaufman, Yoram J., Didier Tanré, and Olivier Boucher. (2002) "A satellite view of aerosols in the climate system." *Nature* 419.6903 (2002): 215–23.

[24] Hess, M., P. Koepke, and I. Schult. (1998) "Optical Properties of Aerosols and Clouds: The Software Package OPAC." *Bulletin of the American Meteorological Society* 79.5 (1998): 831–44.

[25] Emde, Claudia, Robert Buras-Schnell, Arve Kylling, Bernhard Mayer, Josef Gasteiger, Ulrich Hamann, Jonas Kylling, Bettina Richter, Christian Pause, Timothy Dowling, and Luca Bugliaro (2016) "The libRadtran software package for radiative transfer calculations (version 2.0.1)." *Geoscientific Model Development* 9.5 (2016): 1647–72.

[26] Stamnes, Knut, S-Chee Tsay, Warren Wiscombe, and Kolf Jayaweera. (1988) "Numerically stable algorithm for discrete-ordinate-method radiative transfer in multiple scattering and emitting layered media." *Applied Optics* 27.12 (1988): 2502–9.

[27] Kato, Seiji, Thomas P. Ackerman, James H. Mather, and Eugene E. Clothiaux. (1999) "The k-distribution method and correlated-k approximation for a shortwave radiative transfer model." *Journal of Quantitative Spectroscopy and Radiative Transfer* 62.1 (1999): 109–21.

[28] Loutzenhiser, P.G., H. Manz, C. Felsmann, P.A. Strachan, T. Frank, and G.M. Maxwell. (2007) "Empirical validation of models to compute solar irradiance on inclined surfaces for building energy simulation." *Solar Energy* 81.2 (2007): 254–67.

[29] Gracia, Ana María, and Thomas Huld. (2013) "Performance comparison of different models for the estimation of global irradiance on inclined surfaces: Validation of the model implemented in PVGIS." Publication Office

[30] Liu, Benjamin Y.H., and Richard C. Jordan. (1960) "The interrelationship and characteristic distribution of direct, diffuse and total solar radiation." *Solar Energy* 4.3 (1960): 1–19.
[31] Reindl, D.T., W.A. Beckmann, and J.A. Duffie. (1990) "Diffuse fraction correlations." *Solar Energy* 45.1 (1990): 1–7.
[32] Perez, Richard, Robert Seals, Antoine Zelenka, and Pierre Ineichen. (1990) "Climatic evaluation of models that predict hourly direct irradiance from hourly global irradiance: Prospects for performance improvements." *Solar Energy* 44.2 (1990): 99–108.
[33] De Soto, W., S.A. Klein, and W.A. Beckman. (2006) "Improvement and validation of a model for photovoltaic array performance." *Solar Energy* 80.1 (2006): 78–88.
[34] Parretta, Antonio, Angelo Sarno, and Luciano R.M. Vicari. (1998) "Effects of solar irradiation conditions on the outdoor performance of photovoltaic modules." *Optics Communications* 153.1–3 (1998): 153–63.
[35] Skoplaki, E., and J.A. Palyvos. (2009) "Operating temperature of photovoltaic modules: A survey of pertinent correlations." *Renewable Energy* 34.1 (2009): 23–9.
[36] Skoplaki, E., and J.A. Palyvos. (2009) "On the temperature dependence of photovoltaic module electrical performance: A review of efficiency/power correlations." *Solar Energy* 83.5 (2009): 614–24.
[37] Ishaque, Kashif, Zainal Salam, and Hamed Taheri. (2011) "Simple, fast and accurate two-diode model for photovoltaic modules." *Solar Energy Materials and Solar Cells* 95.2 (2011): 586–94.
[38] Seifi, Mohammad, Azura Bt. Che Soh, Noor Izzrib Abd. Wahab, and Mohd Khair B. Hassan. (2013) "A Comparative Study of PV Models in Matlab/Simulink." *International Journal of Electrical, Computer, Electronics and Communication Engineering* 7.2 (2013): 108–13.
[39] Sah, Chih Tang, Robert N. Noyce, and William Shockley. (1957) "Carrier Generation and Recombination in P-N Junctions and P-N Junction Characteristics." *Proceedings of the IRE* 45.9 (1957): 1228–43.
[40] Jordehi, A. Rezaee. (2016) "Parameter estimation of solar photovoltaic (PV) cells: A review." *Renewable and Sustainable Energy Reviews* 61. (2016): 354–71.
[41] Quaschning, Volker (2009) "Regenerative Energiesysteme". Hanser Verlag Muenchen
[42] Miller, Mark A., and Anthony Slingo. (2007) "The ARM Mobile Facility and its first international deployment: Measuring radiative flux divergence in West Africa." *Bulletin of the American Meteorological Society* 88.8 (2007): 1229–44.
[43] U.S. Department of Energy (2017) "ARM Mobile Facility." https://www.arm.gov/capabilities/observatories/amf
[44] Inness, A., F. Baier, A. Benedetti, I. Bouarar, S. Chabrillat, H. Clark, C. Clerbaux, P. Coheur, R.J. Engelen, Q. Errera, J. Flemming, M. George, C. Granier, J. Hadji-Lazaro, V. Huijnen, D. Hurtmans, L. Jones, J.W. Kaiser, J. Kapsomenakis, K. Lefever, J. Leitao, M. Razinger, A. Richter, M.G. Schultz, A.J. Simmons, M. Suttie, O. Stein, J.-N. Thépaut, V. Thouret, M. Vrekoussis, C. Zerefos, and the MACC team. (2013) "The MACC reanalysis: An 8 yr data set of atmospheric composition." *Atmospheric Chemistry and Physics* 13.8 (2013): 4073–109.
[45] Kurnik, Jurij, Marko Jankovec, Kristijan Brecl, and Marko Topic. (2011) "Outdoor testing of PV module temperature and performance under different mounting and operational conditions." *Solar Energy Materials and Solar Cells* 95.1 (2011): 373–6.
[46] Noorian, Ali Mohammad, Isaac Moradi, and Gholam Ali Kamali. (2008) "Evaluation of 12 models to estimate hourly diffuse irradiation on inclined surfaces." *Renewable Energy* 33.6 (2008): 1406–12.
[47] Demain, Colienne, Michel Journée, and Cédric Bertrand. (2013) "Evaluation of different models to estimate the global solar radiation on inclined surfaces." *Renewable Energy* 50. (2013): 710–21.
[48] Dirnberger, Daniela, Gina Blackburn, Björn Müller, and Christian Reise. (2015) "On the impact of solar spectral irradiance on the yield of different PV technologies." *Solar Energy Materials and Solar Cells* 132 (2015): 431–42.
[49] Behrendt, Tanja, Jan Kuehnert, Annette Hammer, Elke Lorenz, Jethro Betcke, and Detlev Heinemann. (2013) "Solar spectral irradiance derived from satellite data: A tool to improve thin film PV performance estimations?" *Solar Energy* 98 (2013): 100–10.
[50] Boucher, Olivier, David Randall, Paulo Artaxo, Christopher Bretherton, Gragam Feingold, Piers Forster, Veli-Matti Kerminen, Yutaka Kondo, Hong Liao, Ulrike Lohmann, Philip Rasch, S.K. Satheesh, Steven Sherwood, Bjorn Stevens, and Xiao-Ye Zhang. (2013) "7. Clouds and Aerosols." in *Climate Change 2013: The Physical Science Basis Contribution of Working Group I to the Fifth Assessment Report of the Intergovernmental Panel on Climate Change*
[51] Taylor, Christopher M., Eric F. Lambin, Nathalie Stephenne, Richard J. Harding, and Richard L.H. Essery. (2002) "The influence of land use change on climate in the Sahel." *Journal of Climate* 15.24 (2002): 3615–29.
[52] Cowie, S.M., P. Knippertz, and J.H. Marsham. (2014) "A climatology of dust emission events from Northern Africa using long-term surface observations." *Atmospheric Chemistry and Physics* 14.16 (2014): 8579–97.

4.2 Analysis at six measuring locations

This section is published as: Neher, I., Buchmann, T., Crewell, S., Pospichal, B., and Meilinger, S. (2019). Impact of atmospheric aerosols on solar power. *Meteorologische Zeitschrift*, 28(4):305–321. The electronic supplementary is given in the Appendix A.

Author contributions: IN is the corresponding author of this publication. She designed the study, developed the model and performed the model calculations and data analysis. The photovoltaic and radiative transfer part of the model was mainly taken from Neher et al. (2017). The parabolic trough power model was newly included here and additional sensitivity studies over the whole model chain were undertaken. SC and SM provided the overall scientific guidance and helped in interpreting the results. IN prepared the first draft of the manuscript and created all figures. All co-authors discussed the results and gave advice during the writing process.

Meteorol. Z. (Contrib. Atm. Sci.), Vol. **28**, No. 4, 305–321 (published online January 21, 2019)

Impact of atmospheric aerosols on solar power

Ina Neher[1,2*], Tina Buchmann[3,4], Susanne Crewell[2], Bernhard Pospichal[2] and Stefanie Meilinger[1]

[1]International Center for Sustainable Development, University of Applied Science Bonn-Rhein-Sieg, Sankt Augustin, Germany
[2]Institute of Geophysics and Meteorology, University of Cologne, Cologne, Germany
[3]Institute of Environmental Physics, Heidelberg University, Heidelberg, Germany
[4]now at E.ON Energie Deutschland GmbH, Munich, Germany

(Manuscript received April 11, 2019; in revised form July 1, 2019; accepted July 19, 2019)

Abstract

Atmospheric aerosols affect the power production of solar energy systems. Their impact depends on both the atmospheric conditions and the solar technology employed. By being a region with a lack in power production and prone to high solar insolation, West Africa shows high potential for the application of solar power systems. However, dust outbreaks, containing high aerosol loads, occur especially in the Sahel, located between the Saharan desert in the north and the Sudanian Savanna in the south. They might affect the whole region for several days with significant effects on power generation. This study investigates the impact of atmospheric aerosols on solar energy production for the example year 2006 making use of six well instrumented sites in West Africa. Two different solar power technologies, a photovoltaic (PV) and a parabolic trough (PT) power plant, are considered. The daily reduction of solar power due to aerosols is determined over mostly clear-sky days in 2006 with a model chain combining radiative transfer and technology specific power generation. For mostly clear days the local daily reduction of PV power (at alternating current) (PVAC) and PT power (PTP) due to the presence of aerosols lies between 13 % and 22 % and between 22 % and 37 %, respectively. In March 2006 a major dust outbreak occurred, which serves as an example to investigate the impact of an aerosol extreme event on solar power. During the dust outbreak, daily reduction of PVAC and PTP of up to 79 % and 100 % occur with a mean reduction of 20 % to 40 % for PVAC and of 32 % to 71 % for PTP during the 12 days of the event.

Keywords: energy meteorology, solar power, West Africa, atmospheric aerosol

1 Introduction

To "ensure access to affordable, reliable, sustainable and modern energy for all", as proposed in the 7th goal of the United Nation's sustainable development goals (United Nations, 2015), a shift away from the use of fossil-fuel based to renewable energy is necessary. Solar power systems are one option to feed the rising global energy demand in a sustainable way (e.g. Haegel et al., 2017; Solangi et al., 2011). Especially in regions prone to high solar irradiance a power system with a considerable share of solar sources is worthwhile. However, meteorologically caused local variability of solar irradiance needs to be investigated carefully in system planning and sizing to ensure long-term investments.

In West Africa electrification rates are still below 50 % (ECOWAS, 2017) while global horizontal irradiance (GHI) is high with an average annual sum of up to 2400 kWh/m^2 (Solargis, 2017). Furthermore, direct normal irradiance (DNI) shows annual sums of over 2000 kWh/m^2 in the northern parts of Niger and Mali (Solargis, 2017). With low cloudiness, sunshine durations of about 6.6 to 9 hours per day can be reached (Kothe et al., 2017). This leads to a high potential of solar power production. However, seasonal and local variability of solar resources needs to be considered. In south and central West Africa a typical annual cloud cycle exists because of the West African Monsoon (WAM) and its associated dry and wet seasons. Clouds occur predominantly during the wet season between June and September and reduce solar irradiance. In the dry season between October and May cloud cover is low, which in principle would lead to high solar transmission in the atmosphere. However, the frequent presence of dust in the dry season (dust emission frequencies go up to 15 % over the whole year (Cowie et al., 2014)) causes a strong variability of irradiance. Thus, the development of a solar power system in West Africa brings challenges even under low cloudiness conditions.

While solar power outputs are sensitive to meteorological parameters, such as temperature and wind speed, atmospheric conditions are the main contributor to their variability. In particular, aerosol and cloud particles as well as trace gases scatter and absorb the incoming solar irradiance (e.g. Wendisch and Yang, 2012; Wallace and Hobbs, 2006). Though clouds are a more efficient

*Corresponding author: Ina Neher, International Center for Sustainable Development, University of Applied Science Bonn-Rhein-Sieg, Germany, e-mail: ina.neher@h-brs.de

modulator of solar radiation than aerosols here we only focus on aerosol effects that can become the decisive factor limiting the availability of solar energy during the dry season, which represents more than half of the year in the Sahel. In a cloud-free atmosphere, aerosols are the main driver for atmospheric extinction. The effect of aerosols on solar irradiance strongly depends on their physical and chemical composition (e.g. Boucher, 2015; Kaufman et al., 2002; Hess et al., 1998). Depending on their optical properties, aerosols reduce GHI by modifying both of its components. Thereby, DNI is strongly reduced while diffuse horizontal irradiance (DHI) increases to some maximum. Different solar power technologies use different components of solar irradiance. While non-concentrating technologies exploit global radiation, concentrating solar power (CSP) plants only use DNI. For CSP plant yields aerosols are also responsible for changes in sunshape and atmospheric extinction between the mirrors and the receiver (Hanrieder et al., 2017; Wilbert, 2014). In addition to atmospheric aerosol, soiling (the deposition of subsiding aerosols on solar panels and collectors), which occurs especially during dust events, causes an additional solar power reduction. Depending on the cleaning cycle and the amount of dust transport, soiling may cause a power reduction of up to 90 % after one week as shown by Sarver et al. (2013).

Different studies, going beyond case studies, were undertaken to quantify the aerosol impact on solar power at single locations (e.g. Ruiz-Arias et al., 2016). Li et al. (2017) predicted the annual average reductions of aerosols on photovoltaic (PV) power in China to 20 %–25 % by using GHI from satellites and a PV power model. Polo and Estalayo (2015) showed a 2 %–16 % difference in CSP power (single days showing effects of up to 95 %) in two desert regions – Tamanrasset, Algeria and Sede Boquer, Israel – using ground-based and satellite observations of DNI as input for power calculations. The aerosol optical depth (AOD) going beyond 2 is in a similar range than in this study. However, these results cannot easily be extrapolated to other regions, as local aerosol loads vary and are strongly connected to aerosol sources and wind conditions.

One tremendous aerosol source are frequent Saharan dust outbreaks (Taylor et al., 2017) persisting several days and being able to reach regions far away from the Sahara (e.g. Rieger et al., 2017). In extreme cases, DNI is reduced to 0, which means that GHI only consists of DHI. The impact of a 5-day Saharan dust outbreak in 2015 on solar power in the eastern Mediterranean was quantified to 40 %–50 % for PV and 80 %–90 % for CSP using the relative impact on GHI and DNI, but no detailed solar power model was considered (Kosmopoulos et al., 2017). Only a few studies analyze the aerosol effect on solar irradiance or solar power in West Africa because relevant meteorological observations are lacking (e.g. Slingo et al., 2006). Using measurements from a dedicated instrument deployment in 2006, the contribution by Neher et al. (2017) quantified the daily impact of atmospheric aerosols on a PV module at a single location (Niamey) on average to 14 % during clear-sky days and up to 48 % during a dust outbreak. However, a systematic investigation of aerosol impacts on solar power generation in West Africa considering different technologies and a wider regional spread is missing.

To quantify the impact of atmospheric aerosols on solar power the ideal aerosol-free and the aerosol-loaded atmosphere need to be compared. This can only be achieved via a modeling approach, which explicitly considers the impact of aerosols on solar irradiance. Solar irradiance based on long-term averages, numerical weather prediction models, reanalysis or satellite data are often used as input for solar power models (e.g. Sengupta et al., 2017; Richardson and Andrews, 2014; Hammer et al., 2003; Gueymard, 2003). A detailed treatment of aerosols is only considered in a few studies for these models (Fountoukis et al., 2018; Gueymard and Jimenez, 2018), none of them focusing on West Africa. In atmospheric science, however, more sophisticated multi-layer radiative transfer (RT) models have been developed to derive radiative fluxes from information on atmospheric composition (e.g. Clough et al., 2005; Mayer and Kylling, 2005). The solar energy community has developed accurate models for solar power. PV power can be modeled, e.g., using a two-diode model with an accuracy of more than 99 % (Ishaque et al., 2011b). In these models, DNI and DHI as well as the ambient temperature and wind speed are needed as inputs. To estimate the power of a parabolic trough (PT) plant, various factors, such as the characteristics of mirrors, absorber tube and thermal power plant, need to be considered, in addition to DNI. When simulating solar power an accurate energy production model and highly reliable irradiance input data are required. For the latter, sophisticated RT models are needed to take the aerosol effect into account. To our best of knowledge a coupling of multi-layer atmospheric RT models with state-of-the-art PV power models has only been performed by Neher et al. (2017) and Rieger et al. (2017). However, Rieger et al. (2017) used the model chain to improve the forecast of PV power by considering aerosols in numerical weather models (NWM) and not to analyze the local impact of aerosols on solar power. Due to computational constraints NWP models need to employ fast RT routines, which use simplified parametrizations.

In this study, we use the library of RT programs and routines (libRadtran) by Mayer and Kylling (2005) to simulate the irradiance. The model chain, "Solar Power modeling including atmospheric Radiative Transfer" (SolPaRT) combines libRadtran with a PV power model (Neher et al., 2017) and a PT power model (Quaschning et al., 2001a). We use a PTPP instead of a solar tower power plant for our analysis. Therewith, we exclude the larger additional aerosol impact in the latter power plant between the mirrors and the receiver (Hanrieder et al., 2017), which is not the focus of this study. SolPaRT is used to assess the impact of aerosols

on both, a PV power plant (PVPP) and a PT power plant (PTPP) for six different locations in West Africa. For this purpose we compile a one-year data set for 2006 of meteorological parameters at these locations, covering different climate and land use zones throughout West Africa. To quantify only the aerosol effect the impact of clouds on solar irradiance has to be excluded. Hence, predominantly clear-sky days (named 'clear days' in the following) are selected (covering 20 % to 46 % of the year, see Section 2) for each location and the daily reduction of solar power due to aerosols is determined using SolPaRT. We analyze the aerosol effect on a daily scale. This day-to-day analysis enables us to detect the variability over the course of one year and during extreme events like dust outbreaks lasting several days.

The goal of this study is two-fold. First, we quantify daily average impacts of aerosols on different solar power technologies during clear days over the course of one year. We generate more realistic estimates for future total power generation at sites in West Africa. Furthermore, we serve economic feasibility studies for PVPP and PTPP, which are important for investment decisions in the solar energy sector. Second, we estimate the variability of daily solar power due to aerosols year round under predominantly clear-sky conditions as well as during a major dust outbreak. This is necessary for the planning of reliable solar power systems including adequately sized energy storage and therewith essential for estimating related costs for power security. Furthermore, it enables us to identify the threat of aerosol-induced blackouts and to evaluate the need for emergency power supply.

This study is the first systematic investigation of aerosol impacts on different solar power technologies (namely PV and PT) for West Africa using a unique set of ground-based meteorological measurements. Furthermore, the impact of aerosols on solar power during a major dust outbreak is quantified.

The data and model chain (SolPaRT) used to quantify the aerosol impact on a PVPP and a PTPP are described in Section 2. In Section 3 SolPaRT is evaluated using measured GHI, and a sensitivity analysis for the impact of different parameters is performed. Section 4 presents and discusses the statistical analysis of daily reductions of solar power due to aerosols in West Africa in 2006. Projected solar power during a major dust outbreak in March 2006 is shown in Section 5 with a regional perspective. Furthermore, the effect of soiling on PV power is analyzed at one location during this dust outbreak. Conclusions and outlook are provided in Section 6.

Additional information about data and further results can be found in the electronic supplementary material.

2 Data and methodology

To quantify the impact of atmospheric aerosols on PV and PT power we use SolPaRT, a model chain that calculates both atmospheric RT and solar power using input data from six locations distributed over West Africa. These locations cover three climate zones according to the Köppen and Geiger climate classification (Peel et al., 2007); hot desert climate (BWh), hot semi-arid climate (BSh) and tropical wet climate (Aw).

2.1 Data

Neher et al. (2017) used the detailed observations from the Atmospheric Radiation Program (ARM) Mobile Facility (AMF) (Ackerman and Stokes, 2003) in Niamey, Niger to assess the aerosol impact on PV power in 2006. Here we expand this study to five additional locations in West Africa (Agoufou, Mali; Banizoumbou, Niger; Dakar, Senegal; Djougou, Benin and Maine-Soroa (called Maine in the following), Niger) using measured AOD with corresponding information on the Ångström exponent and precipitable water vapor (PWV) from AERONET (AErosol RObotic NETwork, version 3, level 2) (Holben et al., 2001; Holben et al., 1998). Additional meteorological input parameters for SolPaRT are collected from the African Monsoon Multidisciplinary Analysis (AMMA) data base (AMMA, 2018) and surface synoptic observations (SYNOP) (see Table 1). Aerosol optical properties, PWV and albedo are used for the RT calculations. Temperature and wind speed at the surface are needed as additional input for PV power calculations. For the PT power calculations temperature, wind speed and direction, relative humidity (named PT-humidity in the following) and pressure are used. All calculations are performed with a temporal resolution of one hour. More information about the measuring equipment is given in the electronic supplementary material.

AOD observations are used to include aerosols in the RT calculations. The AOD is available at 500 nm for Niamey and at 440 nm for all other locations. The Ångström exponent is used to scale the AOD over different wavelengths. Apart from AOD, the single scattering albedo (SSA) and asymmetry parameter (g) have a significant impact on RT-calculations, too. These two parameters are taken from the desert aerosol type of the Optical Properties of Aerosols and Clouds (OPAC) library by Hess et al. (1998). For Banizoumbou a constant pressure value is used, which has been calculated from station height as no direct measurements are available. An overview on the hourly raw data is given in the electronic supplementary material for AOD, Ångström exponent, PWV, temperature, wind speed and PT-humidity as the most important contributors for the calculation to the simulated solar power (see Section 3.2). Surface albedo is assumed to be 0.28 in Agoufou, Banizoumbou, Maine and Niamey (a typical value for savanna), 0.2 in Djougou (a typical value for mixed vegetation) and 0.09 in Dakar (a typical value for coastal regions) (Rockwood and Cox, 1976).

To exclude the impact of clouds in our calculations, we only consider days with a large abundance of AOD measurements, as this can only be observed under clear-sky conditions. The considered days ('clear days') are

Table 1: Data implemented in SolPaRT with indicating the data base for each available parameter at every location.

	Agoufou	Banizoumbou	Dakar	Djougou	Maine	Niamey
AOD	AERONET	AERONET	AERONET	AERONET	AERONET	ARM
Ångström exponent	AERONET	AERONET	AERONET	AERONET	AERONET	ARM
Precipitable water	AERONET	AERONET	AERONET	AERONET	AERONET	ARM
Temperature	AMMA	AMMA	SYNOP	AMMA	SYNOP	ARM
Wind speed	AMMA	AMMA	SYNOP	AMMA	SYNOP	ARM
Wind direction	AMMA	AMMA	SYNOP	AMMA	SYNOP	ARM
PT-humidity	AMMA	AMMA	SYNOP	AMMA	SYNOP	ARM
Pressure	AMMA	–	SYNOP	AMMA	SYNOP	ARM
GHI	AMMA	AMMA	–	AMMA	–	ARM

Table 2: Information about the six analyzed stations, including latitude, longitude, height, climate classification, land use conditions and number of clear days.

Location	Agoufou	Banizoumbou	Dakar	Djougou	Maine	Niamey
Country	Mali	Niger	Senegal	Benin	Niger	Niger
Latitude	15.3 N	13.5 N	14.4 N	9.8 N	13.2 N	13.5 N
Longitude	1.5 NW	2.7 E	17 W	1.6 E	12 E	2.2 E
Height (m)	305	250	0	400	350	205
Climate class	BWh	BSh	BSh	Aw	BSh	BSh
Land use	desert	desert	coastal	savanna	desert	desert
	rural	rural	urban	agriculture	village	airport
No. of clear days	132	168	161	94	71	78

defined as days with at least one measured AOD during each hour for 10 hours per day. In Niamey, the procedure is similar, but one measured AOD during each hour for only 9 hours per day is required since the diurnal measurement time span is shorter there. The geographical coordinates, the climate classification (after Köppen-Geiger), land use conditions and the number of clear days in 2006 at each location are summarized in Table 2. An overview on the identified clear days at each location is given in the electronic supplementary material.

The much lower number of clear days in Niamey compared to Banizoumbou (the stations are only 60 km apart) occurs due to different measuring techniques for AOD. In Banizoumbou the classical AERONET sun photometer measures spectral DNI. In this procedure the cloud-screening process only considers clouds interfering with the sun disk. In contrast, in Niamey, the multifilter shadowband radiometer (MFRSR) measures GHI and DHI at six wavelengths. The cloud-screening process of the MFRSR takes clouds from the whole sky dome into account, which increases the number of time steps being rejected (Russell et al., 2004). Furthermore, misalignment artifacts of the instrument are also screened out as clouds for the MFRSR (Alexandrov et al., 2007). Therefore, less clear days are detected in Niamey compared to Banizoumbou.

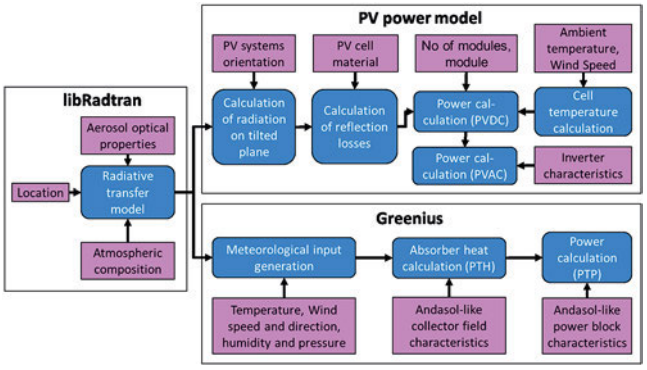

Figure 1: Schematic overview on SolPaRT. The input data is marked in magenta and the single modeling steps in blue.

2.2 Model description

Based on the input data described above, SolPaRT is used to analyze the impact of atmospheric aerosols on a PVPP and a PTPP (see Figure 1 for a schematic overview).

For the estimation of direct horizontal irradiance (DIR) (the horizontal projection of DNI) and DHI we use libRadtran (Emde et al., 2016; Mayer and Kylling, 2005). Similar to the procedure in Neher et al. (2017) two scenarios, an aerosol-loaded (the measured AOD

Table 3: Information about the PV and PTPP.

	PVPP		PTPP
Solar irradiance (W/m^2)	GHI		DNI
Output (W)	PVDC, PVAC		PTH, PTP
Total AC capacity	30 kW		50 MW
Total collector area	214 m^2		510.120 m^2
Land area	825 m^2		2.000.000 m^2
Module	SW235poly	Solar collectors	Eurotrough
No of strings	16	No solar collectors assemblies	624
No of modules per string	9	No solar collectors per assembly	12
Tilting angle	14°	Heat collector element	Schott (PTR70)
Orientation	South	Power block	Steam Rankine
Inverter	Xantrax 30 kW	Turbine	SST-700 by Siemens

and Ångström exponent are included in RT calculations) and an aerosol-free (aerosols are excluded from RT calculations), are simulated. The difference between these scenarios is integrated over each day representing the total daily reduction of power due to atmospheric aerosols.

libRadtran numerically solves the RT equation by using the DISORT (DIScrete Ordinates Radiative Transfer solver) algorithm to calculate the irradiance (Stamnes et al., 1988). In comparison to many clear-sky models (a comparison is given in Badescu et al., 2013), libRadtran allows an altitude-resolved atmospheric profile. Therewith, we are able to include all relevant atmospheric parameters from the ground-based dataset as well as aerosol composition into the model chain. Furthermore, we are able to include spectral information, which is planed for a next version of the model. In this study, the standard tropical atmosphere from Anderson et al. (1986) is used as a baseline to define the atmospheric state. While temperature and trace gases do not show a significant sensitivity for the irradiance calculation, water vapor is highly relevant. Therefore, local measurements of PWV (see electronic supplementary material) are used to scale the climatological moisture profile. Furthermore, we use a typical desert aerosol composition defined by the OPAC library (Hess et al., 1998). The locally measured AOD with its corresponding Ångström exponent is scaled to all atmospheric layers. For the molecular absorption in the atmosphere a correlated-k method developed by Kato et al. (1999) is applied to reduce the computing time.

The calculated irradiances with and without aerosol are then used as input for a PVPP and PTPP model. For the PVPP we consider crystalline silicon modules. Power calculations are undertaken with a two-diode model (Ishaque et al., 2011a; Ishaque et al., 2011b). The PTPP is based on Andasol I (Kistner et al., 2004) in Spain but without storage. Calculations of the power output are performed by using the *green energy system analysis tool* (Greenius) (Quaschning et al., 2001a; Quaschning et al., 2001b). The composition of the PVPP and PTPP are given in Table 3.

Calculations for the efficiency of PV modules, use GHI and ambient temperature as inputs. Modeling PV power is often simplified by determining only one point (the maximum power point (MPP)) of the current-voltage curve. However, to get a better estimate of PV power by the non-linear current-voltage curve, additional knowledge is required about module and inverter characteristics. Therefore, we calculate the power of a PVPP by using the two-diode algorithm (Ishaque et al., 2011a). The power plant is connected to the grid with a single inverter (King et al., 2007). With this model arrangement both the direct current (PVDC) and the alternating current (PVAC) power calculation can be undertaken. All modules are orientated towards the south with a tilt angle of 14°, which is roughly equal to latitude. A model comparison was undertaken with a single module, tilted at 14° and measurements of the PVDC showing a relative bias of −0.2 % between model output and PV power measurements on clear days in Neher et al. (2017).

The effective irradiance used by the PVPP is calculated by transforming DIR and DHI to the tilted plane and considering reflection losses on the modules' surfaces. DIR can be analytically transformed to the tilted plane using an Eulerian transformation. DHI is transformed to the tilted plane by using the model designed by Perez et al. (1990). Neher et al. (2017) showed, that this model performs similar to the detailed libRadtran calculations with radiances analytically transformed to the tilted plan in desert regimes. Reflection losses are considered for three different components: the irradiance coming from the direction of the sun, from the direction of the horizon and the isotropic part of DHI using the incidence angle modifier described in De Soto et al. (2006).

The efficiency of a PV module varies with cell temperature (e.g. Parretta et al., 1998). Thus, ambient temperature and wind speed are used to determine the cell temperature. While different approaches are available from the literature (a review can be found in Skoplaki and Palyvos (2009)), we apply the approach by King et al. (2004) here and assume an open-rack mounting, as it is mostly used in PV applications.

To estimate the parabolic trough power (PTP) and heat absorbed by the collector (parabolic trough

heat – PTH) of a PTPP, the simulation tool *greenius* is applied (Quaschning et al., 2001a). *greenius* allocates detailed technical as well as economic analysis of multiple technologies. This tool provides an interface for specific meteorological input for a certain location. The Andasol I power plant serves as a typical reference plant for PT systems (Quaschning, 2011). Therefore, a similar power plant but without storage is assumed for the PTPP (see Table 3), which allows to directly assess the impact of aerosols. If storage was included, the power reduction due to aerosols could be dampened depending on the storage size. With a maximum power output of 50 MW the PTPP is larger than the PVPP. However, PV is a modular technology, which can be easily scaled up or down. Building up the same PVPP several times would give the same numbers for power reductions due to aerosols as only one of the PVPP.

In summary, SolPaRT includes the effect of temperature, wind speed, PT-humidity, pressure, direct and diffuse irradiance on both solar power technologies. Furthermore, the impact of PWV, albedo, aerosols and a standard tropical atmosphere are considered when calculating solar irradiances. In addition, the technical specifications of the module and the inverter are used for PV calculations and the PTPP characteristics for PT calculations (Table 3). However, other factors can have an impact on PVAC and PTP, which are not included in SolPaRT, e.g., spectral variations of the solar irradiance at the surface and soiling. As soiling is believed to be the most important aspect a rough estimation is given in Section 5.2.

3 Assessment of simulations

As a first step we assess the RT simulations using the observed GHI for comparison and calculate typical statistical parameters. In a second step we evaluate the sensitivity of SolPaRT concerning the impact of different meteorological input parameters.

3.1 Validation of modeled global irradiance

The RT calculations are validated with observed GHI at four stations (Agoufou, Banizoumbou, Djougou and Niamey) where pyranometer measurements are available (see Table 1). For this purpose, data from all clear days are taken into account at hourly resolution. Here the coincidence is rather high and minor deviations are expected due to the different viewing perspectives of both instruments, i.e. hemispheric measurement of pyranometer, tilted beam towards the sun by sun photometer (for AOD). The number of data points (N) and all fitting parameters are given in Figure 2. The highest variation of hourly GHI occurs due to the varying solar zenith angle. However, further factors of influence, such as AOD and PWV, are active as well.

A relative bias of 1.9 %, 5.8 %, −3.5 % and 0.4 % is found for GHI in Agoufou, Banizoumbou, Djougou and Niamey, respectively. The explained variance (R^2) is always higher than 0.95 and root mean square errors (RMSE) range from 37 W/m^2 to 65 W/m^2. Generally there is a good agreement between measurements and simulations. This supports our assumption of a desert aerosol composition for RT calculation. However, for a few situations with high AOD the simulation underestimates the GHI. In libRadtran the AOD is scaled to the different height layers according to the typical desert profile. This leads to uncertainties especially for high AOD. The deviations in N between the two nearby locations Banizoumbou and Niamey originates from the measuring techniques (see Section 2.1). The lower RMSE of 47 W/m^2 in Niamey compared to 60 W/m^2 in Banizoumbou reflects the stronger constraint to rule out cloudy situations in Niamey. In summary, the RT calculations are accurate enough to use them for the further modeling steps.

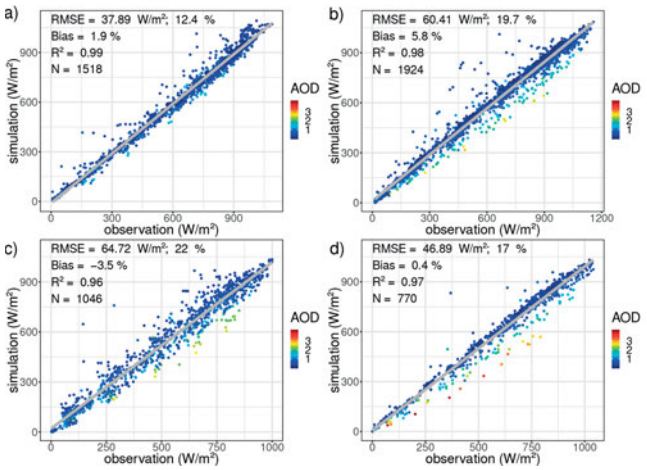

Figure 2: Direct comparison of hourly simulated and observed GHI during clear days in 2006 at four sites: a) Agoufou, b) Banizoumbou, c) Djougou and d) Niamey using the whole daily data set. AOD is indicated by color.

3.2 Sensitivity study for meteorological input parameters

The major driver for the available irradiance is the solar zenith angle, which first needs to be harmonized before the sensitivity of different environmental parameters like albedo or aerosol composition can be investigated. To consider the varying solar zenith angles over the course of the year and all seasons we select 14 representative days, at all six stations separately, for the sensitivity study. First, we determine the minimum zenith angle of each day and sort the days in ascending order. The highest and lowest minimum daily zenith angles are then used as boundaries to define equidistant steps of zenith angles. The days with the minimum zenith angle lying closest to these equidistant steps are then selected for the study. This procedure is separately applied for the first half (January to June) and the second half (July to December) of the year 2006 as zenith angles in spring

and autumn are similar, but other atmospheric parameters may vary. Therefore, both seasons should represent the same amount of days for the sensitivity study. Finally, for each half year seven representative days in equidistant intervals are simulated. The chosen days and the related zenith angles are depicted in the electronic supplementary material.

The variabilities of daily PVAC and PTP due to the meteorological input parameters (aerosol composition, albedo, AOD, PT-humidity, PWV, temperature and wind speed) are assessed for the six stations in West Africa in 2006. For this purpose, the simulation with SolPaRT (on the 14 representative days) is repeated for values at the upper and lower limit of the climatological distribution of a single input parameter while keeping the other parameters at constant reference. For the lower (upper) value the 5 % (95 %) percentile of the measured values in 2006 (for each location separately) is used. As no measurements are available for surface albedo, the highest and lowest assumed values over all sites are taken. To compare the maximum difference in aerosol composition, two contrasting aerosol profiles, urban (polluted) and antarctic (clean), are used as they show major differences for the optical properties SSA and g (SSA = 1 and $g = 0.784$ for antarctic (clean) and SSA = 0.817 and $g = 0.689$ for urban are assumed by Hess et al., 1998). A lower SSA indicates the presence of more absorbing aerosols, e.g. soot, which would lead to less diffuse irradiance than a higher SSA. A higher g states a larger fraction of irradiance being scattered into the forward direction, which would increase the circumsolar irradiance (e.g. Boucher, 2015). In this calculation the AOD is assumed as its constant reference. The constant reference values for AOD, aerosol composition and PWV are taken from defaults of the libRadtran library (typical desert profile for AOD and aerosol composition and standard tropical atmospheric profile for PWV). For PT-humidity, temperature and wind speed measured values are used as references. Furthermore, the mean albedo between the different locations is used as the reference albedo (constant for all time steps). All input parameters are listed in the electronic supplementary material.

The model sensitivity is defined as the relative difference between the model output from the two simulations using the upper and the lower value of each meteorological input parameter. The model sensitivity is calculated for PVAC and PTP. The variability can be attributed to the different locations and varying zenith angles. The results identify aerosols as the main influencing factor on both solar technologies (see Figure 3). Thereby, the AOD has a key role, with a sensitivity of 51 % for PVAC and 100 % for PTP (meaning that no power is generated at high AOD). An additional sensitivity of 11.2 % is found concerning the aerosol composition for PVAC. However, the median sensitivity for aerosol composition on PTP lies below 0.1 %. DNI is mostly influenced by the AOD, whereas DHI is influenced by AOD, SSA and g. As the aerosol composition represents the changes in SSA and g there is hardly

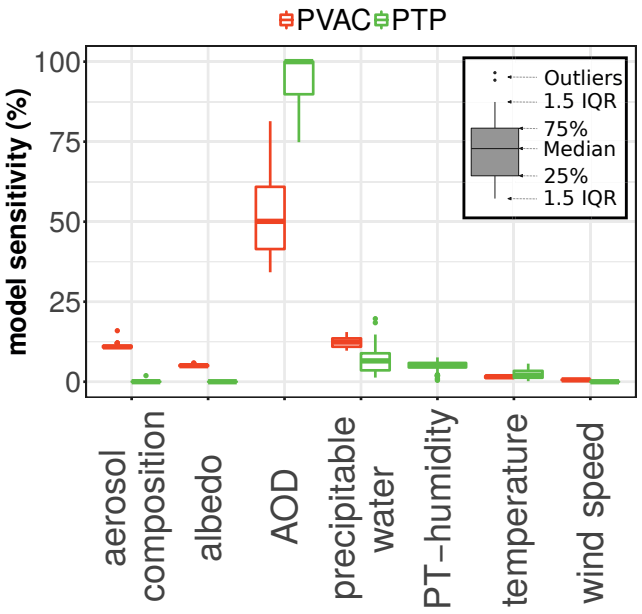

Figure 3: Model sensitivity shown as box plots with the interquantile range (IQR) for PVAC (red) and PTP (green) for the different input parameters on 14 representative days for six locations.

no impact on DNI and therewith on PTP. Furthermore, PWV shows a model sensitivity of 12.4 % for PVAC and 6.5 % for PTP. Median values of model sensitivity of all other parameters are below 10 %. As pressure shows no sensitivity at all, it is not considered in Figure 3.

4 Daily reduction of solar power potential in 2006

To address the first goal of this study (quantification of the general impact of aerosols over the course of one year) daily reductions of power production due to the presence of aerosols are calculated for each clear day at every location. For the PVPP we calculate PVDC and PVAC. For the PTPP we calculate PTH and PTP. To investigate whether the loss of solar power production directly scales with the loss of solar irradiance in the atmosphere or if there are non-linear effects, related to the power conversion process within the solar power plant, we also derive the daily reductions of GHI and DNI for comparison.

4.1 Statistical analysis

The daily reductions of GHI, PVAC, DNI and PTP due to aerosols for all clear days are calculated for the six investigated locations and are presented in Figure 4. In comparison to PVAC with median aerosol-induced daily reductions of 13 % to 22 %, PTP median daily reductions due to aerosols are larger with 22 % to 37 % depending on the location (see Figure 4 and Table 4). Median daily reductions of GHI are less profound, ranging from 9.4 % to 14 %. Median daily reductions of DNI

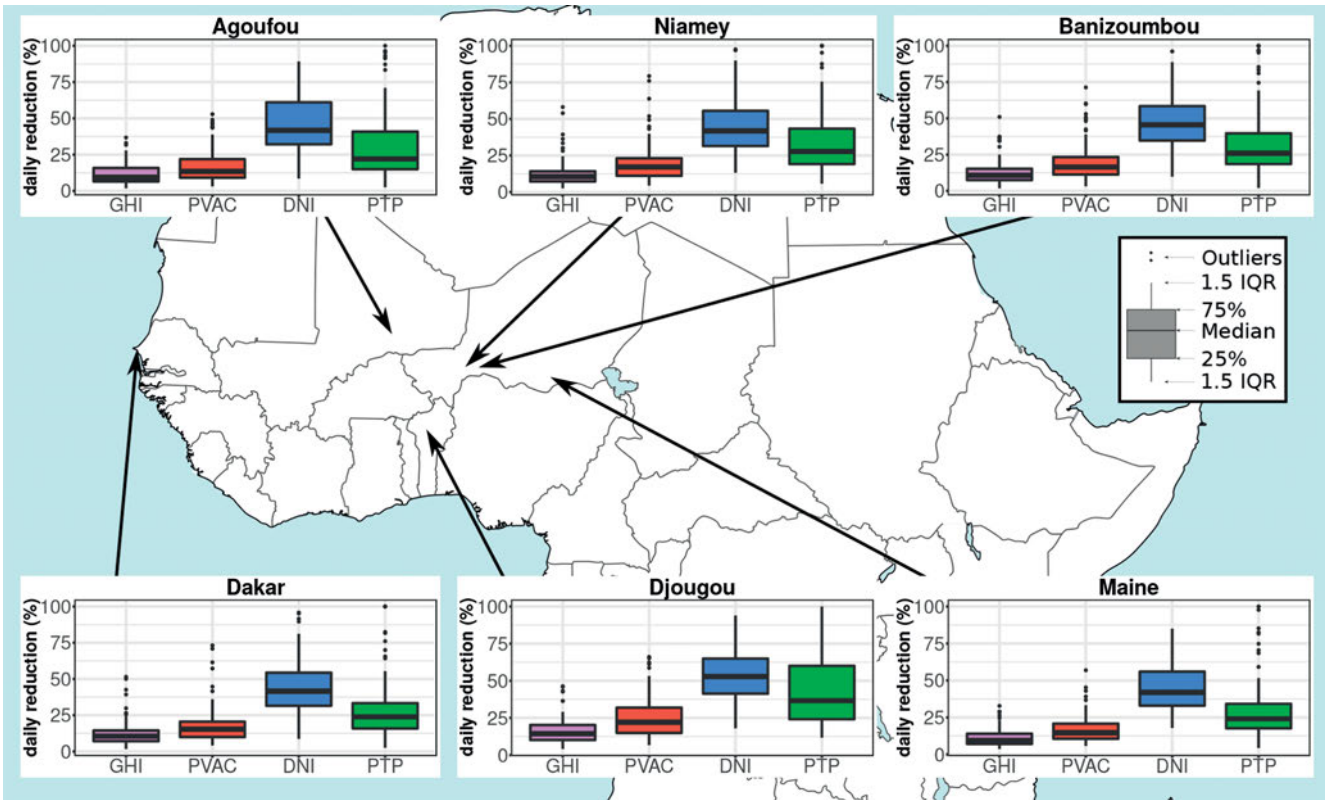

Figure 4: Median daily reduction of GHI (magenta), DNI (blue), PV power (red) and PT power (green) with its interquartile Range (IQR) and outliers over all clear days in 2006 at Agoufou, Banizoumbou, Niamey, Dakar, Djougou and Maine.

Table 4: Median (Md), 5 %, 25 %, 75 % and 95 % quantiles of daily reduction in % for PVAC, PTP, GHI and DNI for the six different locations in 2006.

Location	Md	5 %	25 %	75 %	95 %	Md	5 %	25 %	75 %	95 %
	PVAC					**PTP**				
Agoufou	13	5.1	9.2	22	41	22	6.3	15	41	89
Banizoumbou	16	5.7	11	23	42	26	7.9	19	40	85
Dakar	15	6.3	10	21	35	24	7.6	16	33	66
Djougou	22	9.7	15	31	55	37	15	24	60	85
Maine	15	6.4	11	21	38	24	9.2	18	34	82
Niamey	17	5.4	11	23	50	28	9.1	19	43	96
	GHI					**DNI**				
Agoufou	9.4	3.5	6.5	16	26	42	17	32	61	75
Banizoumbou	11	4	7.4	15	29	46	20	35	58	80
Dakar	11	4	7	15	23	42	19	32	54	71
Djougou	14	6.4	10	20	36	53	29	41	65	87
Maine	9.5	4.5	7.1	14	26	42	21	33	56	75
Niamey	11	3.8	7.2	14	34	42	18	32	56	86

range from 42 % to 53 %. The median, 5 %, 25 %, 75 % and 95 % percentiles for daily reductions of PVAC and PTP as well as for GHI and DNI are summarized in Table 4.

By assuming the desert aerosol type by Hess et al. (1998) being a typical background aerosol in this region, the median daily reduction would be 12 % and 20 % for PVAC and PTP, respectively, averaged over the 14 representative days (used in Section 3.2) and all stations. However, even if these reductions are subtracted from the values in Table 4, the average additional daily reduction by including the measured AOD and atmospheric parameters would lie between 1 % and 10 % for PVAC and between 2 % and 17 % for PTP. Furthermore, the variability by using only one typical background aerosol is much lower, as the variability is mainly driven by AOD variability.

Our results show a similar magnitude for the impact of aerosols on PV power as the study by Li et al. (2017) who found 20 % to 25 % reduction driven by air pollu-

tion in China during 2003 to 2014. Previous studies have used GHI as the primary contributor to derive relative PVAC reductions (Kosmopoulos et al., 2017; Calinoiu et al., 2013), thus not including the effects inside the PV plant. However, our results indicate that the PVAC reduction can be up to 8 percentage points higher than GHI reduction depending on the location. These reductions occur mainly due to reflectance, temperature and inverter losses. The daily reductions for PTP differ from the reductions of DNI by 14 % to 20 %. Thus, to calculate the reductions in PVAC and PTP a more profound approach than only using GHI and DNI is needed, as the relative dependence is not always linear and involves several parameters. The correlation between the daily reduction of solar radiation and power output is shown graphically (see Figure 7) and discussed in section 4.3.

The spatial variability of daily reductions of PVAC and PTP is represented by the distribution of the six locations in West Africa (see Figure 4 and Table 4). Daily reductions vary by up to 9 percentage points for PVAC and up to 15 percentage points for PTP between the locations. On the one hand, the number and seasonal distribution of clear days vary for each location due to the different climate zones. On the other hand, AOD varies at the different locations.

Djougou shows the highest median daily reduction in both, PVAC and PTP, 22 % and 37 % respectively, however there are fewer extreme reductions at this location compared to the others. Djougou is situated in a tropical wet climate (Peel et al., 2007) and south of the Sahel. Therefore the conditions are more humid (higher PWV during the dry season, see input data in the electronic supplementary material) with more frequent rainfall and a longer wet season due to the WAM. Furthermore the effect of dust outbreaks is smaller at this location as the distance to the dust source is larger than for the other locations. Agoufou shows the lowest median daily reduction of 13 % and 22 % for PVAC and PTP, respectively. This station lies in a hot desert climate (Peel et al., 2007) whereas all other locations lie in a hot semi-arid climate. Thus, Agoufou is influenced by less rain than the other stations and thereby a lower humidity and PWV.

4.2 Variability of power output

To investigate the power reductions inside the plants we compare different parameters within the plants. The PVDC before the inverter in a photovoltaic power plant and the PTH of a parabolic trough power plant are the first calculated power characteristics of the two technologies and show the most direct variability due to meteorological parameters. However, the power delivered by the plant (PVAC and PTP) might differ due to technical specifications. The relative difference (in %) between the aerosol-induced daily reduction in PVDC (ΔPVDC, in %) and in PVAC (ΔPVAC, in %) is calculated as

$$\Delta\mathrm{PV} = (\Delta\mathrm{PVAC} - \Delta\mathrm{PVDC})/\Delta\mathrm{PVAC}. \quad (4.1)$$

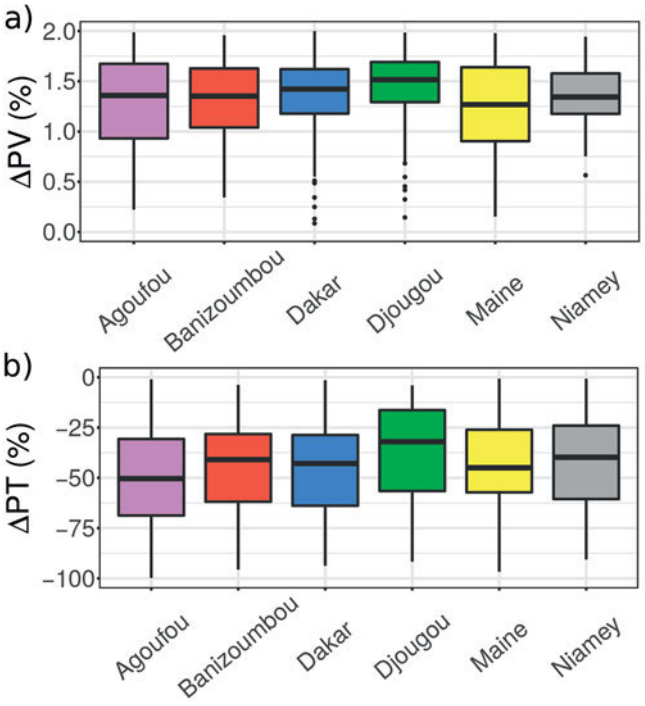

Figure 5: Median differences for daily reductions due to aerosols for ΔPV (relative difference between ΔPVDC and ΔPVAC, a) as well as daily reductions due to aerosols for ΔPT (relative difference between ΔPTH and ΔPTP, b) with its IQR and outliers for every location (Agoufou: magenta, Banizoumbou: red, Dakar: blue, Djougou: green, Maine: yellow, Niamey: grey).

The relative difference (in %) between the aerosol-induced daily reduction in PTH (ΔPTH, in %) and in PTP (ΔPTP, in %) is calculated as

$$\Delta\mathrm{PT} = (\Delta\mathrm{PTP} - \Delta\mathrm{PTH})/\Delta\mathrm{PTP}. \quad (4.2)$$

These differences are calculated separately for each station (see Figure 5).

In general, the transformation to AC power in a PV plant shows an additional power reduction (positive ΔPV), whereas the power block process dampens the impact of aerosols in a PTPP (negative ΔPT). Median differences between daily reductions due to aerosols of PVDC and PVAC range from 1.25 % to 1.5 %, whereas median differences between daily reductions of PTH and PTP range from −23 % to −49 %.

The additional reduction of PVAC compared to PVDC (positive ΔPV) occurs due to the additional losses in the inverter, because the inverter efficiency increases with PVDC (Luoma et al., 2012). However, the additional reductions due to the inverter are comparably low with a maximum of 1.5 %. The PVPP is only slightly over-dimensioned (around 4 %). Therewith, it cannot compensate the reductions due to aerosols during high insolation. An even more significantly over-dimensioned power plant would not stay in the maximum current and voltage range of the inverter.

On the one hand, lower reductions of PTP compared to PTH (negative ΔPT) are based on the fact that

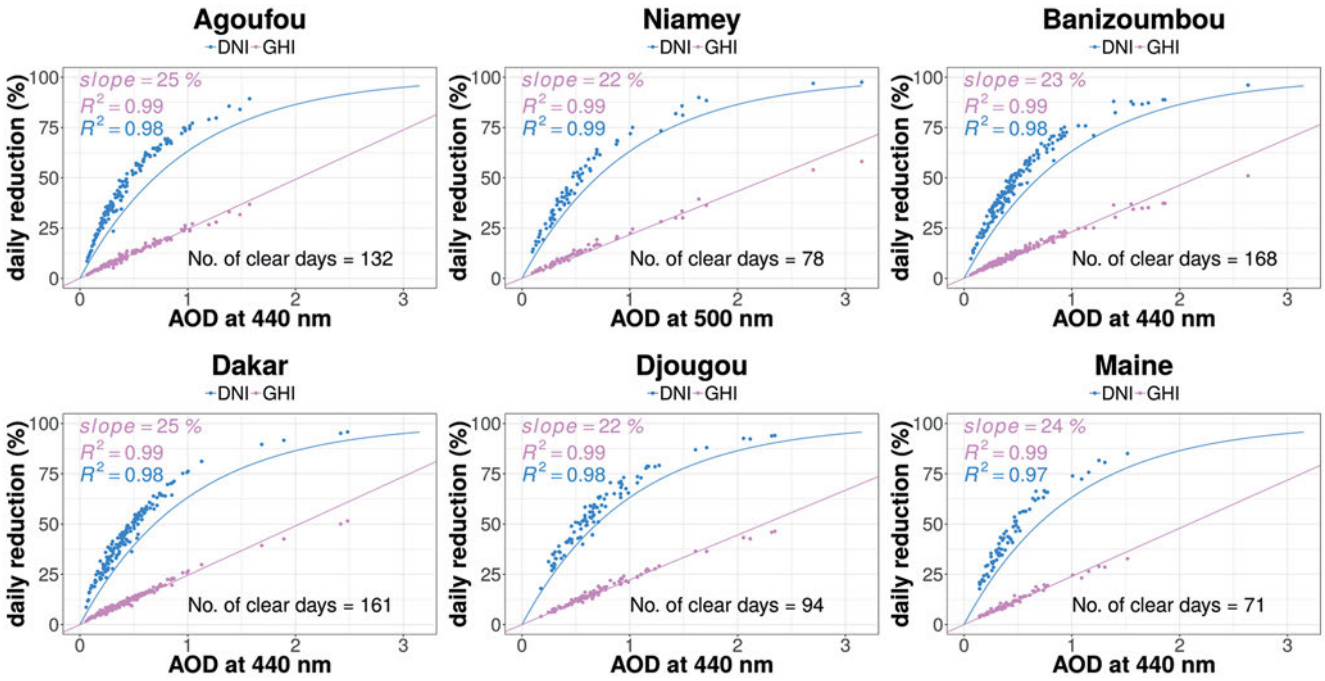

Figure 6: AOD as a function of daily reductions in GHI (magenta) and DNI (blue) at the six locations. A linear fit through the origin is undertaken for the relation between GHI reduction and AOD (slope and R^2 are shown in magenta for this fit). DNI reduction are fitted for an the exponential relation $y = 1 - \exp(-\mathrm{AOD})$ (R^2 is shown in blue for this fit).

the PTPP has a maximum electricity generation limit of 50 MW. On the other hand, reduction due to the power conversion in the steam process can arise at very low heat levels (positive ΔPT). To start the power block, a minimum PTH is needed. When the PTH drops below this limit no PTP can be generated at all.

4.3 Impact of aerosol optical depth on power generation

The daily mean AOD is analyzed as a function of daily reductions in GHI and DNI (see Figure 6). Daily GHI reductions due to aerosols scale nearly linear with the AOD at all stations (slopes are between 22 % and 25 %). Prasad et al. (2007) investigate the relation between the reduction of solar irradiance at the surface (termed radiative forcing) and AOD in desert regions in India (their Figure 6 b). For an AOD = 1.5 they find a daily mean radiative forcing of around −80 W/m^2 during dust outbreak periods. For an average daily irradiance at our six locations ranging from 250 W/m^2 to 270 W/m^2, this would correspond to a reduction of about 30 %. For GHI we find a similar reduction of around 35 % for AOD = 1.5. Under the presence of smoke, Stone et al. (2008) showed, that an AOD of 0.5 at 500 nm would produce a daily radiative forcing of about −40 W/m^2. Compared to the daily mean GHI at the locations in this study, this would be around 13 % daily reduction in GHI. Again comparing this value to the relation in Figure 6a, this result fits very well with the around 12 % of daily reductions in GHI at 0.5 AOD. Even when assuming another aerosol source, the AOD seems to be a good indicator for reductions in irradiances (compare to the results in section 3.2).

The aerosol transmittance T_{AOD} follows an exponential function $T_{\mathrm{AOD}} \sim \exp(-\mathrm{AOD})$. Thus, the daily DNI reductions can be expressed as

$$T_0 - T_{\mathrm{AOD}} \sim 1 - \exp(-\mathrm{AOD}).$$

The R^2 for this correlation ranges from 0.97 to 0.99. However, the shape is not exactly the same.

The relation between daily power reductions and daily reductions in solar irradiances is given in Figure 7, with the AOD indicated as colors. For the PV technology reductions in PVAC and GHI show a linear correlation at all locations (Figure 7 a), with a slope around 1.5 and a R^2 between 0.98 and 0.99. Even if there are other impacts on PV power production (e.g. module temperature), the GHI seems to be a robust indicator to analyze power reductions due to aerosols. There is no linear relation for DNI and PTP reduction. At lower AOD (marked with colors) the relation seems linear. Here the internal power plant dimension reduces the impact of aerosols, as the power plant has a maximum electricity generation limit. With rising AOD the slope of the relation increases. Here, the minimum heat to start the power block in the PTPP might not been reached during all time steps (compare to findings in section 4.2).

In general, PTP is reduced about twice as much as PVAC (the relation of AOD and power reductions is visualized in the electronic supplementary material). For a daily mean AOD of around 1.5 no power can be generated by the PTPP anymore and daily reductions of about 50 % for PVAC are reached.

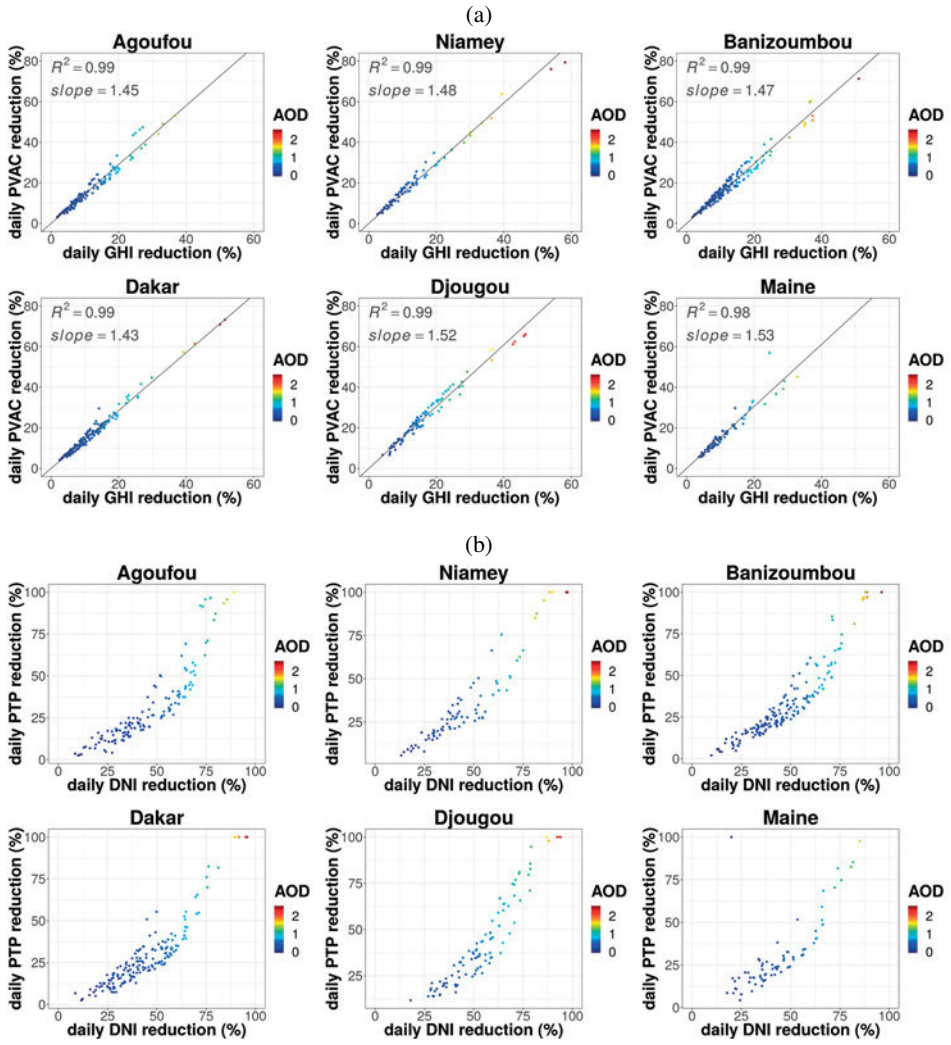

Figure 7: Daily GHI and daily DNI reductions as a function of daily power reduction (PVAC (a) and PTP (b)) at the six locations. The daily AOD is indicated as colors.

5 Regional impact of a major dust outbreak on solar power production

In the Sahara, large-scale dust outbreaks occur frequently (Taylor et al., 2017). Aerosol loads are high during such extreme events and likely show considerable reductions in solar power. During one fourth of the clear days in 2006 (averaged over all locations) daily reductions of PVAC and PTP exceed 20 % and 35 %, respectively (see Figure 8). These reductions due to the presence of aerosols could potentially lead to blackouts and network instabilities in a solar-based power system. Extreme daily reductions of up to 100 % for PTP and of up to 79 % for PVAC would need high storage capacities or other power resources to overcome this lack in power generation. To address the second goal of this study (quantifying the variability of the aerosol impact on solar power), we choose one major well-documented dust outbreak that occurred between March 6 and 17, 2006 (Tulet et al., 2008; Slingo et al., 2006) to investigate its impact on solar power.

5.1 Regional development of the dust outbreak

The dust outbreak was induced in the Atlas Mountains of northern Algeria on March 5, 2006 (Tulet et al., 2008; Slingo et al., 2006). It reached the central region of the Sahel around Agoufou, Banizoumbou and Niamey by March 7, 2006 and coastal regions around Dakar by March 8, 2006 (see Figure 9). More easterly regions of the Sahel around Maine might have been affected between March 8 and 9, 2006 (no AOD is available at this location during those days). The zone south of Sahel around Djougou came under the influence of the storm on March 8 or 9, 2006. The highest AOD of more than 4 was reached at Niamey (see input data in electronic supplementary material).

The highest daily reduction in PVAC of 79 % is modeled for Niamey on March 8, 2006, for Dakar and Banizoumbou on March 9, 2006 (no data was available for Agoufou on this day) and for Djougou on March 11, 2006. The decrease of PVAC at the start of the dust period is fastest in the central Sahel (Agoufou, Banizoum-

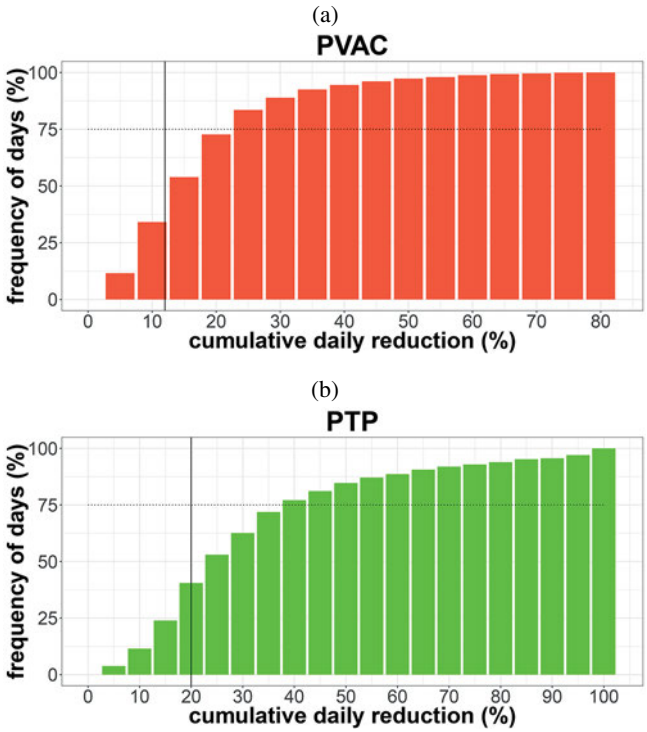

Figure 8: Frequency of the occurrence of cumulative daily reduction due to the presence of aerosols for PVAC (a) and PTP (b) over all clear days at all six stations, same data base as for Table 4 and Figure 4. The dashed horizontal line indicate 75 % of the considered days. The solid vertical line indicates the average daily reduction by using a desert aerosol profile as background aerosol.

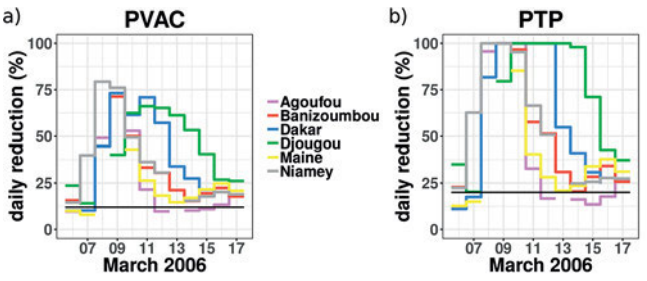

Figure 9: Relative daily power reduction due to aerosols for PVAC (a) and PTP (b) during the major dust outbreak at the six stations, Agoufou (magenta), Banizoumbou (red), Dakar (blue), Djougou (green), Maine (yellow) and Niamey (grey). The solid horizontal line indicates the average daily reduction by using a desert aerosol profile as background aerosol.

bou and Niamey). However, at these locations the recovery phase is faster as well. The duration of high AOD influenced by this dust outbreak on solar power is longest in Dakar and in Djougou (4 days with 100 % daily reduction in PTP).

To overcome these power reductions several days of storage capacities would be needed. Most common storage applications for solar power plants are battery storage for PV systems (Hoppmann et al., 2014) and thermal energy storage for CSP plants (Gallo et al., 2016). Thermal energy storage is currently cheaper than battery storage. Energy costs lie between 120 and 2500 $/kWh for battery storage and between 0.1 and 100 $/kWh for thermal storage (Gallo et al., 2016). Typically, the thermal storage systems of a CSP plant are dimensioned to overcome night times or times with low DNI during one day. The Andasol I power plant, used in this study without storage, has a thermal storage capacity of 982 MWh_e, which represents 7.5 hours peak load (Kistner et al., 2004). Battery storage for PV plants is mainly used in small-scale systems or for mini-grid stabilization with capacities of several kW (IRENA, 2017). Thus, CSP plants have the advantage compared to PVPP, that they are already used in combination with storage systems at high capacities. However, for a completely solar based power system larger storage capacities to overcome desert dust induced power reductions need to be developed.

5.2 Impact of soiling on PV power at Banizoumbou

Up to now, all our results considered atmospheric impacts on solar power due to aerosols. However, soiling causes an additional impact of aerosols on solar panels. Reviews are provided e.g. by Costa et al. (2018); Costa et al. (2016); Sayyah et al. (2014); Sarver et al. (2013) and showed that the impact of soiling can significantly reduce or even completely terminate power generation with solar power plants. Thereby, soiling reduces the transmission of solar irraidiances for PV and causes reflection losses for CSP plants (Sarver et al., 2013). The impact on PV and CSP mainly varies due to the location, the front layer material, the tilting angle and weather. Monthly losses range from 3 % to 90 % for PV and from 14 % to 78 % for CSP depending on the before mentioned impacts. With SolPaRT the impact of aerosols within the atmosphere can be analyzed, but the inclusion of soiling would require more information, e.g., on deposition rates and cleaning cycle. Here we exemplary estimate the effect of soiling on a PV panel during the dust outbreak at Banizoumbou.[1]

Mass concentrations m of particles were measured at Banizoumbou during the whole time of the dust outbreak (AMMA, 2018). A constant falling velocity v_p in the range between 2 and 10 cm/s is assumed, which is typical for a desert region according to Ganor and Foner (2001). For tilting angles of 15° Elminir et al. (2006) found about 20 % lower dust concentration densities on PV panels compared to a zero tilt. Therefore, we use a factor of 80 % to calculate the dust concentration density ρ_{panel} on the panel

$$\rho_{\text{panel}} = v_p \cdot m \cdot 0.8. \tag{5.1}$$

[1]Thereby the effect of wind speed is not included into the algorithm, as its impact lies between −3 and 1.5 % on the cleanness for wind speeds up to 5 m/s (Guo et al., 2015).

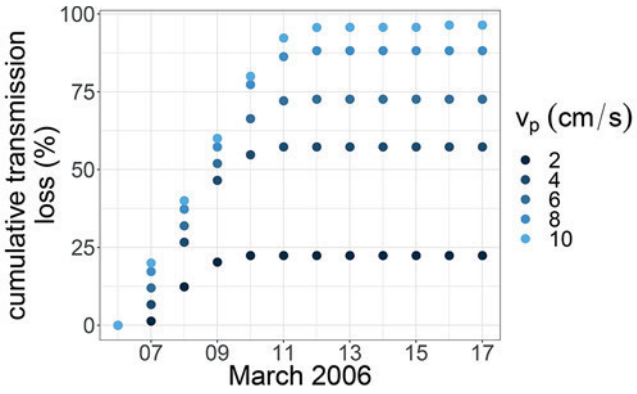

Figure 10: Cumulative transmission losses due to soiling in Banizoumbou for the days of the dust outbreak for several falling velocities (marked in different colors).

Transmission losses ΔT of PVPP depend on the dust concentration density. A linear relation

$$\Delta T = 4 \cdot \rho_{\text{panel}} - 4 \tag{5.2}$$

for $1\,\text{g/m}^2 < \rho_{\text{panel}} < 20\,\text{g/m}^2$, can be derived from Figure 6 in Elminir et al. (2006). For $\rho_{\text{panel}} > 20\,\text{g/m}^2$ we assume 20 % and for $\rho_{\text{panel}} < 1\,\text{g/m}^2$ we assume 0 % transmission losses.

As we do not know the exact falling velocity the transmission losses are calculated for several constant falling velocities for Banizoumbou (Figure 10). Without cleaning transmission losses of solar irradiance would be between 22 % and 96 % depending on the falling velocity. The daily mean transmission loss is 1.9 %, 4.8 %, 6 %, 7.4 % and 8 % for falling velocities of 2, 4, 6, 8 and 10 cm/s, respectively. This implies an additional loss of solar power by the same percentage.

There are only a few studies analyzing power reductions due to soiling on a daily basis (e.g. Jamil et al., 2016; Sayyah et al., 2014). They found daily losses of up to 6 % in Thar Desert in India (Sayyah et al., 2014) and up to 20 % in Malaysia (Jamil et al., 2016).

6 Conclusion

In West Africa the occurrence of aerosol particles significantly modulates the availability of solar power. To quantify these effects we use high temporal resolution meteorological data and aerosol properties from six locations, distributed over different climate zones in West Africa. With this unique data set we analyzed the impact of aerosols on photovoltaic and parabolic trough power plants with the energy meteorological model chain SolPaRT for all clear days in 2006. The combination of both solar power and meteorological models is necessary for solar power predictions to be as realistic as possible. As expected, for cloud-free situations the simulation shows highest sensitivity to AOD compared to other atmospheric parameters. The presence of aerosols is responsible for daily reductions in photovoltaic and parabolic trough power plants of up to 79 % and 100 %, respectively.

Local median daily reductions due to aerosols in 2006 are determined to be 13 % to 22 % for photovoltaic power (PVAC) and 22 % to 37 % for parabolic trough power (PTP) depending on the location. For both technologies daily reduction of solar power production is strongly correlated with AOD (see Figure 6). When AOD is around 1.5 a 100 % loss of PTP and a 50 % loss for PVAC is found on a daily scale.

A parabolic trough power plant can have a compensating effect on the aerosol impact. Due to economic reasons the power block of the power plant is usually underdimensioned to reach a high capacity utilization. This leads to a higher aerosol-induced reduction of absorbed heat than the reduction of PTP. For PVAC no compensating or significantly enhancing effect was found.

Dust outbreaks can have a strong influence on both PVAC and PTP. We analyzed one specific event in March 2006 and estimate that concentrating systems would not produce any electricity for several days in a row during such an event. Photovoltaic modules would reduce their power generation to a minimum of 21 % during one day. Furthermore, soiling would cause an additional reduction for both technologies. For photovoltaic modules and depending on the assumed fall velocity, this effect can be as large as 96 % shading after the analyzed dust outbreak. For both technologies the installation of a storage system to overcome such periods of large power losses, which can also arise during cloudy times, would be reasonable. For the dust outbreak in March 2006, the storage system should have been sized such that it can provide power for a minimum of four days to compensate PTP and up to 79 % of needed PVAC during at least one day for the compensation. However, more events need to be studied to derive more general conclusions on storage needs.

PTP is more susceptible to the impact of aerosols than PVAC. However, combinations of PTPP with large scale thermal storage systems are already used. Furthermore, they can be combined with secondary combustion by fossil fuels to compensate times with low incoming solar irradiance. Battery storage systems for the combination with PVPP are still smaller and more expensive than thermal storage systems (IRENA, 2017).

With SolPaRT, a modeling tool has been developed which includes the major atmospheric effects on GHI and DNI and takes into account the technical parameters and their environmental dependencies for modules, inverters or power plant characteristics to assess PVAC or PTP. However, additional impacts could be caused by the variable composition of aerosols influencing their extinction efficiency or the spectral variability of solar irradiance. These impacts should be subject to further research as well as the impact of clouds.

Acknowledgments

The first author, Ina Neher, is thankful for a PhD fellowship from the Heinrich Böll Foundation. We grate-

fully acknowledge the support by Deutsche Forschungsgemeinschaft via grant DFG LO 901/7–1 for Bernhard Pospichal. Furthermore, we thank Bernhard Mayer and Claudia Emde for their helpful advice concerning the libRadtran simulations and Klaus Pfeilsticker for many fruitful discussions. The authors would like to thank numerous data providers: Data in Niamey were obtained from the Atmospheric Radiation Measurement (ARM) Climate Research Facility, a U.S. Department of Energy Office of Science user facility sponsored by the Office of Biological and Environmental Research. We thank Philippe Goloub and Didier Tanre for their effort in establishing and maintaining AERONET sites in Agougou, Banizoumbou, Dakar, Djougou and Maine and provide aerosol data. Meteorological data was used from the AMMA Database. Based on an French initiative, AMMA was built by an international scientific group and is currently funded by a large number of agencies, especially from France, UK, US and Africa. It has been the beneficiary of a major financial contribution from the European Community's Sixth Framework Research Program. Detailed information on scientific coordination and funding is available on the AMMA International web site http://www.amma-international.org.

List of abbreviations and symbols

ΔPT	Relative difference (in %) between ΔPTH and ΔPTP
ΔPV	Relative difference (in %) between ΔPVDC and ΔPVAC
ΔPTH	Daily reduction in PTH
ΔPTP	Daily reduction in PTP
ΔPVAC	Daily reduction in PVAC
ΔPVDC	Daily reduction in PVDC
ΔT	Transmission loss
AERONET	AErosol RObotic NETwork
AMF	ARM mobile facility
AMMA	African Monsoon Multidisciplinary Analysis
AOD	Aerosol optical depth
ARM	Atmospheric Radiation Program
Aw	Tropical wet climate
BSh	Hot semi-arid climate
BWh	Hot desert climate
CSP	Concentrating solar power
DHI	Diffuse horizontal irradiance
DIR	Direct horizontal irradiance
DISORT	DIScrete Ordinates Radiative Transfer solver
DNI	Direct normal irradiance
g	Asymmetry parameter
GHI	Global horizontal irradiance
IQR	Interquantile range
libRadtran	Library of RT programs and routines
m	Mass concentration
Md	Median
MFRSR	Multifilter shadowband radiometer
MPP	Maximum power point
N	Number of data points
NWM	Numerical weather models
OPAC	Optical Properties of Aerosols and Clouds
PT	Parabolic trough
PT-humidity	Relative humidity
PTH	Parabolic trough heat
PTP	PT power
PTPP	PT power plant
PV	Photovoltaic
PVAC	PV power
PVDC	PV power at direct current
PVPP	PV power plant
PWV	Precipitable water vapor
R^2	Explained variance
RMSE	Root mean square error
RT	Radiative transfer
SolPaRT	Solar power modeling including atmospheric radiative transfer
SSA	Single scattering albedo
SYNOP	Synoptic observations
WAM	West African monsoon
ρ_{panel}	Dust concentration density on the panel
v_p	Falling velocity

References

Ackerman, T.P., G.M. Stokes, 2003: The atmospheric radiation measurement program. – Phys. Today **56**, 38–44, DOI: 10.1063/1.1554135.

Alexandrov, M.D., P. Kiedron, J.J. Michalsky, G. Hodges, C.J. Flynn, A.A. Lacis, 2007: Optical depth measurements by shadow-band radiometers and their uncertainties.. – Appl. Optics **46**, 8027–8038, DOI: 10.1364/AO.46.008027.

AMMA, 2018: Database. – http://baobab.sedoo.fr/AMMA/ (access: 14.03.2018).

Anderson, G., S. Clough, F. Kneizys, 1986: AFGL atmospheric constituent profiles (0–120 km). – Env. Res. Papers AFGL-TR, 86-0110, U.S. Air Force Geophysics Laboratory. Optical Physics Division.

Badescu, V., C.A. Gueymard, S. Cheval, C. Oprea, M. Baciu, A. Dumitrescu, F. Iacobescu, I. Milos, C. Rada, 2013: Accuracy analysis for fifty-four clear-sky solar radiation models using routine hourly global irradiance measurements in Romania. – Renew. Energy **55**, 85–103, DOI: 10.1016/j.renene.2012.11.037.

Boucher, O., 2015: Atmospheric Aerosols: Properties and Climate Impacts, volume 1. – Springer.

Calinoiu, D., M. Paulescu, I. Ionel, N. Stefu, N. Pop, R. Boata, A. Pacurar, P. Gravila, E. Paulescu, G. Trif-Tordai, 2013: Influence of aerosols pollution on the amount of collectable solar energy. – Energy Convers. Manag. **70**, 76–82, DOI: 10.1016/j.enconman.2013.02.012.

Clough, S.A., M.W. Shephard, E.J. Mlawer, J.S. Delamere, M.J. Iacono, K. Cady-Pereira, S. Boukabara, P.D. Brown, 2005: Atmospheric radiative transfer modeling: A summary of the AER codes. – J. Quant. Spectros. Radiative Transfer **91**, 233–244, DOI: 10.1016/j.jqsrt.2004.05.058.

Costa, S.C.S., A. Sonia, A.C. Diniz, L.L. Kazmerski, 2016: Dust and soiling issues and impacts relating to solar energy systems: Literature review update for 2012–2015. – Renew. Sustain. Energy Rev. **63**, 33–61, DOI: 10.1016/j.rser.2016.04.059.

Costa, S.C.S., A. Sonia, A.C. Diniz, L.L. Kazmerski, 2018: Solar energy dust and soiling R&D progress: Literature review update for 2016. – Renew. Sustain. Energy Rev. **82**, 2504–2536, DOI: 10.1016/j.rser.2017.09.015.

Cowie, S.M., P. Knippertz, J.H. Marsham, 2014: A climatology of dust emission events from Northern Africa using long-term surface observations. – Atmos. Chem. Phys. **14**, 8579–8597, DOI: 10.5194/acp-14-8579-2014.

De Soto, W., S.A. Klein, W.A. Beckman, 2006: Improvement and validation of a model for photovoltaic array performance. – Solar Energy **80**, 78–88, DOI: 10.1016/j.solener.2005.06.010.

ECOWAS, 2017: Project Information Document/Integrated Safeguards Data Sheet (PID/ISDS). – Technical Report Phase 1, World Bank Group, ECOWAS – Regional Electricity Access Project (P164044).

Elminir, H.K., A.E. Ghitas, R.H. Hamid, F. El-Hussainy, M.M. Beheary, K.M. Abdel-Moneim, 2006: Effect of dust on the transparent cover of solar collectors. – Energy Convers. Manag. **47**, 3192–3203, DOI: 10.1016/j.enconman.2006.02.014.

Emde, C., R. Buras-Schnell, A. Kylling, B. Mayer, J. Gasteiger, U. Hamann, J. Kylling, B. Richter, C. Pause, T. Dowling, L. Bugliaro, 2016: The libRadtran software package for radiative transfer calculations (version 2.0.1). – Geosci. Model Develop. **9**, 1647–1672, DOI: 10.5194/gmd-9-1647-2016.

Fountoukis, C., L. Martín-pomares, D. Perez-astudillo, D. Bachour, I. Gladich, 2018: Simulating global horizontal irradiance in the Arabian Peninsula: Sensitivity to explicit treatment of aerosols. – Solar Energy **163**, 347–355, DOI: 10.1016/j.solener.2018.02.001.

Gallo, A.B., J.R. Sim~oes-moreira, H.K.M. Costa, M.M. Santos, E. Moutinho, 2016: Energy storage in the energy transition context: A technology review. – Renew. Sustain. Energy Rev. **65**, 800–822, DOI: 10.1016/j.rser.2016.07.028.

Ganor, E., H.A. Foner, 2001: Mineral dust concentrations, deposition fluxes and deposition velocities in dust episodes over Israel. – J. Geophys. Res. Atmos. **106**, 18431–18437, DOI: 10.1029/2000JD900535.

Gueymard, C.A., 2003: Direct solar transmittance and irradiance predictions with broadband models. Part I: detailed theoretical performance assessment. – Solar Energy **74**, 355–379, DOI: 10.1016/j.solener.2003.11.002.

Gueymard, C.A., P.A. Jimenez, 2018: Validation of Real-Time Solar Irradiance Simulations over Kuwait Using WRF-Solar. – EuroSun Conf., Rapperswil, Switzerlang, DOI: 10.18086/eurosun2018.09.14.

Guo, B., W. Javed, B.W. Figgis, T. Mirza, 2015: Effect of dust and weather conditions on photovoltaic performance in Doha, Qatar. – 2015 1st Workshop on Smart Grid and Renewable Energy (SGRE), DOI: 10.1109/SGRE.2015.7208718.

Haegel, N.M., R. Margolis, T. Buonassisi, D. Feldman, A. Froitzheim, R. Garabedian, M. Green, S. Glunz, H.M. Henning, B. Holder, I. Kaizuka, B. Kroposki, K. Matsubara, S. Niki, K. Sakurai, R.A. Schindler, W. Tumas, E.R. Weber, G. Wilson, M. Woodhouse, S. Kurtz, 2017: Terawatt-scale photovoltaics: Trajectories and challenges. – Science **356**, 141–143, DOI: 10.1126/science.aal1288.

Hammer, A., D. Heinemann, C. Hoyer, R. Kuhlemann, E. Lorenz, R. Müller, H.G. Beyer, 2003: Solar energy assessment using remote sensing technologies. – Remote Sens. Env. **86**, 423–432, DOI: 10.1016/S0034-4257(03)00083-X.

Hanrieder, N., S. Wilbert, D. Mancera-guevara, R. Buck, S. Giuliano, R. Pitz-paal, 2017: Atmospheric extinction in solar tower plants – A review. – Solar Energy **152**, 193–207, DOI: 10.1016/j.solener.2017.01.013.

Hess, M., P. Koepke, I. Schult, 1998: Optical Properties of Aerosols and Clouds: The Software Package OPAC. – Bull. Amer. Meteor. Soc. **79**, 831–844, DOI: 10.1175/1520-0477(1998)079<0831:OPOAAC>2.0.CO;2.

Holben, B., T. Eck, I. Slutsker, D. Tanré, J. Buis, A. Setzer, E. Vermote, J. Reagan, Y.J. Kaufman, T. Nakajima, F. Lavenu, I. Jankowiak, A. Smirnov, 1998: AERONET – A Federated Instrument Network and Data Archive for Aerosol Characterization. – Remote Sens. Env. **66**, 1–16, DOI: 10.1016/S0034-4257(98)00031-5.

Holben, B., D. Tanre, A. Smirnov, T. Eck, I. Slutsker, N. Abuhassan, W. Newcomb, J. Schafer, B. Chatenet, F. Lavenu, Y. Kaufman, J. Castle, A. Setzer, B. Markham, D. Clark, R. Frouin, R. Halthore, A. Karneli, N.T. O'Neill, 2001: An Emerging Ground- based Aerosol Climatology: Aerosol Optical Depth from AERONET. – J. Geophys. Res. **106**, 12067–12097, DOI: 10.1029/2001JD900014.

Hoppmann, J., J. Volland, T.S. Schmidt, V.H. Hoffmann, 2014: The economic viability of battery storage for residential solar photovoltaic systems – A review and a simulation model. – Renew. Sustain. Energy Rev. **39**, 1101–1118, DOI: 10.1016/j.rser.2014.07.068.

IRENA, 2017: Electricity Storage and Renewables: Costs and Markets to 2030. – Technical Report October, International Renewable Energy Agency.

Ishaque, K., Z. Salam, H. Taheri, 2011a: Accurate MATLAB Simulink PV System Simulator Based on a Two-Diode Model. – J. Power Electronics **11**, 179–187, DOI: 10.6113/JPE.2011.11.2.179.

Ishaque, K., Z. Salam, H. Taheri, 2011b: Simple, fast and accurate two-diode model for photovoltaic modules. – Solar Energy Materials and Solar Cells **95**, 586–594, DOI: 10.1016/j.solmat.2010.09.023.

Jamil, W.J., H.A. Rahman, K.A. Baharin, 2016: Experiment-based Study on the Impact of Soiling on PV System's Experiment-based Study on the Impact of Soiling on PV System's Performance. – Int. J. Electrical Comp. Engineer. **6**, 810–818, DOI: 10.11591/ijece.v6i1.9606.

Kato, S., T.P. Ackerman, J.H. Mather, E.E. Clothiaux, 1999: The k-distribution method and correlated-k approximation for a shortwave radiative transfer model. – J. Quant.

Spectros. Radiative Transfer **62**, 109–121, DOI: 10.1016/S0022-4073(98)00075-2.

Kaufman, Y.J., D. Tanré, O. Boucher, 2002: A satellite view of aerosols in the climate system.. – Nature **419**, 215–223, DOI: 10.1038/nature01091.

King, D.L., W.E. Boyson, J.A. Kratochvil, 2004: Photovoltaic array performance model. – Technical report, Sandia National Laboratories, DOI: 10.2172/919131.

King, D.L., S. Gonzalez, G.M. Galbraith, W.E. Boyson, 2007: Performance Model for Grid-Connected Photovoltaic Inverters. – Sandia technical report **38**, 655–660, DOI: 10.2172/920449.

Kistner, K. Grethe, M. Geyer, J.A. Nebrera, 2004: The Progress of the AndaSol projects in Spain. – Proceedings of the 12th Solar PACES Symposium Oaxaca, Mexico, 10–107.

Kosmopoulos, P.G., S. Kazadzis, M. Taylor, E. Athanasopoulou, O. Speyer, P.I. Raptis, E. Marinou, E. Proestakis, S. Solomos, E. Gerasopoulos, V. Amiridis, A. Bais, C. Kontoes, 2017: Dust impact on surface solar irradiance assessed with model simulations, satellite observations and ground-based measurements. – Atmos. Measur. Techniques Discus. **10**, 2435–2453, DOI: 10.5194/amt-2017-79.

Kothe, S., U. Pfeifroth, R. Cremer, J. Trentmann, R. Hollmann, 2017: A satellite-based sunshine duration climate data record for Europe and Africa. – Remote Sens. **9**, 429, DOI: 10.3390/rs9050429.

Li, X., F. Wagner, W. Peng, J. Yang, D.L. Mauzerall, 2017: Reduction of solar photovoltaic resources due to air pollution in China. – Proceedings of the National Academy of Sciences **114**, 11867–11872, DOI: 10.1073/pnas.1711462114.

Luoma, J., J. Kleissl, K. Murray, 2012: Optimal inverter sizing considering cloud enhancement. – Solar Energy **86**, 421–429, DOI: 10.1016/j.solener.2011.10.012.

Mayer, B., A. Kylling, 2005: Technical note: The libRadtran software package for radiative transfer calculations - description and examples of use. – Atmos. Chem. Phys. **5**, 1319–1381, DOI: 10.5194/acpd-5-1319-2005.

Neher, I., T. Buchmann, S. Crewell, B. Evers-Dietze, K. Pfeilsticker, B. Pospichal, C. Schirrmeister, S. Meilinger, 2017: Impact of atmospheric aerosols on photovoltaic energy production - Scenario for the Sahel zone. – Energy Procedia **125**, 170–179, DOI: 10.1016/j.egypro.2017.08.168.

Parretta, A., A. Sarno, L.R. Vicari, 1998: Effects of solar irradiation conditions on the outdoor performance of photovoltaic modules. – Optics Comm. **153**, 153–163, DOI: 10.1016/S0030-4018(98)00192-8.

Peel, M.C., B.L. Finlayson, T.A. McMahon, 2007: Updated world map of the Köppen-Geiger climate classification. – Hydrol. Earth Sys. Sci. **11**, 1633–1644, DOI: 10.5194/hess-11-1633-2007.

Perez, R., R. Seals, A. Zelenka, P. Ineichen, 1990: Climatic evaluation of models that predict hourly direct irradiance from hourly global irradiance: Prospects for performance improvements. – Solar Energy **44**, 99–108, DOI: 10.1016/0038-092X(90)90071-J.

Polo, J., G. Estalayo, 2015: Impact of atmospheric aerosol loads on Concentrating Solar Power production in arid-desert sites. – Solar Energy **115**, 621–631, DOI: 10.1016/j.solener.2015.03.031.

Prasad, A.K., S. Singh, S.S. Chauhan, M.K. Srivastava, R.P. Singh, R. Singh, 2007: Aerosol radiative forcing over the Indo-Gangetic plains during major dust storms. – Atmos. Env. **41**, 6289–6301, DOI: 10.1016/j.atmosenv.2007.03.060.

Quaschning, V., 2011: Regenerative Energiesysteme. – Hanser Verlag Muenchen, pp. 180.

Quaschning, V., W. Ortmanns, R. Kistner, M. Geyer, 2001a: Greenius: A New Simulation Environment for Technical and Economical Analysis of Renewable Independent Power Projects. – In: Proceedings of Solar Forum 2001, 413–418.

Quaschning, V., R. Kistner, W. Ortmanns, 2001b: Simulation of parabolic trough power plants. – 5th Cologne Solar Symposium 46–50.

Richardson, D.B., R.W. Andrews, 2014: Validation of the MERRA dataset for solar PV applications. – IEEE 40th Photovoltaic Specialist Conference (PVSC) 809–814, DOI: 10.1109/PVSC.2014.6925039.

Rieger, D., A. Steiner, V. Bachmann, P. Gasch, J. Förstner, K. Deetz, B. Vogel, H. Vogel, 2017: Impact of the 4 April 2014 Saharan dust outbreak on the photovoltaic power generation in Germany. – Atmos. Chem. Phys. **17**, 13391–13415, DOI: 10.5194/acp-17-13391-2017.

Rockwood, A., S. Cox, 1976: Satellite inferred surface albedo over northwestern Africa. – J. Atmos. Sci. **35**, 513–522, DOI: 10.1175/1520-0469(1978)035<0513:SISAON>2.0.CO;2.

Ruiz-Arias, J.A., C.A. Gueymard, F.J. Santos-Alamillos, D. Pozo, 2016: Worldwide impact of aerosol' s time scale on the predicted long-term concentrating solar power potential. – Scientific Reports **6**, 1–10, DOI: 10.1038/srep30546.

Russell, P.B., J.M. Livingston, O. Dubovik, S.A. Ramirez, J. Wang, J. Redemann, B. Schmid, M. Box, B.N. Holben, 2004: Sunlight transmission through desert dust and marine aerosols: Diffuse light corrections to Sun photometry and pyrheliometry. – J. Geophys. Res. Atmos. **109**, 1917-1922, DOI: 10.1182/blood-2006-08-044172.

Sarver, T., A. Al-Qaraghuli, L.L. Kazmerski, 2013: A comprehensive review of the impact of dust on the use of solar energy: History, investigations, results, literature, and mitigation approaches. – Renew. Sustain. Energy Rev. **22**, 698–733, DOI: 10.1016/j.rser.2012.12.065.

Sayyah, A., M.N. Horenstein, M.K. Mazumder, 2014: Energy yield loss caused by dust deposition on photovoltaic panels. – Solar Energy **107**, 576–604, DOI: 10.1016/j.solener.2014.05.030.

Sengupta, M., A. Habte, S. Kurtzn, A. Dobos, S. Wilbert, E. Lorenz, T. Stoffel, D. Renné, D. Myers, S. Wilcox, P. Blanc, R. Perez, 2017: Best practices handbook for the collection and use of solar resource data for solar energy applications: Second Edition. – Technical Report January 2018, NREL, DOI: 10.18777/ieashc-task46-2015-0001.

Skoplaki, E., J.A. Palyvos, 2009: Operating temperature of photovoltaic modules: A survey of pertinent correlations. – Renew. Energy **34**, 23–29, DOI: 10.1016/j.renene.2008.04.009.

Slingo, A., T.P. Ackerman, R.P. Allan, E.I. Kassianov, S.A. McFarlane, G.J. Robinson, J.C. Barnard, M.A. Miller, J.E. Harries, J.E. Russell, S. Dewitte, 2006: Observations of the impact of a major Saharan dust storm on the atmospheric radiation balance. – Geophys. Res. Lett. **33**, published online, DOI: 10.1029/2006GL027869.

Solangi, K.H., M.R. Islam, R. Saidur, N.a. Rahim, H. Fayaz, 2011: A review on global solar energy policy. – Renew. Sustain. Energy Rev. **15**, 2149–2163, DOI: 10.1016/j.rser.2011.01.007.

Solargis, 2017: GeoModel Solar. – https://solargis.com/maps-and-gis-data/download/sub-saharan-africa/.

Stamnes, K., S.C. Tsay, W. Wiscombe, K. Jayaweera, 1988: Numerically stable algorithm for discrete-ordinate-method radiative transfer in multiple scattering and emitting layered media.. – Appl. Optics **27**, 2502–2509, DOI: 10.1364/AO.27.002502.

Stone, R.S., G.P. Anderson, E.P. Shettle, E. Andrews, K. Loukachine, E.G. Dutton, C. Schaaf, M.O.R. Iii, 2008:

Radiative impact of boreal smoke in the Arctic: Observed and modeled. – J. Geophys. Res. **113**, D14S16, DOI: 10.1029/2007JD009657.

Taylor, C.M., D. Belusic, F. Guichard, D.J. Parker, T. Vischel, O. Bock, P.P. Harris, S. Janicot, C. Klein, G. Panthou, 2017: Frequency of extreme Sahelian storms tripled since 1982 in satellite observations. – Nature **544**, 475–478, DOI: 10.1038/nature22069.

Tulet, P., M. Mallet, V. Pont, J. Pelon, A. Boone, 2008: The 7–13 March 2006 dust storm over West Africa: Generation, transport, and vertical stratification. – J. Geophys. Res. Atmos. **113**, DOI: 10.1029/2008JD009871.

United Nations, 2015: Sustainable Development Goals. – https://sustainabledevelopment.un.org/sdgs.

Wallace, J.M., P.V. Hobbs, 2006: Atmospheric Science: An Introductory Survey. – Elsevier.

Wendisch, M., P. Yang, 2012: Theory of atmospheric radiative transfer. – John Wiley & Sons, Weinheim.

Wilbert, S., 2014: Determination of Circumsolar Radiation and its Effect on Concentrating Solar Power. – Ph.D. thesis, Rheinisch-Westfälische Technische Hochschule Aachen, DOI: (No. RWTH-CONV-145307).

The pdf version (Adobe Java Script must be enabled) of this paper includes an electronic supplement:
Electronic supplementary material:
Impact of atmospheric aerosols on solar power production – Dust outbreak in West Africa

Chapter 5

Photovoltaic power potential in West Africa using long-term satellite data

To detect long-term atmospheric variability and trends in West Africa and their impact on photovoltaic yields satellite data is analyzed. The results are published as Neher, I., Crewell, S., Meilinger, S., Pfeifroth, U., and Trentmann, J. (2020). Photovoltaic power potential in West Africa using long-term satellite data. *Atmospheric Chemistry and Physics*, 20:12871–12888,

Author contributions: IN performed the data analysis, developed the photovoltaic yield model and was responsible for the preparation of the manuscript. She is the main author of this publication. JT and UP provided the CMSAF data and gave advise to the manuscript during the writing process. SC and SM provided the overall scientific guidance, discussed results and commented on the manuscript. All figures were prepared by IN. Therefore and for the data analysis, she used the CM SAF R-package and toolbox, which is provided and was developed by the group of JT and UP at the German Weather Service.

Atmos. Chem. Phys., 20, 12871–12888, 2020
https://doi.org/10.5194/acp-20-12871-2020

Atmospheric Chemistry and Physics
Open Access
EGU

Photovoltaic power potential in West Africa using long-term satellite data

Ina Neher[1,2], Susanne Crewell[2], Stefanie Meilinger[1], Uwe Pfeifroth[3], and Jörg Trentmann[3]

[1]International Centre for Sustainable Development, University of Applied Science Bonn-Rhein-Sieg, Grantham-Allee 20, 53757 Sankt Augustin, Germany
[2]Institute of Geophysics and Meteorology, University of Cologne, Albertus-Magnus-Platz, 50923 Cologne, Germany
[3]Deutscher Wetterdienst, Satellite-based Climate Monitoring, Frankfurter Straße 135, 63067 Offenbach, Germany

Correspondence: Ina Neher (ina.neher@h-brs.de)

Received: 30 March 2020 – Discussion started: 20 May 2020
Revised: 25 August 2020 – Accepted: 28 August 2020 – Published: 5 November 2020

Abstract. This paper addresses long-term historical changes in solar irradiance in West Africa (3 to 20° N and 20° W to 16° E) and the implications for photovoltaic systems. Here, we use satellite irradiance (Surface Solar Radiation Data Set – Heliosat, Edition 2.1 – SARAH-2.1) and temperature data from a reanalysis (ERA5) to derive photovoltaic yields. Based on 35 years of data (1983–2017), the temporal and regional variability as well as long-term trends in global and direct horizontal irradiance are analyzed. Furthermore, a detailed time series analysis is undertaken at four locations.

According to the high spatial resolution SARAH-2.1 data record (0.05° × 0.05°), solar irradiance is largest (up to a 300 $W m^{-2}$ daily average) in the Sahara and the Sahel zone with a positive trend (up to 5 $W m^{-2}$ per decade) and a lower temporal variability (< 75 $W m^{-2}$ between 1983 and 2017 for daily averages). In contrast, the solar irradiance is lower in southern West Africa (between 200 $W m^{-2}$ and 250 $W m^{-2}$) with a negative trend (up to −5 $W m^{-2}$ per decade) and a higher temporal variability (up to 150 $W m^{-2}$). The positive trend in the north is mostly connected to the dry season, whereas the negative trend in the south occurs during the wet season. Both trends show 95 % significance. Photovoltaic (PV) yields show a strong meridional gradient with the lowest values of around 4 kWh kWp^{-1} in southern West Africa and values of more than 5.5 kWh kWp^{-1} in the Sahara and Sahel zone.

1 Introduction

The United Nations proposed the Sustainable Development Goals to achieve a better and more sustainable future (United Nations, 2015). The seventh goal, to "ensure access to affordable, reliable, sustainable and modern energy for all", implies a shift away from fossil-fuel-based sources towards renewable energy sources. Particularly in regions with high irradiance, solar power is a promising option (e.g., Haegel et al., 2017; Solangi et al., 2011). However, potential sites and their yield need to be investigated carefully to ensure long-term sustainable investment.

With regard to energy availability and security, West Africa is one of the least developed regions in the world (ECOWAS, 2017). Therefore, the power system will need to be strongly expanded in this region, as a gap exists between electricity supply and demand (Adeoye and Spataru, 2018). West Africa receives high amounts of global horizontal irradiance (GHI) (Solargis, 2019); moreover, due to their locations within the descending branch of the Hadley cell, the Sahara and the Sahel zone are generally dry with little cloudiness, leading to a high sunshine duration (Kothe et al., 2017). Thus, photovoltaic (PV) power seems to be a promising technology in this region, and the development of a PV system would be worthwhile. Before investing in a PV system, three points need to be considered using different resolutions of GHI (the sum of direct irradiance, DIR, and diffuse horizontal irradiance, DHI), which has the major impact on PV systems (Sengupta et al., 2017). First, high spatial resolution GHI is needed to select a profitable

location. Second, the long-term variability and trends in the historical GHI can be analyzed as a basis to project future system performance in order to estimate the profitability and risks of the plant. Finally, high temporal resolution GHI can be used to dimension the plant and storage system as well as the maintenance in order to optimize the plant. However, ground-based measurements of irradiance are not available continuously over long-term timescales and cover only a few discrete locations in the region.

Satellite-based irradiance measurements have the advantage that they are available for long time periods and cover wide spatial regions (Gueymard and Wilcox, 2011). In particular, geostationary satellites can deliver data at a temporal resolution of less than 1 h and at a high spatial resolution. Using these data, potential PV yields can be calculated in order to select a profitable location and to analyze the long-term profitability and risks. Furthermore, such data sets enable the analysis of the diurnal variability that needs to be taken into account for storage sizing and power system design. Here, the first point is addressed using the daily averaged data to provide an overview of the potential PV yields over the entire region. The European Organisation for the Exploitation of Meteorological Satellites (EUMETSAT) Satellite Application Facility on Climate Monitoring (CM SAF) provides the Surface Solar Radiation Data Set – Heliosat, Edition 2.1 (SARAH-2.1), a 35-year-long climate data record at a 30 min resolution that covers the whole of Africa and Europe (Pfeifroth et al., 2019a). The validation of this data set using stations from the Baseline Surface Radiation Network (BSRN) shows high quality, with a target accuracy of $15\,\mathrm{W\,m^{-2}}$ (Pfeifroth et al., 2019b). However, only one of the BSRN stations lies close to the West African region (the majority of the stations are in Europe; see Pfeifroth et al., 2019b, for station details). As solar irradiance is affected by the atmosphere (cloud, aerosol and trace gases), several assumptions regarding optical properties need to be taken into account with respect to the satellite data retrieval. Specifically, aerosol loads can fluctuate greatly (Neher et al., 2019; Slingo et al., 2006), and they reach their highest global values in the West African region (Kinne et al., 2013). Thus, a detailed validation of the full 35-year SARAH-2.1 data set for West Africa is needed and has not yet been performed.

Besides the atmospheric impact, solar irradiance reaching the top layer of a PV power module is affected by the solar zenith and the tilting angle of the module. Furthermore, soiling and reflections on the front of the modules and shade from their surroundings have additional impacts on the amount of radiation that can be transformed to a direct current by the PV cell. The cell temperature (which is impacted by the incoming irradiance, ambient temperature and wind speed) adjusts the efficiency of the PV cell (Skoplaki and Palyvos, 2009). Explicit models for PV power simulation are available (Neher et al., 2019; Ishaque et al., 2011; King et al., 2004); however, they require explicit input data at a high temporal resolution which is often not available. Therefore, a simplified model for PV yield estimations based on daily data has been developed and applied here.

In this study, the central research question "How do long-term atmospheric variability and trends impact photovoltaic yields in West Africa?" is answered by analyzing the SARAH-2.1 data record for the region in question. To give a comprehensive answer, the article is structured using the following sub-questions.

- How accurate is the SARAH-2.1 data set for the considered region of West Africa?
- What are the trends and variability in solar irradiance between 1983 and 2017 in West Africa?
- How different are these trends and variability for varying latitudes and seasons?
- What implications can be drawn for photovoltaic power?

This article is organized as follows. Section 2 introduces the ground- and satellite-based data. Methodologies to estimate photovoltaic power are described in Sect. 3. The satellite data validation with ground-based measurements is presented in Sect. 4. The variability and trend analysis of the GHI and DIR for the time period from 1983 to 2017 is shown in Sect. 5. Furthermore, the temporal variability at different latitudes is analyzed. Section 6 estimates the implications of solar irradiance variability and trends for PV yields focusing on West Africa, using a simplified yield estimation based on measurements at three locations. Finally, the conclusions are given in Sect. 7.

2 Region overview and data sources

West Africa (which is defined as the region from 3 to 20° N and from 20° W to 16° E in this study) is a region with a pronounced dry and wet season. In large parts of West Africa one wet season occurs during the summer months, the duration of which decreases with rising latitude; however, two wet seasons occur along the coastal region (typically during June and July and during September). Nevertheless, here we use one single definition of seasons according to Mohr (2004): one dry season from October to April and one wet season from May to September. To reinforce our results, we performed the analysis with a sharper definition of seasons (a dry season from November to March, and a wet season from June to August) and found similar results. The difference in seasons is mainly caused by the West African monsoon (WAM) circulation and the intertropical convergence zone (ITCZ). The ITCZ moves from north to south and back in an annual cycle according

to the seasons (north during the wet and south during the dry season). West Africa is generally rather flat with the highest elevations typically below 1000 m (Fig. 1a, Global Land One-km Base Elevation Project, GLOBE, database; Hastings and Dunbar, 1999). Some exceptions are Mount Cameroon in the southeast of the study area along the border of Nigeria and Cameroon, Fouta Djallon and the Guinea Highlands in Guinea, Jos Plateau in the center of Nigeria and the Aïr Mountains in northern Niger. In these regions (as well as locally for lower mountain ranges) orographically enhanced cloudiness might occur. The enhanced cloudiness associated with the moist tropical region is clearly visible in the mean cloud albedo used as input for the SARAH-2.1 data retrieval between 1983 and 2017 (see Fig. 1b, from the SARAH-2.1 data set described later). Clouds have the major influence on the irradiance analyzed in this study. The West African climate zones related to the albedo climatology (used for the SARAH-2.1 data retrieval) have a higher albedo of up to 0.35 in the desert region in the north and a lower albedo of down to 0.1 in the forest region in the south (see Fig. 1c; Surface and Atmospheric Radiation Budget, SARB, data from Clouds and the Earth's Radiant Energy System, CERES). Frequent dust outbreaks occur over the entire region (Cowie et al., 2014); therefore, the highest climatological aerosol optical depth (AOD) of up to 0.35 can be found in northern Mali (see Fig. 1d, from the European Center for Medium Range Weather Forecast, Monitoring Atmospheric Composition and Climate, MACC, and used for the SARAH-2.1 data retrieval). However, in local measurements, AOD values reach daily averages of up to 4 in the Sahel region (AERONET, 2014). Hence, aerosols can have a high impact on the irradiance (independent of clouds) and, in turn, on solar power (Neher et al., 2019).

2.1 Satellite-based data

The Surface Solar Radiation Data Record – Heliosat, Edition 2.1 (SARAH-2.1), data set is provided by the EUMETSAT CM SAF and covers the time period from 1983 to 2017 (Pfeifroth et al., 2019a, 2018). In addition to other parameters, the data set provides the surface incoming shortwave radiation (GHI), the surface incoming direct radiation (DIR), the direct normal irradiance (DNI) and the effective cloud albedo (CAL). The products of SARAH-2.1 are retrieved from the first- and second-generation geostationary METEOSAT satellite service, covering the whole of West Africa with a 30 min temporal and a $0.05° \times 0.05°$ spatial resolution. For the retrieval, the Heliosat algorithm to estimate the effective cloud albedo (Hammer et al., 2003) is combined with a cloud-free radiative transfer model (Mueller et al., 2012). Furthermore, several climatological parameters are used for the retrieval: the precipitable water vapor (ERA-Interim), the monthly AOD climatology (see Fig. 1d, MACC), the monthly ozone climatology (standard US atmosphere) and the surface albedo (see Fig. 1c, SARB data from CERES). For the generation of the SARAH-2.1 data record, the visible channel (0.5–0.9 µm) of the METEOSAT Visible and Infrared Imager (MVIRI) is used until 2005, and the two visible channels (0.6 and 0.8 µm) of the Spinning Enhanced Visible and Infrared Imager (SEVIRI) are used after 2005. A detailed description of the retrieval is given in Mueller et al. (2015) and references therein.

The advantage of the SARAH-2.1 data set compared with SARAH-1 is a higher stability in early years (due to the removal of erroneous satellite images) and during the transition from the first- to second-generation METEOSAT satellite in 2006. Furthermore, the water vapor climatology used was topographically corrected and the consideration of situations with high zenith angles was improved to account for an overestimation of cloud detection at low satellite viewing angles. A mean absolute error (MAE; in comparison to 15 BSRN stations between 1994 and 2017) of 5.5 and $11.7\,\mathrm{W\,m^{-2}}$ for the respective monthly and daily GHI is reached (Pfeifroth et al., 2019b).

In this study, the SARAH-2.1 data record (GHI and DIR at a daily resolution) is used for the trend and variability analysis over the whole 35 years and for the entire region. Daily and monthly means of the GHI are compared to the measured GHI at the three African Monsoon Multidisciplinary Analysis (AMMA) sites. CM SAF SARAH-2.1 data are downloaded as daily and monthly averaged data. A detailed description of the averaging approach can be found in Trentmann and Pfeifroth (2019). Instantaneous (30 min) data are used to estimate PV yields at the three AMMA sites to develop a simpler empirical PV model. The 30 min records were linearly interpolated using the diurnal cycle of the clear-sky irradiance, and the temporal resolution of the measured meteorological data (ambient temperature and wind speed) was adjusted to the satellite data.

2.2 Ground-based data

Ground-based measurements of the GHI complemented by ancillary data over several years are available from the African Monsoon Multidisciplinary Analysis program (AMMA, 2018; Redelsperger et al., 2006) at three sites (Agoufou, Mali; Banizoumbou, Niger; and Djougou, Benin; Fig. 1). The sites are distributed over different land areas: one desert site, one site in the Sahel region and one site in the savanna. The data availability is limited to several years at the beginning of the 21st century. All relevant parameters, including the location, instrument information and measuring times are summarized in Table 1. Additionally, measurements of ambient temperature and wind speed were taken at the three sites during the AMMA campaign. AMMA data are measured at a 15 min resolution. To calculate robust daily averages, each of the 15 min values for a day needs to be available to calculating the mean. If only

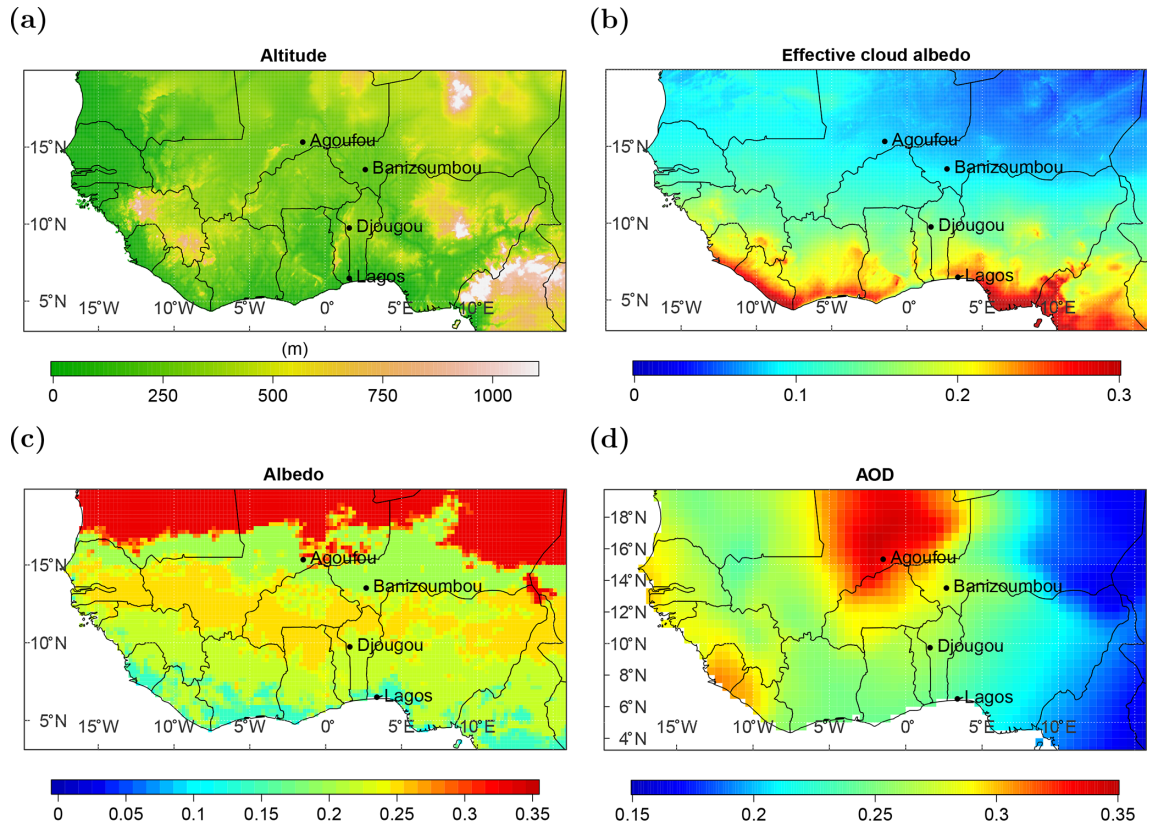

Figure 1. (**a**) Topography of the region considered (Global Land One-km Base Elevation Project, GLOBE, database; Hastings and Dunbar, 1999), (**b**) mean cloud albedo between 1983 and 2017 (from the SARAH-2.1 data set described in Sect. 2.1), (**c**) albedo climatology (Surface and Atmospheric Radiation Budget, SARB, data from Clouds and the Earth's Radiant Energy System, CERES) and (**d**) aerosol optical depth climatology (European Center for Medium Range Weather Forecast, Monitoring Atmospheric Composition and Climate, MACC). The locations of the three ground-based sites (Agoufou, Banizoumbou and Djougou) and the additional location used for the time series analysis in Sect. 5.2 (Lagos) are marked.

one measurement is missing, the day is disregarded. Monthly averages are calculated if there are at least 10 daily averages available over the month.

At all sites, AOD measurements from the Aerosol Robotic Network (AERONET Holben et al., 1998) are available. The AOD measurements are retrieved from solar radiances at certain wavelengths and are cloud screened during post-processing (Giles et al., 2019). Here, the Level 2.0, Version 3, quality-assured data set at a wavelength of 440 nm is used. For the comparison with daily satellite data (see Sect. 4), daily averages are downloaded from AERONET (AERONET, 2014); thus, all data series of 1 d are averaged. Monthly averages are calculated as previously described for the AMMA data set.

3 Photovoltaic yield estimation

Our ultimate goal is to describe the PV potential over the entire region for a standardized PV power plant. For this purpose, a simplified linear regression is fitted on the basis of the three reference sites where the necessary information is available. Furthermore, the uncertainties concerning cell temperature are estimated (see Sect. 3.2) and the GHI used (from the SARAH-2.1 data set) is validated (see Sect. 4). Therefore, ERA5 data are used (Hersbach et al., 2020; Copernicus Climate Change Service, 2017) for the daily mean temperature. The ERA5 archive is based on a global reanalysis and is available from 1979 onward. The single calculation steps, including all necessary input data, are shown in Fig. 2.

3.1 Model development

To estimate the PV power potential, an empirical linear model is developed with a temporal resolution of 1 d, using a normalized GHI (from SARAH-2.1) as input. This linear model is derived by simplifying the widely known two-diode model (e.g., Ishaque et al., 2011). For this purpose, explicit PV power calculations are integrated over the diurnal cycle using AMMA measurements (ambient temperature and wind speed) and SARAH-2.1 data (GHI and DIR) at the three

Table 1. Information on ground-based measuring sites.

Station name	Agoufou	Banizoumbou	Djougou
Country	Mali	Niger	Benin
Latitude	15.3° N	13.5° N	9.7° N
Longitude	1.5° W	2.7° E	1.6° E
Instrument	CNR1	SKS 1110	SP Lite2
Accuracy	±10 % (daily totals)	±5 %	±2.5 % or 10 W m^{-2}
Reference	Campbell Scientific (2010)	Skye Instruments (2019)	Kipp and Zonen (2019)
Time	2005–2011	2005–2012	2002–2009
Resolution	15 min	15 min	15 min
Land use	Desert	Sahel	Savanna

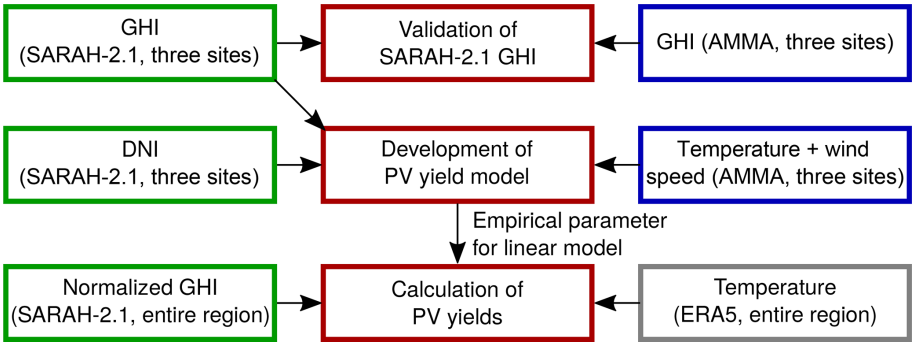

Figure 2. Connection of calculation steps (red) within this study, including all of the input data required (green denotes satellite data, gray denotes reanalysis data and blue denotes observational data).

measuring sites as input for the full model, serving as a reference and to train the linear model.

The two-diode equation calculates the current (I) – voltage (U) – characteristics of a PV module from cell temperature T_c, global tilted irradiance (GTI) and typical modules characteristics:

$$I(U) = I_{PH}(\mathrm{GTI}, T_c) - I_{D_1}(T_c)\left(e^{\frac{U+I\cdot R_S}{n_1\cdot U_T}} - 1\right) - I_{D_2}(T_c)\left(e^{\frac{U+I\cdot R_S}{n_2\cdot U_T}} - 1\right) - \frac{U + I\cdot R_S}{R_P}. \quad (1)$$

Thus, two diodes (D_1 and D_2) are assumed in parallel, with differing saturation currents ($I_{D_1}(T_c)$ and $I_{D_2}(T_c)$), each depending on the cell temperature. The diode "ideality factors" (n_1 and n_2) are constant: $n_1 = 1$ and $n_2 = 2$ (Salam et al., 2010). Furthermore, two resistors are connected, one in parallel (R_P) for the description of leakage currents and one in series (R_S) for the description of voltage drops, with a constant value for the system. The thermal voltage U_T is proportional to the cell temperature. A parallel current source can be assumed for the rayed solar cell. The current source produces the photocurrent $I_{PH}(\mathrm{GTI}, T_c)$ depending on the incoming solar irradiance and the cell temperature. Thus, the following simplification is possible:

$$I(U) = I_{PH}(\mathrm{GTI}, T_c) + f(T_c, I, U), \quad (2)$$

where f is a function, which depend on the cell temperature, the current and the voltage.

The photocurrent depends linearly on the incoming tilted irradiance and is the major term of $I(U)$,

$$I_{PH} = \left(I_{SC}^{STC} + K_i(T_c - T_{STC})\right)\frac{\mathrm{GTI}}{\mathrm{GHI}_{STC}}. \quad (3)$$

By assuming a typical silicon PV module (SolarWorld 235 poly; SolarWorld, 2012), the modules characteristics are given by $I_{SC}^{STC} = 8.35$ A, where STC denotes the short circuit current at standard test conditions, $K_i = 0.00034\ I_{SC}\,\mathrm{K}^{-1}$ is the temperature coefficient for the current, and $T_{STC} = 25\,^{\circ}\mathrm{C}$ and $\mathrm{GHI}_{STC} = 1000\,\mathrm{W\,m^{-2}}$ are the STC conditions for the PV modules. By simplifying Eq. (3) with $I_{SC}^{STC} \gg K_i(T_c - T_{STC})$ (for the typical cell temperature of 46 °C used in the PV community and STC, the right term would be 0.06 A), the temperature dependence is ignored here. The maximum power point (MPP) is calculated as the product of I and U, and the PV yield PV_y is derived as the integrated MPP over each day:

$$\mathrm{PV}_y = \int_{\mathrm{day}} I_{PH}(t)\,U(t)\,\mathrm{d}t. \quad (4)$$

The linear relation of the PV yields and incoming irradiance is used for a simplified linear model for the daily

PV yield (PV_y):

$$\mathrm{PV}_y = a(T) \cdot \mathrm{GTI} + b(T). \quad (5)$$

For our purpose, it is sufficient to replace GTI with a normalized GHI ($\mathrm{GHI}_{\mathrm{norm}}$; also to reduce the seasonal variability) from SARAH-2.1, which is calculated by dividing the GHI by the cosine of the minimum daily zenith angle. Note that due to the high importance of the cell temperature, the fitting parameters (Eq. 5) depend on temperature. The parameter b indicates the impact of the inverter, as it requires a certain amount of power to work. The slope a indicates the efficiency, including the conversion of watts per square meter ($\mathrm{W\,m^{-2}}$) to kilowatt hours per kilowatt peak ($\mathrm{kWh\,kWp^{-1}}$). Uncertainties due to a varying temperature and the coefficients $a_i(T)$ and $b_i(T)$ are estimated by calculating the explicit PV power, including temperature, at three sites and its variability (see Sect. 3.2).

To determine $a_i(T)$ and $b_i(T)$ explicit PV power calculations are undertaken using the PV power model part of the "Solar Power modeling including atmospheric Radiative Transfer" (SolPaRT) model at Agoufou (Mali), Banizoumbou (Niger) and Djougou (Benin) at a 15 min resolution (Neher et al., 2019). These calculations require knowledge of the incoming radiation on the tilted plane and cell temperature over the diurnal cycle. These parameters can be derived using the GHI, DIR, the solar zenith angle, the ambient temperature and the wind speed. The impact of soiling and shading is excluded here, as these factors are highly dependent on the local conditions and the cleaning cycle of the modules. For the explicit calculations, the SARAH-2.1 data record of the GHI, depending on the solar zenith angle, and the modules orientation (latitude assumed as the tilt and southern orientation) are used to determine the radiation on the tilted plane. Assuming an installation with 11 modules (typical size of one row in a PV plant and several can be connected in parallel), the inverter is only slightly (96 %) over-dimensioned, as high irradiance is expected in the region considered. The input data for the model calculations, including the sources, are summarized in Table 2.

3.2 Uncertainties of PV yield estimation

The PV power is explicitly calculated (using Eq. 1, the temperature information from AMMA, and the GHI and DIR from SARAH-2.1) at the three measurement sites (Agoufou, Mali; Banizoumbou, Niger; and Djougou, Benin) at a 15 min resolution. For each day, the PV yield (integral over each day and normalization over the plant peak – given in $\mathrm{kWh\,kWp^{-1}}$) is derived. On a daily basis the GHI itself depends on atmospheric conditions (clouds, aerosols and greenhouse gases) and season (solar zenith angle). PV yields are highly correlated with the daily mean normalized GHI (see Fig. 3).

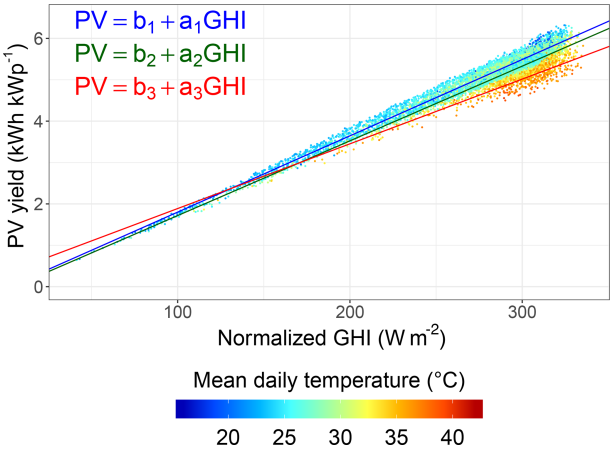

Figure 3. PV yield as a function of normalized global horizontal irradiance combining the calculations at all three measurement sites at three temperature levels: $T \leq 30\,^{\circ}\mathrm{C}$ (blue), $30\,^{\circ}\mathrm{C} < T \leq 35\,^{\circ}\mathrm{C}$ (green), and $T \geq 35\,^{\circ}\mathrm{C}$ (red). The mean daily temperature is marked as shown in the color bar.

However, the mean daily temperature additionally impacts PV yields. Therefore, three regression lines (see Equation 5) are determined at different temperature levels, $T \leq 30\,^{\circ}\mathrm{C}$ (blue), $30\,^{\circ}\mathrm{C} < T \leq 35\,^{\circ}\mathrm{C}$ (green) and $T \geq 35\,^{\circ}\mathrm{C}$ (red). No further significant improvement was found for a finer separation into more temperature classes. The mean daily temperature values from ERA5 are used to define the temperature level of each point during each time step. The explained variance (R^2) is highest for the lowest temperature ranges (0.98) and increases (0.78) for the highest (see Table 3). The root mean square error (RMSE) and R^2 as well as the single fitting parameters a_i and b_i are summarized in Table 3.

The slope a decreases at increasing temperatures. The parameter b was set to zero for $T \geq 35\,^{\circ}\mathrm{C}$, as it can not be positive for physical reasons. The uncertainty is highest at the highest temperature level (RMSE: $\pm 0.67\,\mathrm{kWh\,kWp^{-1}}$) and lowest at the lowest temperature level (RMSE: $\pm 0.16\,\mathrm{kWh\,kWp^{-1}}$). The variability in PV yields increases with the normalized GHI for two reasons: first, temperature levels can reach higher values at a higher normalized GHI, which would induce a higher reduction of PV yields compared with lower temperature levels; second, the temperature effect on PV yields is relative and can reach higher effective PV yield reductions at a higher normalized GHI.

4 Validation of satellite data with ground-based measurements

Previous studies have compared the SARAH-2.1 GHI to ground-based measurements from the BSRN (Pfeifroth et al., 2019b), as they provide benchmarks for accuracy (±2 % or

Table 2. Input data for photovoltaic power calculations.

Name	Value	Resolution	Type	Source
Global horizontal irradiance (GHI)	Continuous	30 min	Linear interpolation	SARAH-2.1
Ambient temperature	Continuous	15 min		AMMA
Wind speed	Continuous	15 min		AMMA
Tilting angle	Latitude			Definition
Orientation	South			Definition
Cell material			Silicon	Definition
No. of modules	11			Definition
Inverter			SMA 2500U	Definition

Table 3. Statistical and fitting parameters of PV yield correlation.

Temperature level	$T \leq 30\,^{\circ}\mathrm{C}$	$30\,^{\circ}\mathrm{C} < T \leq 35\,^{\circ}\mathrm{C}$	$T \geq 35\,^{\circ}\mathrm{C}$
RMSE ($\mathrm{kWh\,kWp^{-1}}$)	0.16	0.25	0.18
R^2	0.98	0.89	0.78
N	5244	1890	474
a_i ($\mathrm{hm^2\,Wp^{-1}}$)	0.018	0.018	0.017
b_i ($\mathrm{kWh\,kWp^{-1}}$)	−0.04	−0.09	0

$5\,\mathrm{W\,m^{-2}}$ for GHI). However, there is currently no BSRN station running in West Africa; therefore, we use ground-based measurements of the GHI from the AMMA campaign at three sites for the satellite data validation (see Table 1). The comparison of the SARAH-2.1 GHI with the observed GHI is conducted for daily and monthly means (see Fig. 4). Statistical parameters, i.e., R^2, root mean square error (RMSE), MAE and bias, are used for comparison.

In Banizoumbou (Fig. 4b; MAE of $15.8\,\mathrm{W\,m^{-2}}$ for daily and $7.6\,\mathrm{W\,m^{-2}}$ for monthly means), the SARAH-2.1 performance is consistent with a previous evaluation against BSRN stations (Pfeifroth et al., 2019b). Similarly, the bias of −0.9 % to −1.2 %, the R^2 of around 0.8, and the RMSE of $20.1\,\mathrm{W\,m^{-2}}$ for the daily mean GHI and $9.5\,\mathrm{W\,m^{-2}}$ for the monthly mean GHI are of the same order of magnitude as those found by Pfeifroth et al. (2019b). However, the GHI is overestimated at the two other sites (bias of up to 12 %). At the desert site (Agoufou), the R^2 is only 0.5 for the monthly mean GHI. Due to the sandy environment, dust deposition on the measurement equipment might have caused errors in the GHI observations (measurement uncertainties are 2 % in Banizoumbou and Djougou and 10 % in Agoufou). Furthermore, the measurement equipment instrument maintenance is unknown and could be a source of additional uncertainty. In Djougou (savanna site), the overestimation is comparably high with a bias of 12 % and an MAE of over $25\,\mathrm{W\,m^{-2}}$. The monthly mean GHI values generally show higher accuracy, as the variability is reduced due to averaging.

The three sites provide evidence of a higher MAE in West Africa (up to $27.6\,\mathrm{W\,m^{-2}}$) compared with the validation with mainly European BSRN stations in Pfeifroth et al. (2019b) (MAE: $11.7\,\mathrm{W\,m^{-2}}$) for the daily GHI. One reason for this deviation could be the generally higher GHI in West Africa (Solargis, 2019) compared with Europe (where most of the BSRN stations used are located). Furthermore, higher aerosol loads, which are not explicitly treated in the satellite retrieval, in West Africa compared with the rest of the world could also cause the deviation.

To study whether deviations from the climatological AOD used in SARAH-2.1 (see Fig. 1d) might explain the deviation, we investigate the impact of the difference between the measured AOD and the climatological AOD for the satellite data retrieval (ΔAOD). A higher overestimation of the GHI was found at higher ΔAOD at all sites (up to $100\,\mathrm{W\,m^{-2}}$ for $1 < \Delta\mathrm{AOD} < 2$; see Fig. 4, the colors in scatter plots and the right column). Therefore, the correlation between ΔAOD and ΔGHI (the latter being the difference between the observed and satellite GHI) shows an overall overestimation at higher ΔAOD in Agoufou and Djougou, whereas an underestimation is visible in some situations in Banizoumbou. The absence of a systematic effect raises our confidence in the use of satellite data to provide an overview of PV potential in West Africa.

As the climatological AOD used in the SARAH-2.1 retrieval shows values between 0.15 and 0.3 (see Fig. 1d), high ΔAOD (e.g., values above 0.5) are connected to high aerosol loads (e.g., dust outbreaks and biomass burning; Marticorena et al., 2011). Thus, the missing explicit treatment of AOD in the satellite retrieval could be a reason for the low accuracy here. Especially during events with high aerosol loads, an explicit treatment in the SARAH-2.1 data retrieval could improve the accuracy of the GHI. Using only values with $\Delta\mathrm{AOD} < 0.5$, the RMSE is reduced by around 1 % to 30 % (Agoufou: 29 % for daily and 25 % for monthly GHI; Banizoumbou: 6 % for daily and 1 % for monthly GHI; Djougou: 13 % for daily and 30 % for monthly GHI).

Ineichen (2010) compared the ground-based measured GHI to different satellite products in Africa for the single year of 2006, including several AMMA sites in West Africa, and found standard deviations between 12 % and 37 % as well as a bias between −1 % and 11 %. These values lie within a similar range to our calculations. However,

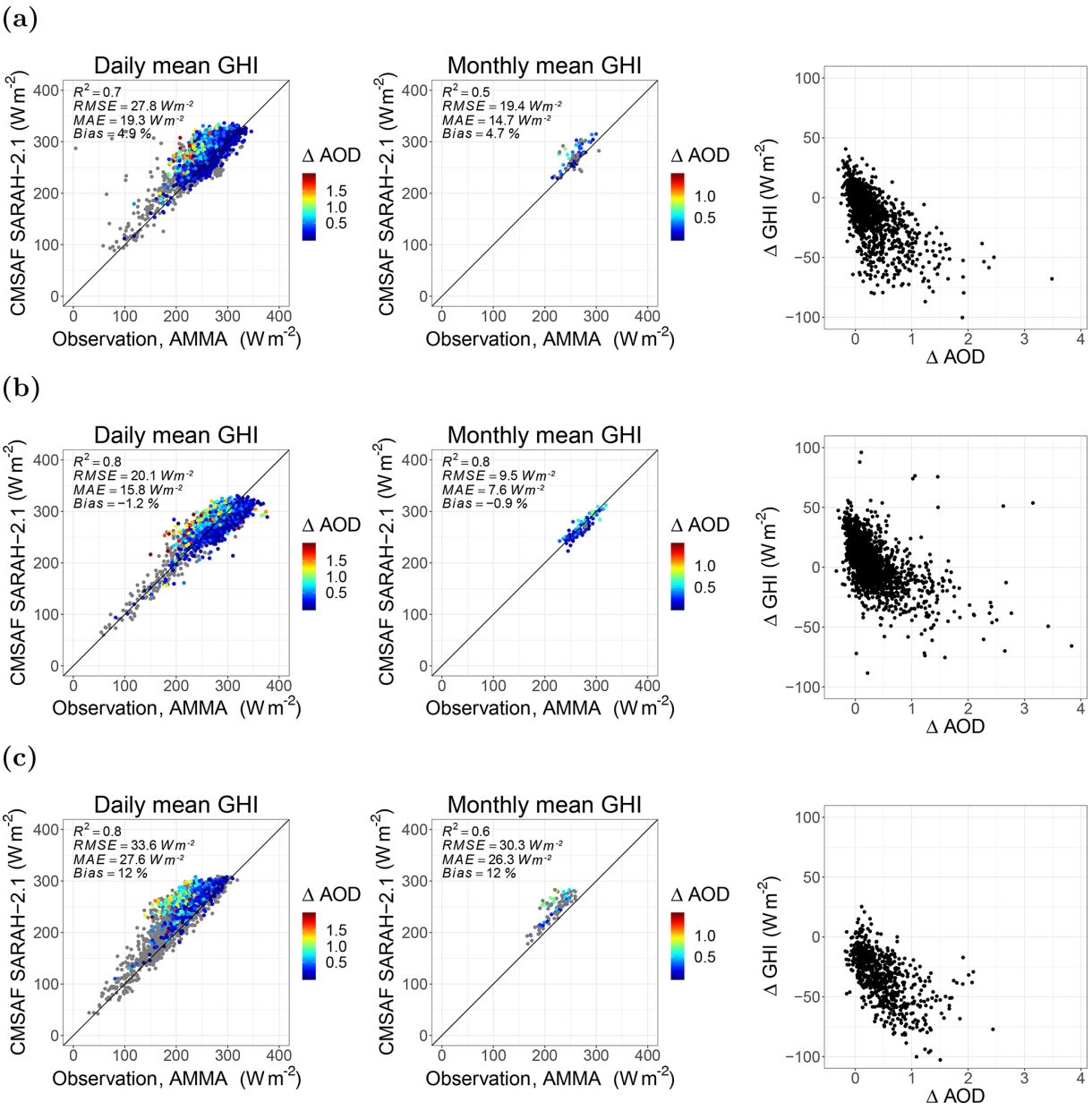

Figure 4. Comparison of the simulated and observed GHI as daily (left column) and monthly (middle column) averages at three sites over the given time horizon: **(a)** Agoufou (2005–2008), **(b)** Banizoumbou (2005–2012) and **(c)** Djougou (2002–2009). The difference between the measured AOD and the climatological AOD for the satellite data retrieval (ΔAOD) is indicated using color. If no measured AOD is available, the points are gray. The third column shows the correlation between ΔAOD and ΔGHI (ΔGHI refers to the observed GHI minus the satellite GHI).

especially during the West African summer monsoon, low-level clouds are likely not realistically represented in satellite products and climate models in southern West Africa (Hannak et al., 2017; Linden et al., 2015). Hannak et al. (2017) found an overestimation of the GHI of up to 50 W m^{-2} in the rainy season (July–September) for SARAH-1 data in comparison with measurements in southern West Africa between 1983 and 2008. In Kothe et al. (2017), monthly sums of sunshine duration from SARAH-2 (1983–2015) were compared to Global Climate Data (CLIMAT) (Deutscher Wetterdienst, 2019) in Europe and Africa. At several stations in West Africa, they found an overestimation of more than 50 h of satellite-based monthly sunshine duration compared with CLIMAT. The majority of the CLIMAT stations are located on the southern edge of the Sahel region or south of it. Thus, the findings are especially relevant for southern West Africa. Pfeifroth et al. (2019b) analyzed the accuracy of the SARAH-2 data record for

Europe and found a slight decadal but stable trend of $-0.8\,\mathrm{W\,m^{-2}}$.

Given these results, we conclude that the SARAH-2.1 data record can be used to get an overview of the temporal and spatial irradiance variability as well as an overview of trends in order to estimate the PV potential in West Africa. However, especially in southern West Africa, the systematical overestimation of solar irradiance in the SARAH-2.1 data set (Kniffka et al., 2019; Hannak et al., 2017) needs to be considered in the conclusions of the variability and trend analysis. As a consequence of the positive offset in southern West Africa, the actual north–south gradient in the satellite data set is underestimated. In particular, the systematic offset would not have an impact on the trend analysis. Overall, an expansion of measurements over longer time periods (the measured data are available for less than 20 % of the time period and at only three sites) could increase the significance of our validation.

5 Changes in solar irradiance

In this section, the temporal and spatial variability in the GHI and DIR is analyzed for West Africa (latitude from 3 to 20° N and longitude from 20° W to 16° E) over a 35-year time period (1983–2017). Therefore, the temporal mean and its interquartile range (IQR; identifying the range for 50 % of the data with the 25 % and 75 % quantile as borders) are derived. The analysis is conducted based on the daily values. For GHI, the analysis is expanded for the respective dry and the wet seasons. Furthermore, a trend analysis is undertaken for the GHI by assuming a simple linear trend based on annual values. The significance of the trend is checked by calculating the 95 % confidence interval. The trends are significantly positive (negative) if the upper and lower value of the 95 % confidence interval are positive (negative). At four locations, distributed over different latitudes, a time series analysis is additionally undertaken. Monthly means and monthly anomalies are derived for all seasons separately.

5.1 Spatial analysis

The spatial distribution of the annual mean GHI and DIR are shown in Fig. 5. For each grid point, the IQR of all daily mean values is also provided for the GHI and DIR.

The irradiance is high in the Sahel zone and the Sahara (with a GHI $> 250\,\mathrm{W\,m^{-2}}$ and a DIR of around $200\,\mathrm{W\,m^{-2}}$ north of around 13° N; see Fig. 5a and b). Towards the southern coast the irradiance decreases as the cloud cover increases (see Fig. 1b). The impact of clouds seems to be especially high in southern West Africa, south of the Sahel zone. However, the satellite-retrieved GHI might even be overestimated in this region (see Sect. 4). The temporal variability is higher in southern West Africa (locally up to $150\,\mathrm{W\,m^{-2}}$) than in the Sahara and the Sahel zone (higher IQR in the south compared with the north), especially for the DIR in coastal or mountainous regions, and is typical for variable cloud conditions. The impact of clouds on the DIR is higher than on the GHI, as forward-scattered light on cloud droplets is still included in the GHI but not in the DIR. The high amount of water vapor in coastal regions could favor the formation of clouds and could, therefore, be a reason for the higher variability in the DIR. Furthermore, the wet season is actually longer in southern West Africa than in the northern regions (CLISS, 2016), which leads to longer periods with high cloud cover that could be further favored by orographic cloud development (see Fig. 1b). However, the same analysis with a more confined definition of seasons (the dry season from November to March and the wet season from May to August) leads to similar results.

When looking at the dry and wet seasons separately, the spatial GHI distribution reveals a complementary structure (see Fig. 6; including the difference in the temporal IQR).

For the GHI, a sharp line at around 13 to 14° N divides the northern region of the Sahel zone and the Sahara from southern West Africa. North of this line, the GHI is lower than the annual mean (up to $-26\,\mathrm{W\,m^{-2}}$) during the dry season and higher (up to $+36\,\mathrm{W\,m^{-2}}$) during the wet season. The northern region experiences low cloudiness throughout the year (the mean effective cloud albedo is lower than 0.1 in the major part of this region; see Fig. 1b). Therefore, the irradiance mainly depends on the solar zenith angle, which is lower during the wet season than during the dry season. Lower solar zenith angles result in higher surface irradiance under clear-sky conditions. In southern West Africa (south of 13° N), the GHI is higher (up to $+33\,\mathrm{W\,m^{-2}}$) during the dry season and lower (up to $-46\,\mathrm{W\,m^{-2}}$) during the wet season, compared with the annual mean. Cloudiness is comparably high in this region (with a mean effective cloud albedo of up to 0.3; see Fig. 1b). Therefore, clouds are the major modulator of solar irradiance in this area. As clouds predominantly occur during the wet season, the GHI is lower during this season.

The difference in the temporal variability is given as the difference in the IQR (season – annual mean). During the dry season, the temporal variability in the GHI shows an overall reduction over land compared with the annual mean. However, in southern West Africa the reduction reaches more than $-50\,\mathrm{W\,m^{-2}}$, whereas the reduction is hardly visible in the northern regions. During the wet season, the temporal variability in the GHI shows the same sharp boundary at around 13 to 14° N as the GHI. The temporal variability is lower (reaching more than a $-50\,\mathrm{W\,m^{-2}}$ difference) in northern West Africa and higher (reaching more than a $+50\,\mathrm{W\,m^{-2}}$ difference) in southern West Africa compared with the annual mean. This variability is mainly driven by the WAM, which occurs during the wet season (Sultan et al., 2003).

The regional mean and its IQR (concerning the spatial variability) for the GHI and DIR are summarized in Table 4.

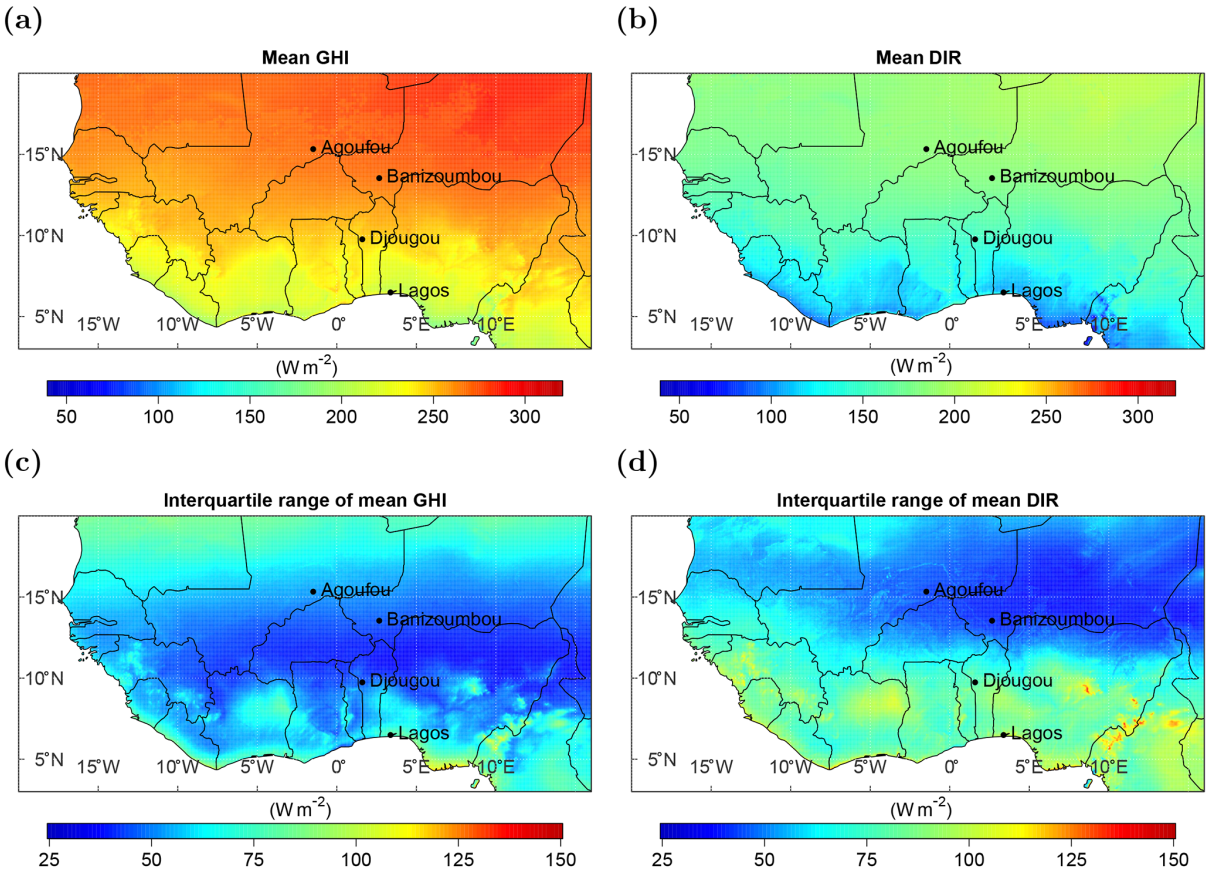

Figure 5. Mean (1983–2017) global horizontal irradiance **(a)** and direct horizontal irradiance **(b)** with their respective temporal interquartile ranges given in panels **(c)** and **(d)**.

Table 4. Regional mean and regional interquartile range (IQR) of the temporal mean GHI and DIR between 1983 and 2017 for the annual mean, the dry season and the wet season.

	Annual mean		Dry season		Wet season	
	Mean	IQR	Mean	IQR	Mean	IQR
GHI ($W m^{-2}$)	250	37	254	20	246	67
DIR ($W m^{-2}$)	159	45	169	34	145	68

The regional variability in the solar irradiance is higher during the wet season than in the dry season, as clouds, which predominantly occur during the wet season, have a large impact on solar radiation. During the wet season, the regional variability of the GHI is within a similar range to that of the DIR, with an IQR of 67 $W m^{-2}$ for the GHI and 68 $W m^{-2}$ for the DIR. As the mean DIR is smaller than the mean GHI, the percentage variability is higher for the DIR. This is a clear sign that variable cloudiness leads to a higher variability in diffuse irradiance.

5.2 Temporal analysis

The results show strong gradients between the north and south as well as between the wet and the dry season. To detect anomalies and changes in variability along the north–south axis, four locations are chosen for a time series analysis of the SARAH-2.1 data record (the three measuring sites from Sect. 4 and one coastal location – Lagos, Nigeria, 6.5° N, 3.4° E; see Fig. 7). The respective data record (see Sect. 2.1) is used between 1983 and 2017 at a daily resolution.

The median GHI and DIR decline with decreasing latitude (see also Fig. 7), while their variability increases with decreasing latitude (as the IQR increases). The higher frequency of clouds in southern West Africa likely drives this variability. At the desert and Sahel locations (Agoufou and Banizoumbou), the IQR of the GHI is larger than the IQR of DIR. Thus, the variability in the north is higher for the GHI than for the DIR, whereas the inverse is found at the southern locations (Djougou and Lagos).

For a more detailed representation, time series of the monthly mean GHI and DIR and their anomalies for the four locations are shown in Fig. 8. At the southernmost location (Lagos) the trends in anomalies are similar for the wet and

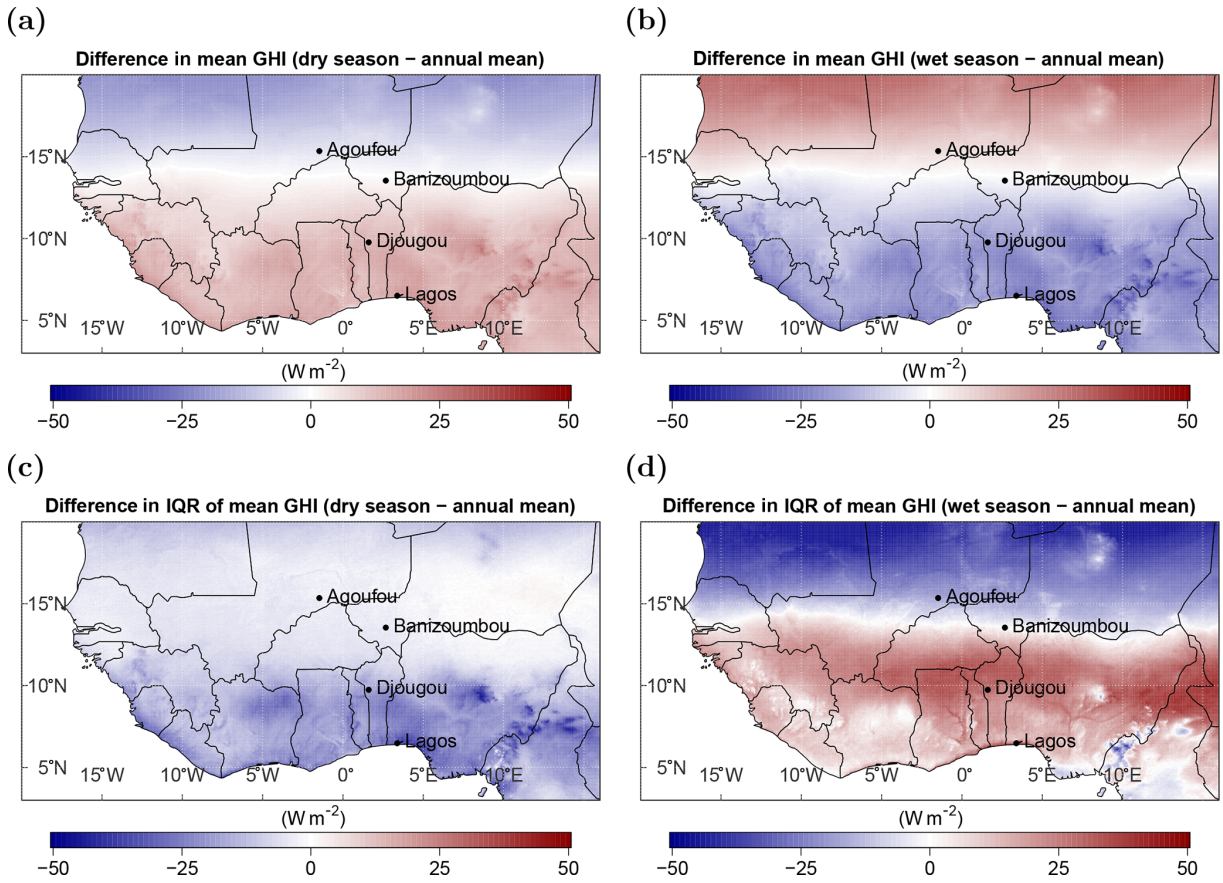

Figure 6. The difference between the mean annual GHI and the mean seasonal GHI during the dry season **(a)** and the wet season **(b)**, and the difference in their respective interquartile ranges **(c, d)**.

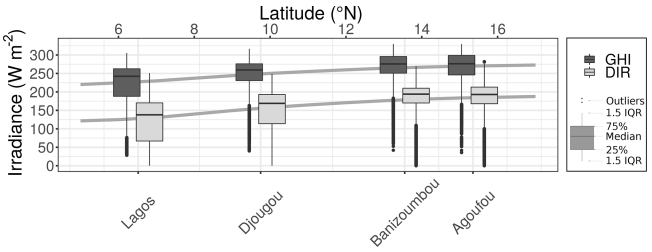

Figure 7. Median daily global (dark gray) and direct horizontal irradiance (light gray) from the SARAH-2.1 data set at Agoufou, Mali; Banizoumbou, Niger; Djougou, Benin; and Lagos, Nigeria as a function of latitude. The variability is illustrated by the box plots, showing the interquartile range and whiskers. The gray line connects the mean GHI (top) and DIR (bottom) over each latitude of the study region.

the dry seasons (negative trend of $-1.8\,\mathrm{W\,m^{-2}}$ per decade). At all of the other locations, the dry season anomalies are rather constant (showing no significance), whereas the wet season anomalies show decreasing significant trends (ranging from -2 to $-2.9\,\mathrm{W\,m^{-2}}$ per decade) which provides a significant trend over the full year for Agoufou, Djougou and Lagos. For all of the locations, no significant partition can be seen for the change from Meteosat first- to second-generation satellites in 2005.

As long-term changes in climate conditions (e.g., temperature and precipitation) have been found over the entire region (Barry et al., 2018), the trends in global irradiance over the last 35 years are analyzed (see Fig. 9) because they are of high importance for a future PV system. Especially during the wet season, mean temperature increased along the coast between 1983 and 2010 (Yaro and Hesselberg, 2016). The general positive trend in temperature over the region (of up to 0.22° per decade) can also be found in the ERA5 data.

Trends in the GHI during the time period from 1983 to 2017 are positive in the West African Sahara and negative south of the Sahel zone. By looking at the respective dry and wet seasons, the major part of the negative trend can be attributed to the wet season. The positive trend mainly occurs during the dry season. Overall, the decadal trends are small (in the range of 1 %–2 % per decade) compared with the absolute surface irradiance and the IQR. However, the absolute values of the trend reach around $\pm 5\,\mathrm{W\,m^{-2}}$ per decade and are significant (based on the 95 % confidence

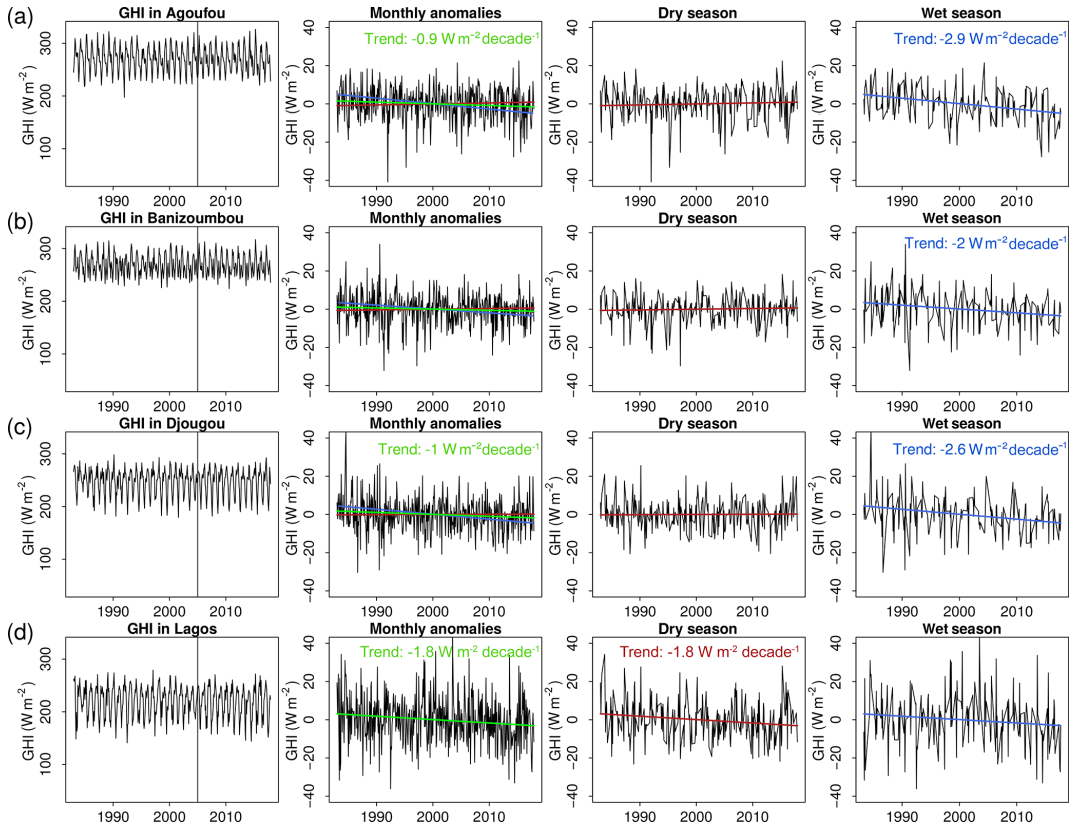

Figure 8. Satellite-based time series of monthly mean global horizontal irradiance and their monthly anomalies and trends for the annual mean (green), the dry season (red) and the wet (blue) season in Agoufou **(a)**, Banizoumbou **(b)**, Djougou **(c)** and Lagos **(d)**. The linear trend in the anomalies is shown monthly as well as for the respective dry and wet seasons. Trends are quantified in the single plot windows if they are significant (p value < 0.05). The black vertical line indicates the change from the Meteosat first- to second-generation satellites.

interval). Compared with the uncertainties of the satellite data (MAE of up to 27.6 W m^{-2}; see Sect. 4), the trends might seem negligible. However, the reported uncertainties are not bias corrected, and they represent, in particular in the case of Djougou, the systematic overestimation of the GHI by the satellite estimate. The estimation of the temporal trend is unaffected by any systematic over- or underestimation; hence, it can still be derived with certain confidence.

The negative trend south from the Sahel region indicates increasing cloud cover or a higher amount of water vapor in the air. Especially low-level clouds are frequent during the wet season in southern West Africa (Linden et al., 2015). These clouds were analyzed during the Dynamics–Aerosol–Chemistry–Cloud Interactions in West Africa (DACCIWA) campaign in 2016 (Knippertz et al., 2015). They form at night and are present during the day with a peak in cloudiness in the mornings. Local aerosols can increase the cloud droplet number concentration by 13 %–22 % (Taylor et al., 2019), brightening the clouds and reducing the GHI. The southern regions of West Africa have been affected by agricultural expansion and urbanization over the last few decades (CLISS, 2016). This leads to a higher portion of local aerosols in the atmosphere that can serve as cloud condensation nuclei and foster cloud formation and cloud optical properties. Furthermore, a positive trend in water vapor was found on the coast of tropical oceans in West Africa from satellite data (Mears et al., 2018), which would reduce the GHI at the surface.

The positive trend in irradiance in the Sahara might be driven by the reduction in the movement of dust, which has been found in several data sets since the 1980s (Cowie et al., 2013). Furthermore, a reduction in cloudiness could be a reason for the increasing irradiance.

The detected trends are within the range of global dimming and brightening tendencies (-9 to $+4$ W m^{-2} per decade), which originate from atmospheric changes (that are caused by factors such as anthropogenic pollution and are visible due to aerosol variation and aerosol–cloud interactions; Wild, 2012). The abovementioned trends in cloud occurrence could be driven by a change in the WAM, the Hadley cell circulation and water vapor as well as the shift of the ITCZ (Byrne et al., 2018; Roehrig et al., 2013). Furthermore, aerosols can also play a decisive role. As mentioned before, aerosols are highly variable in the West

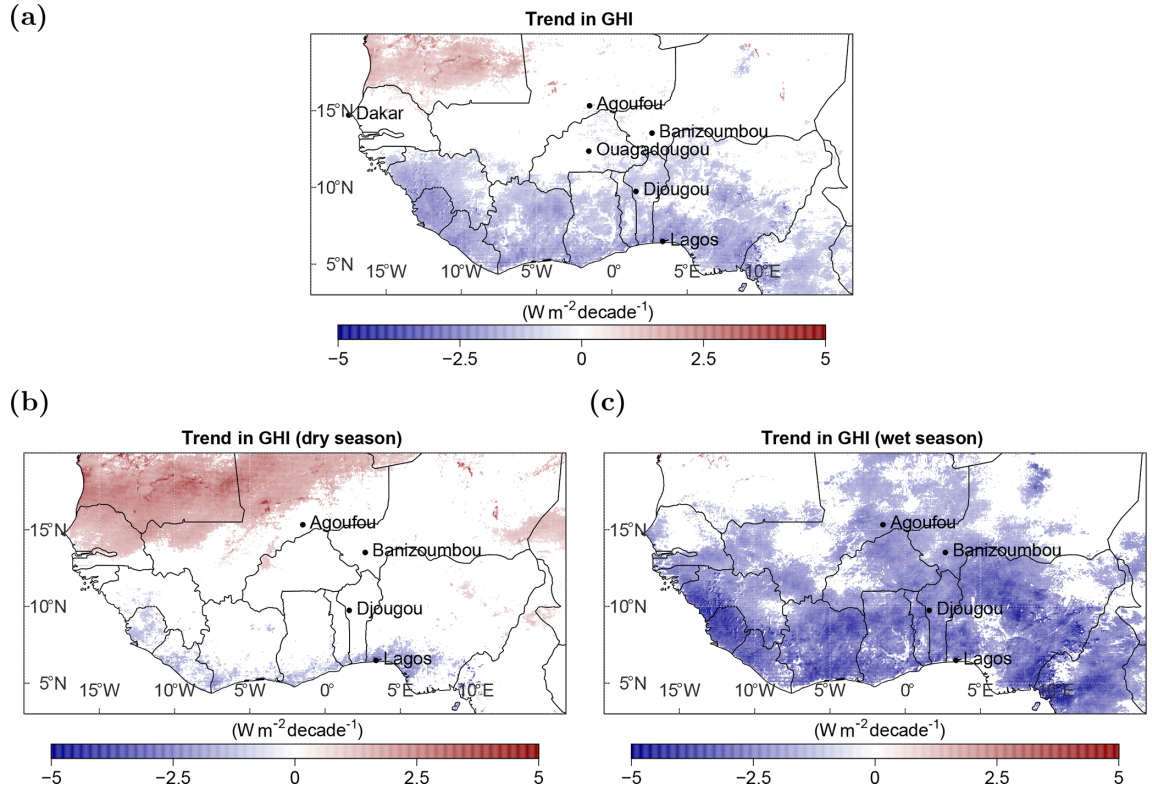

Figure 9. Linear trend for the annual mean global irradiance **(a)** and the global irradiance in the dry **(b)** and wet seasons **(c)** for all significant cases (based on the 95 % confidence interval). Ouagadougou (Burkina Faso) and Dakar (Senegal) are additionally visualized here, as values at these locations are compared within this section.

African region and can reach extreme values (AOD up to 4). Aerosols are not treated explicitly in the satellite retrievals; therefore, their variability can cause high uncertainties in the trend analysis, especially during the dry season, when clouds are mostly absent and aerosols are the major modulator of the GHI. Furthermore, in West Africa, different aerosol types are present in the atmosphere (e.g., dust, marine, anthropogenic and biomass burning aerosols), which differ in their atmospheric impact on the GHI (absorption and scattering as well as spectral dependence). However, Neher et al. (2019) found that the impact of the AOD is around 4 times higher than the impact of the aerosol composition on PV power in West Africa. Yoon et al. (2012) reported a negative trend in AOD for Dakar in Senegal (1996–2009) and Ouagadougou in Burkina Faso (1995–2007) and a positive trend in Banizoumbou in Niger (1995–2009). The detected trends in the GHI from SARAH-2.1 data (1983–2017) at these locations are negative in Banizoumbou and positive in Dakar. Thus, changes in aerosols could be a major driver of trends in the GHI. However, the trend in the GHI is negative in Ouagadougou; thus, other meteorological changes, such as clouds, might be larger than the trend in AOD. In general, trend analysis is a complex topic. However, a clear regional distribution might enable us to better identify the causes of trends when looking at PV power.

6 Implications for photovoltaic yields

Photovoltaic yields are calculated for each day over the whole region using a linear model (Eq. 5) with the parameters derived in Sect. 3.2 for each temperature range (see Fig. 10 for mean PV yields and temporal IQR). The temperature level is taken from ERA5 as daily means. As we used a linear approach, the uncertainty in the satellite data would propagate linearly for PV yield estimates.

As a result of using a linear regression to derive the PV yields, the temporal variability in the PV yields (mean: 4.9 kWh kWp^{-1}; IQR: 20 %) is lower than the temporal variability in the GHI (mean: 250 W m^{-2}; IQR: 24 %). However, the regional variability is 3 percentage points higher for PV yields (IQR: 18 %) than for the GHI (IQR: 15 %). Here, we go a step further and analyze the regional variability over each latitude (in the longitude range between 4° W and 4° E to exclude ocean regions), annually as well as for the respective dry and wet seasons. Figure 11 shows the variability in the temporal mean PV yield for each latitude separately.

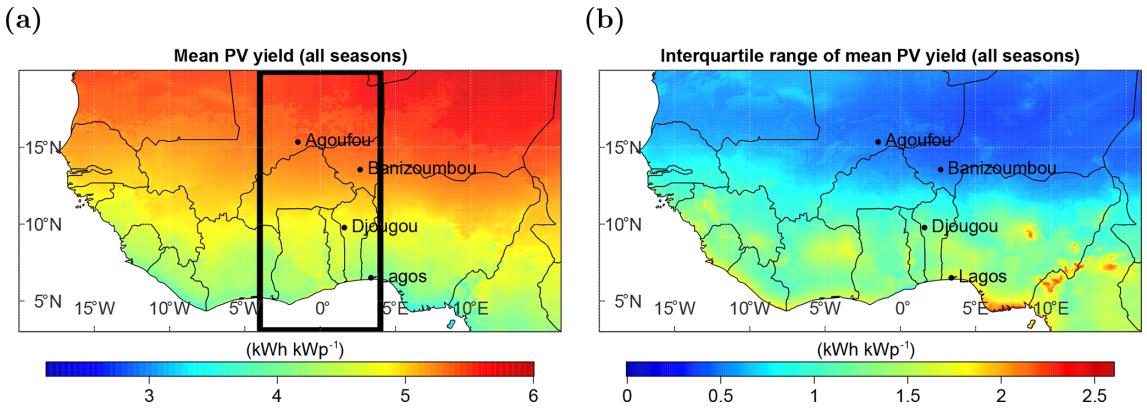

Figure 10. The annual mean (1983–2017) PV yield **(a)** and its interquartile range **(b)** over the full region. The black box in **(a)** marks the longitude range for Fig. 11.

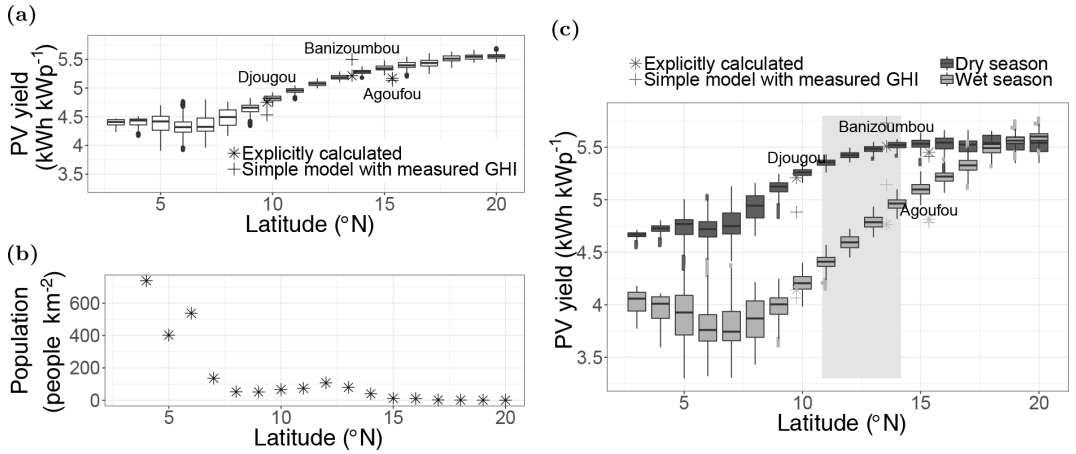

Figure 11. (a) Mean (temporal) PV yield at each latitude for the total year, (**b**) population density for each latitude (NASA, 2020), and **(c)** mean PV yield at each latitude for the dry season (October–April; light gray) and the wet season (May–September; dark gray) in the longitude range between 4° W and 4° E. The single points mark the temporal mean PV yield calculated with the explicit model and the measured ambient temperature (star) as well as the PV yield calculated with the simple model and the measured GHI (cross) at the three sites: Agoufou (2005–2008), Banizoumbou (2005–2012) and Djougou (2002–2009). The gray background box in **(c)** marks the latitude range where the definition of seasons is most accurate.

The explicitly calculated PV yields at Banizoumbou and Djougou lie within the variability range of the corresponding latitude, demonstrating the appropriateness of the simplified model for PV calculations. However, the most northern site, Agoufou, is lower than the daily modeled data at 15° N. A possible reason for this might be the high temperatures encountered here. The uncertainties of the linear model are highest for high temperatures (RMSE: 0.67 kWh kWp^{-1}; see Table 3). In the northern part of West Africa the monthly mean temperature can reach more then 40 °C (Berrisford et al., 2011). Thus, the PV yields at high latitudes could actually be lower. Furthermore, the PV yield at each site is calculated with ground-based measured temperatures, whereas the model uses daily temperatures from ERA5. At Agoufou, the averaged daily mean of the ground-based temperature over the total time span is around 3.5 °C higher than the mean ERA5 temperature.

In general, the overestimation of satellite data in Agoufou and Djougou as well as the slight underestimation in Banizoumbou (see Sect. 4) can be seen in the PV yields calculated with the simple model and using the measured GHI as an input (crosses in Fig. 11a). In Agoufou, the PV yields, calculated with the linear model, are similar to the explicitly calculated PV yields. In Banizoumbou, the results are higher than the PV yields calculated with satellite data, whereas they are lower in Djougou. Especially in Djougou, the irradiance decreases over the 35 years of satellite data availability; this leads to lower values in the 2000s compared with the mean.

By looking at the full latitude range, PV yields are smaller at low latitudes (around 4.5 kWh kWp^{-1}) with a higher

regional variability and more outliers. At high latitudes, the PV yields reach around 5.5 kWh kWp^{-1}, which is around 22 % higher than at low latitudes. Furthermore, an overestimation of solar irradiance was found in southern West Africa (see Sect. 4). Thus, the spacial gradient between north and south could actually be higher than that suggested by the satellite estimation. The population density shows an inverse latitudinal gradient to the PV potential, with a higher density at low latitudes and a lower density at high latitudes (see Fig. 11b).

During the dry season, the PV yields are similarly spread over different latitudes to the annual PV yields. However, the yields are slightly higher (by around 0.25 kWh kWp^{-1}) at low latitudes (between 3 and 10° N). During the wet season, a band of lower PV yields (less than 4 kWh kWp^{-1}) is visible between 3 and 9° N; this is the region where low-level clouds frequently occur (Linden et al., 2015).

7 Challenges for the West African power sector

Currently, a deficit exists between power demand and supply in West African countries (Adeoye and Spataru, 2018). Furthermore, the power demand may increase 5-fold by 2030 compared with the demand in 2013 (IRENA, 2015). Thus, new large-scale power plants need to be developed and current infrastructure needs to be advanced. The West African Power Pool (WAPP) was founded in 1999 to coordinate these developments. The WAPP business plan outlines the connection of 14 countries with respect to high-voltage transmission by 2025 (WAPP, 2015). Specifically, photovoltaic (PV) power is set to expand, with a technical potential of around 100 PWh yr^{-1} (Hermann et al., 2014), and there are high expectations that it will meet a large share of the future power supply (IRENA, 2015). Therefore, long-term changes in PV power potential are relevant and are addressed in this study.

Solar irradiance is the key driver of photovoltaic power potential. The dimension and development of new power plants requires a specific site analysis of solar irradiance to estimate expected economic benefits. Therefore, long-term changes and day-to-day variability need to be taken into account to dimension the plant, the necessary storage capacities and to design the grid. In this study, 35 years of satellite-based irradiance data (the SARAH-2.1 data record) is locally validated and used to get a spatially complete distribution of the photovoltaic potential over West Africa (3 to 20° N and 20° W to 16° E).

In summary and as expected, there is a strong contrast in the photovoltaic potential during the dry and wet seasons, which is controlled by the West African monsoon (WAM) and the accompanying seasonal movement of the intertropical convergence zone. The dry season provides higher photovoltaic yields than the wet season, especially in southern West Africa (around 4.75 kWh kWp^{-1} in the dry season down to 3.75 kWh kWp^{-1} in the wet season). Furthermore, a strong contrast can be seen between the higher potential in the northern regions of West Africa (up to 5.5 kWh kWp^{-1}) and the lower potential in the southern regions of West Africa (around 4.5 kWh kWp^{-1}). The temporal variability is higher in the south and lower in the north as a result of the WAM. Generally, the variability is more pronounced for the photovoltaic potential than for the global horizontal irradiance, as additional impacts of the inverter reduce the yields of a PV power plant by a certain threshold.

In the Sahara and Sahel zone, the daily average global horizontal irradiance reaches up to 300 W m^{-2} and shows a positive trend of up to around +5 W m^{-2} per decade. An inverse trend (with up to around -5 W m^{-2} per decade) and lower irradiance is found in southern West Africa, with a daily average global horizontal irradiance below 250 W m^{-2}. These trends lie within the range of global dimming and brightening tendencies. Furthermore, the temporal variability is higher in southern West Africa (reaching an IQR of up to 150 W m^{-2} in mountainous areas) than in the Sahara and Sahel zone (where the IQR remains below 100 W m^{-2}). With respect to the direct horizontal irradiance, the difference between northern and southern West Africa is similar to the difference in the global horizontal irradiance. However, especially in the mountainous region in Nigeria, the temporal variability is more distinct for direct horizontal irradiance than for global horizontal irradiance.

Regarding seasons, there is a sharp difference between the wet and the dry seasons. During the dry season, the average solar irradiance and its IQR are rather constant (a global irradiance of around 254 W m^{-2} and an IQR of around 20 W m^{-2}), whereas the average solar irradiance varies over the region during the wet season (with higher values in the north than in the south and an IQR of around 67 W m^{-2}). Compared with the annual values, the dry season provides a higher global horizontal irradiance in the south and a lower global horizontal irradiance in the north, whereas the opposite was found during the wet season. Therefore a dividing line can be drawn at about 13° N to separate the south from the north with respect to the daily variability. This seasonal shift is particularly visible at low latitudes (higher urban density than at high latitudes). This seasonality is dominated by high cloudiness caused by the moist monsoon winds from the southwest during the wet season and the dry Harmattan winds from the northeast during the dry season. To overcome such seasonal differences in power generation, a smart combination with other power sources (e.g., hydropower and wind) is necessary to reduce storage capacity requirements (Sterl et al., 2020) and related costs for long-term storage.

By looking at the abovementioned characteristics, the development of PV power plants is more likely in northern West Africa, as higher yields can be reached. However, more power is consumed in the southern parts of West Africa,

close to the coast, where the population is higher. Therefore, power generation in the north would reiterate the necessity of grid development along a north–south axis to transport power from the insolation-rich Sahara to urban regions in the south. Larger investments in PV systems in the south would instead evoke the development of large storage capacities to compensate for fluctuations in PV power generation due to the higher variability in solar irradiance in the south than in the Sahel zone and the Sahara. The difference in the north–south potential has increased over the last 35 years. If this trend is ongoing in the future, the potential PV power in southern and northern West Africa might differ even more. This should be considered in future grid planing.

Besides the constant seasonal and intra-day variability, extreme events can affect power generation drastically. Major dust outbreaks frequently occur during the dry season in the Sahara and the Sahel zone and can cause reductions in power generation of up to 79 % over several days (Neher et al., 2019). For such events, storage capacities for several days might be needed (e.g., in solely solar-based micro grids).

This analysis provides an overview of the photovoltaic potential in West Africa. However, the explicit modeling of a photovoltaic power module at a higher temporal resolution could better resolve the impact of temperature and the inverter for each grid point. Furthermore, to explicitly dimension the grid and the storage capacity required, a demand–supply power model that includes all available power sources is necessary. This should be subject of further research.

Data availability. The SARAH-2.1 dataset can be accessed at https://wui.cmsaf.eu/safira/action/searchProdukt (Pfeifroth et al., 2019a), https://doi.org/10.5676/EUM_SAF_CM/SARAH/V002. The AMMA dataset can be accessed at https://baobab.sedoo.fr/AMMA/ (AMMA, 2018).

Author contributions. IN performed the data analysis and was responsible for the development of the paper. JT and UP provided the CM SAF data and gave advice on the paper during the writing process. SC and SM provided the overall scientific guidance, discussed results and gave advice during the writing process.

Competing interests. The authors declare that they have no conflict of interest.

Acknowledgements. The authors would like to thank the numerous data providers. Meteorological data from the AMMA Database was used in this study. Based on a French initiative, the AMMA was built by an international scientific group and is currently funded by a large number of agencies from countries such as France, the UK, the US and Africa. It has been the beneficiary of a major financial contribution from the European Community's Sixth Framework research program. Detailed information on the scientific coordination and funding is available on the AMMA International website: http://www.amma-international.org, last access: 13 January 2020. We thank Philippe Goloub and Didier Tanre for their effort establishing and maintaining AERONET sites in Agoufou, Banizoumbou and Djougou and for providing aerosol data. The CM SAF SARAH-2.1 data record was accessed via https://www.cmsaf.eu, last access: 15 August 2019.

Financial support. This research has been supported by the Heinrich Böll Foundation though a PhD fellowship to the first author, Ina Neher.

Review statement. This paper was edited by Stelios Kazadzis and reviewed by three anonymous referees.

References

Adeoye, O. and Spataru, C.: Sustainable development of the West African Power Pool: Increasing solar energy integration and regional electricity trade, Energy. Sustain. Dev., 45, 124–134, https://doi.org/10.1016/j.esd.2018.05.007, 2018.

AERONET: Aeronet data description, available at: https://aeronet.gsfc.nasa.gov/new_web/data_description_AOD_V2.html (last access: 2 February 2019), 2014.

AMMA: AMMA database, available at: https://baobab.sedoo.fr/AMMA/ (last access: 13 January 2020), 2018.

Barry, A. A., Caesar, J., Klein Tank, A. M., Aguilar, E., McSweeney, C., Cyrille, A. M., Nikiema, M. P., Narcisse, K. B., Sima, F., Stafford, G., Touray, L. M., Ayilari-Naa, J. A., Mendes, C. L., Tounkara, M., Gar-Glahn, E. V., Coulibaly, M. S., Dieh, M. F., Mouhaimouni, M., Oyegade, J. A., Sambou, E., and Laogbessi, E. T.: West Africa climate extremes and climate change indices, Int. J. Climatol., 38, e921–e938, https://doi.org/10.1002/joc.5420, 2018.

Berrisford, P., Dee, D., Fielding, K., Fuentes, M., Kallberg, P., Kobayashi, S., and Uppala, S.: The ERA-Interim Archive Version 2.0, Tech. rep., European Centre for Medium Range Weather Forecasts, available at: https://www.ecmwf.int/node/8174 (last access: 2 January 2020), 2011.

Byrne, M. P., Pendergrass, A. G., Rapp, A. D., and Wodzicki, K. R.: Response of the Intertropical Convergence Zone to Climate Change: Location, Width, and Strength, Curr. Clim. Change Rep., 4, 355–370, https://doi.org/10.1007/s40641-018-0110-5, 2018.

Campbell Scientific: CNR1, CNR1-L - Solar and Far Infrared Radiation Balance Radiaometers, Tech. rep., Campbel Scientific, 2010.

CLISS: Landscapes of west africa - A Window on a changing world, Tech. rep., U.S. Geological Survey EROS, 47914 252nd St, Garretson, SD 57030, United States, 2016.

Copernicus Climate Change Service (C3S): ERA5: Fifth generation of ECMWF atmospheric reanalyses of the global climate, Copernicus Climate Change Service Climate Data Store (CDS), available at: https://cds.climate.copernicus.eu/cdsapp#/home (last access: 6 January 2020), 2017.

Cowie, S. M., Knippertz, P., and Marsham, J. H.: Are vegetation-related roughness changes the cause of the recent decrease in dust emission from the Sahel?, Geophys. Res. Lett., 40, 1868–1872, https://doi.org/10.1002/grl.50273, 2013.

Cowie, S. M., Knippertz, P., and Marsham, J. H.: A climatology of dust emission events from northern Africa using long-term surface observations, Atmos. Chem. Phys., 14, 8579–8597, https://doi.org/10.5194/acp-14-8579-2014, 2014.

Deutscher Wetterdienst: Global Climate Data, available at: https://www.dwd.de/EN/ourservices/climat/climat.html (last access: 14 June 2019), 2019.

ECOWAS: Project Information Document/Integrated Safeguards Data Sheet (PID/ISDS), Tech. Rep. Phase 1, World Bank, 2017.

Giles, D. M., Sinyuk, A., Sorokin, M. G., Schafer, J. S., Smirnov, A., Slutsker, I., Eck, T. F., Holben, B. N., Lewis, J. R., Campbell, J. R., Welton, E. J., Korkin, S. V., and Lyapustin, A. I.: Advancements in the Aerosol Robotic Network (AERONET) Version 3 database – automated near-real-time quality control algorithm with improved cloud screening for Sun photometer aerosol optical depth (AOD) measurements, Atmos. Meas. Tech., 12, 169–209, https://doi.org/10.5194/amt-12-169-2019, 2019.

Gueymard, C. A. and Wilcox, S. M.: Assessment of spatial and temporal variability in the US solar resource from radiometric measurements and predictions from models using ground-based or satellite data, Sol. Energy, 85, 1068–1084, https://doi.org/10.1016/j.solener.2011.02.030, 2011.

Haegel, N. M., Margolis, R., Buonassisi, T., Feldman, D., Froitzheim, A., Garabedian, R., Green, M., Glunz, S., Henning, H.-m., Holder, B., Kaizuka, I., Kroposki, B., Matsubara, K., Niki, S., Sakurai, K., Schindler, R. A., Tumas, W., Weber, E. R., Wilson, G., Woodhouse, M., and Kurtz, S.: Terawatt-scale photovoltaics: Trajectories and challenges, Science, 356, 141–143, https://doi.org/10.1126/science.aal1288, 2017.

Hammer, A., Heinemann, D., Hoyer, C., Kuhlemann, R., Lorenz, E., Müller, R., and Beyer, H. G.: Solar energy assessment using remote sensing technologies, Remote Sens. Environ., 86, 423–432, https://doi.org/10.1016/S0034-4257(03)00083-X, 2003.

Hannak, L., Knippertz, P., Fink, A. H., Kniffka, A., and Pante, G.: Why do global climate models struggle to represent low-level clouds in the west african summer monsoon?, J. Climate, 30, 1665–1687, https://doi.org/10.1175/JCLI-D-16-0451.1, 2017.

Hastings, D. A. and Dunbar, P. K.: Global Land One-kilometer Base Elevation (GLOBE) Digital Elevation Model, Documentation, Tech. Rep. 34, United States Department of Commerce, National Oceanic and Atmospheric Administration, 1999.

Hermann, S., Miketa, A., and Fichaux, N.: Estimating the Renewable Energy Potential in Africa, Tech. rep., International Renewable Energy Agency, Abu Dhabi, 2014.

Hersbach, H., Bell, B., Berrisford, P., Hirahara, S., Horányi, A., Muñoz-Sabater, J., Nicolas, J., Peubey, C., Radu, R., Schepers, D., Simmons, A., Soci, C., Abdalla, S., Abellan, X., Balsamo, G., Bechtold, P., Biavati, G., Bidlot, J., Bonavita, M., De Chiara, G., Dahlgren, P., Dee, D., Diamantakis, M., Dragani, R., Flemming, J., Forbes, R., Fuentes, M., Geer, A., Haimberger, L., Healy, S., Hogan, R., Hólm, E., Janisková, M., Keeley, S., Laloyaux, P., Lopez, P., Lupu, C., Radnoti, G., de Rosnay, P., Rozum, I., Vamborg, F., Villaume, S., and Thépaut, J.-N.: The ERA5 Global Reanalysis, Q. J. R. Meteorol. Soc., 146, 1999–2049, 2020.

Holben, B., Eck, T., Slutsker, I., Tanré, D., Buis, J., Setzer, A., Vermote, E., Reagan, J., Kaufman, Y. J., Nakajima, T., Lavenu, F., Jankowiak, I., and Smirnov, A.: AERONET - A Federated Instrument Network and Data Archive for Aerosol Characterization, Remote Sens. Environ., 66, 1–16, https://doi.org/10.1016/S0034-4257(98)00031-5, 1998.

Ineichen, P.: Satellite based short wave irradiance validation over Africa Satellite based short wave irradiance validation over Africa, Tech. rep., Université de Genève, Geneva, available at: http://archive-ouverte.unige.ch/unige:23517 (last access: 16 October 2019), 2010.

IRENA: Africa 2030: Roadmap for a Renewable Energy Future, Tech. rep., IRENA, Abu Dhabi, 2015.

Ishaque, K., Salam, Z., and Taheri, H.: Accurate MATLAB Simulink PV System Simulator Based on a Two-Diode Model, J. Power Electron., 11, 179–187, https://doi.org/10.6113/JPE.2011.11.2.179, 2011.

King, D. L., Boyson, W. E., and Kratochvil, J. A.: Photovoltaic array performance model, Tech. rep., Sandia National Laboratories, https://doi.org/10.2172/919131, 2004.

Kinne, S., O'Donnel, D., Stier, P., Kloster, S., Zhang, K., Schmidt, H., Rast, S., Giorgetta, M., Eck, T. F., and Stevens, B.: MAC-v1: A new global aerosol climatology for climate studies, J. Adv. Model. Earth Sy., 5, 704–740, https://doi.org/10.1002/jame.20035, 2013.

Kipp and Zonen: SP Lite2 Silicon Pyranometer, Tech. rep., Kipp and Zonen, 2019.

Kniffka, A., Knippertz, P., and Fink, A. H.: The role of low-level clouds in the West African monsoon system, Atmos. Chem. Phys., 19, 1623–1647, https://doi.org/10.5194/acp-19-1623-2019, 2019.

Knippertz, P., Coe, H., Chiu, J. C., Evans, M. J., Fink, A. H., Kalthoff, N., Liousse, C., Mari, C., Allan, R. P., Brooks, B., Danour, S., Flamant, C., Jegede, O. O., Lohou, F., and Marsham, J. H.: The DACCIWA project: Dynamics-aerosol-chemistry-cloud interactions in West Africa, B. Am. Meteorol. Soc., 96, 1451–1460, https://doi.org/10.1175/BAMS-D-14-00108.1, 2015.

Kothe, S., Pfeifroth, U., Cremer, R., Trentmann, J., and Hollmann, R.: A satellite-based sunshine duration climate data record for Europe and Africa, Remote Sens., 9, 429, https://doi.org/10.3390/rs9050429, 2017.

Linden, R., Fink, A. H., and Redl, R.: Satellite-based climatology of low-level continental clouds in southern West Africa during the summer monsoon season, J. Geophys. Res.-Atmos., 120, 1186–1201, https://doi.org/10.1002/2014JD022614, 2015.

Marticorena, B., Haywood, J., Coe, H., Formenti, P., Liousse, C., Mallet, M., and Pelon, J.: Tropospheric aerosols over West Africa: Highlights from the AMMA international program, Atmos. Sci. Lett., 12, 19–23, https://doi.org/10.1002/asl.322, 2011.

Mears, C. A., Smith, D. K., Ricciardulli, L., Wang, J., Huelsing, H., and Wentz, F. J.: Construction and Uncertainty Estimation of a Satellite-Derived Total Precipitable Water Data Record Over the World's Oceans, Earth Space Sci., 5, 197–210, https://doi.org/10.1002/2018EA000363, 2018.

Mohr, K. I.: Interannual, monthly, and regional variability in the Wet season diurnal cycle of precipitation in sub-Saharan

Africa, J. Climate, 17, 2441–2453, https://doi.org/10.1175/1520-0442(2004)017<2441:IMARVI>2.0.CO;2, 2004.

Mueller, R., Behrendt, T., Hammer, A., and Kemper, A.: A new algorithm for the satellite-based retrieval of solar surface irradiance in spectral bands, Remote Sens., 4, 622–647, https://doi.org/10.3390/rs4030622, 2012.

Mueller, R., Pfeifroth, U., Traeger-Chatterjee, C., Trentmann, J., and Cremer, R.: Digging the METEOSAT Treasure – 3 Decades of Solar Surface Radiation, Remote Sens., 7, 8067–8101, https://doi.org/10.3390/rs70608067, 2015.

NASA: Population density, available at: https://sedac.ciesin.columbia.edu/data/set/gpw-v4-population-density-rev11/data-download (last access: 29 May 2020), 2020.

Neher, I., Buchmann, T., Crewell, S., Pospichal, B., and Meilinger, S.: Impact of atmospheric aerosols on solar power, Meteorol. Z., 28, 305–321, https://doi.org/10.1127/metz/2019/0969, 2019.

Pfeifroth, U., Sanchez-Lorenzo, A., Manara, V., Trentmann, J., and Hollmann, R.: Trends and Variability of Surface Solar Radiation in Europe Based On Surface- and Satellite-Based Data Records, J. Geophys. Res.-Atmos., 123, 1735–1754, https://doi.org/10.1002/2017JD027418, 2018.

Pfeifroth, U., Kothe, S., Trentmann, J., Hollmann, R., Fuchs, P., Kaise, J., and Werscheck, M.: Surface Radiation Data Set – Heliosat (SARAH) – Edition 2.1, Satellite Application Facility on Climate Monitoring, Offenbach, Germany, https://doi.org/10.5676/EUM_SAF_CM/SARAH/V002_01, 2019a.

Pfeifroth, U., Trentmann, J., and Kothe, S.: Validation Report: Meteosat Solar Surface Radiation and Effective Cloud Albedo Climate Data Record SARAH-2 . 1 climate data records, Tech. rep., DWD, https://doi.org/10.5676/EUM_SAF_CM/SARAH/V002, 2019b.

Redelsperger, J.-L., Thorncroft, C. D., Diedhiou, A., Lebel, T., Parker, D. J., and Polcher, J.: African Monsoon Multidiscplinary Analysis: An International Research Project and Field Campaign, B. Am. Meteorol. Soc., 87, 1739–1746, https://doi.org/10.1175/BAMS-87-12-1739, 2006.

Roehrig, R., Bouniol, D., and Guichard, F.: The Present and Future of the West African Monsoon : A Process-Oriented Assessment of CMIP5 Simulations along the AMMA Transect, J. Climate, 26, 6471–6505, https://doi.org/10.1175/JCLI-D-12-00505.1, 2013.

Salam, Z., Ishaque, K., and Taheri, H.: An improved two-diode photovoltaic (PV) model for PV system, in: 2010 Joint International Conference on Power Electronics, Drives and Energy Systems and 2010 Power India, New Delhi, India, 20–23 December 2010, 1–5, https://doi.org/10.1109/PEDES.2010.5712374, 2010.

Sengupta, M., Habte, A., Kurtzn, S., Dobos, A., Wilbert, S., Lorenz, E., Stoffel, T., Renné, D., Myers, D., Wilcox, S., Blanc, P., and Perez, R.: Best practices handbook for the collection and use of solar resource data for solar energy applications: Second Edition, Tech. rep., National Renewable Energy Laboratory, https://doi.org/10.18777/ieashc-task46-2015-0001, 2017.

Skoplaki, E. and Palyvos, J. A.: On the temperature dependence of photovoltaic module electrical performance: A review of efficiency/power correlations, Sol. Energy, 83, 614–624, https://doi.org/10.1016/j.solener.2008.10.008, 2009.

Skye Instruments: Pyranometer SKS 1110, Tech. rep., Skye Instruments, 2019.

Slingo, A., Ackerman, T. P., Allan, R. P., Kassianov, E. I., McFarlane, S. A., Robinson, G. J., Barnard, J. C., Miller, M. A., Harries, J. E., Russell, J. E., and Dewitte, S.: Observations of the impact of a major Saharan dust storm on the atmospheric radiation balance, Geophys. Res. Lett., 33, L24817, https://doi.org/10.1029/2006GL027869, 2006.

Solangi, K. H., Islam, M. R., Saidur, R., Rahim, N. a., and Fayaz, H.: A review on global solar energy policy, Renew. Sust. Energ. Rev., 15, 2149–2163, https://doi.org/10.1016/j.rser.2011.01.007, 2011.

Solargis: Solar Resource Map 2019, available at: https://solargis.com/maps-and-gis-data/download/africa (last access: 27 February 2020), 2019.

SolarWorld: Data sheet of SolarWorld 235 poly module, Tech. rep., Solar World, 2012.

Sterl, S., Vanderkelen, I., Chawanda, C. J., Russo, D., Brecha, R. J., van Griensven, A., Van Lipzig, N. P., and Thiery, W.: Smart renewable electricity portfolios in West Africa, Nat. Sustain., 3, 710–719 https://doi.org/10.1038/s41893-020-0539-0, 2020.

Sultan, B., Janicot, S., and Diedhiou, A.: The West African monsoon dynamics. Part I: Documentation of intraseasonal variability, J. Climate, 16, 3389–3406, https://doi.org/10.1175/1520-0442(2003)016<3389:TWAMDP>2.0.CO;2, 2003.

Taylor, J. W., Haslett, S. L., Bower, K., Flynn, M., Crawford, I., Dorsey, J., Choularton, T., Connolly, P. J., Hahn, V., Voigt, C., Sauer, D., Dupuy, R., Brito, J., Schwarzenboeck, A., Bourriane, T., Denjean, C., Rosenberg, P., Flamant, C., Lee, J. D., Vaughan, A. R., Hill, P. G., Brooks, B., Catoire, V., Knippertz, P., and Coe, H.: Aerosol influences on low-level clouds in the West African monsoon, Atmos. Chem. Phys., 19, 8503–8522, https://doi.org/10.5194/acp-19-8503-2019, 2019.

Trentmann, J. and Pfeifroth, U.: Algorithm Theoretical Baseline Document: Meteosat Solar Surface Radiation and effective Cloud Albedo Climate Data Records – Heliosat: The MAGICSOL method applied for the generation of SARAH-2.1, Tech. rep., DWD, https://doi.org/10.5676/EUM_SAF_CM/SARAH/V001, 2019.

United Nations: Sustainable Development Goals, available at: https://sdgs.un.org/goals (last access: 21 October 2020), 2015.

WAPP: 2016-2019 WAPP Business Plan, Tech. rep., West African Power Pool, available at: http://www.ecowapp.org/sites/default/files/2015-2019_business_plan.pdf (last access: 5 November 2019), 2015.

Wild, M.: Enlightening global dimming and brightening, B. Am. Meteorol. Soc., 93, 27–37, https://doi.org/10.1175/BAMS-D-11-00074.1, 2012.

Yaro, J. A. and Hesselberg, J.: Adaptation to climate change and variability in rural West Africa, Springer, Switzerland, https://doi.org/10.1007/978-3-319-31499-0, 2016.

Yoon, J., von Hoyningen-Huene, W., Kokhanovsky, A. A., Vountas, M., and Burrows, J. P.: Trend analysis of aerosol optical thickness and Ångström exponent derived from the global AERONET spectral observations, Atmos. Meas. Tech., 5, 1271–1299, https://doi.org/10.5194/amt-5-1271-2012, 2012.

Chapter 6

Summary and outlook

A sustainable interaction with our Earth is needed to keep it a livable planet for future generations. For the electricity sector solar energies are one solution for carbon neutrality. However, solar power yields highly depend on fluctuating atmospheric parameters, especially solar irradiance. Therefore, the variability of solar irradiance needs to be precisely examined to ensure long-term investment for solar power plants, grid stability and needed storage capacities.

To better understand the impact of atmospheric variability on solar power in West Africa, this thesis aims to quantify the aerosol impact on different solar power technologies and analyzes the long-term variability and trends of solar irradiances and its implications for photovoltaic power over the whole region. In this chapter the key findings to answer the questions raised in the Introduction (Chapter 1) are summarized separately for the single result parts in Section 6.1 and Section 6.2. Furthermore, an overall conclusion and outlook is given in Section 6.3.

6.1 Impact of atmospheric aerosols on solar power

For building an electricity system based on solar power the reduction of solar irradiance due to aerosols needs to be taken into account. In West Africa, especially desert dust aerosols significantly reduce solar irradiance at ground. The impact of aerosols was isolated from other effects on global horizontal irradiance and quantified by using a combined radiative transfer - solar power model for the year 2006. A model chain to simulate irradiance at ground and photovoltaic power was developed and the impact of atmospheric aerosols on photovoltaic power was investigated in Niamey, Niger and published in Neher et al. (2017) (see Section 4.1). In a second publication (Neher et al. 2019) the model chain was extended to additionally model parabolic trough power and the study region was expanded to six measuring locations distributed over different climatic zones in West Africa (see Section 4.2). Furthermore, the impact of a major dust outbreak in March 2006 was analyzed in detail. In this way the questions phrased in the introduction

1. What is the magnitude of the impact of aerosols on solar power?
2. How sensitive are photovoltaic and concentrating solar technologies to aerosol conditions?
3. Which challenges need to be considered during a desert dust outbreak?

could be answered and the following key findings were derived.

1. Atmospheric aerosols can significantly reduce the output of solar power plants in cloud free situations: Median daily reduction due to atmospheric aerosols are determined to be 13% to 22% and 22% to 37% for photovoltaic and parabolic trough power plants, respectively (see Section 4.2 and Neher et al. (2019)). For a single photovoltaic module the direct current is reduced by up to 48% due to aerosols (see Section 4.1 and Neher et al. (2017)). A linear relation between aerosol optical depth (AOD) and solar power reduction could be derived for both technologies. In this way a reduction of solar power by 32% - 36% per unit of AOD for photovoltaic and 52% - 68% per unit of AOD for parabolic trough power could be derived. These results are in line with the study by Prasad et al. (2007), who found a similar impact of AOD on solar irradiance in the Indian desert, and by Stone et al. (2008), where similar impacts for smoke aerosols were derived.

2. Concentrating solar power is more susceptible to aerosol loads than photovoltaic power: The direct irradiance, which is the major driver for concentrated solar power, is reduced due to the presence of atmospheric aerosols. Photovoltaic power plants also use the diffuse component of solar irradiance, which increases to some maximum under the presence of aerosols. Therewith, concentrated solar power is more sensitive to aerosol loads (reduction of up to 100%) in the atmosphere than photovoltaic power (reduction of up to 79%). However, the concentrating systems are able to be combined with large storage capacities already, while batteries for photovoltaic power storage have lower capacities and are more expensive (IRENA 2017). Middleton (2017) investigated desert dust outbreaks and also found a higher power reduction for concentrating than for photovoltaic technologies. However, they did not analyze the aerosol impact over one total year, which was performed in this thesis.

3. Desert dust outbreaks can cause blackouts: Desert dust outbreaks result in high atmospheric aerosol loads and can last for several days. They are found at all six measuring sites distributed over the whole West African region. For both technologies such a strong event (like the analyzed one in March 2006) highly reduces daily power yields (by up to 79% for photovoltaic and up to 100% for parabolic trough power plants) and would need high storage capacities in a solar based power

system to overcome blackouts. Furthermore, a reliable forecast as well as a long-term climatology of the frequency and duration of the dust outbreaks is needed for the dimension of storage capacities. On average and for the specific 12 day long event in March 2006 the storage capacity would need to be as high as 50% of the installed parabolic trough power plus 30% of the installed photovoltaic power. Typically parabolic trough power plants with storage have capacities of around 7.5 hours peak load (e.g. the Andasol plants in Spain, (Solar Millenium 2008)), which is also needed for night times. Not only solar power close to the source of dust, but also solar power in regions located thousands of kilometers away are highly impacted by dust movements (e.g. the Mediterranean (Kosmopoulos et al. 2017) or Germany (Rieger et al. 2017)). Kosmopoulos et al. (2017) found slightly lower power reductions (40% to 50% for photovoltaic and 80% to 90% for concentrating solar power) for a desert dust outbreak in 2015 in the eastern Mediterranean than this thesis for the event in March 2006 in West Africa. However, the distance from the desert dust source in the Sahara desert to the Mediterranean is about two to three times higher than to West Africa.

With the strong implications of dust storms it is of high interest to investigate how frequent they are. As a first step the ICOsahedral Non-hydrostatic model with its extension for Aerosols and Reactive Trace gases (ICON-ART[1], (Rieger et al. 2015)) is used to identify high aerosol loads over West Africa (using the aerosol optical depth (AOD) as an indicator). The frequency of high desert dust movements is analyzed by using a full-year model output of ICON-ART for 2018. ICON-ART simulates the desert dust AOD in a 0.5° x 0.5° spatial and a 6 hourly temporal resolution (at midnight, 6 am, 12 pm and 6 pm) over total West Africa. An AOD of 0.5 (1) results in a reduction of around 15% (30%) for photovoltaic power and 30% (over 50%) for parabolic trough power (Neher et al. 2019). An AOD of 0.5 (1) is used as a benchmark for high (very high) desert dust movements (see Figure 6.1 a (b)).

Within the Sahel region and based on these model calculations, high desert dust loads are frequent with up to 22% while in southern West Africa dust movements occurs at less than 5% of the time. Thus, major dust outbreaks reducing the output of solar power plants by more than 15% over several days can be expected especially in northern West Africa. As cloudiness is low in northern West Africa, the impact of aerosols plays a major role for solar based power systems there. Thus, the knowledge of aerosol impacts must particularly taken into account for the dimensioning of solar power plants and storage capacity. In southern West Africa, where high cloudiness is present, it is difficult to disentangle the contributions by aerosols and clouds on solar power.

[1]The ICON modeling framework is a joint project of German Weather Service (DWD) and Max Planck Institute for Meteorology (MPI-M). The ART extension was developed at the Karlsruher Institute of Technology (KIT).

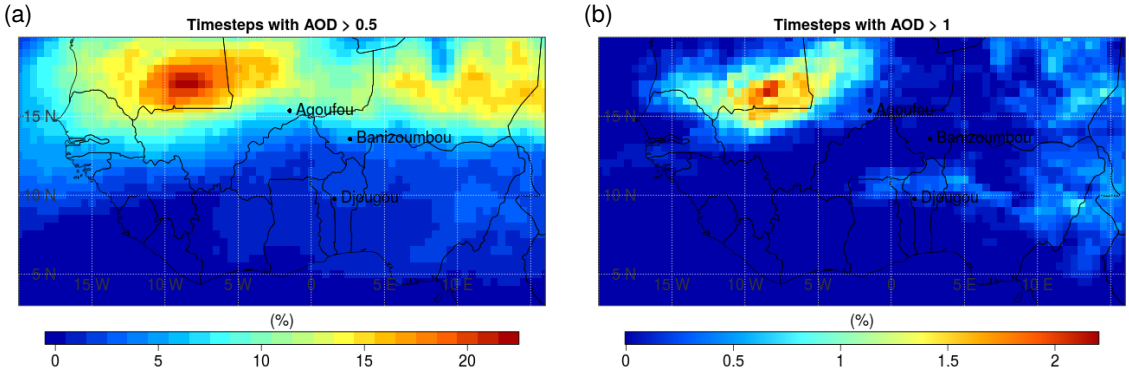

Figure 6.1: Frequency of high aerosol optical depth by using (a) AOD = 0.5 and (b) AOD = 1 as a benchmark. Notice the different scales of the two plots.

Extreme events (AOD > 1) occur with up to 2% of frequency in northern West Africa, especially in the Western part of the Sahara. However, the model calculations only represent the presence of desert dust aerosols. Other sources of aerosols (e.g. biomass burning or industrial combustion) are not yet included in ICON-ART.

6.2 Variability of solar irradiance and its implications for photovoltaic power

Solar irradiance is the major driver of photovoltaic yields. Therefore, a detailed investigation of solar irradiance is needed to identify economically promising sites. The Surface Solar Radiation Data Set-Heliosat, Edition 2.1 (SARAH-2.1) provides 35 years of irradiances, which was used to calculate the related photovoltaic power potential over West Africa (3°N to 20°N and 20°W to 16°E) and to analyze their variability in a temporal and spatial dimension. Therewith the questions raised in Chapter 1

1. How variable is solar irradiance and therewith photovoltaic power potential between 1983 and 2017 in West Africa?

2. What are the trends of solar irradiance during these 35 years and how do they impact photovoltaic potential?

can be answered. The following paragraphs depict the key findings.

1. Complementary photovoltaic potential and variability between northern and southern West Africa as well as between the wet and the dry season: The SARAH-2.1 analysis shows typical seasonal and regional pattern for solar irradiances reflecting the related photovoltaic yield estimations for West Africa.

The northern part of West Africa shows higher photovoltaic yields with a lower temporal variability (around 5.5 kWp/kWp mean photovoltaic yields with an interquantile range of less than 18%). While the southern region provides lower photovoltaic yields with a higher temporal variability (around 4.5 kWp/kWp mean photovoltaic yields with an interquantile range of locally up to around 70%). Thus, sites for photovoltaic systems have higher potential in northern than in southern West Africa. This regional difference is mainly controlled by the West African Monsoon and its associated cloudiness. A similar annual mean of photovoltaic power potential between 1994 and 2016 is given with 3.3 kWh/kWp to 5.5 kWh/kWp over West Africa from Solargis (2019).

Regarding seasons, the dry season is characterized by higher and rather constant solar irradiance (around 254 W/m^2 and 8% interquantile range), while it is lower and highly variable during the wet season (irradiance varies over the region with an interquantile range of around 27%). By looking at the results for different latitudes, the photovoltaic yield is low during the wet season in southern West Africa (around 4 kWh/kWp, in the latitude range from 3°N to 10°N) and shows a high variability. In this region, low level clouds occur frequently (Linden et al. 2015). The photovoltaic yields then increases continuously with rising latitude during the wet season and reach around 5.5 kWh/kWp at 20°N (similar to the value during the dry season at this latitude) and with lower variability (interquantile range of less than 9%). Over all latitudes estimated photovoltaic yields range from around 4.75 kWh/kWp in southern West Africa to 5.5 kWh/kWp in the northern region during the dry season. Thereby, the variability is reduced with increasing latitude. These findings imply that long-term storage systems are needed in a purely solar based power system in West Africa to overcome seasonal differences. The strong contrast between the seasons is especially controlled by the West African Monsoon and the accompanied seasonal movement of the Inter Tropical Convergence Zone. The monsoon time is longer in southern West Africa than in northern West Africa (CLISS 2016), leading to the detected differences between the seasons and regions.

2. Positive (negative) trend of solar irradiance in northern (southern) West Africa during the dry (wet) season: The long-term trends in solar irradiance are also clearly divided into seasons and regions. Whereas, a positive trend of up to +5 W/m^2/decade occurred in northern West Africa, especially during the dry season, a negative trend of up to -5 W/m^2/decade occurred in southern West Africa, mainly taking place during the wet season. Thus, the differences between the northern and southern region were enhanced between 1983 and 2017. The trends are in the range of global dimming and brightening tendency's (Wild 2012). At single locations (Banizoumbou, Niger and Dakar, Senegal) the trends are likely connected to changes in aerosol optical depth (Yoon et al. 2012).

Regarding regions, West Africa is distinguished in population density. The

coastal regions are population rich, while the northern desert region provides low population densities. Therewith, larger amounts of electricity are needed in the south compared to the north. This is contrary to the photovoltaic power potential and implies the need of a massive grid development to transfer the electricity produced by solar power plants in the north to the population in the south.

If the trends are ongoing, the complementary potential between the North and South as well as the wet and dry season will be widened in the future. To provide a stable solar based electricity sector in West Africa long-term storage would be necessary to overcome seasonal differences in power generation, besides the typical overnight storage for solar power plants. Furthermore, the grid infrastructure needs to be built up, especially in the North-South direction, to balance regional differences of power generation and supply.

6.3 Next steps for a carbon neutral electricity system in West Africa

Four major conclusions can be drawn from the studies undertaken in this thesis, with the goal of building up a stable and carbon neutral electricity system based on solar power in West Africa. First, a reliable forecast of dust outbreaks is needed on an intraday scale, to be able to compensate the reductions of such an event with other sources of electricity. Second, short term storage capacities should be installed to avoid blackouts during these dust outbreaks. Third, long-term storage capacities need to be build up to overcome seasonal differences in power generation. And finally, the grid infrastructure needs to be developed, especially in the North-South direction, to compensate regional differences in power generation and supply.

In this thesis the atmospheric impact on solar power was characterized. However, to find solutions for an overall power system in West Africa the inclusion of all available power sources (e.g. wind and hydro power) and the typical load in a demand-supply power model is desirable. Compensating effects could reduce the storage capacity and need to be taken into account for the grid development.

Solar power was modeled in SolPaRT by including major atmospheric drivers for global and direct irradiance as well as technical parameters of power plants. However, spectral effects of solar irradiances are not included and should be subject of further research. With regard to aerosols, this thesis points out the importance of the inclusion of aerosols for site assessment, as they can drastically reduce the incoming solar irradiance. However, they are not explicitly included in many global climate models and reanalysis. The explicit inclusion of aerosols as well as the assimilation of measurements needs to be performed in the future. Furthermore, power modeling should be performed by using detailed atmospheric input data from most reasonable sources and predictions, e.g. reanalysis, satellite data, ground-based measurements

and numerical weather predictions. ICON-ART is a numerical weather prediction model which already includes explicit mineral dust aerosols, however, other types (e.g. biomass burning aerosols, black carbon, etc.) should be explicitly included as well. Furthermore, the connection of aerosol effects with land-use pattern in ICON-ART and other models would give new insights on the interaction between land surface and solar power potential.

For the analysis of long-term variability and trends of solar irradiance and photovoltaic power potential over complete West Africa a simplified photovoltaic model was developed. This model allows a reasonable regional overview. However, including an explicit model could better indicate single impacts (e.g. inverter, temperature) for each grid point. Therefore, detailed meteorological input data in a high temporal and spacial resolution as well as large computational resources would be needed and should be used in future studies.

Appendix A

Supplementary material of Publication II

Electronic supplementary material to Neher, I., Buchmann, T., Crewell, S., Pospichal, B., and Meilinger, S. (2019). Impact of atmospheric aerosols on solar power. *Meteorologische Zeitschrift*, 28(4):305–321.

Measurement instruments information

Table A.1: Information of the measurement equipment for the used data set.

No.	Manufacturer	Location	Parameters	Reference
318A spectral radiometer	CIMEL	All Stations (except for Niamey)	AOD, Ångström exponent, PWV	(Holben et al. 1998)
MFRSR	ARM campaign	Niamey	AOD, Ångström exponent	(Hodges and Michalsky 2016)
Microwave radiometer	ARM campaign	Niamey	PWV	(Cadeddu et al. 2013, Morris 2006)
Sky radiometer	ARM campaign	Niamey	GHI, DNI, DIF	(Andreas et al. 2018)
05106	RM Young	Niamey	Wind direction and speed	(Wind 2007)
05103L	RM Young	Banizoumbou, Djougou	Wind direction and speed	(Vaisala 2006)
HMP 45	Vaisala	Niamey	Temperature, Humidity	(Campbell Scientific 2009a)
HMP 45	Vaisala	Banizoumbou, Djougou	Temperature, Humidity	(Campbell Scientific 2009a)
SKS 1110	Skye Instruments	Banizoumbou	GHI	(Skye Instruments 2019)
A100R	Vector	Agoufou	Wind Speed	(Campbell Scientific 2009b)
No. 278	Setra	Agoufou	Pressure	(Setra Systems 2015)
CNR1	Kipp & Zonen	Agoufou	GHI	(Campbell Scientific 2010)
CS215	Campbell	Agoufou	Temperature, Humidity	(Campbell Scientific 2017)

Table A.1: Information of the measurement equipment for the used data set.

No.	**Manufacturer**	**Location**	**Parameters**	**Reference**
W200P	Vector	Agoufou	Wind direction	(Campbell Scientific 2009b)
RPT 410	Druck	Djougou	Pressure	(Druck 2001)
SP Lite2	Kipp & Zonen	Djougou	GHI	(Kipp & Zonen 2019)
	SYNOP Station	Maine, Dakar	Temperature, Humidity, Pressure, Wind speed, -direction	(WMO 2010)

Input data for the six locations

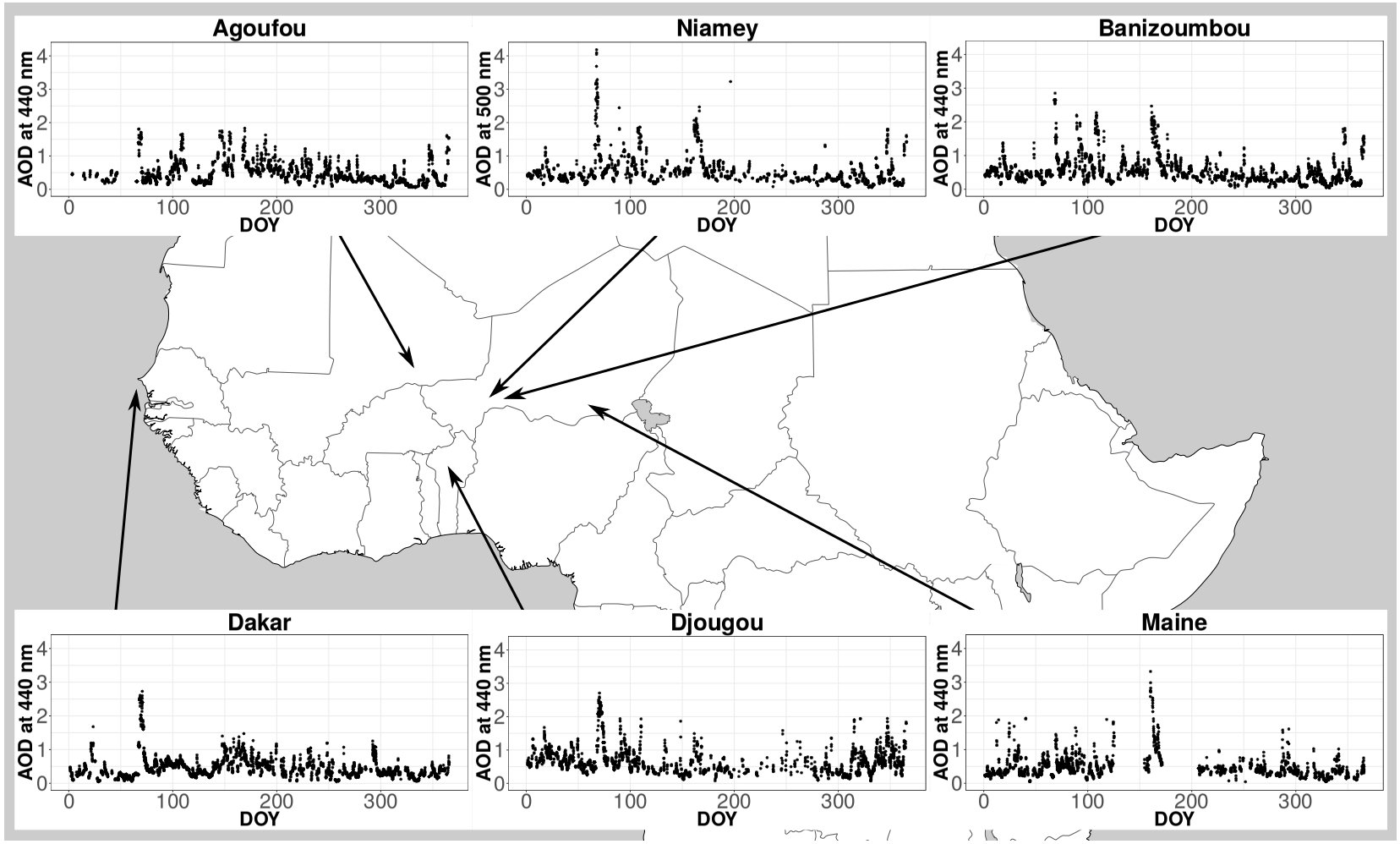

Figure A.1: Hourly AOD over the course of the year for the six locations.

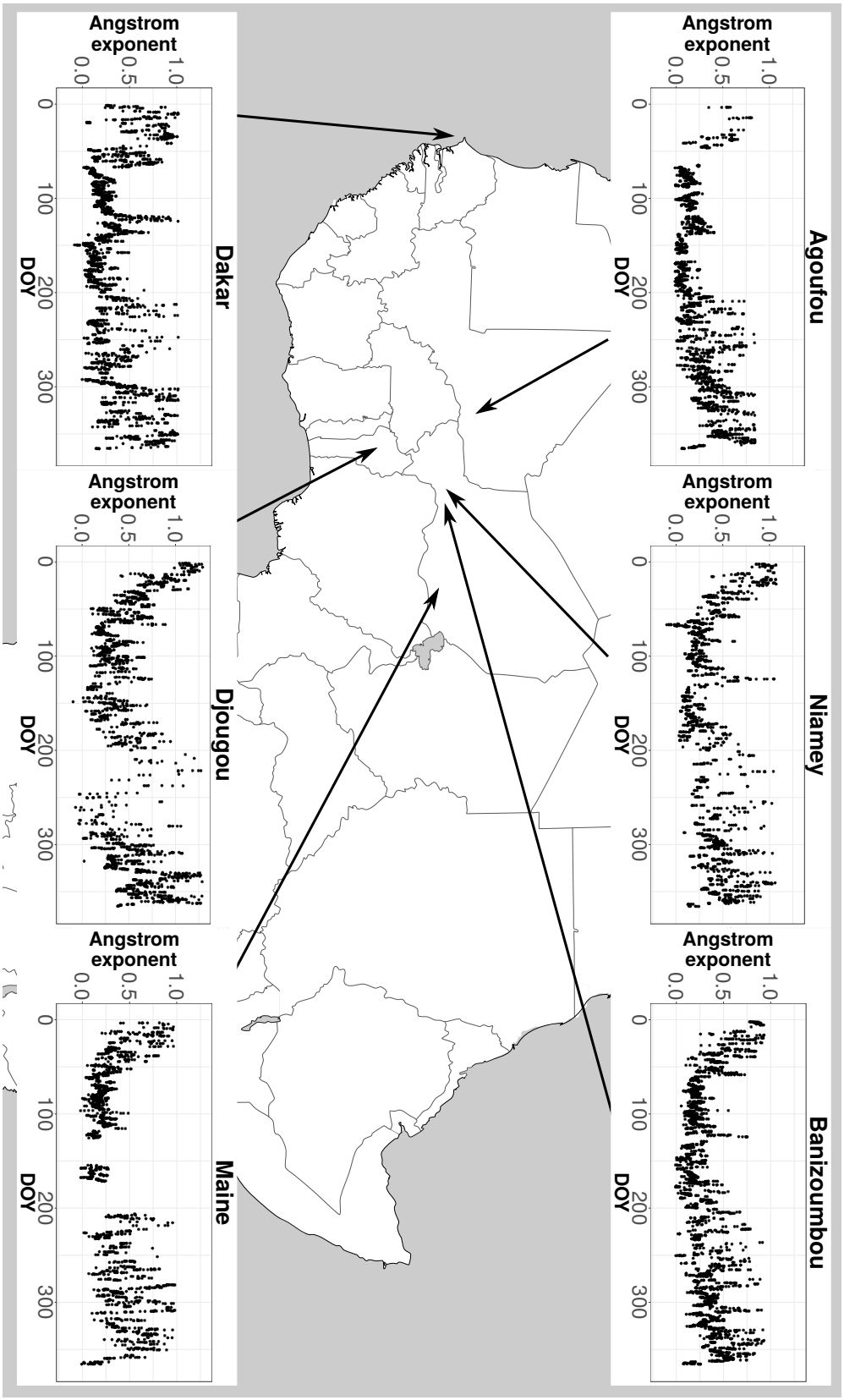

Figure A.2: Hourly Ångström exponents over the course of the year for the six locations.

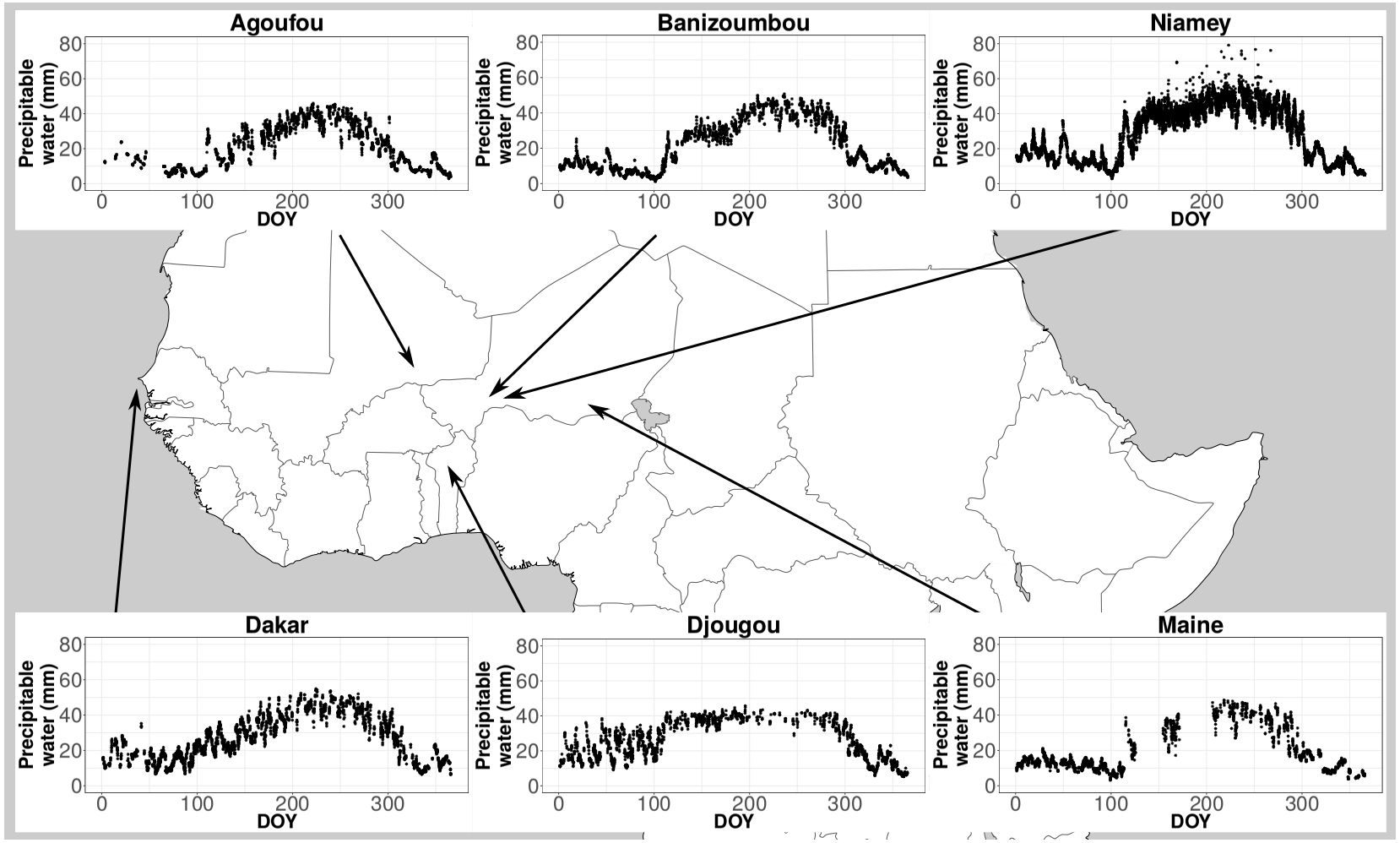

Figure A.3: Hourly PWV column in mm over the course of the year for the six locations.

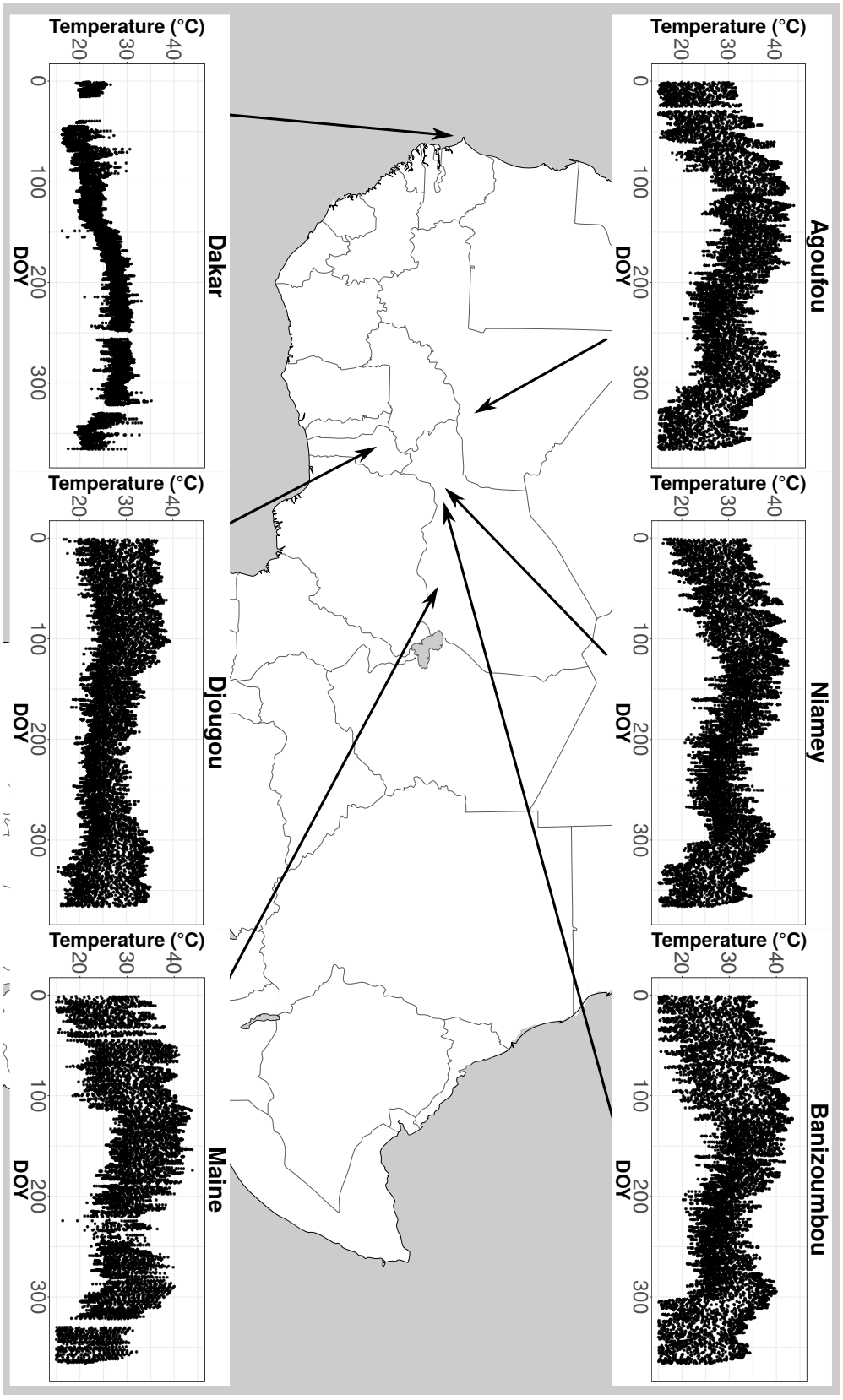

Figure A.4: Hourly ambient temperature in degree over the course of the year for the six locations.

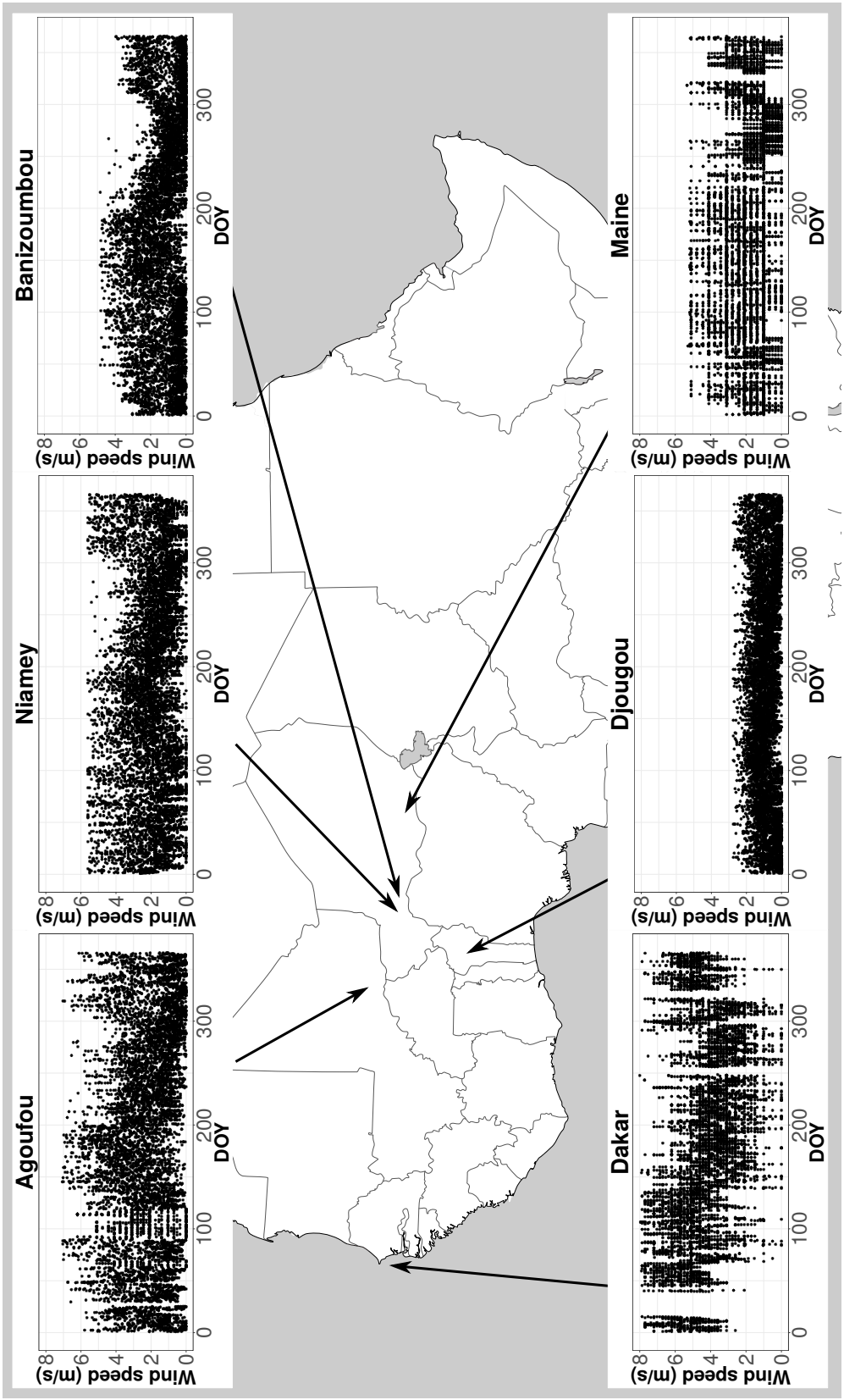

Figure A.5: Hourly wind speed in m/s over the course of the year for the six locations.

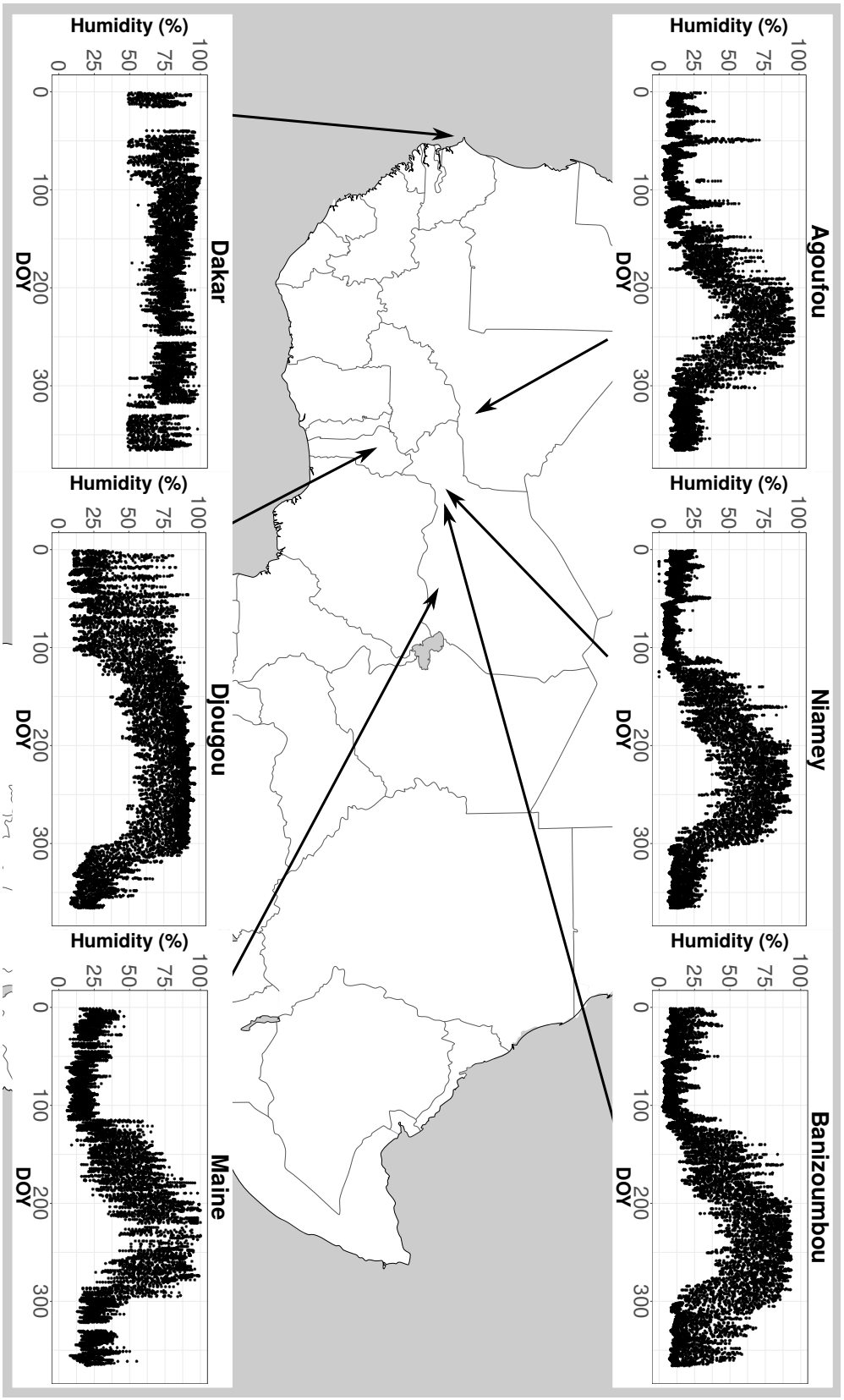

Figure A.6: Hourly relative humidity in % over the course of the year for the six locations.

Clear-sky dates

Table A.2: Dates of clear days in 2006 for the six stations in West Africa. Dates during the rainy season are marked in bold.

Station	**Clear-sky dates**
Agoufou	02/05, 02/14, 03/06, 03/08, 03/10, 03/11, 03/12, 03/14, 03/15, 03/16, 03/17, 03/18, 03/19, 03/21, 03/23, 03/24, 03/25, 03/26, 03/27, 03/28, 04/04, 04/05, 04/06, 04/08, 04/09, 04/11, 04/12, 04/13, 04/14, 04/15, 04/20, 04/22, 05/02, 05/04, 05/11, 05/12, 05/13, 05/14, 05/15, 05/16, 05/17, 05/23, 05/29, 05/30, **06/02, 06/04, 06/17, 06/19, 06/20, 06/22, 06/23, 06/24, 06/25, 06/30, 07/01, 07/04, 07/05, 07/11, 07/12, 07/16, 07/18, 07/20, 07/23, 07/27, 07/30, 08/02, 08/05, 08/08, 08/14, 08/16, 08/19, 08/20, 08/26, 09/02, 09/03, 09/04, 09/13, 09/14, 09/18, 09/22, 09/26, 09/27, 09/29, 09/30, 10/04, 10/05, 10/07, 10/08, 10/11, 10/16, 10/17, 10/18, 10/21, 10/23, 10/29, 10/30, 10/31,** 11/01, 11/02, 11/03, 11/04, 11/07, 11/09, 11/10, 11/11, 11/13, 11/14, 11/15, 11/17, 11/18, 11/19, 11/20, 11/23, 11/24, 12/09, 12/10, 12/11, 12/12, 12/13, 12/14, 12/15, 12/16, 12/17, 12/18, 12/19, 12/20, 12/22, 12/23, 12/24, 12/25, 12/27, 12/28
Bani-zoumbou	01/01, 01/02, 01/03, 01/06, 01/10, 01/12, 01/16, 01/18, 01/19, 01/20, 01/21, 01/22, 01/23, 01/24, 02/01, 02/02, 02/04, 02/05, 02/06, 02/07, 02/08, 02/11, 02/13, 02/14, 02/20, 02/22, 02/23, 02/25, 02/26, 02/27, 03/01, 03/03, 03/04, 03/05, 03/06, 03/09, 03/10, 03/11, 03/12, 03/13, 03/14, 03/15, 03/16, 03/17, 03/18, 03/19, 03/28, 04/04, 04/07, 04/12, 04/13, 04/14, 04/15, 04/16, 04/17, 04/19, 04/20, 04/21, 04/22, 04/23, 04/28, **05/02, 05/12, 05/13, 05/15, 05/23, 05/26, 05/27, 05/28, 06/07, 06/12, 06/13, 06/17, 06/18, 06/19, 06/21, 06/22, 07/03, 07/04, 07/08, 07/10, 07/11, 07/13, 07/16, 07/18, 07/23, 07/28, 07/29, 08/02, 08/10, 08/13, 08/16, 08/19, 08/20, 08/27, 09/02, 09/06, 09/07, 09/15, 09/18, 09/22, 09/27, 09/29, 10/03, 10/04, 10/05, 10/06, 10/10, 10/11, 10/12, 10/16, 10/17, 10/18, 10/21, 10/22, 10/23, 10/24, 10/25, 10/26, 10/27, 10/28, 10/29, 10/30, 10/31,** 11/01, 11/04, 11/05, 11/06, 11/07, 11/08, 11/09, 11/12, 11/13, 11/15, 11/16, 11/17, 11/18, 11/19, 11/20, 11/21, 11/22, 11/23, 11/24, 11/25, 11/26, 11/29, 12/02, 12/04, 12/05, 12/06, 12/07, 12/08, 12/09, 12/10, 12/13, 12/14, 12/15, 12/16, 12/17, 12/18, 12/19, 12/20, 12/22, 12/24, 12/25, 12/27, 12/28, 12/31

Continued on next page

Table A.2 – continued from previous page

Station	Clear-sky dates
Dakar	01/01, 01/02, 01/03, 01/06, 01/10, 01/12, 01/16, 01/18, 01/19, 01/20, 01/21, 01/22, 01/23, 01/24, 02/01, 02/02, 02/04, 02/05, 02/06, 02/07, 02/08, 02/11, 02/13, 02/14, 02/20, 02/22, 02/23, 02/25, 02/26, 02/27, 03/01, 03/03, 03/04, 03/05, 03/06, 03/09, 03/10, 03/11, 03/12, 03/13, 03/14, 03/15, 03/16, 03/17, 03/18, 03/19, 03/28, 04/04, 04/07, 04/12, 04/13, 04/14, 04/15, 04/16, 04/17, 04/19, 04/20, 04/21, 04/22, 04/23, 04/28, **05/02, 05/12, 05/13, 05/15, 05/23, 05/26, 05/27, 05/28, 06/07, 06/12, 06/13, 06/17, 06/18, 06/19, 06/21, 06/22, 07/03, 07/04, 07/08, 07/10, 07/11, 07/13, 07/16, 07/18, 07/23, 07/28, 07/29, 08/02, 08/10, 08/13, 08/16, 08/19, 08/20, 08/27, 09/02, 09/06, 09/07, 09/15, 09/18, 09/22, 09/27, 09/29, 10/03, 10/04, 10/05, 10/06, 10/10, 10/11, 10/12, 10/16, 10/17, 10/18, 10/21, 10/22, 10/23, 10/24, 10/25, 10/26 10/27, 10/28, 10/29, 10/30, 10/31,** 11/01, 11/04, 11/05, 11/06, 11/07, 11/08, 11/09, 11/12, 11/13 11/15, 11/16, 11/17, 11/18, 11/19, 11/20, 11/21, 11/22, 11/23, 11/24, 11/25, 11/26, 11/29, 12/02 12/04, 12/05, 12/06, 12/07, 12/08, 12/09, 12/10, 12/13, 12/14, 12/15, 12/16, 12/17, 12/18, 12/19 12/20, 12/22, 12/24, 12/25, 12/27, 12/28, 12/31
Djougou	01/03, 01/10, 01/22, 01/23, 01/24, 02/01, 02/02, 02/03, 02/04, 02/06, 02/07, 02/08, 02/18, 02/24, 02/25, 02/26, 02/27, 02/28, 03/01, 03/04, 03/05, 03/06, 03/07, 03/09, 03/10, 03/11, 03/12, 03/13, 03/14, 03/15, 03/16, 03/17, 03/18, 03/24, 03/25, 03/30, 04/05, 04/08, 04/09, 04/10, 04/11, 04/12, 04/13, 04/14, 04/15, 04/22, 05/04, 05/29, **06/01, 06/06, 06/13,** 10/21, 10/25, 10/27, 10/28, 10/30, 11/05, 11/08, 11/10, 11/12, 11/13, 11/16, 11/19, 11/20, 11/21, 11/22, 11/24, 11/25, 11/26, 11/28, 11/29, 12/02, 12/04, 12/05, 12/06, 12/07, 12/08, 12/09, 12/10, 12/12, 12/13, 12/15, 12/16, 12/17, 12/18, 12/19, 12/20, 12/21, 12/22, 12/24, 12/25, 12/26, 12/27, 12/28
Maine	01/03, 01/10, 01/22, 01/23, 01/24, 02/01, 02/02, 02/03, 02/04, 02/06, 02/07, 02/08, 02/18, 02/24, 02/25, 02/26, 02/27, 02/28, 03/01, 03/04, 03/05, 03/06, 03/07, 03/09, 03/10, 03/11, 03/12, 03/13, 03/14, 03/15, 03/16, 03/17, 03/18, 03/24, 03/25, 03/30, 04/05, 04/08, 04/09, 04/10, 04/11, 04/12, 04/13, 04/14, 04/15, 04/22, 05/04, 05/29, **06/01, 06/06, 06/13,** 10/21, 10/25, 10/27, 10/28, 10/30, 11/05, 11/08, 11/10, 11/12, 11/13, 11/16, 11/19, 11/20, 11/21, 11/22, 11/24, 11/25, 11/26, 11/28, 11/29, 12/02, 12/04, 12/05, 12/06, 12/07, 12/08, 12/09, 12/10, 12/12, 12/13, 12/15, 12/16, 12/17, 12/18, 12/19, 12/20, 12/21, 12/22, 12/24, 12/25 , 12/26, 12/27, 12/28
Niamey	01/01, 01/02, 01/03, 01/10, 01/11, 01/12, 01/21, 01/22, 01/23, 01/24, 02/01, 02/02, 02/04, 02/05, 02/06, 02/07, 02/08, 02/25, 03/03, 03/06, 03/07, 03/08, 03/09, 03/10, 03/11, 03/12, 03/14, 03/15, 03/16, 03/17, 03/26, 04/08, 04/12, 04/13, 04/14, 04/18, 04/19, 04/23, 05/04, **05/06, 05/27, 06/13, 06/19, 06/21, 06/22, 06/28, 06/29, 07/04, 08/10, 08/19, 09/02, 09/18, 09/29, 10/04, 10/05, 10/11, 10/17, 10/22, 10/26, 10/28, 10/30, 10/31,** 11/04, 11/05, 11/06, 12/06, 12/07, 12/09, 12/10, 12/13, 12/15, 12/16, 12/17, 12/18, 12/19, 12/20, 12/25, 12/27

Used dates for sensitivity study

Table A.3: Used days for the sensitivity study in 2006 with their corresponding minimum zenith angles in brackets.

Agoufou	**Banizoumbou**	**Dakar**	**Djougou**	**Maine**	**Niamey**
1.1. (0.67)	1.1. (0.65)	1.1. (0.65)	1.1. (0.57)	1.1. (0.64)	1.1. (0.64)
3.2. (0.56)	31.1. (0.54)	3.2. (0.55)	30.1. (0.48)	2.2. (0.54)	31.1. (0.54)
22.2. (0.45)	17.2. (0.44)	21.2. (0.44)	15.2. (0.39)	20.2. (0.44)	18.2. (0.44)
11.3. (0.34)	4.3. (0.34)	9.3. (0.34)	2.3. (0.3)	7.3. (0.34)	5.3. (0.34)
26.3. (0.23)	18.3. (0.25)	24.3. (0.23)	28.3. (0.21)	21.3. (0.24)	19.3. (0.24)
2.5. (0.12)	2.4. (0.15)	29.4. (0.13)	14.4. (0.12)	26.4. (0.14)	3.4. (0.14)
3.6. (0.01)	24.4. (0.05)	29.5. (0.02)	28.5. (0.03)	25.5. (0.04)	25.4. (0.05)
12.8. (0.05)	19.7. (0.03)	6.7. (0.05)	14.7. (0.02)	19.8. (0.07)	16.8. (0.02)
5.9. (0.15)	16.8. (0.13)	15.8. (0.15)	27.8. (0.11)	12.9. (0.16)	5.9. (0.12)
21.9. (0.26)	21.9. (0.23)	23.9. (0.26)	13.9. (0.21)	27.9. (0.26)	20.9. (0.23)
6.10. (0.36)	6.10. (0.34)	8.10. (0.36)	10.10. (0.3)	11.10. (0.25)	5.10. (0.33)
23.10. (0.47)	22.10. (0.44)	24.10. (0.46)	25.10. (0.39)	26.10. (0.45)	21.10. (0.44)
11.11. (0.57)	9.11. (0.54)	11.11. (0.56)	12.11. (0.49)	13.11. (0.55)	9.11. (0.54)
22.12. (0.68)	20.12. (0.65)	22.12. (0.66)	21.12. (0.58)	23.12. (0.64)	20.12. (0.65)

Parameter for sensitivity study

Table A.4: Lower (5% quantile) and upper (95% quantile) parameters used for sensitivity study. The reference source is indicated for each parameter.

Parameter	**Station**	**Low**	**High**	**Reference**
Aerosol composition	All stations	Antarctic[1]	Urban[2]	Desert[3]
Albedo	All stations	0	0.3	0.15
AOD	Agoufou	0.12	1.09	Desert
	Banizoumbou	0.13	1.4	Desert
	Dakar	0.13	1.2	Desert
	Djougou	0.27	2.1	Desert
	Maine	0.15	1.3	Desert
	Niamey	0.15	2.3	Desert
Relative humidity (%)	Agoufou	7	85	Measurements

Continued on next page

[1] *Antarctic* indicates the typical aerosol profile defined by (Hess et al. 1998)

[2] *Urban* indicates the typical aerosol profile defined by (Hess et al. 1998)

[3] *Desert* indicates the typical aerosol profile defined by (Hess et al. 1998), corresponding to an AOD of 0.286

Table A.4 – continued from previous page

Parameter	Station	Low	High	Reference
	Banizoumbou	5.7	86	Measurements
	Dakar	49	94	Measurements
	Djougou	14	91	Measurements
	Maine	12	85	Measurements
	Niamey	5.5	82	Measurements
PWV (cm)	Agoufou	0.5	3.9	Default (tropics)[4]
	Banizoumbou	0.4	4.1	Default (tropics)
	Dakar	0.86	4.2	Default (tropics)
	Djougou	0.79	3.6	Default (tropics)
	Maine	0.63	3.9	Default (tropics)
	Niamey	0.72	5.1	Default (tropics)
Pressure (bar)	Agoufou	973	981	Measurements
	Banizoumbou	984	984	984[5]
	Dakar	1006	1012	Measurements
	Djougou	958	965	Measurements
	Maine	967	975	Measurements
	Niamey	981	989	Measurements
Temperature (°)	Agoufou	18	40	Measurements
	Banizoumbou	17	39	Measurements
	Dakar	19	30	Measurements
	Djougou	20	35	Measurements
	Maine	19	39	Measurements
	Niamey	20	39	Measurements
Wind speed (m/s)	Agoufou	0.19	5.5	Measurements
	Banizoumbou	0.018	3.6	Measurements
	Dakar	1.5	7.2	Measurements
	Djougou	0.05	2.1	Measurements
	Maine	0.33	4.4	Measurements
	Niamey	0.3	5	Measurements

[4]Default (tropics) indicates the default values from the tropical atmospheric profile by (Anderson et al. 1986).

[5]The pressure in Banizoumbou is calculated as a constant value with the barometric formula.

AOD as a function of daily power reductions

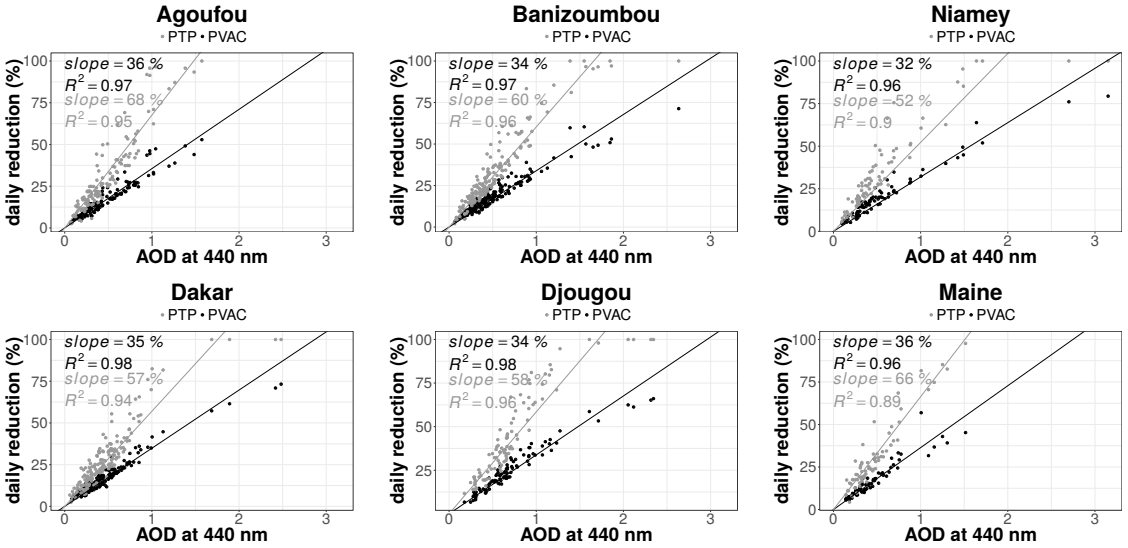

Figure A.7: AOD as a function of daily reductions in PVAC (black) and PTP (gray) at the six locations. A linear fit is given for both relations.

Bibliography

Abdulrahman, J. and Paco, D. (2019). Regional Progress Report on Renewable Energy, Energy Efficiency and Energy Access in ECOWAS region. Monitoring year: 2017. Technical report, ECOWAS Centre for Renewable Energy and Energy Efficiency (ECREEE), Praia, Cabo Verde.

Adeoye, O. and Spataru, C. (2018). Sustainable development of the West African Power Pool: Increasing solar energy integration and regional electricity trade. *Energy for Sustainable Development*, 45:124–134.

AeroCom (2020). Models for AeroCom. Available from: https://aerocom.met.no/participants.html, 2020-07-06.

American Society for Testing and Materials (2003). Reference Solar Spectral Irradiance: AM1.5. Available from: https://rredc.nrel.gov/solar/spectra/am1.5/, 2020-03-24.

AMMA (2018). AMMA database. Available from: https://baobab.sedoo.fr/AMMA/, 2020-01-13.

Anderson, G., Clough, S., and Kneizys, F. (1986). AFGL atmospheric constituent profiles (0-120 km). *Environmental Research Papers*, AFGL-TR86-(954):46.

Andreas, A., Habte, A., Reda, I., Dooraghi, M., Kutchenreiter, M., and Sengupta, M. (2018). Solar Infrared Radiation Station (SIRS), Sky Radiation (SKYRAD), Ground Radiation (GNDRAD), and Broadband Radiometer Station (BRS) - Instrument Handbook. Technical Report April, ARM.

Armaroli, N. and Balzani, V. (2016). Solar Electricity and Solar Fuels: Status and Perspectives in the Context of the Energy Transition. *Chemistry - A European Journal*, 22:32–57.

Babić, K., Adler, B., Kalthoff, N., Andersen, H., Dione, C., Lohou, F., Lothon, M., and Pedruzo-Bagazgoitia, X. (2019). The observed diurnal cycle of low-level stratus clouds over southern West Africa: A case study. *Atmospheric Chemistry and Physics*, 19(2):1281–1299.

Badescu, V. (2002). 3D isotropic approximation for solar diffuse irradiance on tilted surfaces. *Renewable Energy*, 26(2):221–233.

Barry, J., Böttcher, D., Pfeilsticker, K., Herman-Czezuch, A., Kimiaie, N., Meilinger, S., Schirrmeister, C., Deneke, H., Witthuhn, J., and Gödde, F. (2020). Dynamic model of photovoltaic module temperature as a function of atmospheric conditions. *19th EMS Annual Meeting: Europiean Conference for Applied Meteorology and Climatology 2019*, submitted:1–13.

Bazyomo, S. D. Y. B., Lawin, E. A., Coulibaly, O., and Ouedraogo, A. (2016). Forecasted changes in West Africa photovoltaic energy output by 2045. *Climate*, 4(53):1–15.

Bohren, C. F. and Huffman, D. R. (1998). *Absorption and Scattering of Light by Small Particles*. John Wiley & Sons, New York.

Boucher, O. (2015). *Atmospheric Aerosols: Properties and Climate Impacts*. Springer.

Boucher, O., Randall, D., Artaxo, P., Bretherton, C., Feingold, G., Forster, P., Kerminen, V.-M., Kondo, Y., Liao, H., Lohmann, U., Rasch, P., Satheesh, S. K., Sherwood, S., Stevens, B., and Zhang, X. Y. (2013). 7. Clouds and Aerosols. In *Climate Change 2013: The Physical Science Basis. Contribution of Working Group I to the Fifth Assessment Report of the Intergovernmental Panel on Climate Change*, pages 571–657. Cambridge University Press, Cambridge, United Kingdom and New York, NY, USA.

Cabrera, F. J., Fernández-García, A., Silva, R. M., and Pérez-García, M. (2013). Use of parabolic trough solar collectors for solar refrigeration and air-conditioning applications. *Renewable and Sustainable Energy Reviews*, 20:103–118.

Cadeddu, M. P., Liljegren, J. C., and Turner, D. D. (2013). The atmospheric radiation measurement (ARM) program network of microwave radiometers: Instrumentation, data, and retrievals. *Atmospheric Measurement Techniques*, 6(9):2359–2372.

Campbell Scientific (2009a). Model HMP45C Temperature and Relative Humidity Probe. Technical report, Campbell Scientific.

Campbell Scientific (2009b). Wind Speed and Direction Sensors - A100R Anemometer and W200P-1 Windvane. Technical report, Campbell Scientific.

Campbell Scientific (2010). CNR1, CNR1-L - Solar and Far Infrared Radiation Balance Radiaometers. Technical report, Campbel Scientific.

Campbell Scientific (2017). CS215 Temperature and Relative Humidity Probe. Technical report, Campbell Scientific.

Capes, G., Murphy, J. G., Reeves, C. E., McQuaid, J. B., Hamilton, J. F., Hopkins, J. R., Crosier, J., I.Williams, P., and Coe, H. (2009). Secondary organic aerosol from biogenic VOCs over West Africa during AMMA. *Atmospheric Chemistry and Physics*, 9(12):3841–3850.

Cavalieri, O., Donfrancesco, G. D., Cairo, F., Fierli, F., Snels, M., Viterbini, M., Cardillo, F., Chatenet, B., Formenti, P., Marticorena, B., and Rajot, J. L. (2011). The AMMA MULID network for aerosol characterization in West Africa. *International Journal of Remote Sensing*, 32(19):5485–5504.

CLISS (2016). Landscapes of west africa - A Window on a changing world. Technical report, U.S. Geological Survey EROS, 47914 252nd St, Garretson, SD 57030, United States.

Cowie, S. M., Knippertz, P., and Marsham, J. H. (2014). A climatology of dust emission events from Northern Africa using long-term surface observations. *Atmospheric Chemistry and Physics*, 14(16):8579–8597.

Crumeyrolle, S., Gomes, L., Tulet, P., Matsuki, A., Schwarzenboeck, A., and Crahan, K. (2008). Increase of the aerosol hygroscopicity by cloud processing in a mesoscale convective system: a case study from the AMMA campaign. *Atmospheric Chemistry and Physics*, 8(23):6907–6924.

De Soto, W., Klein, S. A., and Beckman, W. A. (2006). Improvement and validation of a model for photovoltaic array performance. *Solar Energy*, 80(1):78–88.

Deetz, K., Vogel, H., Knippertz, P., Adler, B., Taylor, J., Coe, H., Bower, K., Haslett, S., Flynn, M., Dorsey, J., Crawford, I., Kottmeier, C., and Vogel, B. (2018). Numerical simulations of aerosol radiative effects and their impact on clouds and atmospheric dynamics over southern West Africa. *Atmospheric Chemistry and Physics*, 18(13):9767–9788.

Delon, C., Galy-Lacaux, C., Boone, A., Liousse, C., Serça, D., Adon, M., Diop, B., Akpo, A., Lavenu, F., Mougin, E., and Timouk, F. (2010). Atmospheric nitrogen budget in Sahelian dry savannas. *Atmospheric Chemistry and Physics*, 10(6):2691–2708.

Delucchi, M. A. and Jacobson, M. Z. (2011). Providing all global energy with wind, water, and solar power, Part II: Reliability, system and transmission costs, and policies. *Energy Policy*, 39(3):1170–1190.

Dersch, J. (2014). Greenius User Manual. Technical report, Deutsches Zentrum für Luft- und Raumfahrt e.V. 110.

Druck (2001). RPT 410 - Barometric Pressure Sensor. Technical report, Druck.

Duffie, J. A. and Beckman, W. A. (1976). *Solar Engineering of Thermal Processes*. John Wiley & Sons, New Jersey.

ECOWAS (2014). ECOWAS Renewable Energy and Energy Efficiency Status report 2014. Technical report, ECOWAS.

ECOWAS (2019). ECOWREX. Available from: http://www.ecowrex.org/mapView/, 2019-10-17.

ECREE (2017). Regional progress report on renewable energy, energy efficiency and energy access in ECOWAS region. Technical report, ECOWAS Centre for Renewable Energy and Energy Efficiency (ECREEE).

Emde, C., Buras-Schnell, R., Kylling, A., Mayer, B., Gasteiger, J., Hamann, U., Kylling, J., Richter, B., Pause, C., Dowling, T., and Bugliaro, L. (2016). The libRadtran software package for radiative transfer calculations (version 2.0.1). *Geoscientific Model Development*, 9(5):1647–1672.

Fiebig, M. and Ogren, J. a. (2006). Retrieval and climatology of the aerosol asymmetry parameter in the NOAA aerosol monitoring network. *Journal of Geophysical Research: Atmospheres*, 111(D21204).

Fischbach, J. (1982). *Optoelektronik - Bauelemente der Halbleiter-Optoelektronik*. expert verlag, Grafenau, band 16, r edition.

Giles, D. M., Sinyuk, A., Sorokin, M. G., Schafer, J. S., Smirnov, A., Slutsker, I., Eck, T. F., Holben, B. N., Lewis, J. R., Campbell, J. R., Welton, E. J., Korkin, S. V., and Lyapustin, A. I. (2019). Advancements in the Aerosol Robotic Network (AERONET) Version 3 database – automated near-real-time quality control algorithm with improved cloud screening for Sun photometer aerosol optical depth (AOD) measurements. *Atmospheric Measurement Technique*, 12(1):169–209.

Gracia, A. M. and Huld, T. (2013). Performance comparison of different models for the estimation of global irradiance on inclined surfaces: Validation of the model implemented in PVGIS. Technical report, European Commission, Joint Research Centre, Institute for Energy and Transport. 1–26.

Gueymard, C. A. (2018). A reevaluation of the solar constant based on a 42-year total solar irradiance time series and a reconciliation of spaceborne observations. *Solar Energy*, 168:2 – 9.

Gueymard, C. A. and Wilcox, S. M. (2011). Assessment of spatial and temporal variability in the US solar resource from radiometric measurements and predictions from models using ground-based or satellite data. *Solar Energy*, 85(5):1068–1084.

Hammer, A., Heinemann, D., Hoyer, C., Kuhlemann, R., Lorenz, E., Müller, R., and Beyer, H. G. (2003). Solar energy assessment using remote sensing technologies. *Remote Sensing of Environment*, 86(3):423–432.

Hannak, L., Knippertz, P., Fink, A. H., Kniffka, A., and Pante, G. (2017). Why do global climate models struggle to represent low-level clouds in the west african summer monsoon? *Journal of Climate*, 30(5):1665–1687.

Hay, J. E. (1979). Calculation of monthly mean solar radiation for horizontal and inclined surfaces. *Solar Energy*, 23:301–307.

Haywood, J. M., Pelon, J., Formenti, P., Bharmal, N. A., Brooks, M. E., Capes, G., Chazette, P., Chou, C., Christopher, S. A., Coe, H., Cuesta, J., Derimian, Y., Desboeufs, K., Greed, G., Harrison, M., Heese, B., Highwood, E. J., Johnson, B., Mallet, M., Marticorena, B., Marsham, J., Milton, S., Myhre, G., Osborne, S. R., Parker, D. J., Rajot, J. L., Schulz, M., Slingo, A., Tanré, D., and Tulet, P. (2008). Overview of the dust and biomass-burning experiment and African monsoon multidisciplinary analysis special observing period-0. *Journal of Geophysical Research: Atmospheres*, 113(D00C17).

Hermann, S., Miketa, A., and Fichaux, N. (2014). Estimating the Renewable Energy Potential in Africa. Technical report, International Renewable Energy Agency, Abu Dhabi. 1–73.

Hess, M., Koepke, P., and Schult, I. (1998). Optical Properties of Aerosols and Clouds: The Software Package OPAC. *Bulletin of the American Meteorological Society*, 79(5):831–844.

Hodges, G. and Michalsky, J. J. (2016). Multifilter Rotating Shadowband Radiometer Instrument Handbook. Technical Report March, U.S. Department of Energy.

Holben, B., Eck, T., Slutsker, I., Tanré, D., Buis, J., Setzer, A., Vermote, E., Reagan, J., Kaufman, Y. J., Nakajima, T., Lavenu, F., Jankowiak, I., and Smirnov, A. (1998). AERONET - A Federated Instrument Network and Data Archive for Aerosol Characterization. *Remote Sensing of Environment*, 66(1):1–16.

Horvath, H., Kasahara, M., Tohno, S., Olmo, F. J., Lyamani, H., Alados-Arboledas, L., Quirantes, a., and Cachorro, V. (2016). Relationship between fraction of backscattered light and asymmetry parameter. *Journal of Aerosol Science*, 91:43–53.

Hourdin, F., Musat, I., Guichard, F., Ruti, P. M., Favot, F., Filiberti, M. A., Pham, M. A., Grandpeix, J. Y., Polcher, J. A., Marquet, P., Boone, A., Lafore, J. P., Redelsperger, J. L., Dell'Aquila, A., Doval, T. L., Traore, A. K., and Gallée, H. (2010). Amma-Model intercomparison project. *Bulletin of the American Meteorological Society*, 91:95–104.

Hoyer-Klick, C., Lefèvre, M., Schroedter-Homscheidt, M., and Wald, L. (2015). User's guide to the MACC-RAD Services on solar energy radiation resources March 2015. Technical Report March, Copernicus.

IEA (2019). Solar PV. Available from: https://www.iea.org/reports/tracking-power/solar-pv#abstract, 2020-02-21.

IPCC (2013). Summary for Policymakers. In *Climate Change 2013: The Physical Science Basis. Contribution of Working Group I to the Fifth Assessment Report of the Intergovernmental Panel on Climate Change*. Cambridge University Press, Cambridge, United Kingdom and New York, NY, USA.

IPCC (2014a). Summary for Policymakers. In *Climate Change 2014: Synthesis Report.* IPCC, Geneva, Switzerland.

IPCC (2014b). Summary for Policymakers. In *Climate Change 2014: Mitigation of Climate Change. Contribution of Working Group III to the Fifth Assessment Report of the Intergovernmental Panel on Climate Change [Edenhofer, O., R. Pichs-Madruga, Y. Sokona, E. Farahani, S. Kadner, K. Seyboth, A. Adle*, pages 1–33. Cambridge University Press, Cambridge, United Kingdom and New York, NY, USA.

IRENA (2017). Electricity Storage and Renewables: Costs and Markets to 2030. Technical report, International Renewable Energy Agency.

IRENA (2018a). Planning and Prospects for Renewable Power: West Africa. Technical report, International Renewable Energy Agency, Abu Dhabi. 129.

IRENA (2018b). Solar Energy Data. Available from: https://www.irena.org/solar, 2018-12-11.

Kato, S., Ackerman, T. P., Mather, J. H., and Clothiaux, E. E. (1999). The k-distribution method and correlated-k approximation for a shortwave radiative transfer model. *Journal of Quantitative Spectroscopy and Radiative Transfer*, 62(1):109–121.

Kaufman, Y. J., Tanré, D., and Boucher, O. (2002). A satellite view of aerosols in the climate system. *Nature*, 419:215–223.

King, D. L., Boyson, W. E., and Kratochvil, J. A. (2004). Photovoltaic array performance model. Technical report, Sandia National Laboratories. 1–19.

King, D. L., Gonzalez, S., Galbraith, G. M., and Boyson, W. E. (2007). Performance Model for Grid-Connected Photovoltaic Inverters. Technical report, Sandia National Laboratories. 655–660.

King, D. L., Kratochvil, J. A., and Boyson, W. E. (1997). Measuring solar spectral and angle-of-incidence effects on photovoltaic modules and solar irradiance sensors. In *Conference Record of the 26th IEEE Photovoltaic Specialists Conference*, pages 1113–1116.

Kinne, S., O'Donnel, D., Stier, P., Kloster, S., Zhang, K., Schmidt, H., Rast, S., Giorgetta, M., Eck, T. F., and Stevens, B. (2013). MAC-v1: A new global aerosol climatology for climate studies. *Journal of Advances in Modeling Earth Systems*, 5(4):704–740.

Kipp & Zonen (2008). Instruction Manual - Pyrheliometer. Technical report, Kipp&Zonen.

Kipp & Zonen (2016). Instruction Manual - Pyranometer. Technical report, Kipp&Zonen.

Kipp & Zonen (2019). SP Lite2 Silicon Pyranometer. Technical report, Kipp & Zonen.

Kniffka, A., Knippertz, P., and Fink, A. H. (2019). The role of low-level clouds in the West African monsoon system. *Atmospheric Chemistry and Physics*, 19(3):1623–1647.

Knippertz, P., Coe, H., Chiu, J. C., Evans, M. J., Fink, A. H., Kalthoff, N., Liousse, C., Mari, C., Allan, R. P., Brooks, B., Danour, S., Flamant, C., Jegede, O. O., Lohou, F., and Marsham, J. H. (2015). The DACCIWA project: Dynamics-aerosol-chemistry-cloud interactions in West Africa. *Bulletin of the American Meteorological Society*, 96(9):1451–1460.

Köberle, A. C., Gernaat, D. E., and van Vuuren, D. P. (2015). Assessing current and future techno-economic potential of concentrated solar power and photovoltaic electricity generation. *Energy*, 89:739–756.

Koepke, P., Hess, M., Schult, I., and Shettle, E. P. (1997). Global Aerosol Dataset. Technical report, Max-Planck-Institut fuer Meteorologie. 44.

Kopp, G. and Lean, J. L. (2011). A new, lower value of total solar irradiance: Evidence and climate significance. *Geophysical Research Letters*, 38(L01706).

Kosmopoulos, P. G., Kazadzis, S., Taylor, M., Athanasopoulou, E., Speyer, O., Raptis, P. I., Marinou, E., Proestakis, E., Solomos, S., Gerasopoulos, E., Amiridis, V., Bais, A., and Kontoes, C. (2017). Dust impact on surface solar irradiance assessed with model simulations, satellite observations and ground-based measurements. *Atmospheric Measurement Techniques*, 10(7):2435—-2453.

Kothe, S., Pfeifroth, U., Cremer, R., Trentmann, J., and Hollmann, R. (2017). A satellite-based sunshine duration climate data record for Europe and Africa. *Remote Sensing*, 9(5):429.

Kraus, H. (2004). *Die Atmosphäre der Erde*. Springer, Berlin, Heidelberg, New York, Hongkong, London, Mailand, Paris, Tokio, 3 edition.

Kurucz, R. L. (1994). Synthetic Infrared Spectra. In Rabin, D. M., , Jefferies, J. T., , and Lindsey, C., editors, *Infrared Solar Physics: Proceedings of the 154th Symposium of the International Astronomical Union, Held in Tucson, Arizona, U.S.A., March 2–6, 1992*, pages 523–531. Springer Netherlands, Dordrecht.

Lélé, M. I. and Lamb, P. J. (2010). Variability of the Intertropical Front (ITF) and rainfall over the West African Sudan-Sahel zone. *Journal of Climate*, 23(14):3984–4004.

Linden, R., Fink, A. H., and Redl, R. (2015). Satellite-based climatology of low-level continental clouds in southern West Africa during the summer monsoon season. *Journal of Geophysical Research: Atmospheres*, 120:1186–1201.

Liousse, C., Guillaume, B., Grégoire, J. M., Mallet, M., Galy, C., Pont, V., Akpo, A., Bedou, M., Castéra, P., Dungall, L., Gardrat, E., Granier, C., Konaré, A., Malavelle, F., Mariscal, A., Mieville, A., Rosset, R., Serça, D., Solmon, F., Tummon, F., Assamoi, E., Yoboué, V., and Van Velthoven, P. (2010). Updated African biomass burning emission inventories in the framework of the AMMA-IDAF program, with an evaluation of combustion aerosols. *Atmospheric Chemistry and Physics*, 10(19):9631–9646.

Liu, B. Y. H. and Jordan, R. C. (1963). A Rational Procedure for Predicting The Long-Term Average Performance of Flat-Plate Solar-Energy Collectors. *Solar Energy*, 7(2):53–74.

Lorenz, E., Scheidsteger, T., and Hurka, J. (2011). Regional PV power prediction for improved grid integration. *Progress in Photovoltaics: Research and Applications*, 19(7):757–771.

Loutzenhiser, P. G., Manz, H., Felsmann, C., Strachan, P. A., Frank, T., and Maxwell, G. M. (2007). Empirical validation of models to compute solar irradiance on inclined surfaces for building energy simulation. *Solar Energy*, 81(2):254–267.

Luepfert, E., Zarza-Moya, E., Geyer, M., Nava, P., Langenkamp, J., Schiel, W., Esteban, A., Osuna, R., and Mandelberg, E. (2003). EUROTROUGH collector qualification complete performance test results from PSA. *ISES Solar World Congress 2003, Goeteborg, Schweden*, June 14-19(1):1–5.

Marticorena, B., Haywood, J., Coe, H., Formenti, P., Liousse, C., Mallet, M., and Pelon, J. (2011). Tropospheric aerosols over West Africa: Highlights from the AMMA international program. *Atmospheric Science Letters*, 12(1):19–23.

Martin, N. and Ruiz, J. M. (2001). Calculation of the PV modules angular losses under field conditions by means of an analytical model. *Solar Energy Materials and Solar Cells*, 70(1):25–38.

Matsuki, A., Quennehen, B., Schwarzenboeck, A., Crumeyrolle, S., Venzac, H., Laj, P., and Gomes, L. (2010). Temporal and vertical variations of aerosol physical and chemical properties over West Africa: AMMA aircraft campaign in summer 2006. *Atmospheric Chemistry and Physics*, 10(17):8437–8451.

Mayer, B. and Kylling, A. (2005). Technical note: The libRadtran software package for radiative transfer calculations - description and examples of use. *Atmospheric Chemistry and Physics*, 5(2):1319–1381.

Mayer, B., Kylling, A., Emde, C., and Buras, R. (2015). libRadtran user ' s guide. Technical report, libRadtran.

MeteoGroup (2019). Meteomedia - Station Sankt Augustin Hochschule. Available from: http://wetterstationen.meteomedia.de/?map=Nordrhein-Westfalen&station=105191, 2019-02-28.

Middleton, N. J. (2017). Desert dust hazards: A global review. *Aeolian Research*, 24:53–63.

Miller, M. A., Ghate, V. P., and Zahn, R. K. (2012). The radiation budget of the West African Sahel and its controls: A perspective from observations and global climate models. *Journal of Climate*, 25(17):5976–5996.

Mishchenko, M. I. and Travis, L. D. (1998). Capabilities and limitations of a current FORTRAN implementation of the T-matrix method for randomly oriented, rotationally symmetric scatterers. *Journal of Quantitative Spectroscopy and Radiative Transfer*, 60(3):309–324.

Morris, V. R. (2006). Microwave Radiometer Handbook. Technical report, U.S. Department of Energy, Atmospheric Radiaition Measurement Climat Research Facility.

Mueller, R., Pfeifroth, U., Traeger-Chatterjee, C., Trentmann, J., and Cremer, R. (2015). Digging the METEOSAT Treasure—3 Decades of Solar Surface Radiation. *Remote Sensing*, 7(6):8067–8101.

Mueller, R. W., Matsoukas, C., Gratzki, A., Behr, H. D., and Hollmann, R. (2009). The CM-SAF operational scheme for the satellite based retrieval of solar surface

irradiance — A LUT based eigenvector hybrid approach. *Remote Sensing of Environment*, 113(5):1012–1024.

Myhre, G., Shindell, D., Bréon, F.-M., Collins, W., Fuglestvedt, J., Huang, J., Koch, D., Lamarque, J.-F., Lee, D., Mendoza, B., Nakajima, T., Robock, A., Stephens, G., Takemura, T., and Zhang, H. (2013). Anthropogenic and Natural Radiative Forcing. In *Climate Change 2013: The Physical Science Basis. Contribution of Working Group I to the Fifth Assessment Report of the Intergovernmental Panel on Climate Change*, pages 659–740. Cambridge University Press, Cambridge, United Kingdom and New York, NY, USA.

NASA (2016a). Global Total Precipitable Water Vapor for May 2009. Available from: http://www.jpl.nasa.gov/spaceimages/details.php?id=PIA12097, 2016-10-04.

NASA (2016b). Ozone Hole Watch. Available from: http://ozonewatch.gsfc.nasa.gov/, 2016-09-09.

NASA (2018). AERONET. Available from: https://aeronet.gsfc.nasa.gov/, 2018-02-01.

Neher, I., Buchmann, T., Crewell, S., Evers-Dietze, B., Pfeilsticker, K., Pospichal, B., Schirrmeister, C., and Meilinger, S. (2017). Impact of atmospheric aerosols on photovoltaic energy production - Scenario for the Sahel zone. *Energy Procedia*, 125:170–179.

Neher, I., Buchmann, T., Crewell, S., Pospichal, B., and Meilinger, S. (2019). Impact of atmospheric aerosols on solar power. *Meteorologische Zeitschrift*, 28(4):305–321.

Neher, I., Crewell, S., Meilinger, S., Pfeifroth, U., and Trentmann, J. (2020). Photovoltaic power potential in West Africa using long-term satellite data. *Atmospheric Chemistry and Physics*, 20:12871–12888.

Niang, I., Ruppel, O., Abdrabo, M., Essel, A., Lennard, C., Padgham, J., and Urquhart, P. (2014). Africa. In *Climate Change 2014: Impacts, Adaptation and Vulnerability - Contributions of the Working Group II to the Fifth Assessment Report of the Intergovernmental Panel on Climate Change.*, pages 1199–1265. Cambridge University Press, Cambridge, United Kingdom and New York, NY, USA.

Peel, M. C., Finlayson, B. L., and McMahon, T. A. (2007). Updated world map of the Köppen-Geiger climate classification. *Hydrology and Earth System Sciences*, 11(5):1633–1644.

Penide, G., Giraud, V., Bouniol, D., Dubuisson, P., Duroure, C., Protat, A., and Cautenet, S. (2010). Numerical simulation of the 7 to 9 september 2006 AMMA mesoscale convective system: Evaluation of the dynamics and cloud microphysics using synthetic observations. *Quarterly Journal of the Royal Meteorological Society*, 136(s1):304–322.

Perez, R., David, M., Hoff, T. E., Jamaly, M., Kivalov, S., Kleissl, J., Lauret, P., and Perez, M. (2016). Spatial and Temporal Variability of Solar Energy. *Foundations and Trends® in Renewable Energy*, 1(1):1–44.

Perez, R., Seals, R., Zelenka, A., and Ineichen, P. (1990). Climatic evaluation of models that predict hourly direct irradiance from hourly global irradiance: Prospects for performance improvements. *Solar Energy*, 44(2):99–108.

Petty, G. W. (2006). *A First Course in Atmospheric Radiation*. Sundog Publishing, Madison, Wisconsin, second edi edition.

Pfeifroth, U., Kothe, S., Trentmann, J., Hollmann, R., Fuchs, P., Kaise, J., and Werscheck, M. (2019). Surface Radiation Data Set - Heliosat (SARAH) - Edition 2.1, Satellite Application Facility on Climate Monitoring.

Prasad, A. K., Singh, S., Chauhan, S. S., Srivastava, M. K., Singh, R. P., and Singh, R. (2007). Aerosol radiative forcing over the Indo-Gangetic plains during major dust storms. *Atmospheric Environment*, 41(29):6289–6301.

Pu, B. and Ginoux, P. (2018). How reliable are CMIP5 models in simulating dust optical depth? *Atmospheric Chemistry and Physics*, 18(16):12491–12510.

Quaschning, V. (2011). *Regenerative Energiesysteme*. Hanser Verlag Muenchen, 7. edition.

Quaschning, V., Kistner, R., and Ortmanns, W. (2001a). Simulation of parabolic trough power plants. *5th Cologne Solar Symposium*, pages 46–50.

Quaschning, V., Ortmanns, W., Kistner, R., and Geyer, M. (2001b). greenius: A New Simulation Environment for Technical and Economical Analysis of Renewable Independent Power Projects. In *Proceedings of Solar Forum 2001*, pages 413–418.

Ramdé, E. W., Azoumah, Y., Brew-Hammond, A., Rungundu, A., and Tapsoba, G. (2013). Site Ranking and Potential Assessment for Concentrating Solar Power in West Africa. *Natural Resources*, 04(1):146–153.

RECP (2019). Global Market Outlook: For Solar Power 2019-2023. Technical report, Africa-EU Renewable Energy Cooperation Programme. 92.

Redelsperger, J.-L., Thorncroft, C. D., Diedhiou, A., Lebel, T., Parker, D. J., and Polcher, J. (2006). African Monsoon Multidiscplinary Analysis: An International Research Project and Field Campaign. *Bulletin of the American Meteorological Society*, 87(12):1739–1746.

Reindl, D., Beckmann, W., and Duffie, J. (1990). Diffuse fraction correlations. *Solar Energy*, 45(1):1–7.

Rieger, D., Bangert, M., Bischoff-Gauss, I., Förstner, J., Lundgren, K., Reinert, D., Schröter, J., Vogel, H., Zängl, G., Ruhnke, R., and Vogel, B. (2015). ICON-ART 1.0 - A new online-coupled model system from the global to regional scale. *Geoscientific Model Development*, 8(6):1659–1676.

Rieger, D., Steiner, A., Bachmann, V., Gasch, P., Förstner, J., Deetz, K., Vogel, B., and Vogel, H. (2017). Impact of the 4 April 2014 Saharan dust outbreak on the photovoltaic power generation in Germany. *Atmospheric Chemistry and Physics*, 17(21):13391–13415.

Ross, R. and Gonzalez, C. (1980). Reference conditions for reporting terrestrial photovoltaic performance. *AS/ISES Annual Meeting*, pages 1091–1097.

Sakerin, S. M. and Kabanov, D. M. (2006). Spectral Dependences of the Atmospheric Aerosol Optical Depth in the Extended Spectral Region of 0.4-4 μm. In *Sixteenth ARM Science Team Meeting Proceedings*, pages 1–11.

Salam, Z., Ishaque, K., and Taheri, H. (2010). An improved two-diode photovoltaic (PV) model for PV system. *2010 Joint International Conference on Power Electronics, Drives and Energy Systems and 2010 Power India*, pages 1–5.

SCHOTT Solar (2013). SCHOTT PTR®70 Receivers, Dataheet. Technical report, SCHOTT Solar CSP GmbH. 2.

Sengupta, M., Habte, A., Kurtzn, S., Dobos, A., Wilbert, S., Lorenz, E., Stoffel, T., Renné, D., Myers, D., Wilcox, S., Blanc, P., and Perez, R. (2017). Best practices handbook for the collection and use of solar resource data for solar energy applications: Second Edition. Technical report, National Renewable Energy Laboratory. 251.

Setra Systems (2015). Model 278 - Barometric Pressure Transducer. Technical report, Setra Systems.

Sjerps-Koomen, E. A., Alsema, E. A., and Turkenburg, W. C. (1996). A simple model for PV module reflection losses under field conditions. *Solar Energy*, 57(6):421–432.

Skoplaki, E. and Palyvos, J. A. (2009). Operating temperature of photovoltaic modules: A survey of pertinent correlations. *Renewable Energy*, 34(1):23–29.

Skye Instruments (2019). Pyranometer SKS 1110. Technical report, Skye Instruments.

Slingo, A., Ackerman, T. P., Allan, R. P., Kassianov, E. I., McFarlane, S. A., Robinson, G. J., Barnard, J. C., Miller, M. A., Harries, J. E., Russell, J. E., and Dewitte, S. (2006). Observations of the impact of a major Saharan dust storm on the atmospheric radiation balance. *Geophysical Research Letters*, 33(L24817).

Slingo, A., Bharmal, N. A., Robinson, G. J., Settle, J. J., Allan, R. P., White, H. E., Lamb, P. J., Lélé, M. I., Turner, D. D., McFarlane, S., Kassianov, E., Barnard, J., Flynn, C., and Miller, M. (2008). Overview of observations from the RADAGAST experiment in Niamey, Niger: Meteorology and thermodynamic variables. *Journal of Geophysical Research: Atmospheres*, 113(D00E01).

Slingo, A., White, H., Bharmal, N. A., and Robinson, G. J. (2009). Overview of observations from the RADAGAST experiment in Niamey, Niger: 2. Radiative fluxes and divergences. *Journal of Geophysical Research: Atmospheres*, 114(D00E04).

Solar Millenium (2008). The parabolic trough power plants Andasol 1 to 3. Technical report, Solar Millennium. 1–26.

Solargis (2017). Solar Resource Map 2017. Available from: https://solargis.com/maps-and-gis-data/download/africa, 2018-09-24.

Solargis (2019). Solar Resource Map 2019. Available from: https://solargis.com/maps-and-gis-data/download/africa, 2020-02-27.

SolarWorld (2012). Data sheet of SolarWorld 235 poly module. Technical report, Solar World. 1–2.

SREEN (2012). Renewable Energy Sources and Climate Change Mitigation Special Report of the Intergovernmental Panel on Climate Change. Technical report, Intergovernmental Panel on Climate Change.

Srivastava, a. K., Yadav, V., Pathak, V., Singh, S., Tiwari, S., Bisht, D. S., and Goloub, P. (2014). Variability in radiative properties of major aerosol types: A year-long study over Delhi-An urban station in Indo-Gangetic Basin. *Science of the Total Environment*, 473-474:659–666.

Stamnes, K., Tsay, S., and Istvan, L. (2000). DISORT, a general-purpose Fortran program for discrete-ordinate-method radiative transfer in scattering and emitting layered media: documentation of methodology. Technical report, Stevens Institute of Technology, NASA Goddard Space Flight Center, University of Maryland. 112.

Stamnes, K., Tsay, S. C., Wiscombe, W., and Jayaweera, K. (1988). Numerically stable algorithm for discrete-ordinate-method radiative transfer in multiple scattering and emitting layered media. *Applied optics*, 27(12):2502–2509.

Sterl, S., Vanderkelen, I., Chawanda, C. J., Russo, D., Brecha, R. J., van Griensven, A., Van Lipzig, N. P., and Thiery, W. (2020a). Smart renewable electricity portfolios in West Africa. *Nature Sustainability*.

Sterl, S., Vanderkelen, I., Chawanda, C. J., Russo, D., Brecha, R. J., van Griensven, A., Van Lipzig, N. P., and Thiery, W. (2020b). Smart renewable electricity portfolios in West Africa - Supplementary Data 1. *Nature Sustainability*.

Stocker, T., Qin, D., Plattner, G.-K., Tignor, M., Allen, S., Boschung, J., Nauels, A., Xia, Y., Bex, V., and Midgley, P. (2014). *Climate Change 2013 - The Physical Science Basis*. Cambridge University Press, Cambridge, United Kingdom and New York, NY, USA.

Stone, R. S., Anderson, G. P., Shettle, E. P., Andrews, E., Loukachine, K., Dutton, E. G., Schaaf, C., and Roman, M. O. (2008). Radiative impact of boreal smoke in the Arctic: Observed and modeled. *Journal of Geophysical Research: Atmospheres*, 113(D14S16).

Tamizhmani, G., Ji, L., Tang, Y., Petacci, L., and Osterwald, C. (2003). Photovoltaic Module Thermal/Wind Performance : Long-Term Monitoring and Model Development For Energy Rating. In *NCPV and Solar Program Review Meeting*, pages 936–939.

Tanre, D., Geleyn, J. F., and Slingo, J. (1984). First results of the introduction of an advanced aerosol-radiation interaction in the ECMWF low resolution global model. In Deepak, H. E. G. and A., editors, *Aerosols and Their Climatic Effects: Proceedings of the Meetings of Experts, Williamsburg, Virginia, 28–30 March 1983*, pages 133–177. A. Deepak, Hampton, Va.

Taylor, J. W., Haslett, S. L., Bower, K., Flynn, M., Crawford, I., Dorsey, J., Choularton, T., Connolly, P. J., Hahn, V., Voigt, C., Sauer, D., Dupuy, R., Brito, J., Schwarzenboeck, A., Bourriane, T., Denjean, C., Rosenberg, P., Flamant, C., Lee, J. D., Vaughan, A. R., Hill, P. G., Brooks, B., Catoire, V., Knippertz, P., and Coe, H. (2019). Aerosol influences on low-level clouds in the West African monsoon. *Atmospheric Chemistry and Physics*, 19(13):8503–8522.

Thies Clima (2005). Temperature Transmitter. Technical report, Adolf Thies GmbH & Co.KG.

Thies Clima (2019). Wind Transmitter Classic. Technical report, Adolf Thies GmbH & Co. KG.

UNFCCC (2015). Paris Agreement. Technical report, United Nations. 32.

United Nations (2015). Sustainable Development Goals. Available from: https://sdgs.un.org/goals, 2015-08-05.

Vaisala (2006). Vaisala HUMICAP ® Humidity and Temperature Probes - HMP45A/D. Technical report, Vaisala.

Wallace, J. M. and Hobbs, P. V. (2006). *Atmospheric Science: An Introductory Survey*. Academic Press, second edition.

Wendisch, M. and Yang, P. (2012). *Theory of atmospheric radiative transfer: A comprehensive introduction*. John Wiley & Sons, Weinheim.

Wild, M. (2012). Enlightening global dimming and brightening. *Bulletin of the American Meteorological Society*, 93(1):27–37.

Wind (2007). Wind Monitor MA - Model 05106. Technical report, R.M.Young.

Wiscombe, W. J. (1980). Improved Mie scattering algorithms. *Applied optics*, 19(9):1505–9.

WMO (2010). Guide to Meteorological Instruments and Methods of Observation 2008. Technical report, World Meteorological Organization.

Worldpress (2012). Atmospheric Absorption Bands. Available from: https://chiefio.wordpress.com/2012/12/17/co2-water-issue/, 2020-03-25.

Yoon, J., Von Hoyningen-Huene, W., Kokhanovsky, A. A., Vountas, M., and Burrows, J. P. (2012). Trend analysis of aerosol optical thickness and Angström exponent derived from the global AERONET spectral observations. *Atmospheric Measurement Techniques*, 5(6):1271–1299.

Yoshioka, M., Mahowald, N. M., Conley, A. J., Collins, W. D., Fillmore, D. W., Zender, C. S., and Coleman, D. B. (2007). Impact of desert dust radiative forcing on sahel precipitation: Relative importance of dust compared to sea surface temperature variations, vegetation changes, and greenhouse gas warming. *Journal of Climate*, 20(8):1445–1467.

Yushchenko, A., de Bono, A., Chatenoux, B., Patel, M. K., and Ray, N. (2018). GIS-based assessment of photovoltaic (PV) and concentrated solar power (CSP) generation potential in West Africa. *Renewable and Sustainable Energy Reviews*, 81(June):2088–2103.

List of Figures

List of Tables

List of abbreviations and symbols

α	Ångström exponent
α_{PV}	Modules azimuth angle
α_{sun}	Suns azimuth
β	Ångström coefficient
β_{abs}	Absorption coefficient
β_{ext}	Extinction coefficient
β_{sca}	Scattering coefficient
Δ	Brightness
γ	Suns zenith
λ	Wavelength
ν	Scattering angle
Ω	Spatial direction of light
Φ	Modules tilt angle
ϕ_r	Angle of refraction
σ_{abs}	Absorption cross section
σ_{sca}	Scattering cross section
τ	Transmittance
CH_4	Methane
CO_2	Carbon dioxide
H_2SO_4	Sulfuric acid
N_2O	Nitrous oxide
O_2	Oxygen
O_3	Ozone
$\vec{s}$	Path
A	Anisotropy index
a, b	Empirical parameters for different models
alb	Albedo
$B_\lambda(T)$	Planck function
C_i	Empirical parameters of the inverter model
D_i	Diodes
F_i	Empirical parameters for the Perez model
f_{ij}	Coefficients of the Perez model
I_λ	Radiance

I_{Di}	Saturation current of diode
I_{PH}	Photocurrent
I_{SC}	Short-circuit current
K	Glazing extinction coefficient
k_{boltz}	Boltzmann constant
L	Glazing thickness
m_r	Relative optical air mass
n	Effective index of refraction
$n(r)$	Size distribution
N_C	Particle number concentration
n_i	Diode ideality factor
N_s	Number of cells in series
p	Phase function
q	Elementary charge
Q_{abs}	Absorption efficiency
Q_{ext}	Extinction efficiency
Q_{sca}	Scattering efficiency
r	Radius
R_P	Resistor in parallel
R_S	Resistor in series
T	Ambient temperature
T_c	Cell temperature
U_T	Thermal voltage
U_{OC}	Open-circuit voltage
U_{PH}	Cell voltage
v_w	Wind speed
w_i, *const*	Coefficients for cell temperature model
x	Size parameter
z	Vertical height
greenius	Green energy system analysis tool
AC	Alternating current
AM	Air mass
AOI	Angle of incidence
CAL	Effective cloud albedo
CdTe	Cadmium telluride
CERES	Clouds and the Earth's Radiant Energy System
CIS	Copper indium diselenide
CM SAF	Climate monitoring satellite application facility
DACCIWA	Dynamics-Aerosol-Chemistry-Cloud Interactions in West Africa
DC	Direct current
DLR	German Aerospace Centre
DRT	Direct tilted irradiance

DTI	Diffuse tilted irradiance
DWD	German weather service
ECMWF	European Center for Medium Range Weather Forecast
ECOWAS	Economic community of West African states
ERA	ECMWF Re-Analysis
EREP	ECOWAS Renewable Energy Policy
EUMETSAT	European organisation for the exploitation of meteorological satellites
EXI	Extraterrestrial irradiance
GERB	Geostationary Earth Radiation Budget
GHG	Greenhouse gas
GTI	Global tilted irradiance
HBRS	University of Applied Science Bonn-Rhein-Sieg
I	Current
IAM	Incident angle modifier
INSO	Insoluble aerosols
IPCC	Intergovernmental Panel on Climate Change
IRENA	International renewable energy agency
ITCZ	Intertropical convergence zone
KIT	Karlsruher institute of technology
labVIEW	Laboratory virtual instrumentation engineering workbench
MACC	Monitoring Atmospheric Composition and Climate
MIAM	Mineral aerosols in accumulation mode
MICM	Mineral aerosols in coarse mode
MINM	Mineral aerosols in nucleation mode
MITR	Mineral aerosols transported
MPI-M	Max Planck Institute for Meteorology
MVIRI	Visible-infrared imager
NOCT	Nominal operating cell temperature
PT	Parabolic trough
PTP	PT power
PV	Photovoltaic
PVAC	PV power
REF	Reflected irradiance
RTE	Radiative transfer equation
SARAH-2.1	Surface Solar Radiation Data Record – Heliosat Edition 2.1
SARB	Surface and Atmospheric Radiation Budget
SDG	Sustainable Development Goals
SDU	Daily sunshine duration
SEVIRI	Spinning enhanced visible and infrared imager
SOOT	Black carbon aerosols
SRI	Spectral resolved irradiance

SSAM	Sea salt in accumulation mode
SSCM	Sea salt in coarse mode
STC	Standard test conditions
SUSO	Sulfate droplets
SW235poly	Solar World 235 polycrystalline PV module
TOA	Top of the atmosphere
U	Voltage
WASO	Water-soluble aerosols

Acknowledgment

First, I would like to thank the Heinrich Böll Foundation for my PhD fellowship, the financial and ideally support during the last four years.

Stefanie, thank you for the constant and regularly supervision you provided. For your support during my whole PhD time and the help and discussion on all my questions, which significantly improved this thesis.

Susanne, thank you for supervising this work and giving me the possibility to write my thesis at the University of Cologne. Thanks for all the wonderful and inspiring discussions and remarks during the last four years.

A great thank goes to the complete IZNE team as well as to Bernd, for giving me the scientific surrounding to research and let me take part on interdisciplinary projects within the group. And of coarse, to talk about different topics than my PhD during lunch or coffee breaks.

Tina, thank you for being my frequent discussion partner, especially during the first two years of my PhD. Thanks for all your remarks on presentations, manuscripts and your friendship!

Bernhard, thank you for your always open ear. For answering all my questions and proof-reading my work.

Uwe and Jörg, thank you for your advise and help during the preparation of the SARAH publication.

Vanessa, thank you for the preparation and provision of the ICON-ART data.

Bernhard Meyer and Claudia Emde, thank you for your help with the simulation in libRadtran.

Thanks to all data providers of the different publications (Neher et al. 2020, 2019, 2017). Data in Niamey were obtained from the Atmospheric Radiation Measurement (ARM) Climate Research Facility, a U.S. Department of Energy Office of Science user facility sponsored by the Office of Biological and Environmental Research and from ECMWF/MACC project. Data in Sankt Augustin have been obtained in close collaboration with MeteoGroup. The installation of the equipment was partly financed by the ministry for Innovation, Science and Research of the federal state Nordrhein-Westfalen, Germany. We thank Philippe Goloub and Didier Tanre for their effort in establishing and maintaining AERONET sites in Agougou, Banizoumbou, Dakar, Djougou and Maine and provide aerosol data. Meteorological data was used from the AMMA Database. Based on an French initiative, AMMA was built by an international scientific group and is currently funded by a large number

of agencies, especially from France, UK, US and Africa. It has been the beneficiary of a major financial contribution from the European Community's Sixth Framework Research Program. Detailed information on scientific coordination and funding is available on the AMMA International web site http://www.amma-international.org.

I want to express my biggest gratitude to my family, Michael, Amaya, Pauline and Layla, thanks for being what you are!

Erklärung

Hiermit versichere ich an Eides statt, dass ich die vorliegende Dissertation selbstständig und ohne die Benutzung anderer als der angegebenen Hilfsmittel und Literatur angefertigt habe. Alle Stellen, die wörtlich oder sinngemäß aus veröffentlichten und nicht veröffentlichten Werken dem Wortlaut oder dem Sinn nach entnommen wurden, sind als solche kenntlich gemacht. Ich versichere an Eides statt, dass diese Dissertation noch keiner anderen Fakultät oder Universität zur Prüfung vorgelegen hat; dass sie - abgesehen von unten angegebenen Teilpublikationen und eingebundenen Artikeln und Manuskripten - noch nicht veröffentlicht worden ist sowie, dass ich eine Veröffentlichung der Dissertation vor Abschluss der Promotion nicht ohne Genehmigung des Promotionsausschusses vornehmen werde. Die Bestimmungen dieser Ordnung sind mir bekannt. Darüber hinaus erkläre ich hiermit, dass ich die Ordnung zur Sicherung guter wissenschaftlicher Praxis und zum Umgang mit wissenschaftlichem Fehlverhalten der Universität zu Köln gelesen und sie bei der Durchführung der Dissertation zugrundeliegenden Arbeiten und der schriftlich verfassten Dissertation beachtet habe und verpflichte mich hiermit, die dort genannten Vorgaben bei allen wissenschaftlichen Tätigkeiten zu beachten und umzusetzen. Ich versichere, dass die eingereichte elektronische Fassung der eingereichten Druckfassung vollständig entspricht.

Florstadt, den 08. April 2020

Ina Neher

Teilpublikationen

Neher, I., Buchmann, T., Crewell, S., Evers-Dietze, B., Pfeilsticker, K., Pospichal, B., Schirrmeister, C., and Meilinger, S. (2017). Impact of atmospheric aerosols on photovoltaic energy production - Scenario for the Sahel zone. *Energy Procedia*, 125:170–179.

Neher, I., Buchmann, T., Crewell, S., Pospichal, B., and Meilinger, S. (2019). Impact of atmospheric aerosols on solar power. *Meteorologische Zeitschrift*, 28(4):305–321.

Neher, I., Crewell, S., Meilinger, S., Pfeifroth, U., and Trentmann, J. (2020). Photovoltaic power potential in West Africa using long-term satellite data. *Atmospheric Chemistry and Physics*, 20:12871–12888.